TECHNISCHE UNIVERSITÄT MÜNCHEN

Max-Planck-Institut für Physik
(Werner-Heisenberg-Institut)

Search for Light Charged Higgs Bosons in Hadronic τ Final States with the ATLAS Detector

Thies Ehrich

Vollständiger Abdruck der von der Fakultät für Physik der Technischen Universität München zur Erlangung des akademischen Grades eines

Doktors der Naturwissenschaften (Dr. rer. nat.)

genehmigten Dissertation.

Vorsitzender: Univ.-Prof. Dr. A. Ibarra
Prüfer der Dissertation:
1. Priv.-Doz. Dr. H. Kroha
2. Univ.-Prof. Dr. L. Oberauer

Die Dissertation wurde am 17. Juni 2010 bei der Technischen Universität München eingereicht und durch die Fakultät für Physik am 7. Juli 2010 angenommen.

Abstract

Charged Higgs bosons are predicted in theories with a non-minimal Higgs sector like the Minimal Supersymmetric Extension of the Standard Model (MSSM). At the LHC, light charged Higgs Bosons might be produced in on-shell top quark decays $t \rightarrow H^+b$, if $m_{H^\pm} < m_t - m_b$. In most of the MSSM parameter space, the decay $H^+ \rightarrow \tau\nu$ is the dominant decay channel and suggests the possibility of using the unique signature of hadronic τ final states to suppress the backgrounds.

The subject of this study is the estimation of the sensitivity of the ATLAS detector for charged Higgs boson searches in $t\bar{t}$ events. Leptons from the decay chain of the second top quark allow for efficient triggering. A search strategy is developed and estimates of signal significances and exclusion limits in the MSSM m_h-max scenario are presented based on Monte Carlo simulations. For an integrated luminosity of 10 fb^{-1}, the discovery of charged Higgs bosons is possible for $\tan\beta > 32$. Exclusion limits are given for values of $\tan\beta > 17$, significantly improving the current best limits from the Tevatron.

The most important systematic uncertainties were found to be the errors on the jet energy scale and the missing transverse energy, resulting in a total systematic uncertainty of 40% on the signal. To reduce the systematic uncertainty for the most important Standard Model background, $t\bar{t}$ production, emphasis is put on estimating this background using data instead of Monte Carlo simulations. The $t\bar{t}$ background consists of two contributions, one with a correctly identified τ-jet in the final state, which is irreducible, and one where the hadronic τ decay is faked by a light parton jet. For each background a method has been developed to estimate its contribution with minimal use of Monte Carlo simulations. In this way, the systematic uncertainty on the background can be significantly reduced.

Contents

Chapter 1

Introduction

In the nineteen-sixties, the Standard Model of particle physics was developed to describe the elementary constituents of matter and their interactions. Three of the four known interactions, namely the electromagnetic, the weak and the strong interactions, are described by gauge theories requiring invariance under transformations of the gauge symmetry group $U(1) \otimes SU(2) \otimes SU(3)$. To date, the predictions of the Standard Model are in excellent agreement with experimental data.
However, one basic ingredient of the Standard Model has not been observed so far. The Higgs boson, associated with the generation of particle masses by spontaneous gauge symmetry breaking, remains elusive. Electroweak precision measurements indicate a rather light Higgs boson with a mass below 186 GeV, which allows for either its discovery or its exclusion at the LHC.
Even if the Higgs boson is found, there are doubts that the Standard Model fully describes nature up to the highest energies far beyond the electroweak scale of about 1 TeV since it cannot explain why the Higgs boson should be light. Another argument for physics beyond the Standard Model is the unification of the couplings of the three gauge interactions at high energies. Finally, the matter in the universe is dominated by dark matter, not described by the Standard Model.
These problems are solved by extending the Standard Model with Supersymmetry, a symmetry relating fermions and bosons. It postulates superpartners for each Standard Model particle and at least five Higgs bosons, three of them neutral and two charged. One neutral Higgs boson is predicted to be naturally light and the three gauge couplings can unify at high energies. Depending on the choice of parameters, one of the new particles is a candidate for the observed dark matter in the universe.
The Minimal Supersymmetric Extension of the Standard Model (MSSM) is the most simple and best studied supersymmetric theory of elementary particles. Charged Higgs bosons $(H^{\pm})$[1] are produced in decays of the top quark, $t \rightarrow H^{+}b$, if they are light enough. Due to the high production cross section of $t\bar{t}$ quark pairs in proton-proton collisions at a center of mass energy of 14 TeV, light charged Higgs bosons are copiously produced at the LHC, if they exist. In most of the MSSM parameter space, the decay $H^{+} \rightarrow \tau\nu$ acquires a branching ratio of close to one, allowing for searches in $t\bar{t}$ events with final states including τ leptons. In this thesis, a strategy is developed to search for light charged Higgs bosons in the semi-leptonic decay channel

[1] In the following, only one of the two charged Higgs boson states H^{+} is mentioned implying the corresponding relation for the charged conjugated state H^{-}.

$t\bar{t} \rightarrow (H^+b)\left(W\bar{b}\right) \rightarrow (\tau_{\text{had}}\nu b)\left(\ell\bar{\nu}\bar{b}\right)$ with the ATLAS detector. Emphasis is put on the reduction of detector related systematic uncertainties by estimating the dominant Standard Model background of $t\bar{t}$ production without decays in charged Higgs bosons from data. This background consists of two contributions, one with a correctly identified τ-jet and one where a light parton jet is wrongly reconstructed as a τ-jet. In each case, the accuracies of the proposed methods are investigated using different τ-jet identification algorithms. Signal significances and exclusion limits are calculated for the MSSM m_h-max scenario.

This thesis is organized as follows: In Chapters 2 and 3 the Standard Model and its supersymmetric extension are outlined. The phenomenology of charged Higgs boson production and decay at the LHC is presented in Chapter 4, while the ATLAS experiment is described in Chapter 5. Chapter 6 is dedicated to the investigation of the particle reconstruction and identification performance of the ATLAS detector using Monte Carlo simulation. The search strategy for light charged Higgs bosons is presented in Chapter 7, while in Chapters 8 and 9 the methods for estimating the $t\bar{t}$ background from the data are described and their accuracies are estimated. The resulting expectations for the achievable signal significances and exclusion limits for light charged Higgs bosons are summarized in Chapter 10.

Chapter 2

The Standard Model of Particle Physics

The **S**tandard **M**odel of particle physics is a theoretical framework that describes three of the four known fundamental interactions:

- the electromagnetic interaction,
- the weak interaction and
- the strong interaction.

Gravitation is not included in this framework. The energy scale where quantum effects of gravitation have to be taken into account in the description of particle interactions is the reduced Planck mass $M_{\text{Planck}} = 2.4 \times 10^{18}$ GeV. At this scale, at the latest, the Standard Model has to be replaced by a more general theory.
In the sixties of the 20th century it was shown by Glashow, Salam and Weinberg that the weak and electro-magnetic interactions can be unified to the electroweak interaction. Today the Standard Model of particle physics is understood as a theory of electroweak and strong interactions.
Both are described by quantum field theories governed by symmetry principles. In addition to the transformations of the Poincaré group, these theories obey local gauge symmetries determining the fundamental interactions.
Over several decades, the Standard Model has been confirmed by many measurements with impressive precision. However, there are several open questions and limitations indicating the need for an extension of the theory.
After the introduction of the Lagrange formalism in Section 2.1, Quantum Electrodynamics (QED), the electroweak theory (Glashow-Salam-Weinberg theory, GSW) and Quantum Chromodynamics (QCD) will be shortly described in Section 2.2, 2.3 and 2.4. In Section 2.5 the Higgs mechanism is introduced, which provides an elegant solution to one of the most important questions in particle physics: the origin of the particle masses. Section 2.6 is dedicated to the new particle predicted by this mechanism, the Higgs boson. In Section 2.7 the limitations of the Standard Model are discussed.

2.1 Lagrange Formalism

Classical mechanics is governed by the Lagrange function $L(q^i, \dot{q}^i)$, a function of the particle coordinates q^i and their time derivatives $\dot{q} = dq^i/dt$. Given the kinetic energy T and the potential energy U, the Lagrange function for systems with conserved energy is given by $L = T - U$. A particle with the mass m and coordinates $\vec{x}$ moving in a force field is described by the Lagrange function $L = \frac{1}{2}m\dot{\vec{x}}^2 - U(\vec{x})$.
The equations of motion of a physical system are the Euler-Lagrange equations

$$\frac{d}{dt}\frac{\partial L}{\partial \dot{q}^i(t)} - \frac{\partial L}{\partial q^i(t)} = 0, \tag{2.1}$$

which, in the above example, yield Newton's second law: $\vec{F}(\vec{x}(t)) \equiv -\nabla U(x) = m\ddot{\vec{x}}(t)$. The Euler-Lagrange equations are derived from Hamilton's principle of least action. This fundamental law states that the action

$$S\left[q^i(t)\right] = \int_{t_0}^{t_1} L\left(q^i(t), \dot{q}^i(t)\right)\, dt \tag{2.2}$$

has an extremum for the true trajectory $q^i(t)$ [1].
These principles can be extended to field theories by replacing the coordinates and velocities q^i and $\dot{q}^i(t)$ by the fields $\varphi^i(x)$ and the associated momenta $\pi^i(x) = \partial L/\partial\dot{\varphi}^i$, respectively. The Lagrange function is then given by the integral over the Lagrange density or Lagrangian $\mathscr{L}$:

$$L = \int \partial x^\mu\, \mathscr{L}\left(\varphi^i, \partial^\mu\varphi^i\right). \tag{2.3}$$

For example, the Lagrange densities for a free spin-0 scalar field φ and a Dirac fermion field ψ with the masses m are (with $\hbar = c = 1$)

$$\mathscr{L}_{\text{scalar}} = \partial_\mu\varphi\partial^\mu\varphi^* - m^2\varphi^*\varphi \quad \text{and} \tag{2.4}$$

$$\mathscr{L}_{\text{fermion}} = i\overline{\psi}(x)\gamma^\mu\partial_\mu\psi(x) - m\overline{\psi}\psi, \tag{2.5}$$

respectively, where $\partial^\mu = \partial/\partial x^\mu$ and γ^μ are the Dirac gamma matrices [2]. Here and in the following summation over equal indices is always implied. The Euler-Lagrange equation (2.1) yields the Dirac equation for the fermion field and the Klein-Gordon equation for the scalar field.

2.2 Quantum Electrodynamics

The gauge interactions of the Standard Model are determined by the requirement that the Lagrangian is invariant under local phase transformations. One example is the $U(1)_Q$ group, the group of linear transformations of complex numbers leaving their norm unchanged. The local $U(1)_Q$ gauge transformations $U(x)$ of a Dirac spinor field $\psi(x)$, for example, are represented by the local phase transformations:

$$\psi(x) \to \psi'(x) = U(x)\psi(x) = e^{iQ\Lambda(x)}\psi(x), \tag{2.6}$$

where e is the elementary charge. Since the phase Λ depends on x, the derivatives of the field ψ in (2.5) transform differently than the field itself:

$$\partial^\mu \psi(x) \to (\partial^\mu \psi(x))' = e^{iQ\Lambda(x)} \left(\partial^\mu + iQ\partial^\mu \Lambda\right) \psi(x). \tag{2.7}$$

To construct a gauge invariant Lagrangian, the derivative ∂^μ is replaced by the covariant derivative D^μ which transforms like the field:

$$D^\mu \psi \to (D^\mu \psi)' = U D^\mu \psi. \tag{2.8}$$

The covariant derivative is given by

$$D^\mu \equiv \partial^\mu + ieQA(x) \tag{2.9}$$

introducing the gauge field A^μ in order to cancel the term $iQ\partial_\mu \Lambda$ in Equation (2.7). This requirement completely fixes the transformation rule for the gauge field A^μ [3]:

$$A'^\mu = A^\mu - \frac{1}{e}\partial^\mu \Lambda. \tag{2.10}$$

The Lorentz 4-vector field A^μ corresponds to a spin-1 field, the photon field. It fulfills the Maxwell equations, which are covariant under the gauge transformations (2.10). By substituting the derivatives ∂^μ in (2.5) by the new covariant derivatives D^μ, a term containing the gauge field A^μ is added to the Lagrangian. It describes the electromagnetic coupling of the Dirac fermion ψ to the photon field A^μ.
The complete Lagrangian of quantum electrodynamics then reads:

$$\mathscr{L}_{\text{QED}} = -\frac{1}{4} F_{\mu\nu}(x) F^{\mu\nu}(x) + i\overline{\psi}(x)\gamma^\mu \partial_\mu \psi(x) - m\overline{\psi}\psi - eQA_\mu(x)\overline{\psi}\gamma^\mu \psi(x), \tag{2.11}$$

including a kinetic term for the free photon field:

$$\mathscr{L}_{\text{kin}} = -\frac{1}{4} F_{\mu\nu}(x) F^{\mu\nu}(x) \tag{2.12}$$

with the electromagnetic field tensor

$$F^{\mu\nu} \equiv \partial^\mu A^\nu - \partial^\nu A^\mu.$$

Consistent with all experimental results, no mass term $\frac{1}{2}m^2 A^\mu A_\mu$ for the photon field appears in the Lagrangian. In fact, such a term would violate the $U(1)_Q$ gauge symmetry since

$$\frac{1}{2}m^2 A^\mu A_\mu \to \frac{1}{2}m^2 (A^\mu - \frac{1}{e}\partial^\mu \Lambda)(A_\mu - \frac{1}{e}\partial_\mu \Lambda) \neq \frac{1}{2}m^2 A^\mu A_\mu. \tag{2.13}$$

2.3 The Electroweak Interaction

The unified theory of electromagnetic and weak interactions introduced by Glashow, Salam and Weinberg (GSW) [4, 5, 6] is based on the gauge symmetry group $SU(2)_L \otimes U(1)_Y$. It describes the electroweak interactions between fermions by the exchange of spin-1 gauge bosons. The Lagrange densities for the gauge fields (bosons) and the matter fields (fermions) can be formulated similarly as in Section 2.2. The local weak isospin symmetry group $SU(2)_L$ implies the existence of three gauge bosons corresponding to the three generators of the group, the components of the weak isospin vector. The requirement of $U(1)_Y$ gauge invariance results in a fourth gauge boson corresponding to the conserved weak hypercharge Y.
An important observable of the electroweak theory is chirality. Each fermion field consists of a right- and a left-handed component. In the case of massless particles, these components are identical with the helicity eigenstates. The right- (left-) handed massless states $\Psi_{R(L)}$ have positive (negative) helicity implying (anti-) parallel orientation of spin and momentum. Experiments have shown that only left-handed fermions take part in weak interactions. These are therefore arranged in $SU(2)_L$ doublets Ψ_L^d ($d = e, \mu, \tau, u, c, t$)

$$\Psi_L^d = \begin{pmatrix} \nu_e \\ e^- \end{pmatrix}_L, \begin{pmatrix} \nu_\mu \\ \mu^- \end{pmatrix}_L, \begin{pmatrix} \nu_\tau \\ \tau^- \end{pmatrix}_L, \begin{pmatrix} u \\ d \end{pmatrix}_L, \begin{pmatrix} c \\ s \end{pmatrix}_L, \begin{pmatrix} t \\ b \end{pmatrix}_L, \tag{2.14}$$

The right handed charged fermions Ψ_R^s ($s = e, \mu, \tau, u, d, c, s, t, b$)

$$\Psi_R^s = e_R^-, \mu_R^-, \tau_R^-, u_R, d_R, c_R, s_R, t_R, b_R \tag{2.15}$$

are $SU(2)_L$ singlet states and do not interact weakly. In addition, for each fermion field ψ an anti-fermion $\overline{\psi}$ is included in the Standard Model. Right handed neutrinos are not listed because they interact only gravitationally.
The Lagrangian $\mathscr{L}_{\text{GSW}}$ of the electroweak theory consists of a term for the fermion and one for the gauge fields:

$$\mathscr{L}_{\text{GSW}} = \mathscr{L}_{\text{gauge}} + \mathscr{L}_{\text{fermions}}. \tag{2.16}$$

The first term in Equation (2.16) describes the free gauge fields:

$$\mathscr{L}_{\text{gauge}} = -\frac{1}{4} F^i_{\mu\nu} F^{\mu\nu}_i - \frac{1}{4} f_{\mu\nu} f^{\mu\nu} \text{ with} \tag{2.17}$$

$$F^i_{\mu\nu} = \partial_\mu W^i_\nu - \partial_\nu W^i_\mu - g\epsilon^{ijk} W^j_\mu W^k_\nu \text{ and} \tag{2.18}$$

$$f_{\mu\nu} = \partial_\mu B_\nu - \partial_\nu B_\mu. \tag{2.19}$$

W^i_μ ($i = 1, 2, 3$) denotes the three gauge fields of the $SU(2)_L$ group and B_μ the one of the $U(1)_Y$ group. The gauge couplings are given by g and g', respectively. The generators of $SU(2)_L$ and $U(1)_Y$ are represented by the Pauli matrices σ_i ($i = 1, 2, 3$) and the weak hypercharge Y, respectively [2]. The quadratic term in Equation (2.18) is due to the non-Abelian nature of the $SU(2)_L$ group, leading to self-interactions of the weak gauge fields W^i.
The charged mass eigenstates $W^\pm$ of the weak gauge bosons are given by the linear combinations

$$W^\pm_\mu = \frac{1}{\sqrt{2}} \left(W^1_\mu \mp i W^2_\mu \right). \tag{2.20}$$

Table 2.1: Fermion and gauge boson content of the Standard Model. In (a) the three fermion generations are given. The index i of the quarks denotes the color quantum number ($i =$ red, green, blue). In (b) the fundamental interactions and the corresponding gauge bosons are listed. The strengths of the interactions are given in relation to the strong force [3]. Gravitation is added for comparison.

(a)

	Generations 1	2	3
Leptons	ν_e	ν_μ	ν_τ
	e	μ	τ
Quarks	u_i	c_i	t_i
	d_i	s_i	b_i

(b)

Force	Mediating Bosons	Rel. Strength	Range
Strong	Gluons $g_1, \ldots, g_8$	1	10^{-15} m
Electromagnetic	Photon γ	10^{-2}	∞
Weak	$W^\pm, Z$	10^{-5}	10^{-18} m
Gravitation	Graviton	10^{-40}	∞

Similarly the fields B_μ and W_μ^3 mix to give the physical neutral Z boson and the photon A:

$$\begin{pmatrix} Z_\mu \\ A_\mu \end{pmatrix} = \begin{pmatrix} \cos\theta_W & -\sin\theta_W \\ \sin\theta_W & \cos\theta_W \end{pmatrix} \begin{pmatrix} W_\mu^3 \\ B_\mu \end{pmatrix}. \tag{2.21}$$

The mixing angle θ_W, referred to as the *Weinberg* angle, is determined by the two coupling constants g and g' according to the relations

$$\cos\theta_W = g/\sqrt{g^2 + g'^2} \quad \text{and} \tag{2.22}$$

$$\sin\theta_W = g'/\sqrt{g^2 + g'^2}. \tag{2.23}$$

The Lagrangian for the fermions including their electroweak interactions via gauge bosons is given by

$$\mathscr{L}_{\text{fermions}} = i \sum_{\text{doublets d}} \overline{\psi}_L^d \gamma^\mu D_{\mu_L} \psi_L^d + i \sum_{\text{singlets s}} \overline{\Psi}_R^s \gamma^\mu D_{\mu_R} \Psi_R^s. \tag{2.24}$$

The covariant derivatives

$$D_{\mu_L}\psi_L = \left[\partial_\mu + i\frac{g}{2}\sigma_i W_\mu^i + i\frac{g'}{2} Y B_\mu\right] \psi_L \quad \text{and} \tag{2.25}$$

$$D_{\mu_R}\Psi_R = \left[\partial_\mu + i\frac{g'}{2} Y B_\mu\right] \Psi_R \tag{2.26}$$

ensure local gauge invariance under $SU(2)_L \otimes U(1)_Y$ transformations.

2.4 Quantum Chromodynamics

Also the strong interaction is described by a gauge theory named Quantum Chromodynamics [7, 8]. The strong interaction takes place between particles carrying color charges, namely quarks

and gluons. The QCD Lagrangian

$$\begin{aligned} \mathscr{L}_{\text{QCD}} &= -\frac{1}{4}F^i_{\mu\nu}F_i^{\mu\nu} + \overline{\psi}(i\gamma_\mu D^\mu - m)\psi \\ F_i^{\mu\nu} &= \partial^\mu G_i^\nu - \partial^\nu G_i^\mu - g_s f_{ikl} G_k^\mu G_l^\nu \end{aligned} \tag{2.27}$$

is invariant under local $SU(3)_C$ transformations. Here the index i ($i = 1, .., 8$) denotes the eight $SU(3)_C$ gauge boson fields, the gluon fields G_i^μ. f_{jkl} are the structure constants of the gauge group and g_s the coupling constant. The interactions between quarks and gluons arise via covariant derivatives

$$D_\mu = \partial_\mu + i\frac{g_s}{2}\lambda_i G_\mu^j, \tag{2.28}$$

where λ_j are the Gell-Mann matrices representing the $SU(3)_C$ generators. Due to the non-Abelian nature of $SU(3)_C$, gluon self-interactions are introduced as in the electroweak gauge theory.
No free color-charged particles have been observed. They only appear bound in colorless mesons and baryons. This phenomenon, called "confinement", is reproduced by QCD. In addition the quarks and gluons behave almost as free particles at short distances within the bound states, an effect called "asymptotic freedom". Indeed experiments confirm the QCD prediction that the coupling constant g_s depends on the momentum transfer Q^2 of a strong process, diverging for $Q^2 \to 0$ and decreasing for $Q^2 \to \infty$ [9, 10, 11].
The fermions and gauge bosons of the Standard Model are summarized in Table 2.1.

2.5 Spontaneous Electroweak Symmetry Breaking – The Higgs Mechanism

The Lagrangian (2.16) does not include mass terms for the weak gauge bosons since they would violate the local $SU(2)_L \otimes U(1)_Y$ gauge symmetry. However, experiments have proven that the weak gauge bosons are heavy objects. Inspired by condensed matter physics[1], spontaneous local gauge symmetry breaking has been proposed by P. Higgs [12, 13] and others [14, 15] to solve this problem. An additional weak isospin doublet

$$\Phi = \begin{pmatrix} \Phi^+ \\ \Phi^0 \end{pmatrix} = \frac{1}{\sqrt{2}} \begin{pmatrix} \Phi^1 - i\Phi^2 \\ \Phi^3 - i\Phi^4 \end{pmatrix} \tag{2.29}$$

is introduced with the electrically charged and neutral complex scalar fields Φ^+ and Φ^0, respectively. The Lagrangian for the field Φ is given by

$$\mathscr{L}_{\text{Higgs}} = (D_\mu \Phi)^\dagger (D^\mu \Phi) - V(\Phi, \Phi^\dagger), \quad \text{where} \tag{2.30}$$

$$V(\Phi, \Phi^\dagger) = \mu^2(\Phi\Phi^\dagger) + \lambda(\Phi\Phi^\dagger)^2. \tag{2.31}$$

[1] Spontaneous symmetry breaking, for instance, occurs in the superconducting phase transition: Below the critical temperature the electrons in superconductors form Cooper pairs constituting a scalar field and static magnetic fields are expelled from the superconductor. This effect can be understood by the photon acquiring mass in the superconducting phases.

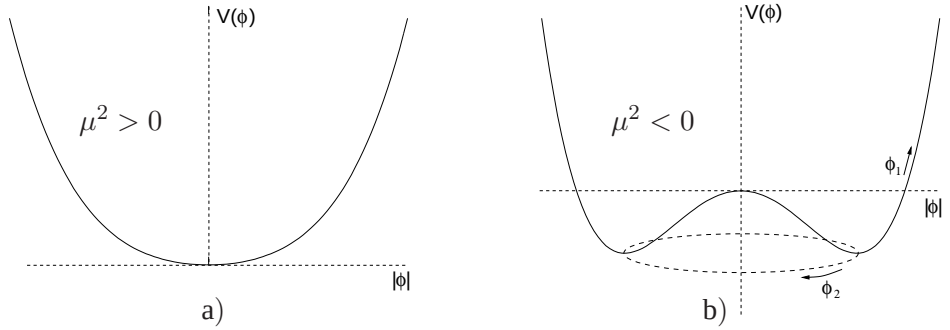

Figure 2.1: One-dimensional analogon of the Standard Model scalar potential in Equation (2.30) with one complex scalar field $V(\phi) = \mu|\phi|^2 + \lambda|\phi|^4$ for (a) $\mu^2 > 0$ and for (b) $\mu^2 < 0$. In the latter case the set of degenerated ground states is visualized by the dashed circle.

The covariant derivatives (2.25) are used to ensure for invariance under local $SU(2)_L \otimes U(1)_Y$ transformations. The self-coupling λ and the mass parameter μ of the scalar field are real parameters describing the shape of the potential $V(\Phi, \Phi^\dagger)$. In order to ensure ground states with positive finite energy, λ has to be positive. Figure 2.1 shows the one-dimensional projection of the scalar potential for positive and negative μ^2. For positive μ^2, the potential has only the trivial minimum at $|\Phi| = 0$. If μ^2 is taken to be negative, a degenerated set of ground states with

$$|\Phi_0| = \sqrt{\frac{-\mu^2}{2\lambda}} \equiv \frac{v}{\sqrt{2}}, \tag{2.32}$$

occurs. In other words, the field Φ acquires a non-zero vacuum expectation value $|\Phi_0|$.
By choosing a particular ground state, the $SU(2)_L \otimes U(1)_Y$ symmetry gets *spontaneously* broken to the electromagnetic gauge group $U(1)_Q$. Owing to the $SU(2)_L$ invariance of the Lagrangian the phase factor can be eliminated by local gauge transformations and Φ becomes after spontaneous symmetry breaking:

$$\Phi = \frac{1}{\sqrt{2}} \begin{pmatrix} 0 \\ v + H(x) \end{pmatrix}. \tag{2.33}$$

Only one real neutral scalar field $H(x)$ is left describing excitations from the ground state. Inserting Equations (2.33) and (2.20), (2.21) into the Lagrangian (2.30) one obtains:

$$\mathscr{L}_{\text{Higgs}} = \frac{1}{2}\partial_\mu H \partial^\mu H + \frac{g^2 v^2}{8}\left(W_\mu^+ W^{+\mu} + W_\mu^+ W^{-\mu}\right) + \frac{g^2 v^2}{8\cos^2\theta_W} Z_\mu Z^\mu - V(\Phi, \Phi^\dagger) \tag{2.34}$$

with mass terms for the weak gauge bosons

$$\begin{aligned} m_W &= \frac{gv}{2} \quad \text{and} \\ m_Z &= \frac{gv}{2\cos\theta_W} = \frac{m_W}{\cos\theta_W}. \end{aligned} \tag{2.35}$$

The Standard Model predicts masses for the W and Z gauge bosons which are related by $\cos\theta_W$. The measured mass values of the weak gauge bosons are [16]:

$$m_W = 80.398 \pm 0.025\,\text{GeV} \quad \text{and} \tag{2.36}$$

$$m_Z = 91.1876 \pm 0.0021\,\text{GeV}. \tag{2.37}$$

Since $U(1)_Q$ remains unbroken no photon mass term arises in agreement with the experiment. Inserting Equation (2.33) into the potential (2.31) yields a Higgs boson mass term with

$$m_H = \sqrt{-\mu^2} = \sqrt{\lambda v^2} \tag{2.38}$$

as well as Higgs-gauge boson interactions proportional to m_W and m_Z. By measuring the lifetime of the muon, the vacuum expectation value

$$v = 246\,\text{GeV} \tag{2.39}$$

has been determined. λ and m_H are free parameters of the Higgs sector of the Standard Model and have to be determined by the experiment.
Also fermion mass terms are introduced in the Standard Model by the spontaneous breaking of the electroweak symmetry. Adding mass terms explicitly of the form $m\psi\overline{\psi}$ would break the electroweak gauge symmetry. The generation of fermion masses is mediated by the Higgs field by the Yukawa interactions with couplings with the fermion fields y:

$$\begin{aligned}\mathscr{L}_{\text{Yukawa}} = &- \left(y_e \overline{\Psi}^e_L \left(\Phi \Psi^e_R\right) + y_\mu \overline{\Psi}^\mu_L (\Phi \Psi^\mu_R) + y_\tau \overline{\Psi}^\tau_L \left(\Phi \Psi^\tau_R\right)\right) + \text{h. c.} \\ &+ \text{analog quark terms}\end{aligned} \tag{2.40}$$

These couplings are the most general renormalizable couplings allowed by the $SU(2)_L \otimes U(1)_Y$ group. Once one of the non-zero ground states of Φ is chosen, Equation (2.40) leads to fermion mass terms. The fermion masses are proportional to the Yukawa couplings, hence the Higgs boson couples to fermions proportional to their masses.

2.6 Higgs Mass Bounds

The Higgs boson is the only particle of the Standard Model which has not yet been directly observed. Nevertheless limits can be obtained from theoretical arguments, electroweak precision measurements and the direct searches.

2.6.1 Theoretical Limits

The Higgs boson mass m_H can be constrained by requiring self consistency of the electroweak theory. The limits depend on the energy Λ, the scale where new physics appears and the Standard Model becomes invalid. The highest energy scale to be considered is given by the reduced Planck mass $M_{\text{Planck}} = 2.4 \times 10^{18}$ GeV, where gravitational quantum effects become large.

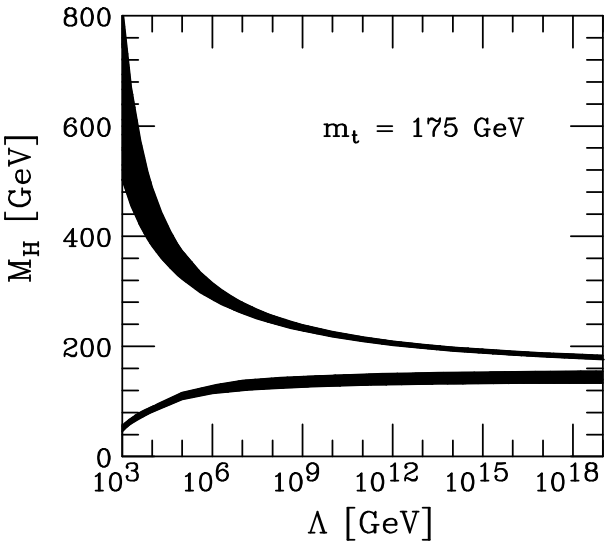

Figure 2.2: Theoretical bounds on the Higgs boson mass m_H as a function of the scale up to which the Standard Model is valid. The areas above and below the black bands are excluded, the width of the bands represents the theoretical uncertainties. The mass of the top quark has been assumed to be $m_t = 175\,\text{GeV}$ [17].

- The Higgs self-coupling λ is not a constant, but depends on Λ. For small Higgs boson masses λ becomes negative and the electroweak vacuum defined by the potential $V(\Phi, \Phi^\dagger)$ in Equation (2.31) unstable. Lower bounds on the Higgs boson mass are obtained as a function of Λ, visualized in Figure 2.2.
  At lower energy scales the relatively loose limit of $m_H \gtrsim 50\,\text{GeV}$ can be set. It increases up to $m_H \gtrsim 160\,\text{GeV}$ when approaching the Planck scale.

- The upper band in Figure 2.2 corresponds to Higgs masses for which the Higgs self-coupling λ diverges. Using this argument a limit $m_H \lesssim 600\,\text{GeV}$ is set for a low scale $\Lambda = 1\,\text{TeV}$, decreasing down to $m_H \lesssim 170\,\text{GeV}$ for λ equal to the Planck scale.

- In the Standard Model, the unitarity of the scattering process $W_L W_L \to W_L W_L$ of longitudinally polarized W bosons is violated if the Higgs boson is too heavy, i.e. $m_H \gtrsim 800\,\text{GeV}$.

Given no new physics exists up to the Planck scale the Higgs boson mass is constrained by these theoretical arguments to the range $160\,\text{GeV} < m_H < 170\,\text{GeV}$. Assuming the value $\Lambda = 1\,\text{TeV}$ the limits are released to $50\,\text{GeV} < m_H < 600\,\text{GeV}$.

2.6.2 Experimental Limits

Direct Searches The combined results of direct Higgs boson searches carried out by the four LEP[1] experiments ALEPH, OPAL, L3 and DELPHI allow an exclusion of the Standard Model

[1] LEP: Large Electron-Positron Collider, running from 1989-2000 in the same tunnel as the LHC.

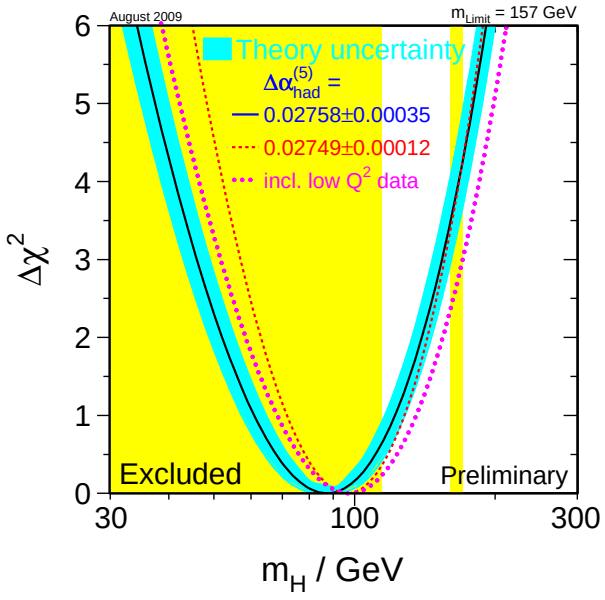

Figure 2.3: $\Delta\chi^2 \equiv \chi^2 - \chi^2_{\text{min}}$ of the global fit of the electroweak precision data from SLAC, LEP and Tevatron as a function of the Higgs boson mass m_H. The yellow shaded area indicates the region excluded from direct searches, the blue band the theoretical uncertainties. The dotted line shows the result when using the low Q^2 data [20].

Higgs boson masses below $m_H = 114.4\,\text{GeV}$ at 95% confidence level [18]. The combined results of the Tevatron[2] experiments DØ and CDF currently exclude the mass range $162\,\text{GeV} < m_H < 166\,\text{GeV}$ [19].

Indirect Indications Indications on the Higgs boson mass come also from electroweak precision measurements. Higher order corrections to electroweak observables include Higgs boson loops. Due to the high precision of the measurements of the LEP and the Tevatron experiments the Higgs boson mass can be constrained by performing a χ^2-fit of the Standard Model predictions to the data. The minimum of the χ^2 function corresponds to the preferred value of m_H. In Figure 2.3 the quantity $\Delta\chi^2 \equiv \chi^2 - \chi^2_{\text{min}}$ is shown as a function of the Higgs boson mass with the estimation of the Higgs boson mass of $84^{+34}_{-26}\,\text{GeV}$ corresponding to an upper limit of $m_H < 157\,\text{GeV}$ at 95% confidence level [20]. Taking into account the lower bound from the LEP searches, the upper limit increases to 186 GeV. Hence the electroweak precision data favors a rather light Higgs boson in the framework of the Standard Model.

[2]Tevatron: $p\bar{p}$ collider at the Fermi National Accelerator Laboratory in the USA.

2.7 Limitations of the Standard Model

Despite the success of the Standard Model in describing numerous experimental observations of high-energy experiments, there are several problems. They are of experimental and theoretical nature. The most important ones are summarized in the following:

- The number of free parameters of the Standard Model is rather large. 19 parameters have to be determined experimentally:
  - twelve fermion masses (quarks and leptons),
  - three gauge couplings,
  - two parameters, λ and μ, describing the Higgs potential,
  - three quark mixing angles in the Cabibbo-Kobayashi-Maskawa (CKM) matrix [21, 22],
  - one complex phase of the CKM matrix and
  - the QCD vacuum angle.
- The values and hierarchy of the fermion masses is not explained by the Standard Model.
- A quantum theory of gravitation is not included in the Standard Model.
- Astrophysical observations indicate that about 30% of the total energy density of the universe is non-baryonic dark matter which is not described by the Standard Model [23].
- In the previous section it was shown that in the Standard Model the Higgs boson mass has to be smaller than 1 TeV to be consistent. Theoretically this is rather unnatural, because the mass of the Higgs field receives large quantum corrections in the Standard Model which drive the Higgs boson mass to the highest energy scale Λ where the Standard Model becomes invalid. If Λ is the Planck scale, the corrections to m_H are about 15 orders of magnitude larger than the expected value [24]. In order to keep the observable Higgs mass near the electroweak scale unnaturally precise fine-tuning has to be performed. This problem, often referred to as the *hierarchy problem*, can be solved by introducing the concept of Supersymmetry.

Chapter 3

Supersymmetric Extensions of the Standard Model

Although the Standard Model is a very successful theory describing high-energy physics up to energies of about 100 GeV, it has theoretical problems, including the hierarchy problem, described in the previous section. The hierarchy problem can be solved by introducing a new symmetry, namely Supersymmetry [25]. After an introduction in Section 3.1, an extensively studied supersymmetric extension of the Standard Model is described in Section 3.2, the Minimal Supersymmetric Extension of the Standard Model (MSSM).

3.1 General Concept of Supersymmetry

In supersymmetric theories, the constituents of matter and radiation, namely fermions and bosons, are related by supersymmetry transformations Q which turn fermionic into bosonic states and vice versa:

$$Q\,|\text{Boson}\rangle = |\text{Fermion}\rangle\,,$$
$$Q\,|\text{Fermion}\rangle = |\text{Boson}\rangle\,.$$

Supersymmetry is not an internal symmetry like the local gauge symmetries of the Standard Model. The superalgebra of the operators Q and their hermitian conjugates $Q^\dagger$ rather defines a non-trivial extension of the space-time symmetries of the Poincaré algebra [26, 27].
A supersymmetric state, called supermultiplet, contains a bosonic and a fermionic state. Two different kinds of supermultiplets exist: Chiral supermultiplets, consisting of a spin-1/2 and spin-0 field $\Psi(x)$ and $\phi(x)$, as well as gauge supermultiplets with a spin-1 and a spin-1/2 field $A^\mu(x)$ and $\lambda(x)$, respectively. The members of a supermultiplet exhibit equal masses and gauge quantum numbers. In a supersymmetric extension of the Standard Model all known fundamental particles reside in separate supermultiplets together with a "superpartner". The scalar superpartners of the fermions are named with a leading "s", the names of the superpartners of the gauge and Higgs bosons end with "ino".
Due to the different spin-statistical nature of fermionic and bosonic states, the radiative loop corrections of fermions and bosons to the Higgs boson mass have opposite sign. In Figure 3.1 the

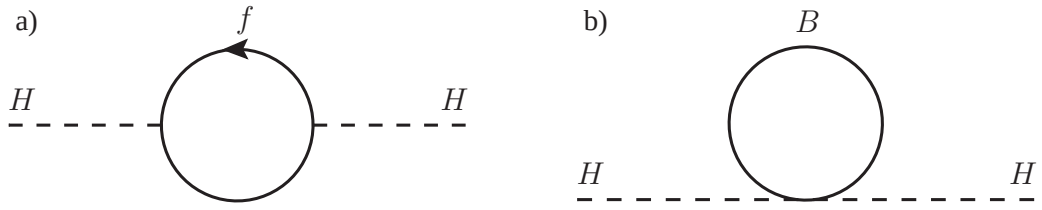

Figure 3.1: Radiative corrections to the Higgs mass due to (a) fermion (f) loops and (b) boson (B) loops.

Table 3.1: Chiral supermultiplets of the MSSM. Each supermultiplet contains a complex scalar and a spin-1/2 field. The superpartners of the Standard Model particles are denoted with the tilde. The indices L/R of the superpartners denote the chirality of the corresponding Standard Model particle.

Chiral Supermultiplets	Scalar ϕ Spin 0	Fermion ψ Spin 1/2
Squarks, Quarks ($\times$3 families)	$\widetilde{Q} = (\widetilde{u}\ \widetilde{d})_L$ $\widetilde{u}_R$ $\widetilde{d}_R$	$Q = (u\ d)_L$ u_R d_R
Sleptons, Leptons ($\times$3 families)	$\widetilde{L} = (\widetilde{\nu}\ \widetilde{e})_L$ $\widetilde{e}_R$	$L = (\nu\ e)_L$ e_R
Higgs, Higgsinos	$H_u = (H_u^+\ H_u^0)$ $H_d = (H_d^0\ H_d^-)$	$\widetilde{H}_u = (\widetilde{H}_u^+\ \widetilde{H}_u^0)$ $\widetilde{H}_d = (\widetilde{H}_d^0\ \widetilde{H}_d^-)$

first-order contributions are shown. The corresponding corrections to the Higgs mass m_H are:

$$\begin{aligned} \text{Fermion Loops:} \quad \Delta m_H^2 &= \frac{\lambda_f^2}{16\pi^2}\left[-2\Lambda^2 + 6m_f \ln(\Lambda/m_f)\right], \\ \text{Boson Loops:} \quad \Delta m_H^2 &= \frac{\lambda_B}{16\pi^2}\left[+2\Lambda^2 - 6m_B \ln(\Lambda/m_B)\right]. \end{aligned} \tag{3.1}$$

Since Supersymmetry ensures identical masses and the coupling constants of fermions and bosons are related ($\lambda_f^2 = \lambda_B$), the corrections to the Higgs mass cancel. However, Supersymmetry must be a broken symmetry in nature because the superpartners would have been already observed otherwise. In order to keep Supersymmetry as a solution for the hierarchy problem, the cancellation of the Higgs boson mass corrections has to be maintained. This requires that the masses of the lightest superpartners are of the order of 1 TeV or lighter [24].

3.2 The Minimal Supersymmetric Extension of the Standard Model

The Minimal Supersymmetric Extension of the Standard Model (MSSM) is a supersymmetric theory with minimal amount of additional particles. One superpartner is introduced for each Standard

Table 3.2: Gauge supermultiplets of the MSSM. Each supermultiplet contains a spin-1/2 and a spin-1 field. The superpartners of the Standard Model particles are denoted with the tilde.

Gauge Supermultiplets	Fermion λ Spin 1/2	Boson A^μ Spin 1
Gluinos, Gluons	$\widetilde{g}_1, \ldots, \widetilde{g}_8$	$g_1, \ldots, g_8$
Winos, W Bosons	$\widetilde{W}^\pm, \widetilde{W}^0$	$W^\pm, W^0$
Bino, B Boson	$\widetilde{B}$	B

Model particle. Furthermore, the MSSM obeys the same gauge symmetries $SU(3)_C \otimes SU(2)_L \otimes U(1)_Y$ as the Standard Model. In contrast to the Standard Model separate Higgs doublets H_u and H_d for up- and down-type particles and the corresponding superpartners are required, because terms including complex conjugate fields are forbidden by Supersymmetry. The particle content of the MSSM is summarized in Table 3.1 and Table 3.2. The MSSM makes the remarkable prediction that the three gauge couplings $\alpha_a = g_a^2/4\pi$ $(a = 1, 2, 3)$ unify at the Grand Unification scale $M_{\text{GUT}} \approx 2 \times 10^{16}$ GeV. In Figure 3.2 the effect of the superpartners on the running of the gauge couplings is visible at energies above 1 TeV.

3.2.1 The Superpotential

The scalar and Yukawa interactions of a supersymmetric theory can be expressed by the superpotential $W(\phi_i)$ which has the general form [24]:

$$W(\phi_i) = L^i \phi_i + \frac{1}{2} M^{ij} \phi_i \phi_j + \frac{1}{6} y^{ijk} \phi_i \phi_j \phi_k \quad . \tag{3.2}$$

The linear term is only allowed for gauge singlets. Since no such particles are included in the MSSM this term is neglected in the following. M^{ij} are the mass matrix elements for the fermion fields and y^{ijk} couplings of the scalar fields ϕ_k to two fermion fields $\psi_i \psi_j$. The corresponding Lagrangian is derived according to:

$$\mathscr{L}_{\text{Yukawa}} = -\frac{1}{2} \frac{\delta^2 W}{\delta \phi_i \delta \phi_j} \psi_i \psi_j + \text{c.c.} \tag{3.3}$$

The superpotential of the MSSM is given by:

$$W_{\text{MSSM}} = \widetilde{u}_i \left(y_u\right)^{ij} \widetilde{Q}_j H_u - \widetilde{d}_i \left(y_d\right)^{ij} \widetilde{Q}_j H_d - \widetilde{e}_i \left(y_e\right)^{ij} \widetilde{L}_j H_d + \mu H_u H_d, \tag{3.4}$$

where the indices i, j denote the three fermion generations. The last term gives the Higgs boson mass term.

3.2.2 R parity

More terms could be added to the superpotential W_{MSSM} without violating Supersymmetry. Nevertheless these terms are excluded in the MSSM, because they would either violate lepton or baryon

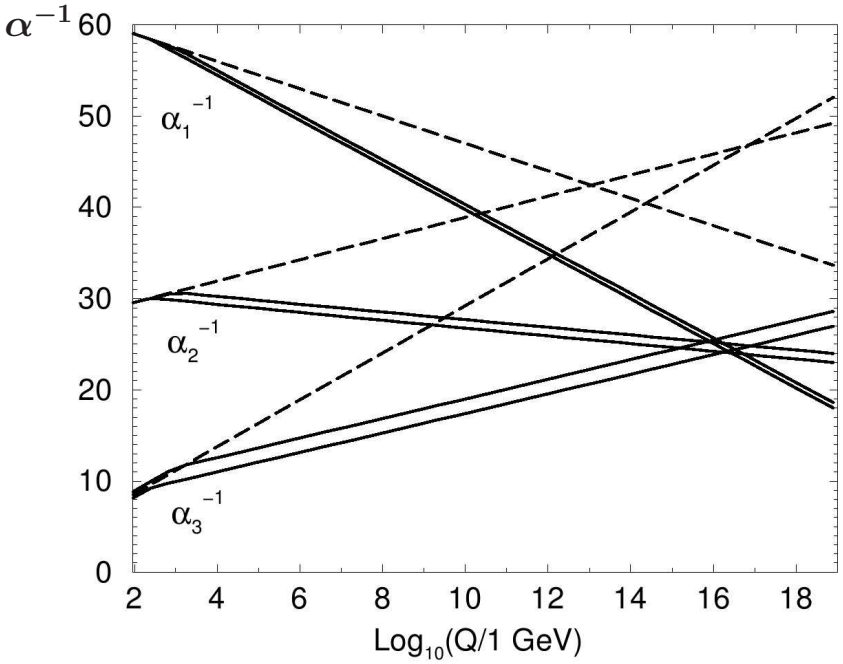

Figure 3.2: Running inverse gauge couplings $\alpha_a^{-1} = 4\pi/g_a^2$ ($g_1 = \sqrt{5/3}\,g', g_2 = g, g_3 = g_S$) in the Standard Model (dashed lines) and in the MSSM (solid lines) up to energy scales Q of 10^{19} GeV [24]. To reflect the theoretical uncertainties, the masses of the superpartners are varied between 250 GeV and 1 TeV and $\alpha_3\,(m_Z)$ between 0.113 and 0.123, respectively. In the MSSM, the couplings unify at $\sim 2 \times 10^{16}$ GeV, while in the Standard Model they do not.

number conservation. The absence of such terms is formally enforced by a new discrete symmetry called "R parity", with the quantum number

$$R = (-1)^{3(\mathrm{B}-\mathrm{L})+2\mathrm{s}} \quad (\mathrm{s=spin}). \tag{3.5}$$

Baryon number $\mathrm{B} = 1/3$ ($\mathrm{B} = -1/3$) is assigned to the left- (right-) handed quarks and squarks and $\mathrm{B} = 0$ to all others. Similarly, lepton number $\mathrm{L} = 1$ ($\mathrm{L} = -1$) is assigned to left- (right-) handed leptons and sleptons. Thus Standard Model particles and Higgs bosons have even, their superpartners odd R parity.
Although conservation of R parity is not required from the theoretical point of view, it is favored by the very long lifetime of the proton. An additional consequence is that superpartners are only produced in pairs and decay to the lightest superpartner which is stable. Given that this particle is electrically neutral it provides a dark matter candidate.

3.2.3 Supersymmetry Breaking in the MSSM

In the MSSM so called "soft" Supersymmetry breaking terms have to be added to the MSSM Lagrangian explicitly. They preserve the cancellation of Higgs mass corrections:

$$\begin{aligned}
\mathscr{L}_{\mathrm{soft}}^{\mathrm{MSSM}} = & -\frac{1}{2}\left(M_3\tilde{g}\tilde{g} + M_2\widetilde{W}\widetilde{W} + M_1\widetilde{B}\widetilde{B} + \mathrm{c.c.}\right) \\
& - \left(\tilde{u}\boldsymbol{A_u}\widetilde{Q}H_u - \tilde{d}\boldsymbol{A_d}\widetilde{Q}H_d - \tilde{e}\boldsymbol{A_e}\widetilde{L}H_d + \mathrm{c.c.}\right) \\
& - \widetilde{Q}^\dagger\boldsymbol{m_Q^2}\widetilde{Q} - \widetilde{L}^\dagger\boldsymbol{m_L^2}\widetilde{L} - \tilde{u}^\dagger\boldsymbol{m_u^2}\tilde{u}^\dagger - \tilde{d}^\dagger\boldsymbol{m_d^2}\tilde{d}^\dagger - \tilde{e}^\dagger\boldsymbol{m_e^2}\tilde{e}^\dagger \\
& - m_{H_u}^2 H_u^* H_u - m_{H_d}^2 H_d^* H_d - (bH_uH_d + \mathrm{c.c.})
\end{aligned} \tag{3.6}$$

with the gluino, wino and bino mass terms M_3, M_2 and M_1 in the first line. The terms in the second line contain scalar couplings in one-to-one correspondence with the Yukawa couplings of the superpotential. The third line describes slepton and squark mass terms and the last line supersymmetric contributions to the Higgs potential. All together the MSSM Lagrangian contains in general 105 new parameters in addition to the Standard Model parameters:

- five real parameters,
- 43 CP violating phases,
- 36 mixing angles and
- 21 mass parameters.

However, in certain models of the Supersymmetry breaking mechanism the number of free parameters is greatly reduced. An example is the "mSUGRA" model, where only five additional parameters are used [28]. In fact, experimental data set strong bounds on many parameters, which lead to flavor mixing or CP violation.

3.2.4 The MSSM Higgs Sector and Gauge Symmetry Breaking

As in the Standard Model, the gauge symmetry is broken: $SU(2)_L \otimes U(1)_Y \rightarrow U(1)_Q$ [29]. The two vacuum expectation values of the Higgs doublets $H_u = \left(H_u^+, H_u^0\right)$ and $H_d = \left(H_d^0, H_d^-\right)$ are chosen to be

$$\langle H_u \rangle = \frac{1}{\sqrt{2}} \begin{pmatrix} 0 \\ v_u \end{pmatrix} \quad \text{and} \quad \langle H_d \rangle = \frac{1}{\sqrt{2}} \begin{pmatrix} v_d \\ 0 \end{pmatrix}. \tag{3.7}$$

The breaking of gauge symmetry results in five physical Higgs boson mass eigenstates, two charged ones,

$$H^\pm = H_d^\pm \sin\beta + H_u^\pm \cos\beta, \tag{3.8}$$

one CP-odd scalar,

$$A = \sqrt{2}\left(\mathrm{Im}H_d^0 \sin\beta + \mathrm{Im}H_u^0 \cos\beta\right) \tag{3.9}$$

and two CP-even scalars,

$$\begin{aligned} h &= -\left(\sqrt{2}\,\mathrm{Re}H_d^0 - v_d\right)\sin\alpha + \left(\sqrt{2}\,\mathrm{Re}H_u^0 - v_u\right)\cos\alpha, \\ H &= +\left(\sqrt{2}\,\mathrm{Re}H_d^0 - v_d\right)\cos\alpha + \left(\sqrt{2}\,\mathrm{Re}H_u^0 - v_u\right)\sin\alpha, \end{aligned} \tag{3.10}$$

with $\tan\beta$ given by the ratio of the vacuum expectation values, $\tan\beta = v_u/v_d$, and $\tan 2\alpha = \tan 2\beta \left(\frac{m_A^2+m_Z^2}{m_A^2-m_Z^2}\right)$. Also the superpartners of the Standard Model particles mix with each other if they share equal quantum numbers. The neutral bino, wino and Higgsinos mix to neutralino and the charged winos and higgsinos to chargino mass eigenstates. Significant mixing occurs also among the third generation sfermions, see Table 3.3.
At tree level, the MSSM Higgs sector is determined by one Higgs boson mass, chosen to be m_A, and the ratio of the vacuum expectation values $\tan\beta$. The other Higgs boson masses are given by the expressions

$$\begin{aligned} m_{H^\pm}^2 &= m_A^2 + m_W^2, \quad \text{and} \\ m_{H,h}^2 &= \frac{1}{2}\left(m_A^2 + m_Z^2 \pm \sqrt{\left(m_A^2 + m_Z^2\right)^2 - 4m_Z^2 m_A^2 \cos^2 2\beta}\right). \end{aligned} \tag{3.11}$$

From relation (3.11), the limit h

$$m_h^2 \leq m_Z^2 \cos 2\beta \leq m_Z^2 \tag{3.12}$$

on the mass of the light Higgs boson h is obtained at tree level. Even after radiative correction at least one Higgs boson of the MSSM is light.
The interactions of charged Higgs bosons to fermions are determined by the superpotential (3.4). In the MSSM, the Yukawa coupling strengths for up- and down-type fermions are:

$$y_u = \frac{m_u}{v\,\sin\beta}, \quad y_d = \frac{m_d}{v\,\cos\beta} \qquad \left(v^2 = v_u^2 + v_d^2\right). \tag{3.13}$$

Hence the Yukawa coupling strengths are proportional to the fermion masses and also depend on the angle β. Since they are known to be sizable for particles of the third generation, the most

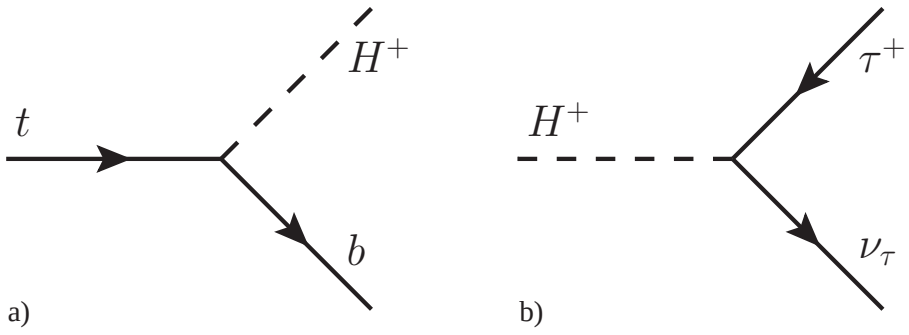

Figure 3.3: Couplings of charged Higgs bosons to third generation particles: (a) tbH^+ (b) $H^+ \to \tau\nu$

Table 3.3: Gauge eigenstates and mass eigenstates of Higgs bosons, sfermions, charginos and neutralinos. Only third sfermion generation particles are listed, the mixing for the first two generations is assumed to be negligible. The gluino cannot mix with other particles.

Name	Gauge eigenstates	Mass eigenstates
Higgs Bosons	$H_u^0, H_d^0, H_u^+, H_d^-$	$h, H, A, H^\pm$
Squarks	$\widetilde{t}_L, \widetilde{t}_R, \widetilde{b}_L, \widetilde{b}_R$	$\widetilde{t}_1, \widetilde{t}_2, \widetilde{b}_1, \widetilde{b}_2$
Sleptons	$\widetilde{\tau}_L, \widetilde{\tau}_R, \widetilde{\nu}_\tau$	$\widetilde{\tau}_1, \widetilde{\tau}_2, \widetilde{\nu}_\tau$
Neutralinos	$\widetilde{B}, \widetilde{W}^0, \widetilde{H}_u^0, \widetilde{H}_d^0$	$\widetilde{\chi}_1^0, \widetilde{\chi}_2^0, \widetilde{\chi}_3^0, \widetilde{\chi}_4^0$
Charginos	$\widetilde{W}^\pm, \widetilde{H}_u^+, \widetilde{H}_d^-$	$\widetilde{\chi}_1^\pm, \widetilde{\chi}_2^\pm$

important couplings of charged Higgs bosons to fermions (see Figure 3.3) are:

$$g_{H^+tb} = \frac{g}{\sqrt{2}m_W}\left[m_t \cot\beta\, P_R + m_b \tan\beta\, P_L\right] \quad \text{and} \tag{3.14}$$

$$g_{H^+\tau\nu} = \frac{g}{\sqrt{2}m_W}\left[m_\tau \tan\beta\, P_L\right], \tag{3.15}$$

with the projection operators for left- and right-handed particles $P_L \equiv 1/2\left(1-\gamma^5\right)$ and $P_R \equiv 1/2\left(1+\gamma^5\right)$. From Equation (3.14) it follows that the tbH^+ coupling has a global minimum around $\tan\beta \approx 7$. In addition the coupling to τ leptons (3.15) increases linearly with $\tan\beta$.

Chapter 4

Charged Higgs Bosons

In this Chapter important aspects of the phenomenology of charged Higgs bosons are outlined. In Section 4.1 the general formalism for calculating production cross sections in proton-proton collisions is described. The production and decay channels of charged Higgs bosons at the LHC are explained in Section 4.2. Finally an overview of the current limits for charged Higgs bosons is given in Section 10.2.

4.1 Luminosity and Cross Sections

The event rate dN/dt of a certain physics process in collider experiments is given by the product of the instantaneous luminosity $\mathcal{L}$ and the cross section σ:

$$\frac{dN}{dt} = \mathcal{L} \cdot \sigma. \tag{4.1}$$

At colliders, the luminosity depends only on the accelerator parameters:

$$\mathcal{L} = f N_b \frac{N_1 N_2}{4\pi \sigma_x \sigma_y}, \tag{4.2}$$

with the circulation frequency f and the number N_b of circulating bunches per beam. N_1 and N_2 denote the number of particles per bunch in each beam, σ_x and σ_y the transverse beam widths.
The generic structure of a hadronic scattering process with collision of two hadrons A, B is depicted in Figure 4.1. The cross section of the hadronic process $\sigma\left(AB \to X + Y\right)$ is obtained by correlating the cross section of the partonic subprocess $\hat{\sigma}\left(ab \to X\right)$ with the parton distribution functions f of the hadrons:

$$\sigma_{AB \to X+Y} = \int \partial x_a \partial x_b \, f_{a/A}\left(x_a, \mu_{\mathrm{F}}^2\right) f_{b/B}\left(x_b, \mu_{\mathrm{F}}^2\right) \, \hat{\sigma}_{a,b \to X}. \tag{4.3}$$

The cross section of the hard-scattering $ab \to X$, characterized by a high momentum transfer, is calculated perturbatively as a power series in α_{S}:

$$\hat{\sigma}_{a,b \to X} = \sigma_0 + \alpha_{\mathrm{S}}\left(\mu_{\mathrm{R}}^2\right) \, \sigma_1 + \ldots \tag{4.4}$$

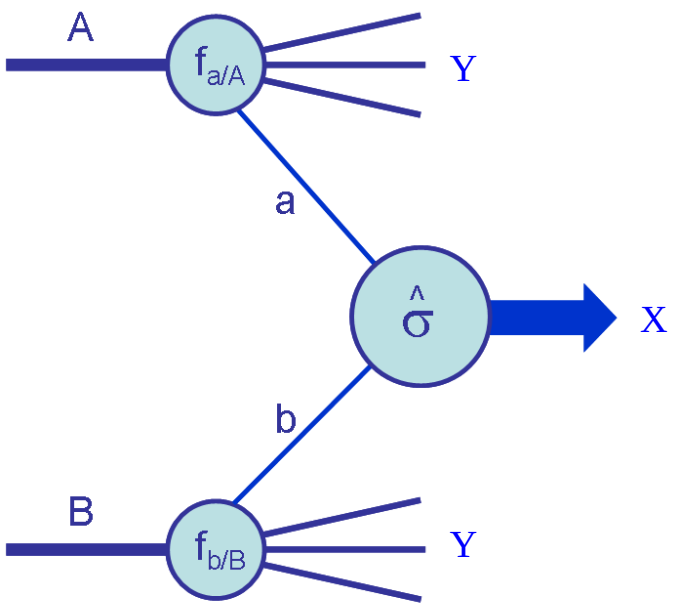

Figure 4.1: Schematic structure of a hadronic scattering process.

The parton distribution functions $f_{a/A}\left(x_a, Q^2\right)$ are the probability density distributions of the momentum fraction x_a of a parton a in the hadron A at a momentum transfer of Q^2 which have to be determined experimentally.
In the Equations (4.3) and (4.4) two unphysical scales show up. The factorization scale μ_{F} is the scale which separates the short- and long-distance physics, while μ_{R} is the renormalization scale of which the running strong coupling is evaluated. If the calculation of the cross section $\hat{\sigma}_{a,b\to X}$ could be carried out to all orders of the perturbation theory, the dependence on both scales would disappear. However, for finite order calculations the results depend on the explicit choice of μ_{F}^2 and μ_{R}^2, reflecting the theoretical uncertainty due to the missing higher order contributions.
Even though the probability density functions have been measured by several experiments, they are not precisely known in the entire parameter space covered by high energy pp collisions [31], giving rise to further theoretical uncertainties.
The predictions for several Standard Model processes in $p\bar{p}$ collisions around 1.96 TeV at the Tevatron and in pp collisions around 14 TeV at the LHC are shown in Figure 4.2. The production cross section for top quark pairs is roughly 800 pb at the LHC design energy of 14 TeV, leading to a rate of eight $t\bar{t}$ events per second at a luminosity of $10^{34}\,\mathrm{cm}^{-2}\mathrm{s}^{-1}$. The main challenge will be to extract the top events out of the 8 orders of magnitude higher background of other Standard Model processes.

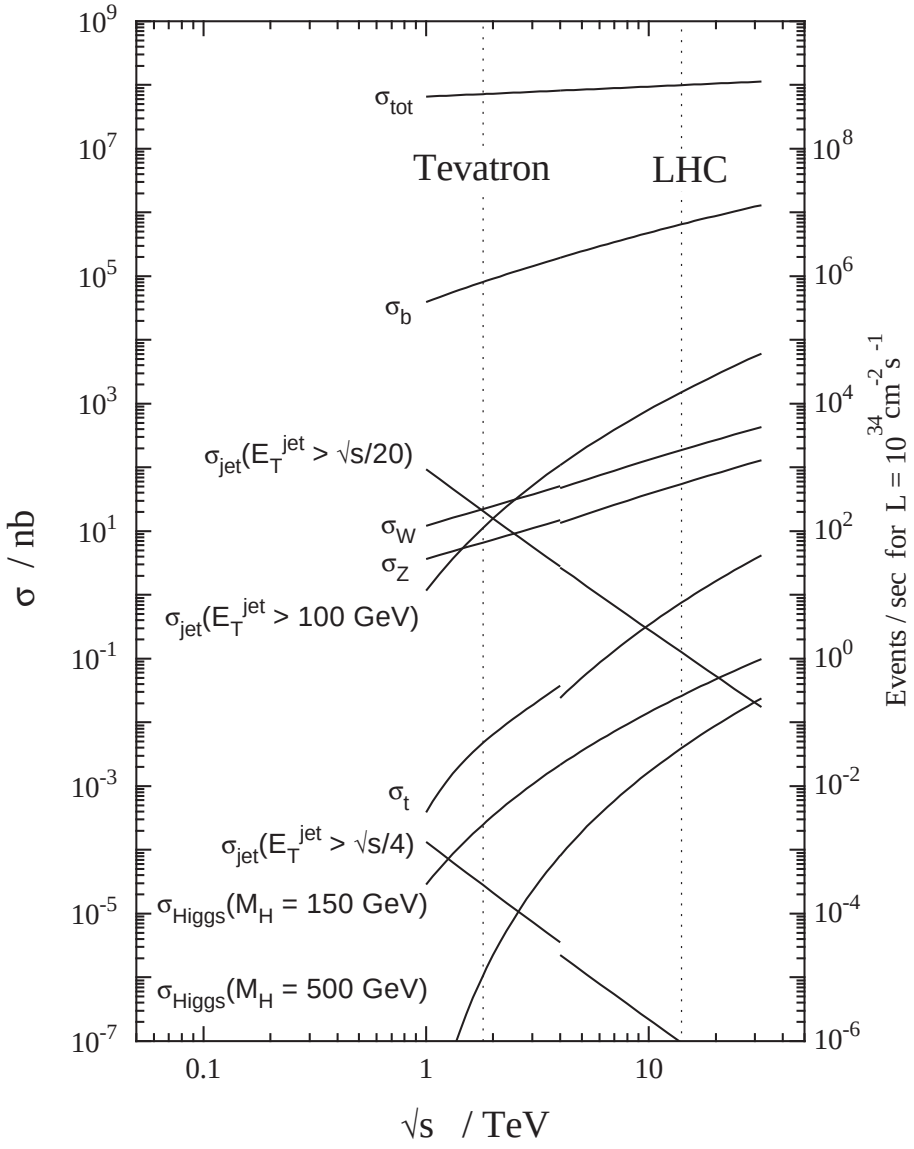

Figure 4.2: Predictions for Standard Model production cross sections and event rates at a luminosity of $10^{34}\,\mathrm{cm}^{-2}\mathrm{s}^{-1}$ as a function of the center-of-mass energy $\sqrt{s}$. The left part shows the values for $p\bar{p}$ collisions around 1.96 TeV at the Tevatron and the right part for pp collisions around 14 TeV at the LHC [30].

4.2 Charged Higgs Boson Production and Decay at the LHC

4.2.1 Models with Charged Higgs Bosons

The most viable theories that predict charged Higgs bosons is the Standard Model with a non-minimal Higgs sector including supersymmetric extensions. Charged Higgs bosons also appear in the more exotic Higgs triplet model [32], the Little-Higgs model [33] or left-right symmetric models [34], but these are out of the scope of this thesis.
The extension of the Standard Model with a second Higgs doublet is called "Two Higgs-Doublet Model" (2HDM). Depending on the couplings of the Higgs doublets to quarks and leptons three different types of 2HDMs are distinguished:

- **2HDM(I)**
  In this 2HDM the fermions couple to only one Higgs doublet, while the second contributes only to the W and Z masses. As a result, fermionic decays of the charged Higgs boson can be suppressed.

- **2HDM(II)**
  Here the masses of the up-type fermions are provided by couplings to the first Higgs doublet and the masses of the down-type fermions by the couplings to the second.

- **2HDM(III)**
  In this model the masses of up- and down-type fermions are provided by couplings to both Higgs doublets, allowing for flavor changing neutral currents at tree level.

The MSSM belongs to the 2HDM(II) class. However, due to supersymmetry it is more constrained than the simple Standard Model extension with two Higgs doublets. In most of the 2HDM(II) parameter space, charged Higgs bosons decay to the heaviest kinematically allowed fermions, namely to $\tau\nu$ and quark pairs. The two corresponding limiting cases are called *Tauonic Model* and *Leptophobic Model*, respectively.
Although the MSSM Higgs sector is at tree level determined by m_A and $\tan\beta$, additional parameters enter through higher order corrections. Therefore several scenarios are investigated for the MSSM [35]. In this thesis, the so-called m_h-max scenario is studied.
Motivated by the low tree-level bound (3.12), the parameters of the m_h-max scenario, shown in Table 4.1, are chosen such that the mass of the lightest Higgs boson h is maximal for all $\tan\beta$. The masses of squarks and sleptons are set to the common value of 1 TeV. For the stop-mixing parameter, $X_t = (A_t - \mu \cot\beta)$, where A_t denotes the Higgs-stop coupling, see Equation 3.6, the value 2 TeV is chosen. The gaugino and gluino masses M_2 and M_3 are set to 200 GeV and 800 GeV, respectively, while the bino mass M_1 is given by the relation $M_1 = 5/3 \tan\theta_W M_2$.

4.2.2 Mass Relations in the m_h-max Scenario

In Figure 4.3 the masses of the Higgs bosons h, H and $H^\pm$ are shown as a function of the mass of the Higgs boson A for $\tan\beta = 5$ and $\tan\beta = 40$ taking into account higher order corrections. For the lightest Higgs boson h, an upper limit max ≈ 130 GeV is reached exceeding the tree-level bound (see Equation 3.12) due to higher order corrections. The masses of the other

Table 4.1: Parameters of the m_h-max scenario.

Name	Parameter	Value / GeV
Sfermion masses	M_{SUSY}	1000
Stop mixing	X_{t}	2000
Higgs mass parameter	μ	200
Gaugino masses	M_2	200
Gluino mass	M_3	800

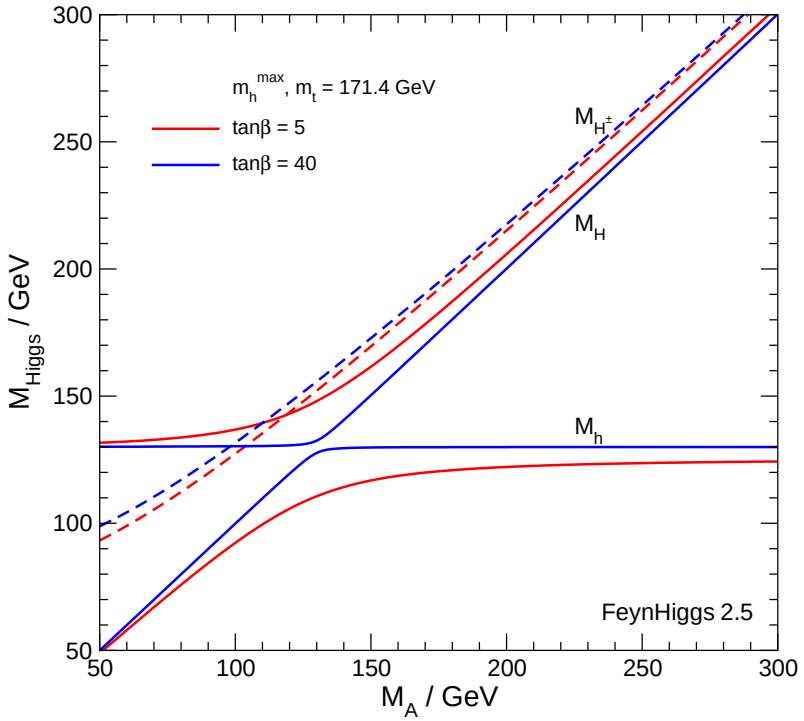

Figure 4.3: Masses of the light CP-even (m_h), the heavy CP-even (m_H) and charged Higgs bosons $(m_{H^\pm})$ as a function of the mass of the CP-odd Higgs boson m_A for two values $\tan\beta = 5$ and $\tan\beta = 40$. The numbers are evaluated for the m_h-max scenario and $m_t = 171.4\,\mathrm{GeV}$ using the software FEYNHIGGS [36, 37].

Higgs bosons have no such limit in the MSSM. A and one of the other neutral Higgs bosons are approximately degenerate in mass, provided $\tan\beta$ is not too small. This is H in the decoupling regime ($m_A \gg$ max) and h in the anti-decoupling regime ($m_A \ll$ max). For $m_A \approx$ max all neutral Higgs bosons are quasi degenerate. The small mass splitting between A and h/H has a large impact on the phenomenology of the Higgs sector of the MSSM. Finally, the charged Higgs boson mass always exceeds m_A (see Equation (3.11)). It should be noted that this picture changes drastically in more complicated models than the MSSM. An example is the next-to-Minimal Supersymmetric Extension of the Standard Model (NMSSM) where a gauge singlet is added to the MSSM [38].

4.2.3 Production of Charged Higgs Bosons

Depending on their mass charged Higgs bosons can be produced at the LHC in two channels:

(1) For $m_{H^+} < m_t - m_b$ via top quark decays:

$$gg, q\bar{q} \to t\bar{t},\, t \to H^+ b.$$

(2) For $m_{H^+} \gtrsim m_t - m_b$ via gluon-gluon and gluon-quark fusion:

$$gg \to \bar{t}bH^+ \text{ and } g\bar{b} \to \bar{t}H^+.$$

Channel (1) involves top quark pair production, according to a cross section of $\sigma_{t\bar{t}} = 833 \pm 100\,\text{pb}$ at the design energy of the LHC of 14 TeV [39]. The production of charged Higgs bosons is possible through decays of on-shell top quarks, $t \to H^+ b$, since in this case the charged Higgs boson is lighter than the top quark. Hence the charged Higgs bosons in this scenario are referred to as *light* charged Higgs bosons. The Feynman diagrams for this process and the corresponding Standard Model $t\bar{t}$ production and decay are shown in Figures 4.4(a) and 4.4(b). At the LHC, also single top quarks will be produced, but with a lower cross section and higher backgrounds.
The branching ratio for the decay $t \to H^+ b$ has been calculated in the m_h-max scenario using the FEYNHIGGS program [37]. The total cross section for channel (1) MSSM H^+ production,

$$\sigma = 2 \cdot \sigma_{t\bar{t}} \cdot \mathcal{B}\left[t \to H^+ b\right] \cdot \left(1 - \mathcal{B}\left[t \to H^+ b\right]\right), \tag{4.5}$$

is shown in Figure 4.5(a) as a function of $\tan\beta$. Characteristic for all $m_{H^\pm}$ masses is the minimum near $\tan\beta \approx 7$ caused by the minimum in the tbH^+ coupling (see Equation (3.14)). This $\tan\beta$ region is often referred to as the intermediate region and is experimentally difficult to investigate. The cross section decreases here down to about $5 - 40\,\text{pb}$ for light charged Higgs bosons. Outside this region at smaller and larger $\tan\beta$ charged Higgs bosons are produced at much higher rates.
The so called *heavy* charged Higgs bosons with $m_{H^\pm} \gtrsim m_t - m_b$ are produced by the two processes of channel (2) [40]. The production cross section has its lowest value of 0.01 pb in the intermediate region for $m_{H^\pm} \approx 600\,\text{GeV}$ and reaches up to 10 pb for high $\tan\beta$ and $m_{H^\pm} \approx 170\,\text{GeV}$ (see Figure 4.5(a)). Alternative production modes like $q\bar{q}' \to H^+$, H^++jet production, associated H^+W^- production or charged Higgs pair production have suppressed rates and are very difficult to detect at the LHC [41].

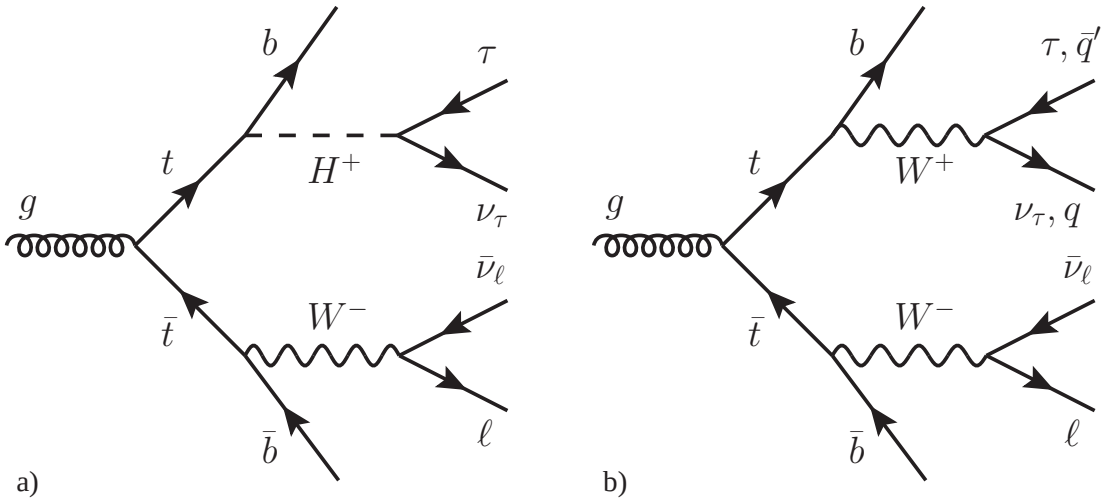

Figure 4.4: (a) Light charged Higgs boson production in decays of top quarks at the LHC and (b) Standard Model $t\bar{t}$ production and decay. The latter constitutes the irreducible background with the W decay into a τ lepton and the reducible background with the W decay into quarks.

4.2.4 Decays of Charged Higgs Bosons

The decay modes of charged Higgs bosons include $q\bar{q}'$, $\tau\nu$, $Wh/H/A$ and sparticle final states. Figure 4.5(b) shows the branching ratios of the most important decay modes into Standard Model particles as a function of the charged Higgs boson mass for the MSSM m_h-max scenario according to FEYNHIGGS.

- **Light Charged Higgs Bosons:**
  The decay $H^+ \to \tau\nu$ is dominant for $\tan\beta > 3$ and therefore the favored search channel below the threshold for decays into top quarks. The decay $H^+ \to c\bar{s}$ has a not-negligible branching ratio only for $\tan\beta < 3$, see Equation (3.15), because the $H^+ \to \tau\nu$ coupling decreases for low $\tan\beta$. In spite of the low branching ratio, this process may be observable at the LHC due to the clear signature of the reconstructible invariant mass peak.
  Due to the mass relation (3.11), the decays $H^+ \to W^*h/A/H$ are kinematically suppressed. They can only proceed via off-shell W^* bosons and are negligible for the MSSM charged Higgs boson searches. These channels are, however, important in the NMSSM due to larger mass splittings. In this case the decay channel with an on-shell W boson opens and becomes dominant for a large mass range [43].

- **Heavy Charged Higgs Bosons:**
  For heavy charged Higgs bosons, the decay $H^+ \to tb$ has the highest branching ratio in the MSSM m_h-max scenario. Especially at low $\tan\beta$ the branching ratio is close to one. In this decay channel a direct measurement of the mass of the charged Higgs boson is possible, but the complex jet final state is difficult to reconstruct.
  For higher $\tan\beta$, the tauonic mode $H^+ \to \tau\nu$ becomes sizable due to the enhanced $H^+ \to$

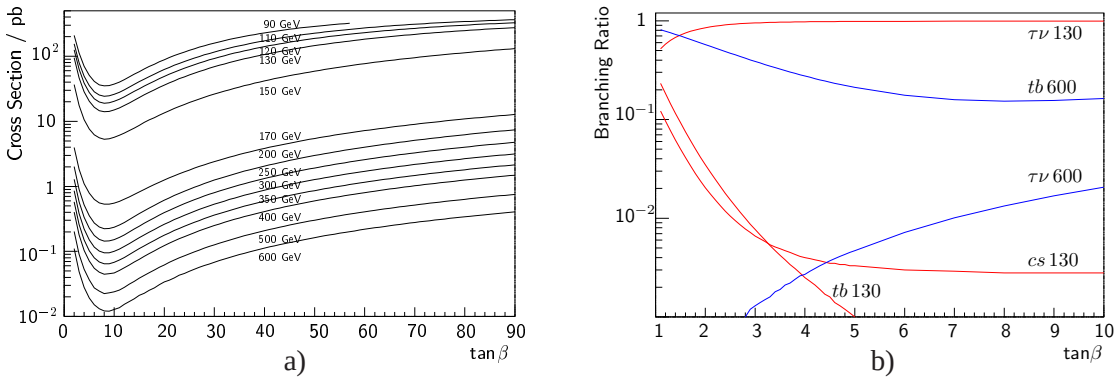

Figure 4.5: (a) Cross section for MSSM charged Higgs boson production for 14 TeV pp collisions for different $H^{\pm}$ masses [42]. (b) Branching ratios of charged Higgs boson decays into $c\bar{s}$, $t\bar{b}$, $\tau\nu$ in the MSSM m_h-max scenario as calculated by FEYNHIGGS for light and heavy $H^{\pm}$ [37].

$\tau\nu$ coupling. The distinct signature of τ-jets in the final state allows for suppression of the backgrounds.

The branching ratios of other decays involving lighter Higgs bosons and the W boson are very small. But again the situation changes for the NMSSM where these decays may become dominant.

At higher masses also the decay channels into chargino-neutralino pairs $H^+ \rightarrow \chi_i^+ \chi_j^0$ in the MSSM open up and the branching ratios into Standard Model particles decrease.

4.2.5 Final States with τ Leptons

In the MSSM the decay of light charged Higgs bosons into a charged τ lepton and τ neutrino is preferred for most of the parameter space $(\tan\beta > 3)$. This decay mode is therefore of particular interest for H^+ searches. The selection of such final states is complicated since τ leptons are not directly detectable. Instead they decay weakly with a life time of $\tau = 290.6 \times 10^{-15}$ s, corresponding to $c\tau = 87\,\mu$m, well before reaching the detector. The observation of τ leptons is only possible by reconstruction of their visible decay products. A large variety of decay modes, listed in Table 4.2, has to be taken into account.

A fraction of 35.2% of the τ lepton decays is into leptons while the remaining 64.8% include hadrons. The hadronic decay products appear as a hadron jet in the detector called τ-jet. Depending on the number of charged particles in the final state, the hadronic decay modes are divided into one-prong, three-prong, etc. decays. Because more than 99% off all hadronic decays contain one or three charged particles an important property of τ-jets is low charged track multiplicity. In addition, since τ leptons at the LHC are mainly produced in decays of W and Z bosons and also $H^{\pm}$ bosons, the decay products are highly energetic and collimated resulting in a distinct shower shape in the calorimeters. In 72% of all hadronic τ-decays the charged hadrons are accompanied by π^0s which have a very short life time of $(8.4 \pm 0.6) \times 10^{-17}$ s and decay with a branching ratio of 98.8% into two photons. These photons deposit additional energy in the electromagnetic

Table 4.2: The most relevant decay modes and branching ratios of the τ lepton in % [16].

Leptonic Modes		*35.2*
	$e^-\nu_\tau\bar{\nu}_e$	17.9
	$\mu^-\nu_\tau\bar{\nu}_\mu$	17.4
Hadronic Modes		*64.8*
One Prong	$\pi^-\nu_\tau$	10.9
	$\pi^-\nu_\tau\,1\pi^0$	25.5
	$\pi^-\nu_\tau\,2\pi^0$	9.3
	$\pi^-\nu_\tau\,3\pi^0$	1.0
	$K^-\nu_\tau \geq 0\,(\pi^0, K^0, \gamma)$	1.6
	Rest one-prong	1.9
Three Prong	$\pi^-\pi^+\pi^-\nu_\tau$	9.3
	$\pi^-\pi^+\pi^-\nu_\tau\,\pi^0$	4.6
	$K^-\pi^+\pi^-\nu_\tau$	0.3
	Rest three-prong	0.3
	Five Prong	0.1

calorimeter or convert in the material in front of the calorimeter into electron-positron pairs, leading to additional tracks within the τ-jet.
A τ-jet is therefore characterized by narrow calorimeter clusters, low track multiplicity and a displaced decay vertex which can be reconstructed with the pixel detector.

4.3 Experimental Limits

4.3.1 Direct Searches

At e^+e^- collider like LEP, charged Higgs bosons are pair produced according to $e^+e^- \to H^+H^-$. All four LEP experiments have reported limits on the charged Higgs boson mass $m_{H^\pm}$ within the generic THDM(II), assuming that the decays $H^+ \to \tau\nu$ and $H^+ \to c\bar{s}$ exhaust the entire $H^\pm$ decay width. Combining all results, the bound

$$m_{H^\pm} > 78.6\,\text{GeV} \quad \text{(95\% C.L.)}$$

has been obtained, independent on the branching ratio $\mathcal{B}\,(H^+ \to \tau\nu)$ [46].
The results of all experiments are summarized in Table 4.3 [47, 48, 49, 50]. The DELPHI and OPAL collaborations included the additional supersymmetric charged Higgs decays leading to final states $(W^*A)\,(W^*A)$ and $(W^*A)\,(\tau\nu)$, as they are enhanced in the THDM(I). The limits were determined assuming a neutral Higgs Bosons mass of $m_A > 12\,\text{GeV}$, such that A decays mainly into $b\bar{b}$.
The experiments CDF and DØ at the Tevatron $p\bar{p}$ collider at Fermilab performed searches for light charged Higgs bosons in decays of top quarks. At CDF the decay channel $H^+ \to c\bar{s}$ has been

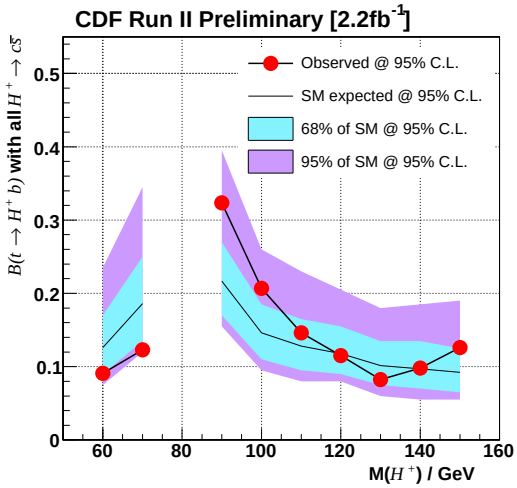

Figure 4.6: Upper limits of the CDF experiment on the branching ratio $\mathcal{B}(t \to H^+b)$ as a function of the charged Higgs boson mass in the leptophobic model [44]. The results correspond to the observed limit and the thin line with systematic error bands to the expected limit.

Table 4.3: Observed limits on the charged Higgs bosons of the experiments at LEP. The limits for the THDM(II) correspond to the decay modes $\tau\nu, c\bar{s}$, while for the THDM(I) the additional decay $H^+ \to W^*A$ has been taken into account.

	THDM(I)	THDM(II)
ALEPH	–	79.3 GeV
DELPHI	76.7 GeV	74.4 GeV
OPAL	56.5 GeV	76.6 GeV
L3	–	76.5 GeV

investigated by searching for a second resonance next to the $W \to q\bar{q}'$ invariant mass peak. Upper limits were set on the branching ratio $\mathcal{B}(t \to H^+b)$ in the mass range $90\,\text{GeV} < m_{H^\pm} < 150\,\text{GeV}$, except under the W peak between 70 GeV and 90 GeV for the leptophobic model. Branching ratios above the values $0.08 - 0.32$ are excluded, depending on $m_{H^\pm}$ (see Figure 4.6) [44].
The DØ collaboration combined single-lepton and dilepton final states. Upper limits of $\mathcal{B}(t \to H^+b) < 0.22$ and $\mathcal{B}(t \to H^+b) < 0.19$ were obtained, independent of the charged Higgs boson mass in the range $80\,\text{GeV} < m_{H^\pm} < 150\,\text{GeV}$, for the leptophobic and the tauonic model, respectively (see Figures 4.7(a) and 4.7(b)). For the MSSM m_h-max scenario, the $\tan\beta$ values depicted in Figure 4.7(c) are excluded [45].

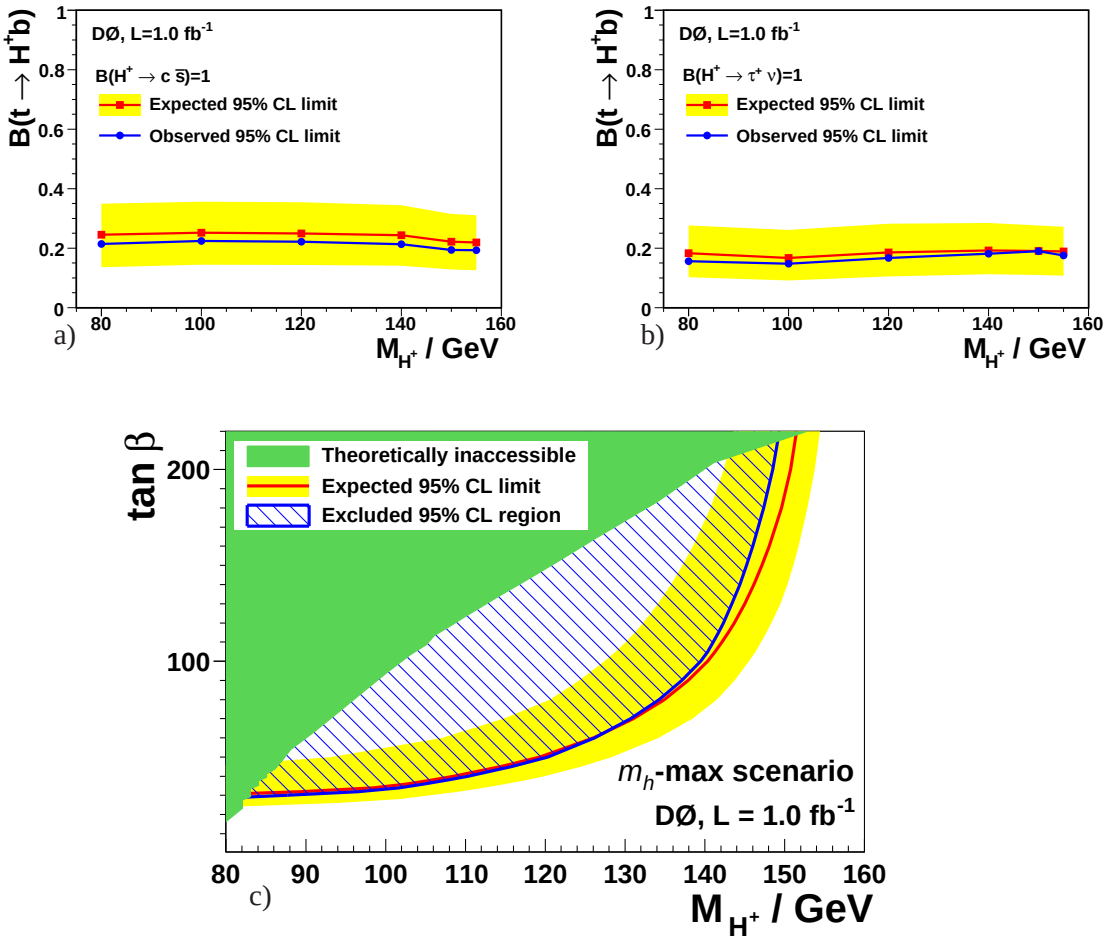

Figure 4.7: Exclusion limits for charged Higgs bosons by the DØ collaboration. The blue lines indicate the observed and the red lines the expected limits with yellow systematic uncertainty bands. Figures (a) and (b) show the upper limits on the branching ratio $\mathcal{B}(t \to H^+b)$ for the leptophobic and the tauonic model, respectively. The excluded branching ratios are $\mathcal{B}(t \to H^+b) > 0.22$ and $\mathcal{B}(t \to H^+b) > 0.19$, respectively. In Figure (c) the exclusion limits for the MSSM m_h-max scenario in the $m_{H^\pm}$-$\tan\beta$ plane are presented [45].

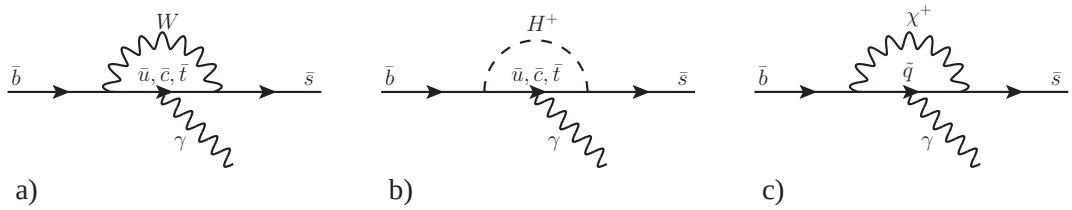

Figure 4.8: (a) $b \to s\gamma$ transition process as expected by the Standard Model, (b) H^+ contribution, (c) χ^+ contribution to this process.

4.3.2 Indirect Limits

The best indirect limits on the charged Higgs boson masses have been obtained by the BaBar[1] and Belle[2] experiments at e^+e^- B meson factories. Large data samples and well understood detectors made it possible to search for deviations of the decay rates of rare B meson decays from the Standard Model predictions. In the following three important processes are discussed:

- **Radiative B Meson Decays $B \to X_s\gamma$**
  The underlying process at quark level $b \to s\gamma$ transition is a flavor changing neutral current process and forbidden in the Standard Model at tree level. At loop level of perturbation theory, this decay can proceed via penguin processes (see Figure 4.8(a)). If physics beyond the Standard Model is realized, the $b \to s\gamma$ transition might proceed via new particles like charged Higgs bosons in the virtual loops instead of the W boson, as depicted in Figure 4.8(b). In this case the branching ratio $\mathcal{B}(b \to s\gamma)$ is enhanced compared to the Standard Model prediction. Contributions from chargino loops (Figure 4.8(c)) are possible as well in the case of the MSSM which can partially cancel the charged Higgs contribution possibly hiding new Physics.
  A limit $m_{H^\pm} > 295\,\text{GeV}$ is determined for a generic 2HDM without additional contributions from SUSY particles [51, 52].

- **Rare Leptonic B Meson Decays $B \to \tau\nu$**
  In the Standard Model, leptonic decays of B mesons are mediated by the exchange of W bosons. Charged Higgs bosons replacing W modify the branching ratio $\mathcal{B}(B \to \tau\nu)$ at tree level by a correction factor:

$$r_{H^\pm} = \left(1 - \tan^2\beta \frac{m_B^2}{m_{H^\pm}^2}\right)^2 . \tag{4.6}$$

  According to this expression, deviations from the Standard Model prediction are expected at high $\tan\beta$ and low $m_{H^\pm}$, except for the parameter space where the charged Higgs contribution is not visible since $r_H \approx 1$ [53].

- **Semi-leptonic B Meson Decays $B \to D\tau\nu$**
  Semileptonic decays of B mesons can also serve as a test of the Standard Model. Compared

[1] Experiment at the SLAC electron-positron collider PEP II.
[2] Experiment at the KEK electron-positron collider KEK-B.

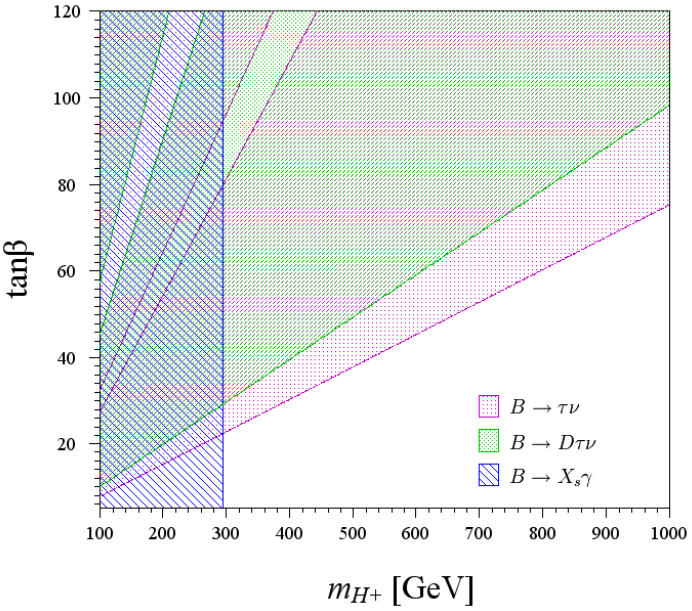

Figure 4.9: Indirect limits on the charged Higgs Bosons in the $m_{H^\pm}$, $\tan\beta$-plane. The results are obtained for the 2HDM(II) model at a 95% confidence level [51].

to the leptonic decays, the branching ratio is much higher but deviations from the Standard Model are more difficult to detect.

The excluded parameter space for the 2HDM(II) without extra SUSY particle contributions is presented in Figure 4.9. The $b \to s\gamma$ process allows for the exclusion of charged Higgs bosons up to $m_{H^\pm} < 295\,\text{GeV}$ for all $\tan\beta$. Leptonic and Semileptonic B meson decays constrain the allowed region also at higher masses and $\tan\beta$.

Chapter 5

The ATLAS Experiment at the Large Hadron Collider

In this chapter an overview of the **L**arge **H**ardon **C**ollider (LHC) (Section 5.1) and the ATLAS (**A** **T**oroidal **L**HC **A**pparatu**s**) experiment (Section 5.2) at the **C**onseil **E**uropéen pour la **R**echerche **N**ucléaire, the European Laboratory for High Energy Physics, (CERN) is given.

5.1 The Large Hadron Collider

Near Geneva in Switzerland the LHC has been built in the 26.66 km long former LEP tunnel [54]. The tunnel is embedded between the Lac Léman and the Jura mountains at a depth of 45 m to 170 m.

After the decommissioning of LEP and its experiments, the LHC has been constructed with the purpose to collide two counter-rotating beams of protons or lead ions. The LHC is the world's highest energy particle collider, designed to accelerate protons up to 7 TeV and lead ions to 2.76 TeV per nucleon, respectively. Before injection into the LHC, the particles are accelerated in several smaller machines up to 450 GeV. The injection of particles into the LHC takes place in bunches via two transfer lines. At four interaction regions the two beams are brought to collision as depicted in Figure 5.1. When the LHC is completely filled, the two beams contain 2835 bunches of 1.15×10^{11} particles each. The bunches circulate in a vacuum beam pipe at a frequency of 40 MHz corresponding to a beam current of 0.56 A. During each turn, the particles are accelerated by RF cavities with an electric field gradient of 5.5 MV/m.

The particles are forced on a circular path by 1232 dipole magnets of 15 m length, each providing a magnetic field of 8.33 T. Such high field strengths can only be achieved using superconducting coils which are operated at a temperature of 1.9 K. In order to focus the beams and to increase the interaction rate the LHC is equipped with 392 quadrupole magnets of $5 - 7$ m length. At the ATLAS interaction point the bunches are squeezed to a size of 7.55 cm in length and $16.7\,\mu$m in diameter. Once the LHC reaches its design luminosity of $\mathcal{L} = 10^{34}\,\mathrm{cm}^{-2}\mathrm{s}^{-1}$, on average 23 proton-proton interactions per bunch crossing are expected with a beam lifetime will be about 14.9 hours after which the LHC has to be refilled.

At the four collision points of the LHC the following main experiments are installed: ALICE

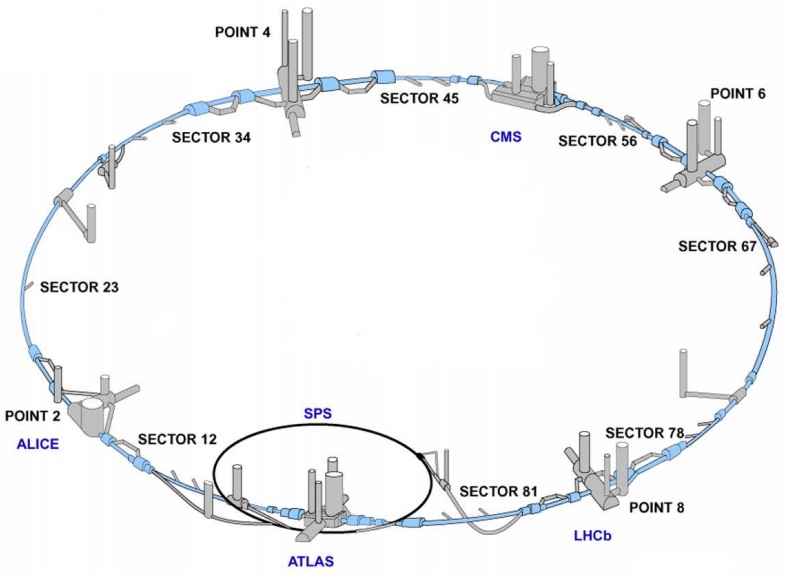

Figure 5.1: Schematic picture of the Large Hadron Collider. The particles are pre-accelerated by the Super-Proton-Synchrotron (SPS) and injected into the LHC via the transfer lines in sectors 12 and 81.

(**A** **L**arge **I**on **C**ollider **E**xperiment) [55] is a detector designed to explore the physics of strong interacting matter in high energetic collisions of lead ions. Especially the measurement a new phase of matter, the quark-gluon plasma, is in the focus of the ALICE collaboration. LHCb [56] is dedicated to the measurement of rare B meson decays in order to shed light on the origin of CP-violation. ATLAS [57] and CMS (**C**ompact **M**uon **S**olenoid) [58] are multi-purpose detectors designed to explore a wide range of particle physics at the TeV scale. The most prominent physics goals of the ATLAS experiment experiments are:

- Precise measurement of Standard Model parameters, in particular the properties of the top quark:
  The expected high production rate of W and Z bosons as well as top quarks at the LHC makes it possible to precisely measure the production cross sections and masses as well as the couplings and spin of the top quark.

- Exploration of the mechanism of electroweak symmetry breaking:
  ATLAS is designed to discover or to exclude the Standard Model Higgs boson associated to the Higgs mechanism of the electroweak symmetry breaking up to the maximum mass of about 1 TeV.

- The search for supersymmetric particles:
  Especially the discovery of the lightest supersymmetric particle as possible dark matter candidate is of high interest.

- Extra dimensions:
  The hierarchy of the electroweak and of the Planck scale is a serious puzzle in particle physics. Extra spatial dimensions provide an alternative solution to the hierarchy problem to Supersymmetry and can, for instance, lead to the production of mini-black holes [59].

- Other new Physics:
  Any new particles with masses at the TeV scale as well as new interaction scales up to several 10 TeV can be explored by the ATLAS experiment. For example, many extensions of the Standard Model predict the existence of heavy vector boson resonances, fourth family quarks and leptons or rare decays of heavy quarks and leptons.

5.2 The ATLAS Detector

Currently around 3000 physicists from 37 countries are involved in the ATLAS experiment. The ATLAS detector is housed in between the two LHC injections lines next to the main CERN complex. Its construction and commissioning was completed in 2008 right before the first protons circulated in the LHC on the 10^{th} of September 2008. Measuring 44 m in length and 25 m in height, ATLAS is the largest collider detector ever built. Its design covers the solid angle around the interaction point as completely as possible (see Figure 5.2): The interaction point is surrounded by several cylindrical detector systems in the barrel region designed to reconstruct and identify final states containing electrons, photons, muons, tau leptons and hadron jets. In the forward and backward regions the barrel is closed by end-caps. The large solid angle coverage of the detector allows for the indirect detection of weakly interacting particles like the neutrino or hypothetical neutralinos in supersymmetric extensions of the Standard Model via the measurement of missing energy in the detector. Since the colliding protons have no momentum component transverse to the beam axis, the sum of the transverse momenta of all final state particles must be zero. A deviation from zero due to undetected particles is thus called missing transverse energy $E_{\text{T}}^{\text{miss}}$.

Coordinate System

The ATLAS experiment uses a right-handed coordinate system. The x-axis pointing from the interaction point towards the center of the LHC ring, the y-axis pointing upwards and the z-axis in the direction of the counter-clock wise rotating beam. The transverse momentum p_{T} of a particle is defined as the momentum component perpendicular to the LHC beam axis. The azimuthal angle ϕ is measured from the positive x-axis in clock direction when looking into the positive z direction. The polar angle θ is measured from the positive z-axis. The pseudorapidity η is defined by

$$\eta \equiv -\ln\left(\tan\frac{\theta}{2}\right). \tag{5.1}$$

Design Requirements

The general requirements for the ATLAS detector design are imposed by the LHC collision energy and the physics goals mentioned in Section 5.1:

- Precise tracking and high momentum resolution for charged particles and precise energy measurement of electrons, photons and jets up to the TeV scale.
- High detector granularity.
- Fast and radiation-hard detectors and read-out electronics.

Detector Layout

The main detector layout is determined by the magnet system. For the inner detector an axial magnetic field with a strength of 2 T is provided by a thin superconducting solenoid measuring 2.56 m in diameter and 5.80 m in length. At larger radii from the beam axis follows the superconducting air-core toroid magnet system of the ATLAS muon spectrometer which generates magnetic field strengths from $0.2 - 3.5$ T. In the barrel region, the toroid magnet consists of eight coils, oriented radially symmetric around the beam pipe, with an inner bore (outer circumference) diameter of 9.4 m (20.1 m) and a length of 25.3 m. The cylindrical barrel toroid system is closed in the forward regions by two end-cap toroid magnets each consisting of eight superconducting coils in a common cryostat.
The main sub-detectors of ATLAS are:

- The inner tracking detector using silicon strip and pixel detectors and straw-tube layers, the latter with integrated transition radiation detection for the identification of electrons.
- Electromagnetic and hadron sampling calorimeters of high granularity and large solid angle coverage to measure the energy of electrons, photons, jets and $E_{\mathrm{T}}^{\mathrm{miss}}$.
- A stand-alone muon spectrometer with precision tracking detectors combined with muon trigger chambers.

5.2.1 Inner Detector

The Inner Detector of ATLAS is 7 m long and 2.30 m in diameter (see Figure 5.3). It houses three independent sub-detectors, namely the pixel detector, the semiconductor tracker (SCT) and the transition radiation tracker (TRT). Their main purpose is the track reconstruction and momentum measurement for transverse momenta $p_{\mathrm{T}} > 0.5$ GeV within $|\eta| < 2.5$. In the early phase of LHC operation, the track p_{T} threshold has been lowered to 0.1 GeV. In the solenoidal magnetic field of 2 T, a momentum resolution of

$$\sigma_{p_{\mathrm{T}}}/p_{\mathrm{T}} = 0.05\% \oplus 1\%$$

is achieved. For the identification of B meson and hadronic τ lepton decays also secondary vertices have to be reconstructed with high precision. The resolution of the track impact parameter transverse to the beam direction for a perfectly aligned and calibrated inner detector is

$$\sigma_{d^0} = 12\,\mu\mathrm{m}\,(1 \oplus 20\,\mathrm{GeV}/p_{\mathrm{T}}),$$

for the η-regions with the largest amount of scattering material in the tracking detector.
Each sub-detector of the Inner Detector is divided into three regions. In the barrel part, the detector

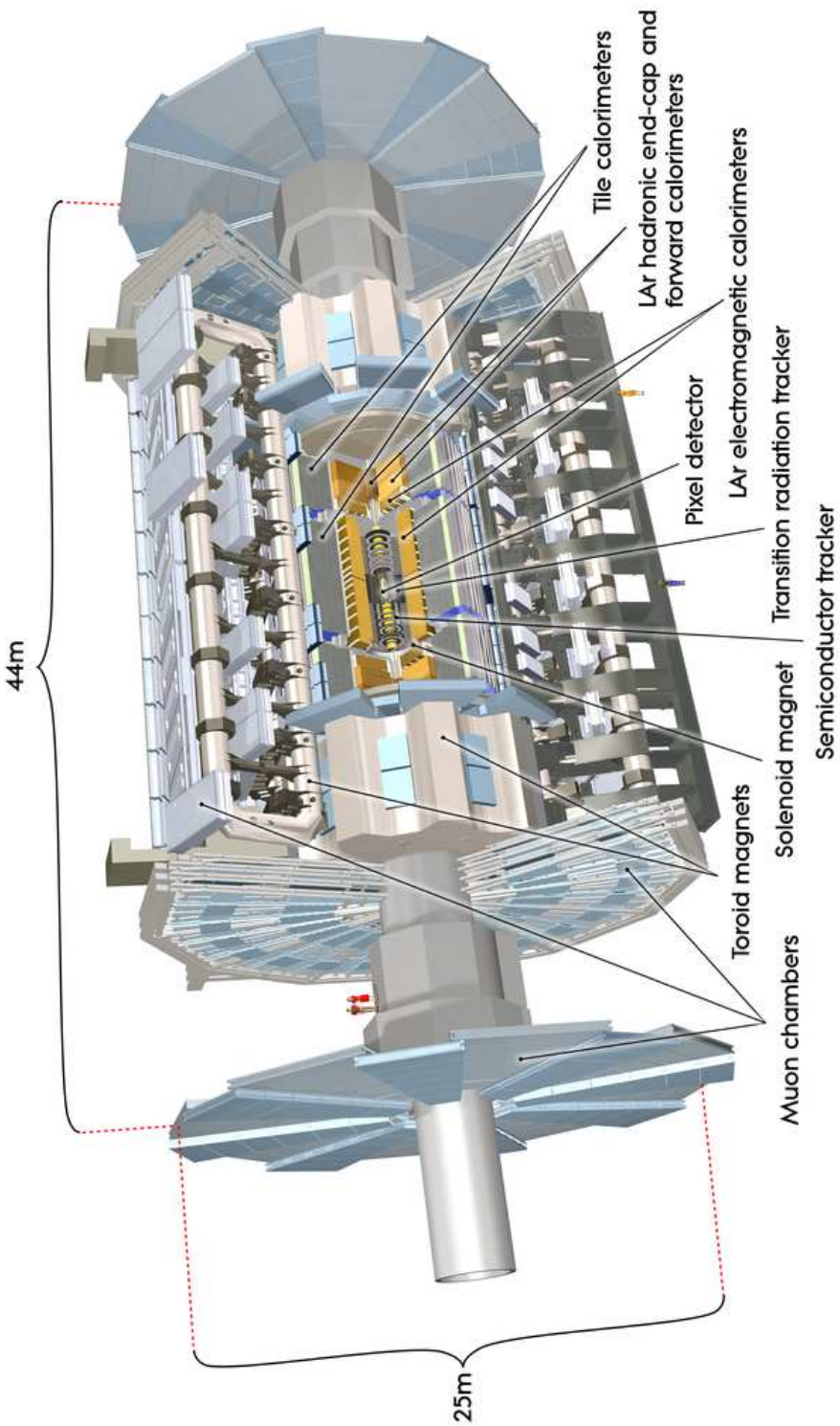

Figure 5.2: Schematic view of the ATLAS detector. The tracking detectors, calorimeters and magnets are indicated in the Figure.

modules are arranged in concentric cylindrical layers around the beam pipe. At each end it is extended by an end-cap. Each pixel and SCT end-cap consists of three and nine discs perpendicular to the beam axis, respectively, covering a pseudorapidity up to $|\eta| < 2.5$.
The pixel and SCT detectors consist of silicon pixel and silicon strip sensor modules, respectively. Even though the silicon sensors suffer under the radiation caused by the LHC collisions, the material has proven to withstand the high radiation doses of $> 2 \cdot 10^{34}$ protons/cm^2 over 10 years of LHC running. To control radiation damage, the silicon detectors and read-out electronics are operated at temperatures between $-5\,^{\circ}$C and $-10\,^{\circ}$C.

Pixel Detector

The pixel detector is closest to the interaction point. 1744 sensor modules are mounted in three layers in the barrel and each end-cap (see Figure 5.3). The sensor dimensions are $16.4\,\text{mm} \times 60.8\,\text{mm} \times 250\,\mu\text{m}$. Each sensor contains 46080 pixels with a nominal pixel size of $50\,\mu\text{m} \times 400\,\mu\text{m}$. The pixel detector has 80.6×10^6 read out channels in total. A spatial resolution of $10\,\mu$m is achieved in the $R\phi$ bending plane in the solenoidal field and $115\,\mu$m in the $z(R)$ direction in the barrel (end-caps). 12 read out chips are connected to each sensor via bump bonds.
In order to meet the radiation hardness requirements the sensors were fabricated using oxygenated n-type wafers with n^+-type pixel implants.

Semiconductor Tracker

The semiconductor tracker (SCT) consists of 4088 modules containing 15912 silicon strip sensors arranged in four cylindrical layers in the barrel and nine discs in each end-cap. In the barrel each module comprises two pairs of rectangular shaped n-type sensors which are glued back-to-back on a carbon substrate with high thermal conductivity allowing for efficient cooling. On the front- and backside of the module the strips of the two adjacent sensors are connected by wire bonds forming long strips. The sensors on opposite sides are rotated with respect to each other by a small stereo angle of 40 mrad to provide sensitivity to the coordinate in strip direction. Each of the $285 \pm 15\,\mu$m thick sensors has 768 p-type strip implants with a pitch of $80\,\mu$m and a length of 6 cm. In the end-caps, four different types of trapezoidal shaped sensors with varying pitch and strip length are used depending on the radial position. All together the SCT detector comprises 6.2×10^6 read out channels and an active area of about 61 m^2.
The spatial resolutions of the sensors are $17\,\mu$m in the bending plane $R\phi$ and $580\,\mu$m in the $z(R)$ direction in the barrel (end-caps).

Transition Radiation Tracker

The Transition Radiation Tracker (TRT) consists of 370.000 cylindrical drift tubes, operated with a gas mixture 70% xenon, 27% CO_2 and 3% oxygen. In the barrel, the 144 cm long straws are aligned parallel to the beam axis. The gold-plated tungsten anode wires located in the center of the straws are kept at 1530 V high voltage with respect to the tube walls. The latter are made of Kapton with a conductive coating. To reduce the occupancy the wires are split into two parts with equal lengths which are read out at opposite ends. In the end-caps the straws are 37 cm long and

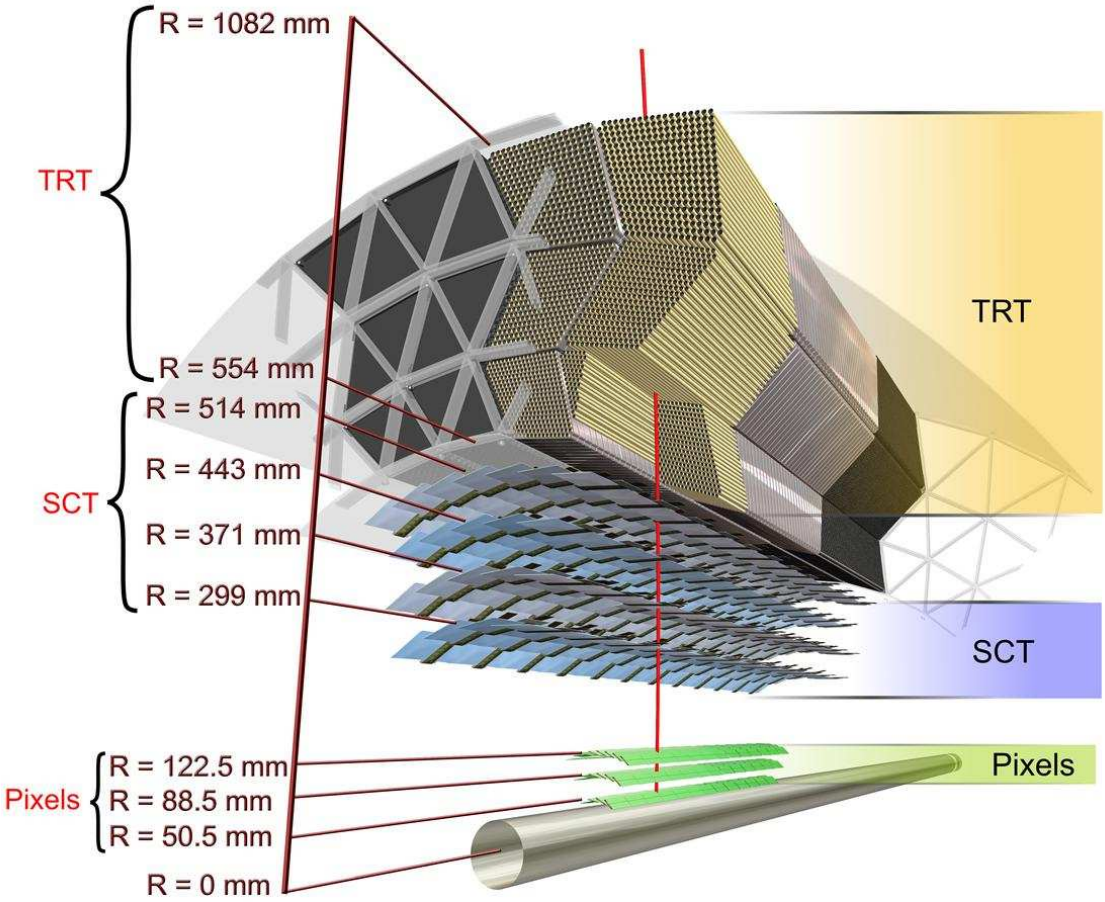

Figure 5.3: Schematic view of the beam pipe and the barrel part of the ATLAS Inner Detector with the pixel, SCT and TRT sub-detectors. The red line indicates a charged particle with $p_{\mathrm{T}} = 10\,\mathrm{GeV}$ and $\eta = 0.3$ traversing the beam pipe and the three sub-detectors.

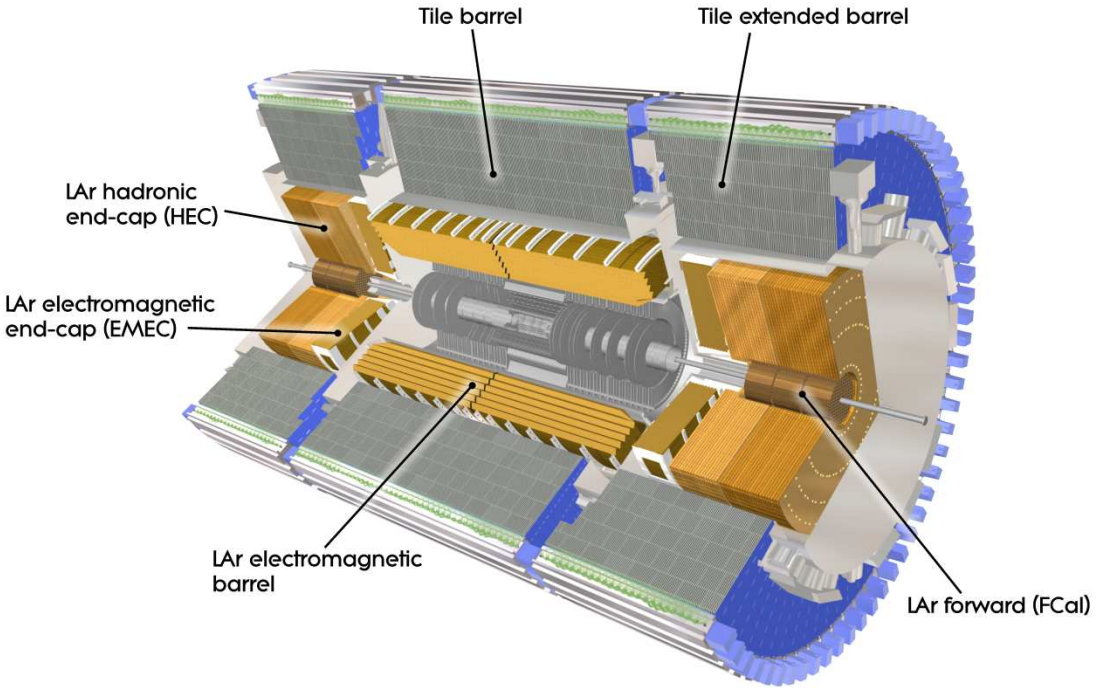

Figure 5.4: Cut-away view of the ATLAS calorimeter system consisting of the liquid argon Electromagnetic Calorimeter (barrel and end-cap), the scintillating tile Hadron Calorimeter (barrel and extended barrel), the liquid argon Hadron End-cap Calorimeter and the liquid argon Forward Calorimeters.

oriented radially.
The TRT provides on average 36 two-dimensional coordinate measurements along a track allowing for good pattern recognition and track reconstruction efficiency at the high track densities at the LHC. The spatial resolution in the $R\phi$ plane is $130\,\mu$m.
In addition, polypropylene fibers and foils in the barrel and in the end-caps, respectively, initiate transition radiation when a charged particle crosses the detector. In this way traversing electrons emit photons of about $7 - 10\,$keV detected in the straw tubes, while the corresponding energy for pions is lower. Therefore the TRT also allows for discrimination between electron and pion tracks.

5.2.2 The Calorimeters

The calorimeter system of ATLAS, depicted in Figure 5.4, consists of several components. All of them are sampling calorimeters, segmented in the longitudinal and the lateral direction. As the innermost part, the Electromagnetic Calorimeter measures the energies of electrons and photons which produce electromagnetic showers. It is followed by the Hadron Calorimeter which absorbs the hadrons traversing the Electromagnetic Calorimeter. For both calorimeters different technologies are used depending on the pseudorapidity.

The Electromagnetic Calorimeter

The barrel part of the Electromagnetic Calorimeter covers the region $|\eta| < 1.475$. It is 6.4 m long and has a inner (outer) radius of 1.4 m (2 m). Liquid argon (LAr) is used as active material ionized by charged particles. It offers stable response over time as well as intrinsic radiation hardness. The interleaved absorber platers are made of lead and are, like the electrodes in the LAr gaps, accordion shaped. With this geometry, insensitive regions are avoided and uniformity in ϕ is achieved. As depicted in Figure 5.5, the Electromagnetic Calorimeter is longitudinally divided into three segments. The first layer is highly segmented in η with strip-shaped read-out cells. They enable a spatial resolution high enough to disentangle two nearby photon showers from $\pi^0 \rightarrow \gamma\gamma$ decays. In η direction, eight strips of the first layer correspond to one read-out cell in the second layer. The second layer is segmented into squared cells extending the segmentation in ϕ direction. Here the main part of the electromagnetic cluster is measured. The third layer collects the tail of the deposited energy and is segmented coarser in η.
The Electromagnetic Calorimeter is completed by the pre-sampler, a 11 mm thick liquid argon calorimeter, which is mounted in front of the first layer. This detector provides a first energy sampling in order to estimate the energy loss by electrons and photons in the material in front of the calorimeter.
The Electromagnetic Calorimeter is extended up to $|\eta| = 3.25$ by two end-caps (EMEC) of similar design. The very forward region $3.1 < |\eta| < 4.9$ is covered by the electromagnetic liquid argon Forward Calorimeter FCAL1. It consists of copper as absorber material with 12.260 holes measuring 5.75 mm in diameter for the liquid argon.
The minimum radiation length of the Electromagnetic Calorimeter is 22 X_0. The energy resolution has been estimated in test-beam measurements to be

$$\frac{\sigma}{E} = \frac{10\%}{\sqrt{E}} \oplus 0.7\%,$$

where the unit for E is GeV. The first term corresponds to the statistical fluctuations in the shower process while the constant contribution is due to mechanical non-uniformities and calibration uncertainties.

The Hadron Calorimeter

The barrel Hadron Calorimeter is a scintillating tile calorimeter enlarging the ATLAS calorimeter system up to a radius of 4.25 m. Plastic scintillating tiles read out by photomultipliers are used as active medium and steel plates as absorber. The tiles are combined to cells of size $\Delta\eta \times \Delta\phi = 0.1 \times 0.1$ and 0.2×0.1 in the first two and the third layer, respectively. The central part of the tile calorimeter measures 5.8 m in length and covers $|\eta| < 1.0$. It is supplemented up to $|\eta| = 1.7$ by two 2.6 m long extensions on either end.
The pseudorapidity range $1.5 < |\eta| < 3.2$ is covered by the Hadronic End-cap Calorimeter (HEC). The end-caps are placed inside the extensions of the tile calorimeter behind the Electromagnetic End-cap Calorimeters. Like for the Electromagnetic Calorimeter liquid argon is used as active medium and copper plates as absorber material. Each end-cap consist of two cylindrical layers which share the cryostat with the Electromagnetic End-cap Calorimeter. The Hadronic End-cap

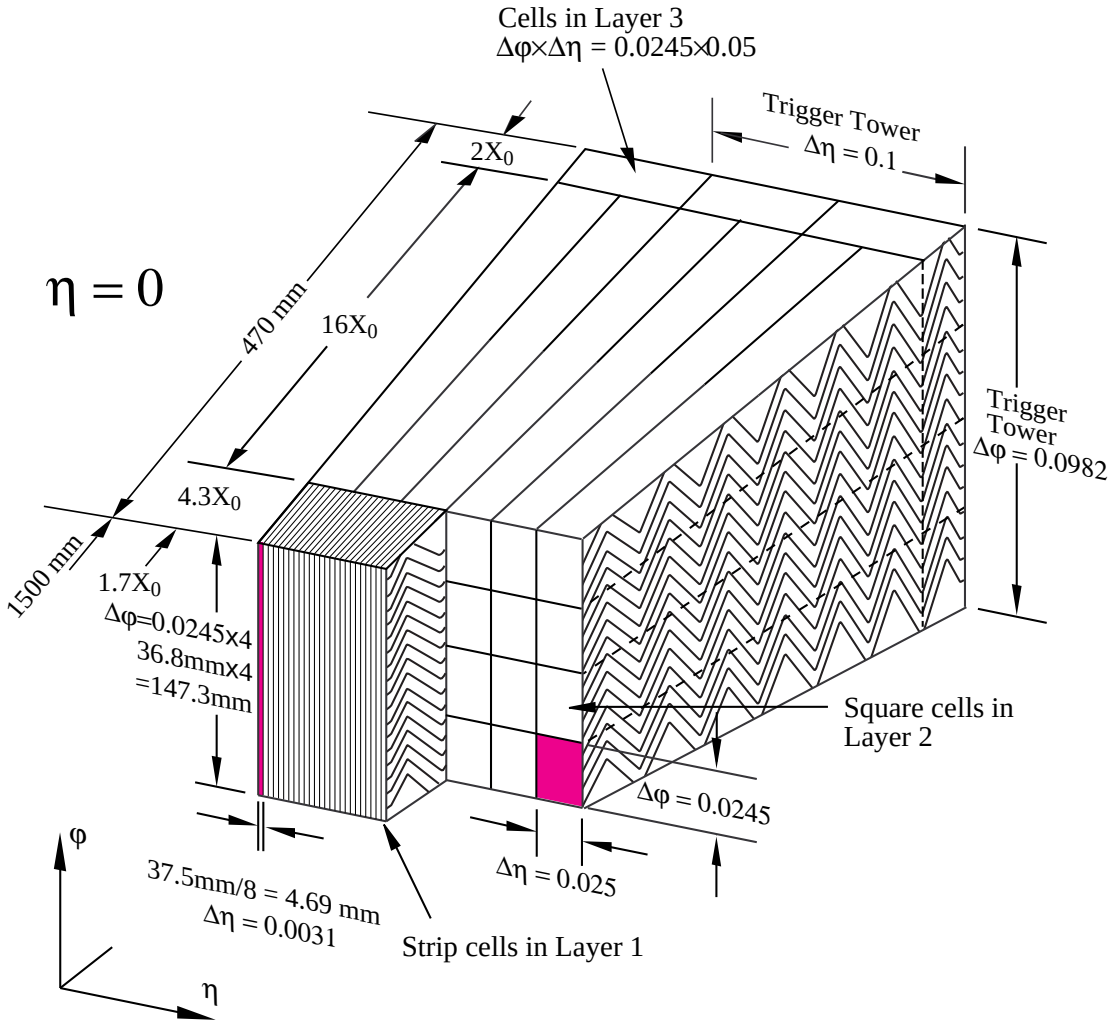

Figure 5.5: Sketch of a barrel module of the Electromagnetic Calorimeter with the accordion shaped absorber plates and electrodes consisting of three longitudinal segments with different cell sizes in η and ϕ.

Calorimeter is segmented into cells of $\Delta\eta \times \Delta\phi = 0.1 \times 0.1$ size for pseudorapidities $|\eta| < 2.5$ and $\Delta\eta \times \Delta\phi = 0.2 \times 0.2$ for larger values of $|\eta|$.
In the extreme forward region $3.1 < |\eta| < 4.9$, the Hadron Calorimeter is completed by the hadron Forward Calorimeters FCAL2 and FCAL3. Their design was chosen by the high particle fluxes expected in this region. Thus the absorber are made of tungsten to maximize radiation length and minimize lateral spread of the showers. Again liquid argon is used as active medium.
A total interaction length of at least 10 λ is provided by the Electromagnetic and Hadron Calorimeters together as a requisite for good energy and $E_{\mathrm{T}}^{\mathrm{miss}}$ resolution and minimized leakage of particles out of the calorimeter and into the muon spectrometer.
The overall energy resolutions of the hadronic calorimeters are:

$$\frac{\sigma_{\mathrm{Tile/HEC}}}{E} = \frac{50\%}{\sqrt{E}} \oplus 3\%, \qquad \frac{\sigma_{\mathrm{FCAL}}}{E} = \frac{100\%}{\sqrt{E}} \oplus 10\%,$$

where the unit for E is GeV.

5.2.3 The Muon Spectrometer

With an active area of $5500\,\mathrm{m}^2$ the muon spectrometer is the largest detector system of ATLAS. Its purpose is the triggering and reconstruction of muons with transverse momenta above 3 GeV which is the mean energy loss in the calorimeter. A design of the muon spectrometer has been chosen which allows for stand-alone momentum measurement with a resolution of 10% for tracks with $p_{\mathrm{T}} \approx 1\,\mathrm{TeV}$. The magnetic field is provided by a superconducting air-core toroid magnet system which minimizes the multiple-scattering of the muons. The high momentum resolution at high energies puts stringent requirements on the mechanical precision and spatial resolution of the muon spectrometers and on their calibration and alignment. The following detector systems are operated in the muon spectrometer:

Precision Tracking Chambers

Precision measurements of muon tracks are carried out by 1088 Monitored Drift Tube (MDT) chambers. The MDT chambers are arranged in three detector layers in barrel and in the end-caps covering the pseudorapidity range $|\eta| < 2.7$. Each MDT chamber is composed of two multilayers with three or four layers of drift tubes filled with a Ar:CO_2 (93:7) gas at an absolute pressure of 3 bar. A radial electrical field is produced by a high voltage between the tube wall and a thin, accurately centered gold plated tungsten-rhenium anode wire. The traversing muons create ions and electrons which drift towards the tube wall and the wire, respectively. About $150\,\mu$m in front of the wire, the energy of the electrons is sufficient to ionize the gas themselves, amplifying the primary charge by a factor $2 \cdot 10^4$. In this way enough ions are created to induce a measurable signal. The time difference between the rising edge of the signal and the time of the bunch crossing corrected for the muon flight time is a measure of the *drift time* of the ionization electrons to the anode wire. The corresponding drift radius r, obtained via the $r(t)$-relationship, is used to reconstruct the muon track.
The $r(t)$-relationship depends on the properties of the gas mixture chosen as well as the environmental conditions like the magnetic field strength, temperature and background rate. To account

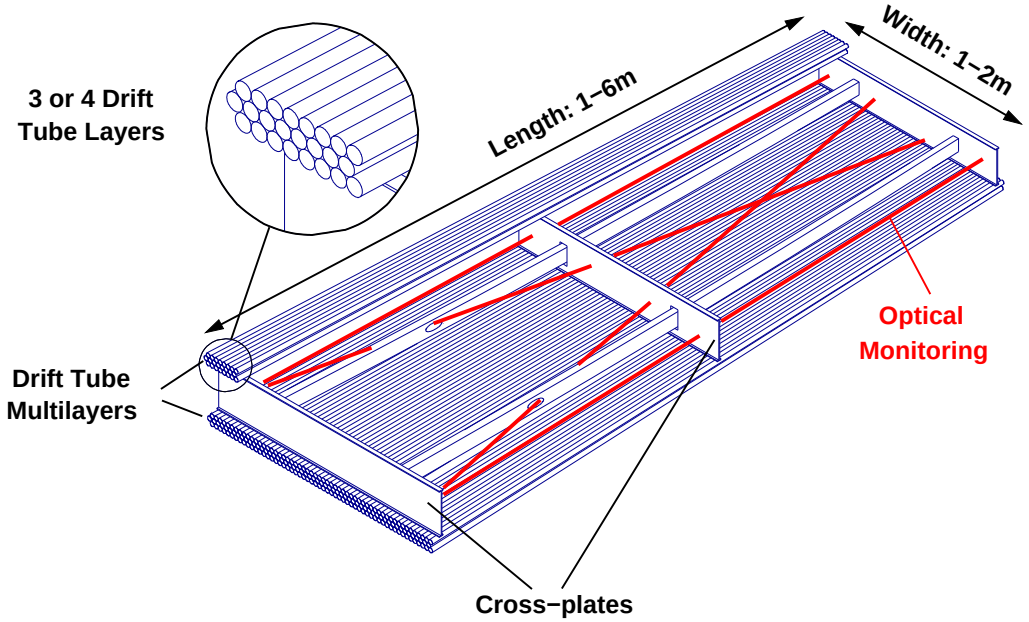

Figure 5.6: Schematic view of a Monitored Drift Tube chamber. Indicated are the two multilayers containing three or four drift tube layers mounted on the cross-plates. In addition the light paths used for the optical monitoring are indicated.

for the varying conditions, the calibrated $r(t)$-relationship is calibrated regularly taking into account data from 1800 Hall probes and 12.220 temperature sensors. An average drift-tube resolution of $80\,\mu$m and a chamber resolution of $35\,\mu$m are achieved with this gas mixture which was chosen to prevent aging of the drift tubes.
In the very forward region $2.0 < |\eta| < 2.7$ of the inner end-cap layers the background particle flux is too high for the operation of MDT chambers. Cathode strip chambers (CSC) are used there instead which are characterized by a higher granularity and shorter response time. Each CSC chamber consists of four individual planes equipped with radially oriented wires in combination with two orthogonally segmented cathodes. Charged particles ionize the gas mixture in the chambers (80% argon, 20% CO_2) inducing signals in the cathode strips. The average spatial resolution of a CSC chamber in the bending plane is $60\,\mu$m.
To reach the desired momentum resolution, the precision tracking chambers of the muon spectrometer have to be accurately aligned with respect to each other. Therefore 12.000 optical sensors monitor the internal deformations of the MDT chambers and their relative positions with an accuracy of typically $50\,\mu$m.

The Trigger Chambers

Two different trigger chamber types have been chosen for the barrel and for the end-cap regions (Figure 5.7). Resistive Plate Chambers (RPC) are employed in the barrel ($|\eta| < 1.05$). They are mounted on top and bottom of the middle MDT chambers layer and on top or bottom of the outermost MDT barrel chambers layer. These detectors are made of two parallel resistive

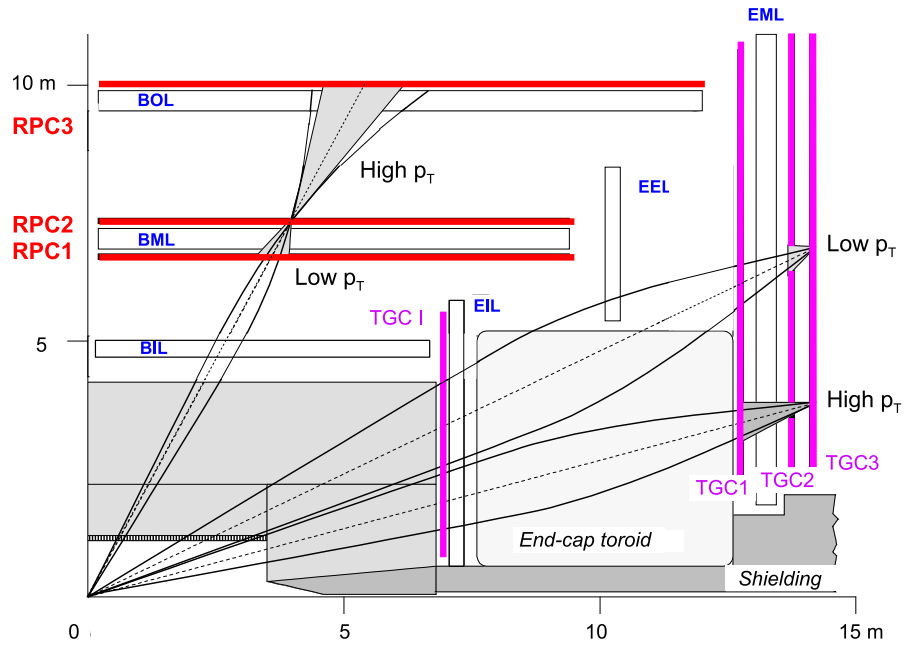

Figure 5.7: Schematic view of the muon trigger system.

Bakelite plates forming a 2 mm gas gap filled with a $C_2H_2F_4$, Iso-CH_4H_{10} and SF_6 (94.7:5:0.3) gas mixture. The charge avalanche induced by the crossing muons in the high electric field of 4.9 kV/mm between the parallel plates is detected via two capacitive coupled orthogonal layers of metallic strips on the outer surface of the plates.
The remaining pseudorapidity range in the end-caps ($|\eta| < 2.4$) is covered by Thin Gap Chambers (TGC). One TGC layer is located in front and two behind the middle MDT wheel. A fourth layer is located in front of the innermost tracking layer of the end-caps. The TGCs are multi-wire proportional chambers with wire-cathode distance (1.4 mm) smaller than the wire-wire distance (1.8 mm). As gas mixture CO_2 and n-pentane (55:45) is used.
The muon trigger chambers provide fast signals with few nano seconds time resolution and are therefore capable to identify the bunch crossing to which the muon belongs. Muon tracks are triggered by coincidences between hits in the various trigger chamber layers which are compatible with tracks originating from the interaction point. The trigger chambers also complete the track coordinate measurement providing the second coordinate information in the direction along the MDT tubes.

5.2.4 Trigger System

The overwhelming majority of inelastic interactions at the LHC produces events which are not interesting for the physics program. In order to be able to store the interesting data, the data rate must be greatly reduced from the very high interaction rate of about 1 GHz. At the same time it must be ensured that the interesting rare events are not lost.

The trigger system selects events according to the following criteria:

- Events with high p_{T} leptons, jets, b-jets, $E_{\mathrm{T}}^{\mathrm{miss}}$ and $\sum E_{\mathrm{T}}$.
- Background rejection by a factor of 10^7.
- Flexible and easily adaptable in order to deal with changing data taking conditions like collision energy and luminosity as well as background rates.

To achieve these goals, a three-level trigger system has been chosen minimizing both the data flow and the latencies of the trigger decisions:

1. The Level-I trigger is a hardware trigger examining the events for every bunch crossing. To cope with the high event rates, reduced granularity is used by combining for instance calorimeter cells to trigger towers. The trigger towers have a separate electronics path and are used to trigger electromagnetic clusters, jets, hadronically decaying τ leptons and $E_{\mathrm{T}}^{\mathrm{miss}}$. The muon system uses the information from RPC and TGC chambers. During the trigger latency of $2.5\,\mu$s the complete detector information is saved in pipeline memories in the front-end electronics. If an event is selected, the data is transfered to the Level-II central processor and regions of interest are defined around the triggering object. The maximum acceptable event rate is currently 75 kHz and can be upgraded to 100 kHz.

2. The Level-II software trigger has access to the regions of interest provided by the Level-I trigger. Within a time window of about 10 ms the full detector granularity within the regions of interest is used to refine the reconstruction and to classify the event with the help of dedicated fast algorithms. At this stage also Inner Detector tracks are incorporated into the trigger decision. The Level-II trigger reduces the data rate to about 3.5 kHz.

3. The final trigger decision is carried out by the Event Filter. At this stage the standard off-line reconstruction software is used to process the complete data from all detector systems. The events are fully reconstructed using up-to-date calibration and alignment constants and optimized thresholds. The events are finally written to mass storage devices at a rate of about 200 Hz. The available time for the event filter to take the trigger decision amounts to $1-2$ seconds.

Chapter 6

ATLAS Detector Performance

In this chapter the ATLAS detector performance is discussed which was studied with simulated events. The Monte Carlo simulation is performed using the ATLAS software package ATHENA [60]. In the first step, the physics processes at the interaction point are simulated using event generators described in Section 6.1. After the detailed simulation of the detector response with the GEANT4 package [61], the different observable objects in the final state, like electrons, muons or jets, are reconstructed. In Section 6.2 the particle reconstruction and identification algorithms are explained and their performance is studied. The results shown were obtained with the ATHENA software releases 12.0.6 and 14.2.25 for events at center-of-mass energies of 14 TeV and 10 TeV, respectively. Release 12.0.6 has been used for the charged Higgs boson search in this thesis which is part of ATLAS Higgs studies published in [42]. In the following releases major changes have been implemented especially affecting the τ-jet reconstruction and identification algorithms. Release 14.2.25 incorporates all important software developments and is therefore used for the subsequent studies related to the background estimation from data.

6.1 Monte Carlo Event Generators

A large variety of Monte Carlo generators is available to simulate physics processes as input for the ATLAS detector simulation. These programs generate the outgoing particles produced in the interactions of the colliding protons.
The following generators have been used for this study:

- **PYTHIA**
  PYTHIA is a flexible multi-purpose event generator [62] using leading order matrix element calculations for a wide class of electroweak and strong physics processes. While the hard scattering part of this event generator is optimized for $2 \rightarrow 1$ and $2 \rightarrow 2$ processes, additional hadronic activity is implemented by means of the parton shower model. This algorithm adds splittings of one into two or more partons providing a good description of soft jets. Spin correlations for top quark pairs, for instance, are not taken into account.

- **ALPGEN**
  For the generation of events with high multiplicity of hard jets the parton shower model does not always provide an accurate description. The ALPGEN generator employs leading order matrix-element calculations for processes with several hard jets in the final state like Z/W+jets production [63]. The HERWIG program is employed for the hadronization process of the colored particles via parton showers [64]. To avoid double counting, the jet generation according to the matrix elements and the one from the parton shower are matched following the MLM matching scheme [65]. The simulation of the beam remnants, the underlying event, is done by the JIMMY package [66].

- **MC@NLO**
  The MC@NLO package is a matrix element generator also combined with the HERWIG parton shower [67]. It allows the incorporation of $2 \rightarrow 2$ next-to-leading-order QCD matrix elements.

- **ACERMC**
  This program [68] provides a library for the generation of processes not covered by the multi-purpose event generators PYTHIA and HERWIG. For the parton showering and hadronization as well as for the simulation of the underlying event the HERWIG package is used.

- **TAUOLA/PHOTOS**
  The TAUOLA program is dedicated to the description of hadronic decays of the τ leptons [69] taking into account the effects of the polarization of the τ leptons. Radiative corrections are provided by the PHOTOS package [70].

6.2 Particle Reconstruction and Identification

To quantify the reconstruction and particle (electron, muon, τ lepton or b quark) identification performance of the ATLAS detector in the Monte Carlo simulation, three quantities – efficiency, misidentification rate and background rejection are defined as:

$$\begin{aligned} \text{Efficiency} &= \frac{N_{\text{correctly identifed}}}{N_{\text{generated signal}}}, \\ \text{Misidentification rate} &= \frac{N_{\text{misidentified}}}{N_{\text{identified}}}, \\ \text{Rejection} &= \frac{N_{\text{generated background}}}{N_{\text{generated and misidentifed background}}}, \end{aligned} \tag{6.1}$$

where $N_{\text{generated signal}}$ and $N_{\text{generated background}}$ denote the number of generated signal and background particles. $N_{\text{correctly identifed}}$ is the number of reconstructed and identified particles that can be matched to a generated signal particle of the correct type while $N_{\text{misidentified}}$ is the number of reconstructed and identified particles where this is not possible. Finally, $N_{\text{generated and misidentifed background}}$ denotes the number of generated background particles which are misidentified.
The efficiency is the probability that a generated particle type is reconstructed and correctly identified. Similarly, the misidentification rate is the probability that an identified particle does not

correspond to the original generated particle of the same type. The rejection is the inverse probability that a generated particle of a certain type is misidentified, for instance as a b-jet or a τ-jet. For the matching of generated and reconstructed particles, their momentum vectors are required to have a small angular separation $\Delta R = \sqrt{\Delta\eta^2 + \Delta\phi^2}$. For electrons and muons the condition $\Delta R < 0.1$ has to be fulfilled, for the association of jets to partons a larger separation $\Delta R < 0.25$ is allowed. The performance is evaluated for Standard Model $t\bar{t}$ production events since it is the most relevant background process for light charged Higgs searches. The events were generated with the MC@NLO generator where the W boson from one of the top quark decays was forced to decay into an electron, muon or τ lepton.

6.2.1 Muon Reconstruction

For the reconstruction of muons, two algorithms, STACO [71] and MUID [72], are available in the ATHENA framework. Both combine information from the inner detector, the calorimeter and the muon spectrometer with similar performance. The following discussion is restricted to the STACO package which was used for all analysis results.
Three classes of reconstructed muons are provided:

- **Stand-alone Muons**
  The reconstruction of tracks in the muon spectrometer alone, so called stand-alone muons, starts with track segments in the individual chambers provided by a pattern finding algorithm. Tracks are fitted to the segments taking into account the inhomogeneous magnetic field and the material traversed by the muons. Due to the energy loss of muons in the calorimeter (on average 3 GeV) and the small bending radius of low p_{T} muon tracks, only muons with $p_{\mathrm{T}} \gtrsim 5$ GeV can be reconstructed by the stand-alone algorithm. The geometrical acceptance of the muon spectrometer covers the pseudorapidity region up to $|\eta| < 2.7$.

- **Combined Muons**
  Within $|\eta| < 2.5$ the stand-alone muons are extrapolated to the inner detector taking into account the energy loss in the calorimeter. The latter is determined by means of a parameterization table. In case a corresponding track is reconstructed also in the inner detector, the muon trajectory is re-fitted using track segments from both detectors. In this way the momentum resolution is improved for $p_{\mathrm{T}} < 100$ GeV. Also the backgrounds from in-flight pion or kaon decays as well as from particles escaping the calorimeter are suppressed.

- **Low-p_{T} Muons**
  Muons with $p_{\mathrm{T}} \lesssim 5$ GeV loose a large part of their energy in the calorimeter and cannot be reconstructed in the muon spectrometer. The reconstruction of such muons starts from an inner detector track. This track is subsequently extrapolated to the inner layer of the muon spectrometer. The middle and outer layers of the muon spectrometer are not reached by the tracks due to the small bending radius in the magnetic field.

An overview of the performance of the combined muon reconstruction is given in Figure 6.1. On the generator level muons from W decays are selected. Muons originating from semi-leptonic decays of B mesons are less suitable for this study due to their lower transverse momenta and

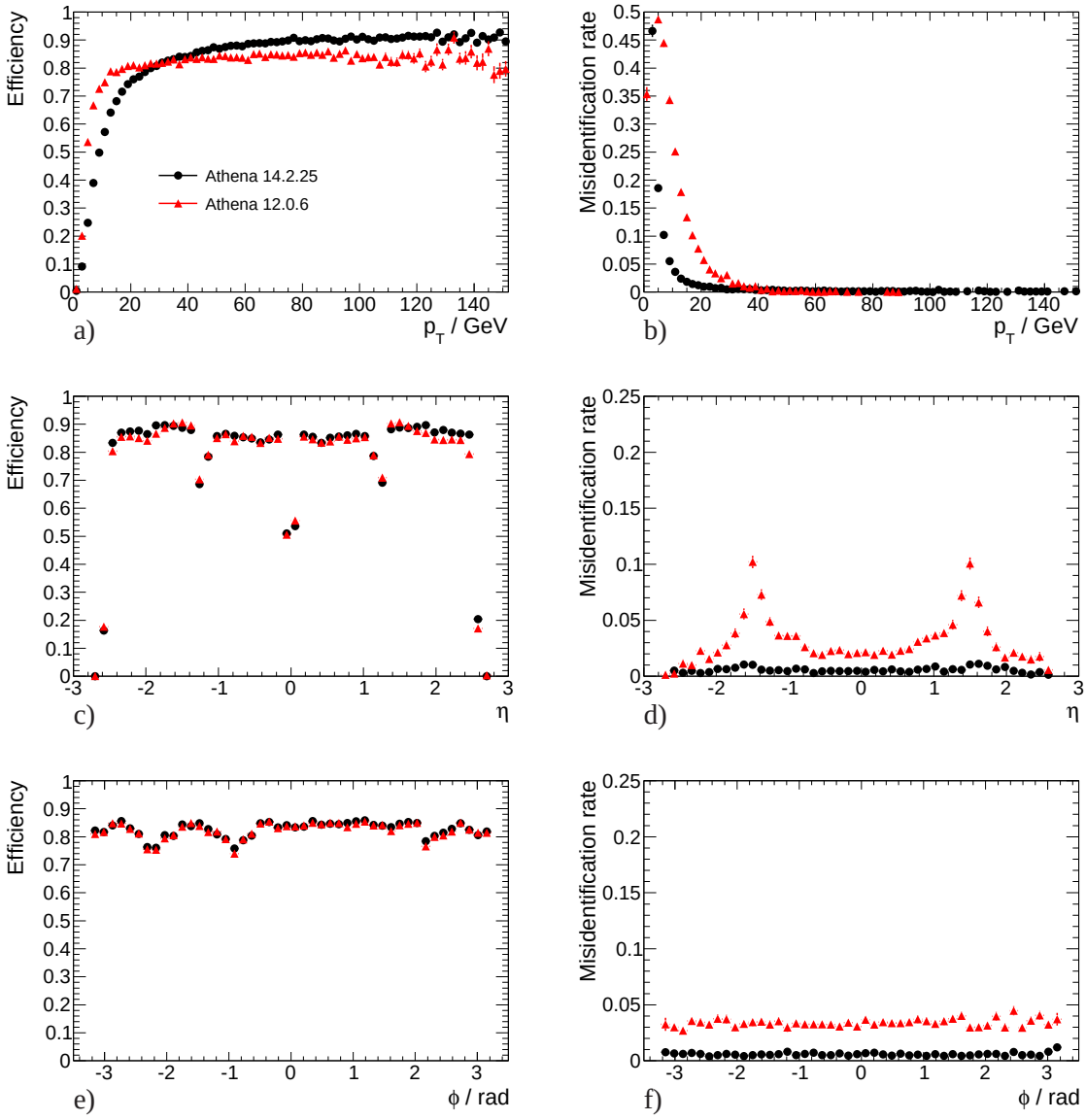

Figure 6.1: Performance of the combined reconstruction of isolated muons in releases 12.0.6 and 14.2.25. The p_{T} dependence of (a) efficiency and (b) misidentification rate is shown for $|\eta| < 2.5$, (c) and (d) show the η dependence for $p_{\mathrm{T}} > 20\,\mathrm{GeV}$. For the ϕ dependence (e,f) both cuts are applied. The red triangles indicate the results for ATHENA release 12.0.6, the black circles the ones for release 14.2.25.

the neighboring hadronic activity. In Athena release 12.0.6, isolated muons are selected requiring the transverse energy deposition $E_{\mathrm{T}}^{\mathrm{cone}}$ in the calorimeter in a cone $\Delta R = 0.4$ around the muon direction to be smaller than 9 GeV. In release 14.2.25, the energy $E_{\mathrm{T}}^{\mathrm{cone}}$ in a cone of the same size divided by the p_{T} of the muon track is required to be smaller than 0.2. The p_{T} dependence of the muon reconstruction efficiency and misidentification rate is shown in Figures 6.1(a) and 6.1(b) for muons within $|\eta| < 2.5$. The η dependence is shown for the muons with $p_{\mathrm{T}} > 20$ GeV in Figures 6.1(c) and 6.1(d). For the ϕ dependence, shown in Figures 6.1(e) and 6.1(f), both cuts are applied.
The differences in the p_{T} dependence between the two reconstruction software releases can be explained by the different isolation requirements. The relative isolation requirement in release 14.2.25 is more effective for the selection of high-p_{T} muons. For both releases, the muon efficiency is degraded at $\eta \approx 0$ due to a gap in the muon detector coverage for calorimeter services and at $|\eta| \approx 1.5$ in the transition regions from the barrel to the end-caps. The scattering material in the feet region of the detector is responsible for the efficiency drops at $\phi \approx -2.1^{\circ}$ and $\phi \approx -1.0^{\circ}$.
The transverse momentum resolution of combined muons with a $p_{\mathrm{T}} < 100$ GeV is $2 - 3\%$ in the simulated data.

6.2.2 Electron Reconstruction

The standard ATHENA software package for the reconstruction and identification of isolated high-p_{T} electrons and photons is EGAMMA [73]. The reconstruction of electron candidates is performed by the so-called *sliding window* algorithm. The calorimeter cells of the pre-sampler and the three layers of the electromagnetic calorimeter are combined in depth, forming towers of the size $\Delta\eta \times \Delta\phi = 0.025 \times 0.025$. The calorimeter is scanned with a search window of $\Delta\eta \times \Delta\phi = 0.125 \times 0.125$ size. For each window position a cluster seed is defined if the transverse energy in the window exceeds 3 GeV. Starting from the cluster seed, cluster formation and energy calibration is performed [74]. Finally, an inner detector track not associated to a reconstructed photon conversion and with a momentum compatible with the cluster energy is searched for and matched with the cluster in a window $\Delta\eta \times \Delta\phi = 0.05 \times 0.1$.
The efficiency of the electron reconstruction is very high $(> 90\%)$ and mainly limited by the energy loss and scattering in the material of the inner detector. However, at the LHC backgrounds of jets from QCD processes are large. Hence, additional identification of the electron candidates is performed by exploiting several variables which discriminate between electrons and jets. These are calculated based on information from the calorimeter and inner detector:

- **Calorimeter Information**
  Unlike jets, electrons deposit most of their energy in the electromagnetic calorimeter. Therefore the ratio of the energies deposited in the hadronic and in the electromagnetic calorimeter is smaller for electrons than for jets. In addition, the high granularity of the electromagnetic calorimeter enables a precise measurement of the lateral and longitudinal shower shapes. The showers of QCD jets are more stretched compared to electron showers of the same energy. Large part of the jets can be rejected by requiring a small shower length.

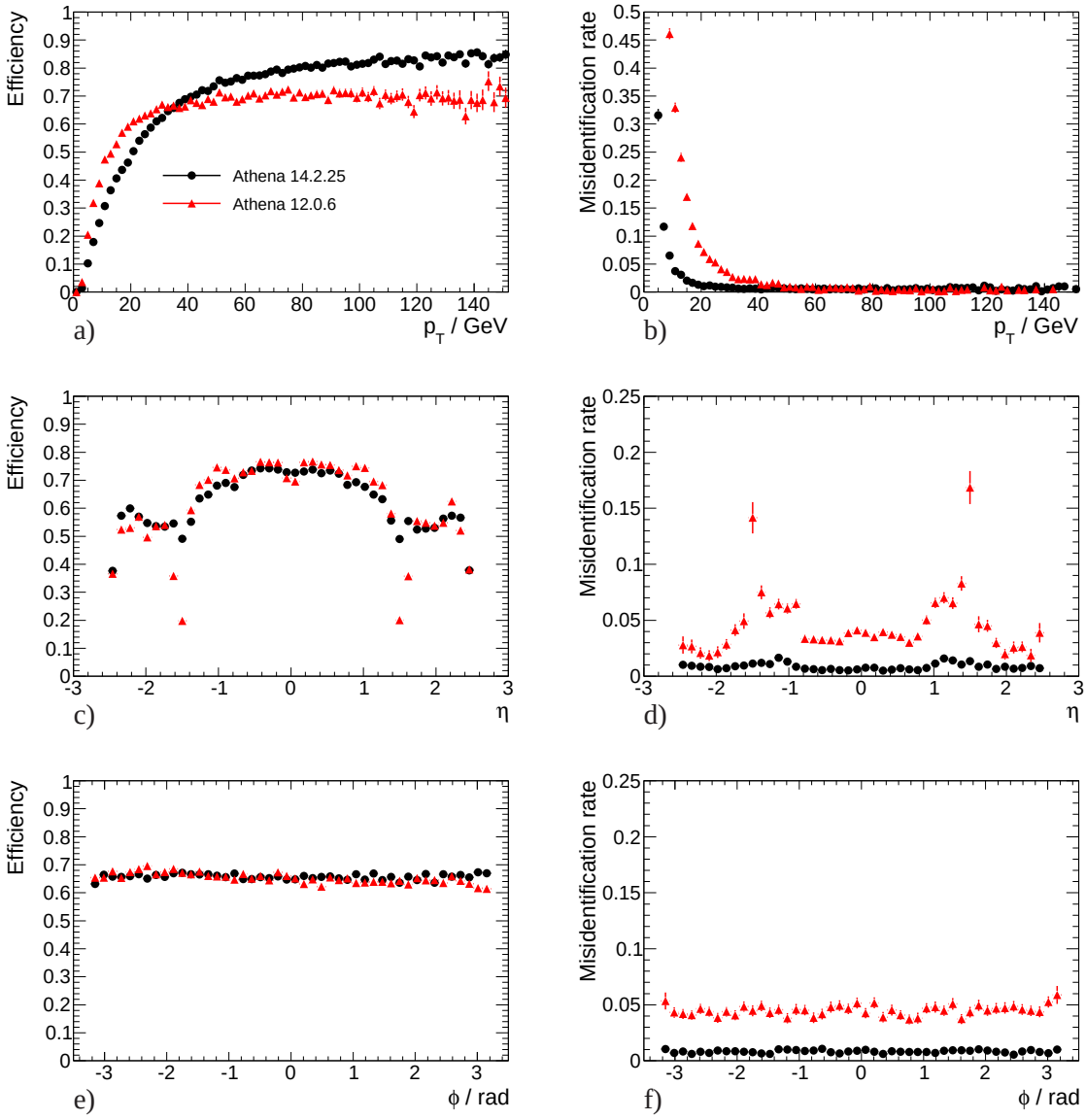

Figure 6.2: Performance of the combined reconstruction and identification of isolated electrons in releases 12.0.6 and 14.2.25. The p_{T} dependence of (a) efficiency and (b) misidentification rate is shown for $|\eta| < 2.5$, (c) and (d) shown the η dependence for $p_{\mathrm{T}} > 20\,\mathrm{GeV}$. For the ϕ dependence (e,f) both cuts are applied. The red triangles indicate the results for ATHENA release 12.0.6, the black circles the ones for release 14.2.25.

- **Inner Detector Information**
  Tracks belonging to electron candidates are demanded to be of high quality with maximum numbers of hits in the pixel, SCT and TRT detectors. The transition radiation information is used to explicitly reject pions.

- **Combined Track-Shower Information**
  The extrapolation of an electron track into the Electromagnetic Calorimeter has to match with the barycenter of the corresponding shower. For jets this is usually not the case since additional charged particles and photons shift the shower position. The ratio E/p of the shower is usually close to unity for electrons if they do not loose a significant part of their energy by bremsstrahlung in the Inner Detector. For jets, larger E/p values are expected since several tracks can belong to one jet and there is additional energy from neutral particles in the calorimeter.

In release 14.2.25 there are three pre-defined sets of cuts with different jet rejection power available corresponding to loose, medium and tight electron quality criteria. The medium selection is used as it approximately corresponds to the selection criteria in release 12.0.6.
In addition, as for the muons, an isolation requirement has to be fulfilled. In release 12.0.6 the scalar sum $E_{\mathrm{T}}^{\mathrm{cone}}$ of the transverse momenta of tracks in a cone with radius $R = 0.3$ around the electron direction is calculated where the electron track itself is excluded from the sum. Electron candidates with a $E_{\mathrm{T}}^{\mathrm{cone}} < 6\,\mathrm{GeV}$ are accepted. A calorimeter based isolation criterium is used in release 14.2.25 with cone size $\Delta R = 0.4$ and $E_{\mathrm{T}}^{\mathrm{cone}}/p_{\mathrm{T}} < 0.2$.
In Figure 6.2 the performance of the combined electron reconstruction and identification is shown. As for the muons, the isolation requirement in release 14.2.25 leads to lower efficiency for low p_{T} and higher efficiency for high p_{T} (see Figure 6.2(a) and 6.2(b)). The efficiencies in the transition region $1.37 < |\eta| < 1.52$ between barrel and end-cap calorimeters is recovered in release 14.2.25 as be seen in Figure 6.2(c) and 6.2(d). Due to the ϕ symmetry of the calorimeter, the efficiency and misidentification rate is uniform in this direction (see Figure 6.2(e) and 6.2(f)).
The p_{T} resolution of electrons with a transverse momentum $p_{\mathrm{T}} > 20\,\mathrm{GeV}$ is better than 5% for both ATHENA releases.

6.2.3 Jet Reconstruction

The first step of the jet reconstruction is the clustering of calorimeter cells. In the topological cluster algorithm [74] calorimeter cells with high signal-to-noise ratio act as cluster seeds. The noise in the calorimeter cells, mainly from electronics and pile-up, can be measured during data taking. A cell is considered as a cluster seed only if its energy is greater than $4\sigma_{\mathrm{noise}}$ where σ_{noise} is the root mean square of the energy fluctuations in the cell. Hence the formation of fake clusters is suppressed. The cluster seed is extended by successively collecting neighboring cells with energy above $2\sigma_{\mathrm{noise}}$. These cells act as seeds themselves and the cluster is expanded further by adding the next neighboring cells which satisfy the threshold $0\sigma_{\mathrm{noise}}$. Consequently, the number of cells per cluster is not fixed as opposed to the fixed-size clusters produced by the sliding window algorithm. The decreasing threshold ensures that the tails of the showers are not discarded.
In the second step of the jet reconstruction the clusters are grouped together by a seeded cone algorithm [75] forming jets within a cone of radius $R = 0.4$. Finally the jet energies are calibrated

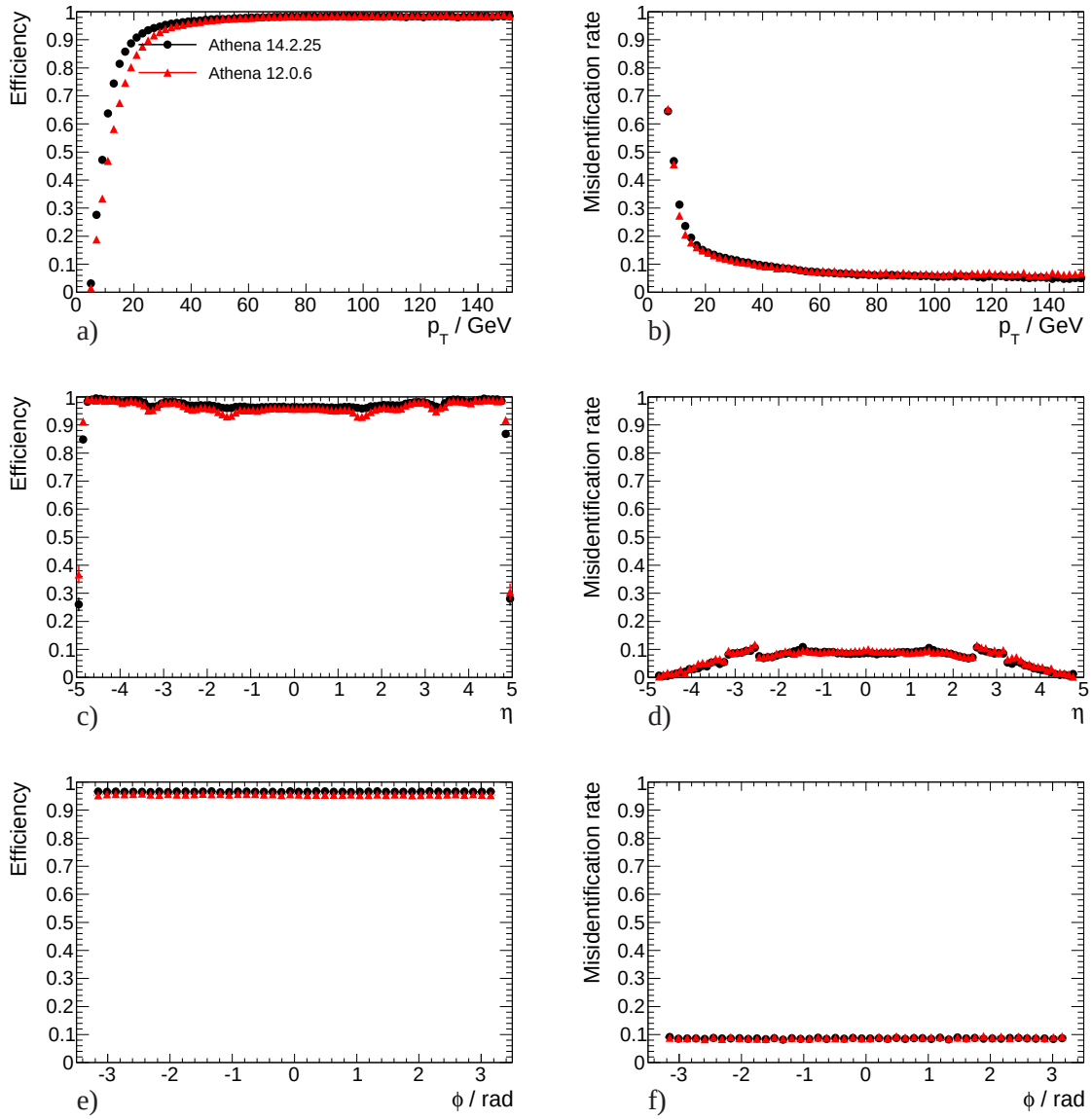

Figure 6.3: Performance of the reconstruction of jets in releases 12.0.6 and 14.2.25. The p_{T} dependence of (a) efficiency and (b) misidentification rate is shown for $|\eta| < 5$, (c) and (d) shown the η dependence for $p_{\mathrm{T}} > 20\,\mathrm{GeV}$. For the ϕ dependence (e,f) both cuts are applied. The red triangles indicate the results for ATHENA release 12.0.6, the black circles the ones for release 14.2.25.

by applying cell weights following the method developed by the H1 experiment [76].
The performance of the jet reconstruction is shown in Figure 6.3. In both ATHENA releases the reconstruction efficiency for jets with $p_{\mathrm{T}} > 20\,\mathrm{GeV}$ is close to one. Due to major changes in the jet reconstruction and calibration packages, slightly more jets are reconstructed at low p_{T} in release 14.2.25 compared to release 12.0.6 resulting in higher efficiency but also higher misidentification rate at low p_{T} (see Figures 6.3(a) and 6.3(b)). The η and ϕ dependence is very similar in both ATHENA releases.

6.2.4 $E_{\mathrm{T}}^{\mathrm{miss}}$ Reconstruction

At hadron colliders the total sum of the transverse energy E_{T} vanishes because of momentum conservation if no particles escape the detector undetected. Therefore a deviation from zero indicates the production of neutrinos or other weakly interacting particles like the lightest SUSY particle. The missing transverse energy $E_{\mathrm{T}}^{\mathrm{miss}} = \sqrt{\left(E_{\mathrm{x}}^{\mathrm{miss}}\right)^2 + \left(E_{\mathrm{y}}^{\mathrm{miss}}\right)^2}$ is calculated according to:

$$E_{\mathrm{x,y}}^{\mathrm{miss}} = -\left(\sum_{\mathrm{Cells}} E_{\mathrm{x,y}} + \sum_{\mathrm{Muons}} E_{\mathrm{x,y}} + E_{\mathrm{x,y}}(\mathrm{dead\ material})\right). \tag{6.2}$$

The muon p_{T} is measured by the stand-alone reconstruction in the muon spectrometer. In this way the energy deposit of the muons in the calorimeter is not double counted. To suppress the contribution from misidentified muons, the stand-alone muons are also required to match with a combined muon track. The third term corrects for energy absorbed in the inactive material, mainly the cryostat walls of the liquid-argon calorimeter. Finally, in the last step the algorithm searches for reconstructed physics objects (e.g. photons, electrons, jets, τ-jets, unused topoclusters and muons) matching the selected calorimeter cells. The energy of matched cells is then refined according to the dedicated energy calibration for the reconstructed particle.
In Figure 6.4 the $E_{\mathrm{T}}^{\mathrm{miss}}$ resolution is shown as a function of the scalar sum $\sum E_{\mathrm{T}}$ of the transverse cell energies in the calorimeter [42]. The resolution deteriorates with the square root of $\sum E_{\mathrm{T}}$ as expected from the energy resolution of the calorimeter which dominates the $E_{\mathrm{T}}^{\mathrm{miss}}$ resolution. For the search for light charged Higgs bosons $t\bar{t}$ events are of largest interest. For these events a $E_{\mathrm{T}}^{\mathrm{miss}}$ resolution of $10\% - 15\%$ is expected from the ATLAS detector simulation.

6.2.5 Reconstruction and Identification of Hadronic τ Lepton Decays

Reconstruction of Hadronic τ Lepton Decays

τ leptons decay into a large variety of final states (listed in Table 4.2) of which hadronic final states are the largest fraction. Because of the boost of the τ leptons in decays of heavy particles like top quarks or Higgs bosons, the hadronic τ final states form jets.
The reconstruction of hadronic τ-jets suffers from the very large gluon and quark jet backgrounds at the LHC. Additional τ-jet identification requirements are needed for the suppression of these backgrounds.
In release 12.0.6 the reconstruction of τ-jet candidates starts with calorimeter clusters reconstructed by the sliding window algorithm fulfilling $E_{\mathrm{T}} > 15\,\mathrm{GeV}$. The cells within $\Delta R < 0.4$

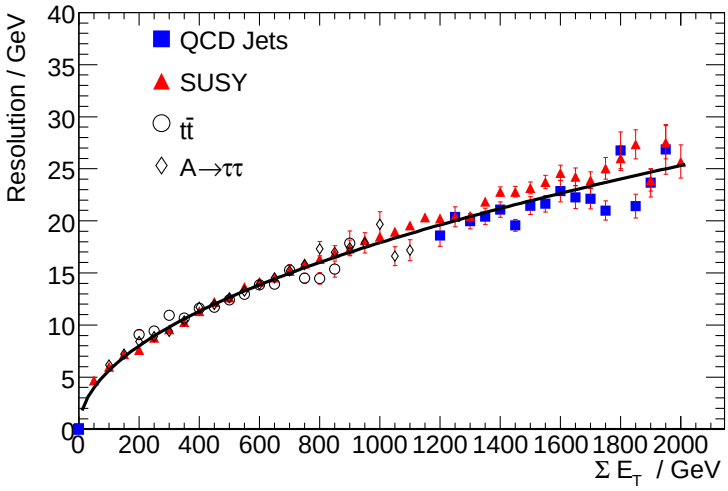

Figure 6.4: Resolution of the $E_{\mathrm{T}}^{\mathrm{miss}}$ as a function of the scalar sum of the transverse cell energies in the calorimeter $\sum E_{\mathrm{T}}$. The curve is a fit of a square root function $a\sqrt{\sum E_{\mathrm{T}}}$ yielding the parameter $a = 0.57$ [57].

around the barycenter are calibrated with dedicated cell weights following the H1 method [77]. The reconstruction of τ-jet candidates in release 14.2.25 is performed by a combination of calorimeter and track based algorithms:

- The calorimeter based algorithm is seeded by reconstructed jets, as described in Section 6.2.3. All jets within the geometrical acceptance of the track reconstruction $|\eta| < 2.5$ and with a transverse energy $E_{\mathrm{T}} > 10\,\mathrm{GeV}$ are referred to as "calorimeter seeds". The jets are re-calibrated with dedicated cell weights following the H1 method. For the subsequent τ-jet identification step tracks are associated to the jet. The tracks are required to fulfill the loose quality criteria in Table 6.1 and are collected in a cone with size $\Delta R = 0.3$ around the E_{T}-weighted barycenter of the cluster. The momentum vector of the τ-jet candidate is determined by the energy of the calibrated cluster and by the direction of the E_{T}-weighted barycenter of its cells.

- The second algorithm starts with a well reconstructed track with $p_{\mathrm{T}} > 6\,\mathrm{GeV}$ and fulfilling the "first track" requirements listed in Table 6.1. Additional tracks reconstructed in a cone of size $\Delta R = 0.2$ around the "track seed" are associated if they pass a relaxed set of cuts. In case only two tracks are found in total, a third track is searched for by dropping the requirements on the χ^2 of the track fit as well as on the ratio $N_{\mathrm{TRT}}^{\mathrm{HT}}/N_{\mathrm{TRT}}^{\mathrm{LT}}$ of hits exceeding high and low TRT thresholds $\left(N_{\mathrm{TRT}}^{\mathrm{HT}}/N_{\mathrm{TRT}}^{\mathrm{LT}}\right)$. For all τ-jet candidates with three tracks a total charge of $|\sum_i Q_i| = 1$ is demanded. Candidates with more than eight tracks are discarded. Using the selected set of tracks the barycenter of the τ-jet candidate is determined and calorimeter cells fulfilling $E_{\mathrm{T}} > 2\sigma_{\mathrm{noise}}$ are associated to it within a cone of radius $\Delta R = 0.4$ around the barycenter. The energy of track seeded τ-jet candidates is calculated using an energy flow algorithm [78]. This method employs the accurate tracking resolution at lower

Table 6.1: Track quality cuts used for τ-jet reconstruction. The cuts for the highest momentum track of track-seeded candidates are given in the first column. A second set of cuts is used to associate additional tracks to the track seed as listed in the second column. The cuts in the third column are imposed for tracks matched to calorimeter seeded τ-jet candidates.

Track Criteria		First Track	Associated Track	Loose Track
p_{T} / GeV	$>$	6	1	1
$\lvert\eta\rvert$	$<$	2.5	2.5	2.5
d_0 / mm	$<$	1	1	1.5
No. Silicon Hits	$\geq$	8	8	6
No. TRT Hits	$\geq$	10	–	–
χ^2 / dof	$<$	1.7	1.7	3.5
No. Pixel Hits	$\geq$	–	1	1
No. B-layer Hits	$\geq$	–	1	–
$N_{\mathrm{TRT}}^{\mathrm{HT}}/N_{\mathrm{TRT}}^{\mathrm{LT}}$	$<$	–	0.2	–

energies where the energy resolution of the calorimeter is limited. Therefore the tracks are associated to calorimeter clusters and the energy measurement for charged particles is taken from the tracking, for neutral particles from the calorimeter. Finally ambiguities are resolved by discarding τ-jet candidates, which have a match with a higher energetic candidate within a cone with the radius $R = 0.1$.

Discriminating Variables for τ-Jet Identification

To reject the large background from parton jets, discriminating variables are constructed which exploit the typical signatures of τ-jets:

- Narrow shower shape in the calorimeter,
- low track multiplicity and
- a displaced secondary vertex.

In the following all discriminating variables used for the different τ-jet identification methods are listed. The association of the variables to the different identification methods is given in Table 6.2.

1. **Electromagnetic Radius R_{em}**

   The electromagnetic radius is the transverse energy weighted average distance between the jet axis of the τ-jet candidate and the associated calorimeter cells:

$$R_{\mathrm{em}} = \frac{\sum_i E_{\mathrm{T},i}^{\mathrm{cell}} \sqrt{(\eta_i - \eta_{\mathrm{cluster}})^2 - (\phi_i - \phi_{\mathrm{cluster}})^2}}{\sum_i E_{\mathrm{T},i}^{\mathrm{cell}}}. \tag{6.3}$$

The average extends over all cells of the pre-sampler and the first and second layer of the electromagnetic calorimeter within a cone of radius $R = 0.4$ around the cluster of the τ-jet candidate. This variable is used to quantify the shower width.

2. **Isolation Fraction $\Delta E_{\mathrm{T}}^{12}$**

   The isolation fraction is the transverse energy in the hollow cone corresponding to distances in the $\eta\phi$-plane of $0.1 < \Delta R < 0.2$ to the τ-jet candidate axis, normalized to the total energy within a cone of radius $R = 0.4$:

$$\Delta E_{\mathrm{T}}^{12} = \frac{\sum\limits_{0.1<\Delta R<0.2} E_{\mathrm{T},\,i}^{\mathrm{cell}}}{\sum\limits_{\Delta R<0.4} E_{\mathrm{T},\,i}^{\mathrm{cell}}}. \tag{6.4}$$

   All layers of the calorimeter are taken into account. This variable exploits the fact that the τ lepton is usually boosted and its decay products appear as a collimated jet without nearby activity in the calorimeter.

3. **Number N_{Tracks} of Associated Tracks**

   Hadronic decays of τ leptons almost always result in one or three charged particles (one- or three-prong τ-jet candidates). A higher number of reconstructed tracks (> 3) can be caused by five prong τ decays, photon conversions, the underlying event or pile-up. On the other hand, for parton jets the number of tracks is correlated with their energy. Therefore, track counting provides high discrimination power, especially at higher p_{T}.
   In release 12.0.6, all tracks within a cone $\Delta R < 0.3$ and with $p_{\mathrm{T}} > 2\,\mathrm{GeV}$ are associated to the τ-jet candidate. A set of track quality cuts is applied as described in [77]. In the case that no associated track is found or the number of tracks is larger than three, the τ-jet candidate is rejected.
   In release 14.2.25 the number N_{Tracks} of associated tracks is counted within in a hollow cone with $0.2 < \Delta R < 0.4$ for track seeded τ-jet candidates. If the τ-jet candidate is seeded only by a calorimeter cluster, this variable is not considered.

4. **Charge of the τ-Jet**

   The charge of the τ-jet candidate is calculated as the sum of the charges of associated tracks. For real τ-jets the absolute value of the total charge is mostly correctly determined to be one while also different values are obtained for jets originating from partons.

5. **Shower Width $\Delta\eta$ in the η-Strip Layer**

   The shape of the τ-jet candidate shower can be estimated already in the first layer of the electromagnetic calorimeter, the η-strip layer. In release 12.0.6 the shower width is defined as the transverse energy weighted root mean square of the η-distances of the cells to the barycenter of the τ-jet candidate cluster:

$$(\Delta\eta)^2 = \frac{\sum_i E_{\mathrm{T},i}^{\mathrm{cell}} \left(\eta_i - \eta_{\mathrm{cluster}}\right)^2}{\sum_i E_{\mathrm{T},i}^{\mathrm{cell}}}. \tag{6.5}$$

This value is normalized by the total energy within a cone $\Delta R < 0.4$.
In release 14.2.25 the definition of the $\Delta\eta$ variable is changed:

$$(\Delta\eta)^2 = \frac{\sum_i E_{\mathrm{T},i}^{\mathrm{cell}} \, (\eta_i - \eta_{\mathrm{cluster}})^2}{\sum_i E_{\mathrm{T},i}^{\mathrm{cell}}} - \left[\frac{\sum_i E_{\mathrm{T},i}^{\mathrm{cell}} \, (\eta_i - \eta_{\mathrm{cluster}})}{\sum_i E_{\mathrm{T},i}^{\mathrm{cell}}} \right]^2 \tag{6.6}$$

The variable $\Delta\eta$ exploits the lower number of π^0 mesons in hadronic τ decays and their subsequent higher boosts compared to parton jets of the same energy.

6. **Number N_{Strip} of Hits in the η Strip Layer**

   The number N_{Strip} of hits in the first layer of the electromagnetic barrel calorimeter can also be used as a discriminating variable. Energy depositions in cells of the η-strip layer within $\Delta R = 0.4$ around the cluster axis are counted if the deposited energy exceeds 200 MeV. The variable N_{Strip} provides particular discrimination for the decay channel $\tau \to \pi\nu$ where it is considerably smaller for τ-jets than for parton jets. In particular at high p_{T}, the parton jets tend to deposit more energy in the η-strip layer than the τ-jets.

7. **Ratio $E_{\mathrm{T}}/p_{\mathrm{T1}}$ of Total Transverse Energy and p_{T} of the Leading Track**

   For hadronic τ decays a large fraction of the τ-jet energy is expected to be carried by the leading track whereas the energy is more uniformly distributed for parton jets.

8. **Signed Transverse Flight Path Significance $\sigma^{\mathrm{tr}}_{\mathrm{Flight\ Path}}$**

   For multi-prong track-seeded τ-jet candidates the decay vertex can be reconstructed. Despite the relatively short life time of the τ lepton, $c\tau = 87\,\mu$m, the mean flight path length $\langle l \rangle = \beta\gamma c\tau$ is increased to several mm by the boost of the τ lepton. However, since the opening angle of the decay products scales with $1/\gamma$, the resolution of the flight path length measurement decreases with increasing boost. The significance of the transverse flight path is defined as

$$\sigma^{\mathrm{tr}}_{\mathrm{Flight\ Path}} = \mathrm{sign}\left([\boldsymbol{r}_{\mathrm{SV}} - \boldsymbol{r}_{\mathrm{PV}}]_{\mathrm{T}} \cdot \boldsymbol{r}_{\mathrm{T}}^{\tau} \right) \frac{|\boldsymbol{r}_{\mathrm{SV}} - \boldsymbol{r}_{\mathrm{PV}}|_{\mathrm{T}}}{\sigma\left(\boldsymbol{r}_{\mathrm{SV}} - \boldsymbol{r}_{\mathrm{PV}}\right)}, \tag{6.7}$$

   where $\boldsymbol{r}_{\mathrm{PV}}$ and $\boldsymbol{r}_{\mathrm{SV}}$ are the vectors of the primary and the secondary vertex, respectively, and σ is the uncertainty of the vertex fit. The sign is positive if the distance vector between primary and secondary vertex and the direction $\boldsymbol{r}_{\mathrm{T}}^{\tau}$ of the τ-jet axis in the transverse plane enclose an angle of less than 90°, i.e. the decay happens in flight direction (see Figure 6.5). For τ-jets this variable has a tail towards positive values while it is symmetrically distributed around zero for the parton jets.

9. **Transverse Impact Parameter Significance $\sigma^{\mathrm{tr}}_{\mathrm{IP}}$**

   The transverse impact parameter d_0 is the distance of closest approach of a track to the primary vertex in the transverse plane (see Figure 6.5). Since τ leptons have finite life time, a non-zero impact parameter provides discrimination power against the light parton (u, d, s quark and gluon) jets. In release 12.0.6 a two dimensional *signed* transverse impact

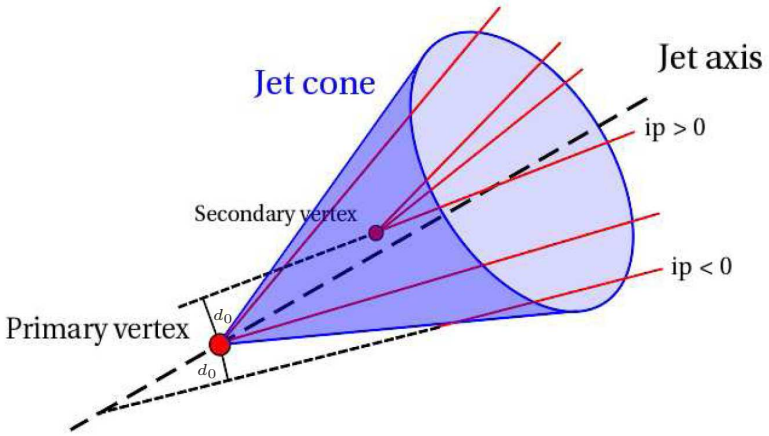

Figure 6.5: Sketch of the hadronic decay of a particle with finite life time.

parameter is calculated for the leading track using the jet axis defined by the calorimeter cluster. The sign is defined to be positive for tracks crossing the jet axis in τ-jet direction and negative otherwise. This variable tends to be larger for τ-jets compared to the background. In release 14.2.25 no sign is used since the jet axis is obtained from the tracks themselves for track seeded τ-jet candidates.
To evaluate the impact parameter for a given track, the primary vertex is re-fitted excluding this track. Finally the impact parameter d_0 is divided by the uncertainty $\sigma(d_0)$ to account for the uncertainty of the vertex fits. The transverse impact parameter significance is given by

$$\begin{aligned} \sigma_{\mathrm{IP}}^{\mathrm{tr}} &= \frac{d_0}{\sigma\left(d_0\right)} \cdot \operatorname{sign}\left(\sin\left(\phi_{\mathrm{jet}} - \phi_{\mathrm{track}}\right)\right) && \text{release 12.0.6,} \\ \sigma_{\mathrm{IP}}^{\mathrm{tr}} &= \frac{d_0}{\sigma(d_0)} && \text{release 14.2.25.} \end{aligned} \tag{6.8}$$

10. **Longitudinal Impact Parameter Significance $\sigma_{\mathrm{IP}}^{\mathrm{z}}$**

    The impact parameter significance in z direction $\sigma_{\mathrm{IP}}^{\mathrm{z}}$ is used only for the identification of single-prong track seeded τ-jet candidates:

$$\sigma_{\mathrm{IP}}^{\mathrm{z_0}} = \frac{z_0 \sin\left(\theta_{\mathrm{track}}\right)}{\sigma\left(z_0 \sin\left(\theta_{\mathrm{track}}\right)\right)}. \tag{6.9}$$

11. **Ratio $E_{\mathrm{T}}^{\mathrm{EM}}/p_{\mathrm{T}}^{\mathrm{Tracks}}$ of Electromagnetic Energy and Transverse Momenta of Leading Tracks**

    Due to the low track multiplicity of τ-jets, the ratio of the transverse energy deposited in the electromagnetic calorimeter and the scalar sum of the transverse momenta of up to three

leading tracks,

$$E_{\mathrm{T}}^{\mathrm{EM}}/p_{\mathrm{T}}^{\mathrm{Tracks}} = E_{\mathrm{T}}^{\mathrm{EM}}/\sum_{i=1}^{3} p_{\mathrm{T}}^{\mathrm{track}(i)}, \tag{6.10}$$

is expected to be smaller for τ-jets than for other jets of the same energy.

12. **Ratio $E_{\mathrm{T}}^{\mathrm{HAD}}/p_{\mathrm{T}}^{\mathrm{Tracks}}$ of Hadronic Energy and Transverse Momenta of Leading Tracks**

Similarly as the previous variable, this ratio is calculated using the energy deposited in the hadronic calorimeter:

$$E_{\mathrm{T}}^{\mathrm{HAD}}/p_{\mathrm{T}}^{\mathrm{Tracks}} = E_{\mathrm{T}}^{\mathrm{HAD}}/\sum_{i=1}^{3} p_{\mathrm{T}}^{\mathrm{track}(i)}. \tag{6.11}$$

13. **Ratio $p_{\mathrm{T}}^{\mathrm{Tracks}}/E_{\mathrm{T}}$ of Leading Track Momenta and the Total Energy**

Also the inverse ratio of the total transverse energy and the scalar sum of the three leading tracks is used:

$$p_{\mathrm{T}}^{\mathrm{Tracks}}/E_{\mathrm{T}} = \sum_{i=1}^{3} p_{\mathrm{T}}^{\mathrm{track}(i)}/E_{\mathrm{T}}. \tag{6.12}$$

14. **Fraction $E_{\mathrm{T}}^{\mathrm{EM}}/E_{\mathrm{T}}$ of Electromagnetic Energy**

About two thirds of all τ-jets are accompanied by photons (see Table 4.2). Hence they are expected to deposit a large fraction of their energy in the electromagnetic calorimeter. This is exploited by the ratio:

$$E_{\mathrm{T}}^{\mathrm{EM}}/E_{\mathrm{T}} = \frac{E_{\mathrm{T}}^{\mathrm{EM}}}{E_{\mathrm{T}}^{\mathrm{EM}} + E_{\mathrm{T}}^{\mathrm{HAD}}}, \tag{6.13}$$

where $E_{\mathrm{T}}^{\mathrm{EM}}$ and $E_{\mathrm{T}}^{\mathrm{HAD}}$ are the cluster energies of the τ-jet candidate in the electromagnetic and the hadronic calorimeter, respectively.

15. **Visible Invariant Mass $m_{\mathrm{Vis}}^{\mathrm{Tracks}}$**

The visible invariant mass $m_{\mathrm{Vis}}^{\mathrm{Tracks}}$ of track seeded multi-prong τ-jet candidates is calculated from the track four-momenta. In hadronic τ decays this variable has an upper limit defined by the τ mass $m_\tau = 1.777\,\mathrm{GeV}$, while it can be higher correlated with the transverse momentum for parton jets. Therefore increasing discrimination power is expected against parton jets at higher momenta.

16. **Visible Energy Flow Invariant Mass $m_{\mathrm{Vis}}^{\mathrm{Eflow}}$**

For track seeded τ-jet candidates, the invariant mass is calculated combining track and calorimeter (energy flow) information. The four-momenta of calorimeter cells in the first two layers of the electromagnetic calorimeter associated to the τ-jet shower but not to tracks are used.

This variable is strongly correlated to the previous one. However, it allows for calculating the visible mass also for single-prong τ-jet candidates.

17. **Minimal Distance ΔR_{min}**

    For multi-prong τ-jet candidates this variable is defined as the minimal separation between the seed position and the associated tracks within a cone of radius $R = 0.2$. For τ-jets this distance is expected to be smaller than for parton jets. No quality requirements are used for the selection of the tracks.

18. **Maximal Distance ΔR_{max}**

    Similar as ΔR_{min} also the maximal separation between the seed position and the associated tracks provides discrimination against parton jets. Especially at higher transverse momentum this variable exploits the strong collimation of the tracks in τ-jets. Again it is only considered for multi-prong τ-jet candidates.

19. **Shower Width $\Delta\eta_{\text{Tracks}}$ from Tracks**

    Similarly as in Equation 6.6, the track transverse momentum weighted jet width $\Delta\eta_{\text{Tracks}}$ is determined for track seeded multi-prong τ-jet candidates:

$$\Delta\eta^2_{\text{Tracks}} = \frac{\sum_i p_{\text{T},i}\,(\Delta\eta_i)^2}{\sum_i p_{\text{T},i}} - \left[\frac{\sum_i p_{\text{T},i}\,\Delta\eta_i}{\sum_i p_{\text{T},i}}\right]^2, \tag{6.14}$$

    where $\Delta\eta_i = \eta_i^{\text{track}} - \eta_{\text{jet axis}}^{\text{track}}$ is calculated with respect to the track jet axis.

τ-Jet Identification

In the following two τ-jet identification methods are described. One is based on cuts applied on the discriminating variables while the other uses a likelihood-based combination of the discriminating variables to identify the τ-jet. Since the discriminating variables depend on the jet kinematics, p_{T}-dependent identification criteria are used in both ATHENA releases. The p_{T} bins chosen are summarized in Table 6.3. In release 14.2.25 the τ-jet candidates are further classified as single-prong and multi-prong decays. In addition, the likelihood-based identification method distinguishes between the single-prong track seeded τ-jet candidates with and without neutral pions. The single-prong calorimeter seeded τ-jet candidates are always considered to contain no neutral pions.
The choice of track seeded or calorimeter seeded τ-jet reconstruction algorithm has a large impact on the τ-jet identification. For all track seeded candidates the τ-jet axis is calculated as the direction from the primary vertex to the p_{T}-weighted barycenter of the tracks. If there is no track seed available, the barycenter of the calorimeter cluster is used. As described in the Section 6.2.5, certain discriminating variables are only defined for track seeded τ-jet candidates.
In the following the two τ-jet identification methods are explained in more detail.

Likelihood-Based τ-Jet Identification This method uses probability density functions given by the distributions of the discriminating variables for τ-jets and parton jets [77, 79]. The τ-jet distributions are obtained from $Z \to \tau\tau$ and $A \to \tau\tau$ events while parton jets are taken from QCD dijet events. At the LHC, QCD dijet events are produced at very high rates allowing for an early

Table 6.2: Variables used for the identification of τ-jets in releases 12.0.6 and 14.2.25. Filled circles indicate the variables used by the different algorithms. The numbering of the variables corresponds to the one in the text.

Variable	Rel. 12.0.6	Rel. 14.2.25	
	Likelihood	Likelihood	Cut-based
1	●	●	●
2	●	●	●
3	●	●	○
4	●	○	○
5	●	●	●
6	●	●	○
7	●	○	●
8	○	●	○
9	●	●	○
10	○	●	○
11	○	●	●
12	○	●	●
13	○	●	●
14	○	○	●
15	○	●	○
16	○	●	○
17	○	●	○
18	○	●	○
19	○	●	●

Table 6.3: p_{T} intervals (in GeV) used for the τ-jet identification methods. In the first row the intervals for release 12.0.6, in the second and third row the ones for release 14.2.25 are given. "LLH" denotes the likelihood-based and "Cuts" the cut-based identification algorithms.

LLH (12)	15-28	28-44	44-62	62-88	88-134	134-218	218-334	434-600	$>$600
LLH (14)	10-20	20-30	45-70	70-100	100-150	150-220	220-500	$>$500	
Cuts (14)	10-25	25-45	45-70	70-100	$>$100				

measurement of their probability density functions rather than relying on Monte Carlo predictions. The likelihoods P_S and P_B for the τ-jet and the QCD jet hypotheses are calculated for each τ-jet candidate, as

$$P_{S(B)}(\boldsymbol{x} = x_1, \ldots, x_n) = \prod_{k=1}^{n} p^k_{S(B)}(x_k) \tag{6.15}$$

neglecting correlations between the variables. $p^k(x)$ denotes the value of the probability density function k of the variable x_k. Correlations between the discriminating variables can only be taken into account using multi-dimensional probability density functions. However, due to the limited statistics of the Monte Carlo samples multi-dimensional probability density functions have not been used.

The likelihood discriminant $P(\boldsymbol{x})$ is defined by the expression:

$$P(\boldsymbol{x}) \equiv \frac{P_S(\boldsymbol{x})}{P_B(\boldsymbol{x}) + P_S(\boldsymbol{x})}. \tag{6.16}$$

For an easier numerical treatment the equivalent logarithmic likelihood discriminant

$$P'(\boldsymbol{x}) \equiv -\ln(1/P(\boldsymbol{x}) - 1) = \sum_k \ln \frac{p^k_S(x_k)}{p^k_B(x_k)} \tag{6.17}$$

is used. In release 14.2.25 the likelihood-based method provides quality flags of the τ-jet candidates (loose, medium and tight) which correspond to fixed cut values on the discriminant P' chosen such that 70%, 50% and 30% of the τ-jets in $Z \rightarrow \tau\tau$ events are accepted for the loose, medium and tight selections, respectively.

In Figure 6.6 the performance of likelihood-based τ-jet reconstruction and identification is shown depending on p_{T}. The η and ϕ dependences can be found in the Appendix B. All τ-jet candidates overlapping with identified muons and electrons are removed. In release 12.0.6, first electrons are rejected by the requirement $E_{\mathrm{T}}^{\mathrm{HAD}}/p_{\mathrm{T}}^{\text{lead. track}} > 0.1$ before the τ-jet candidates are further identified by requiring the logarithmic likelihood discriminant to be greater than six. In release 14.2.25, after the rejection of electrons [80], the τ-jet identification is performed using the medium quality cut of the likelihood-based method.

Comparing the likelihood based identification methods in release 12.0.6 and 14.2.25, better performance is achieved in the newer release. The topological clustering allows for a lower p_{T} threshold as can be seen in Figure 6.6(a) and Figure 6.6(b). Higher efficiency and lower misidentification rate are achieved for all p_{T}. Comparing the τ-jet efficiency with the rejection of the dominant background of light parton jets (see Figure 6.6(c)), reveals the improved performance of the new identification especially in the range $20 < p_{\mathrm{T}} < 50\,\mathrm{GeV}$. At higher p_{T} the old identification rejects more jets, but at the expense of lower efficiency. In Figure 6.7 the overall efficiency is plotted against the rejection of light parton jets. The working points of the two corresponding ATHENA releases are indicated. As can be seen a better performance is achieved in release 14.2.25 compared the release 12.0.6 for efficiencies $> 30\%$. The reduction of the misidentification rate in release 14.2.25 also stems from the new electron veto (see Figure 6.6(d)).

The rejections of c- and b-jets (Figure 6.6(e) and 6.6(f)) are comparable in both releases. Especially for b-jets, because of the high track multiplicity and broad shower shape, a high and constant rejection of about 1000 is achieved.

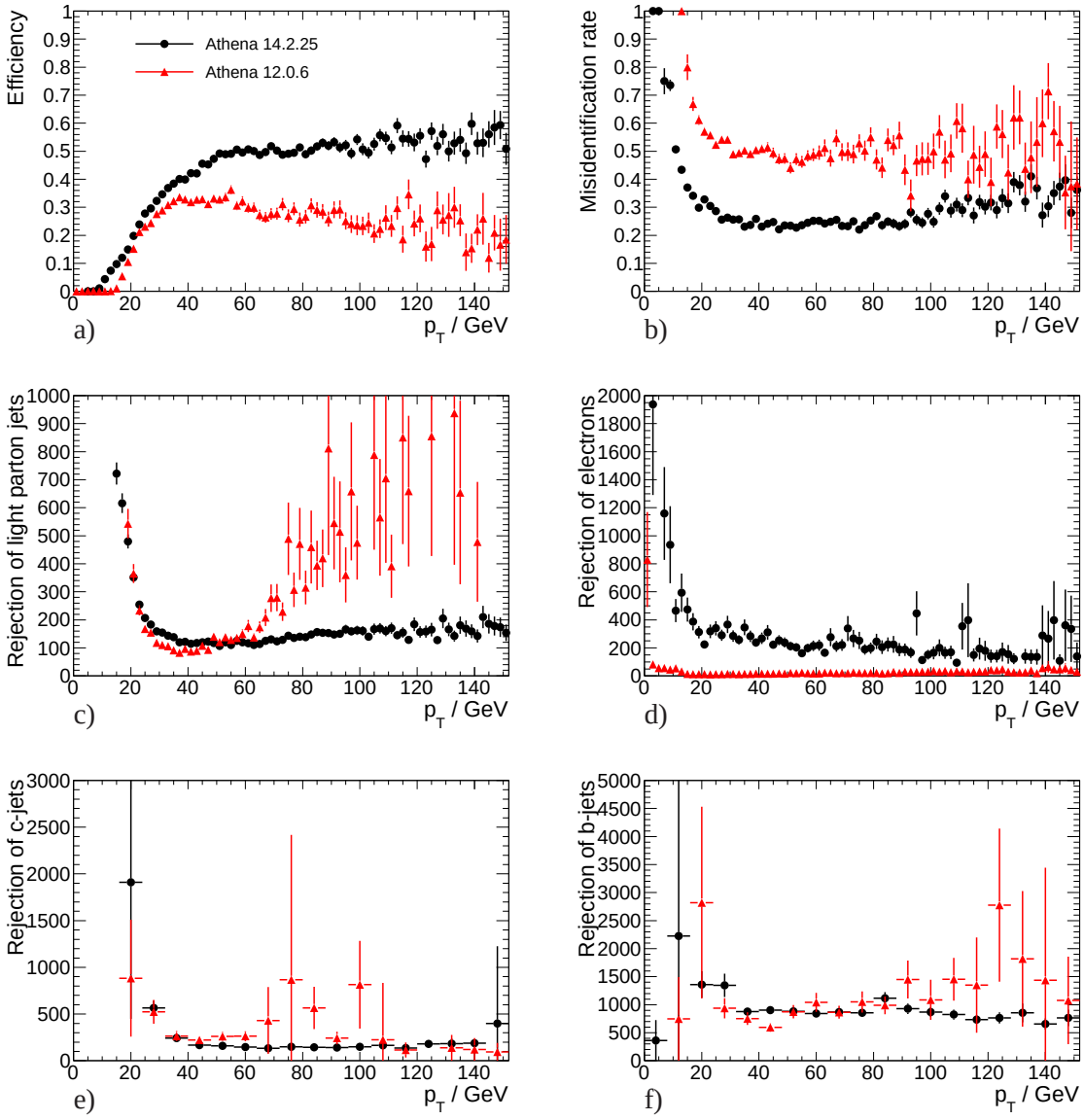

Figure 6.6: Performance of the likelihood-based τ-jet identification methods in releases 12.0.6 and 14.2.25. The p_{T} dependence of (a) efficiency and (b) misidentification rate is shown for $|\eta| < 2.5$, (c), (d), (e) and (f) show the rejections of the τ-jet identification of light parton (u, d, s quark and gluon) jets, electrons, c-jets and b-jets as a function of p_{T}. The red triangles indicate the results for the release 12.0.6, the black circles the ones for release 14.2.25.

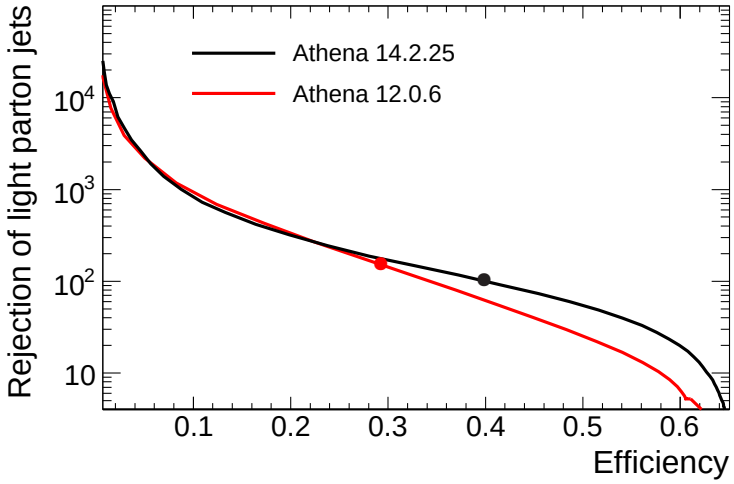

Figure 6.7: Rejection versus τ-jet identification efficiency for the likelihood-based methods in releases 12.0.6 and 14.2.25 for all τ-jets with $p_{\mathrm{T}} > 20\,\mathrm{GeV}$ and $|\eta| < 2.5$. In both cases the corresponding working points are indicated.

Cut-Based τ-Jet Identification For the early data taking of ATLAS an alternative τ-jet identification method has been implemented in release 14.5.1 which considers only variables that are supposed to be well under control at an early stage of detector calibration. The cut-based identification is performed using a selection of the discriminating variables ("safe cuts") from Table 6.2 [81]. As for the likelihood-based identification method three τ quality flags are defined corresponding to different sets of cuts. These cuts have been optimized to obtain the highest possible rejection at fixed τ-jet identification efficiencies of 70%, 50% and 30%. Again $Z \rightarrow \tau\tau$ and $A \rightarrow \tau\tau$ events as well as QCD dijet events were used for the cut optimization procedure. The cut values [81] are defined in five p_{T} bins summarized in Table 6.3 separately for single- and multi-prong τ lepton decays.

The performance of the cut-based identification method is intrinsically inferior to the likelihood discriminant. In addition, the cut-based method uses a smaller number of discriminating variables in larger p_{T} bins which also decreases the discrimination power. The performance degradation can be seen in Figure 6.8 where the two identification methods are compared. The steps in the p_{T} dependence of the efficiency and misidentification rate of the cut-based method in Figure 6.8(a) and 6.8(b) are due to the separate cut optimization in the p_{T} bins of Table 6.3. The striking improvement of the efficiency at low p_{T} is compensated by high misidentification rate and very low rejection against light, b- and c-jets, shown in Figure 6.8(b), 6.8(c), 6.8(e) and 6.8(f). At higher p_{T}, the performance of the cut-based method improves, but does not reach the performance of the likelihood-based method. The rejection against electrons in Figure 6.8(d) is comparable for the two methods because the same electron veto is used.

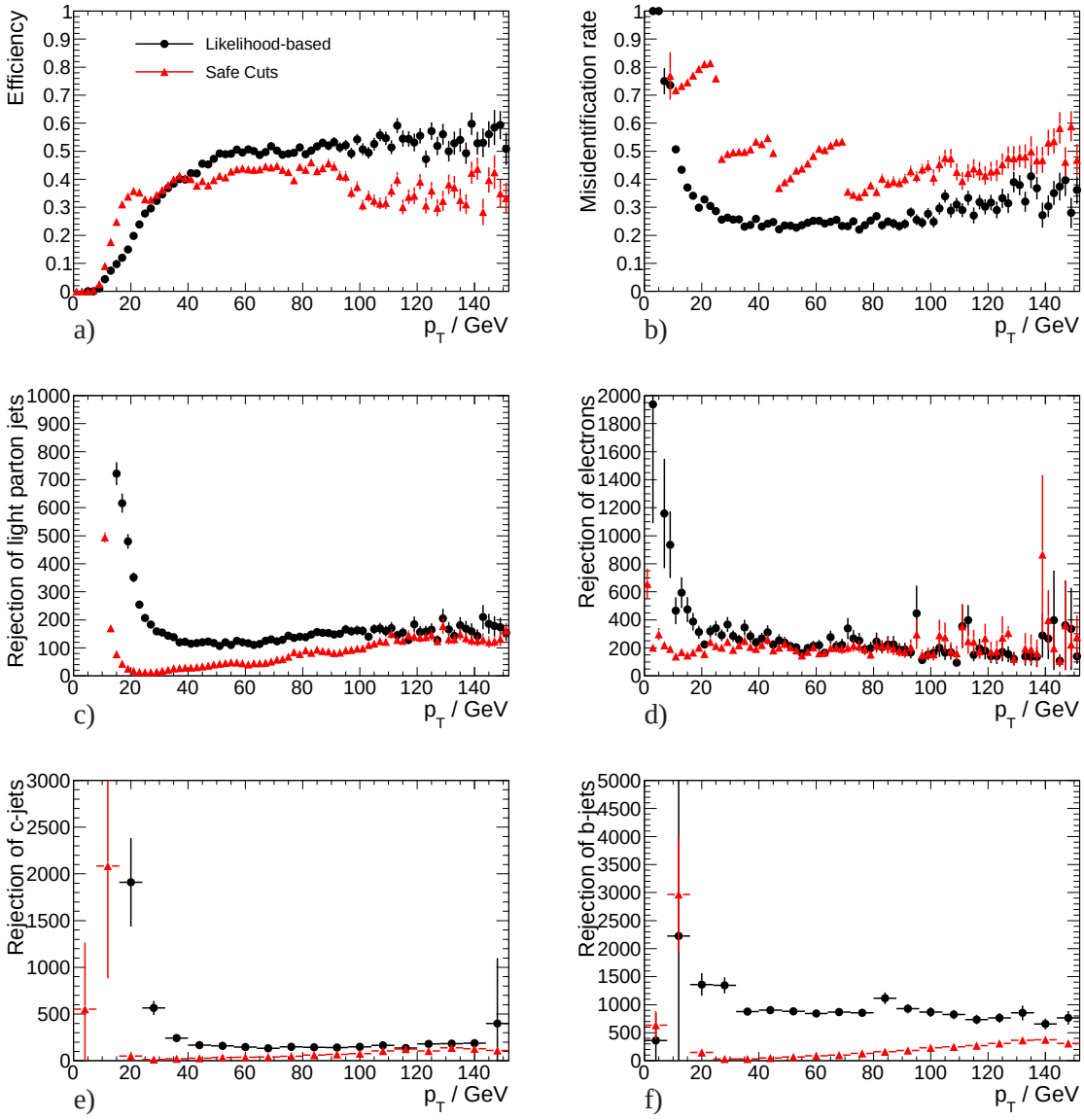

Figure 6.8: Performance of the cut-based and the likelihood-based τ-jet identification methods in release 14.2.25. The p_{T} dependence of (a) efficiency and (b) misidentification rate is shown for $|\eta| < 2.5$, (c), (d), (e) and (f) show the rejections of the τ-jet identification of light parton (u, d, s quark and gluon) jets, electrons, c-jets and b-jets as a function of p_{T}. The red triangles indicate the results for the cut-based, the black circles the ones for the likelihood-based identification method.

6.2.6 *b*-Jet Identification

The signature of jets originating from b quarks differs from the signature of jets stemming from lighter quarks and gluons due to the production and decay properties of heavy b hadrons. These differences are exploited to discriminate b-jets from other jets. The average life time of weakly decaying b hadrons is 1.5 ps. For a b-jet with transverse momentum of 50 GeV the mean flight path length is $\langle \ell \rangle = \beta\gamma c\tau \approx 3\,\text{mm}$. In addition, due to the hard fragmentation function of b quarks, b hadrons carry a large fraction of the b quark energy leading to high transverse momentum and a relatively large opening angle of the fragmentation hadrons and their decay products with respect to the b-jet axis.
Three methods can be used to identify b-jets (b-tagging):

- The tracks from a decayed b hadron are incompatible with originating from the primary vertex. As for τ-jet identification a signed impact parameter is used for b-jet identification.
- Algorithms for the reconstruction of secondary vertices are used to determine the weak decay vertex of the b hadron in the b-jet. Track pairs compatible with photon conversions or K_s^0 decays are removed for this purpose. Three vertex properties are used for the b-tagging:
  - The invariant mass of all tracks associated to the secondary vertex,
  - the ratio of the sum of the track transverse momenta associated to the vertex and the sum of transverse momenta of all tracks in the jet and
  - the number of two-track vertices inside the jet.
- Additional soft lepton b-tagging algorithms make use of the leptons originating from semi-leptonic decays of b hadrons. Due to the relatively small semi-leptonic branching ratio of 20% for b-decays into electrons and muons the efficiency of this method is limited and will not be used in this analysis.

Using the probability density functions of the impact parameter and the secondary vertex displacement a likelihood-based discriminant is used to separate b-jets from other jets.
In Figure 6.9 the b-tagging performance is shown as a function of p_{T}. The η and ϕ dependence can be found in Appendix B. After removing muons, electrons and τ-jets overlapping with the b-jet candidate, the b-jet candidates are identified by requiring the b-tagging discriminant to be larger than three. It can be seen that the efficiency is generally higher in release 14.2.25 compared to release 12.0.6. However, also the misidentification rate is higher and the rejection of light parton jets and c-jets lower.

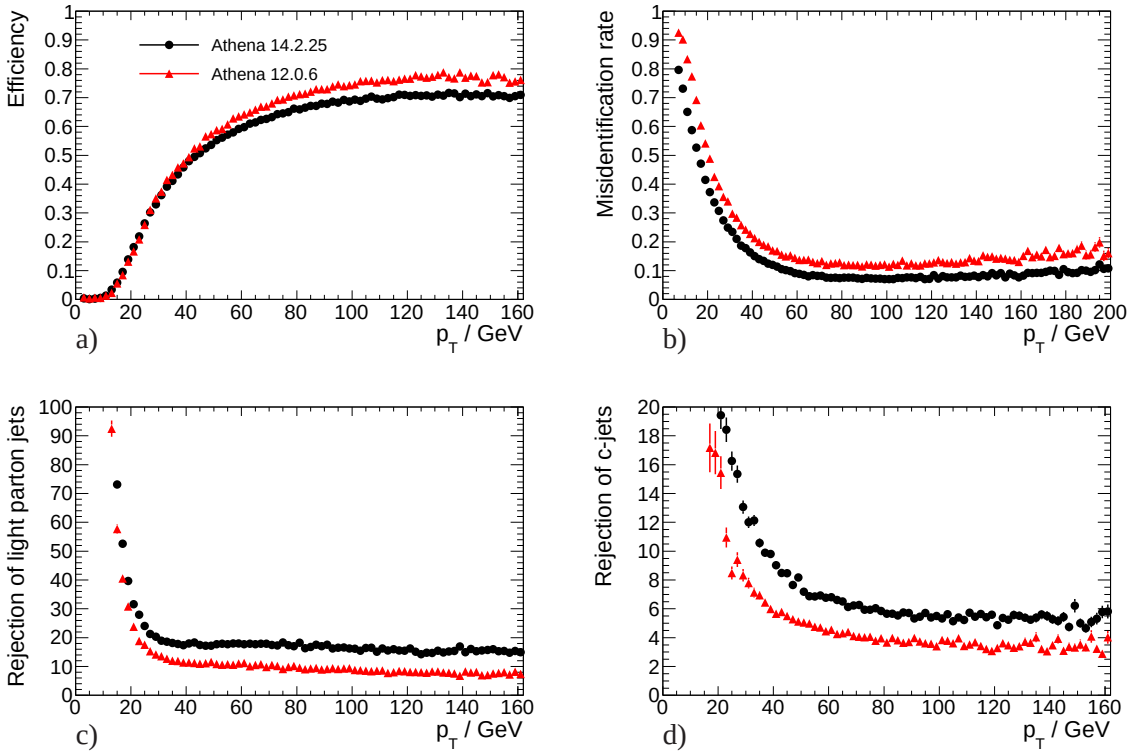

Figure 6.9: Performance of the b-jet identification algorithm in releases 12.0.6 and 14.2.25. The p_{T} dependence of (a) efficiency and (b) misidentification rate is shown for $|\eta| < 2.5$, (c) and (d) show the rejections of light parton (u, d, s quark and gluon) jets and c-jets as a function of p_{T}. The red triangles indicate the results for the release 12.0.6, the black circles the ones for release 14.2.25.

Chapter 7

The Search for Light Charged Higgs Bosons

As described in Section 4.2, two Higgs doublets are needed in the MSSM to give masses to up- and down-type quarks and leptons. They result in five physical states, the neutral Higgs bosons h, H, A and the charged Higgs bosons $H^{\pm}$. At the LHC, charged Higgs bosons can be copiously produced in on-shell top quark decays $t \to bH^+$, if their mass $m_{H^{\pm}}$ is smaller than $m_t - m_b$. In the 2HDM(II) the subsequent decay $H^+ \to \tau\nu$ is favored and proceeds even exclusively in the MSSM m_h-max scenario, given that $\tan\beta > 3$. In this chapter, the strategy for the search for light charged Higgs bosons in $t\bar{t}$ events with one semi-leptonic top decay and hadronic τ lepton decays is discussed.
The signal and background processes, introduced in Section 7.1, have been simulated for a center of mass energy of 14 TeV using the ATHENA release 12. Section 7.2 covers the event selection and cut optimization. Finally, in Section 7.3 the systematic uncertainties are discussed.

7.1 Signal and Background Simulation

The signal and background Monte Carlo samples considered are listed in Table 7.1. The cross sections were calculated at next-to-leading order in perturbation theory and have been validated by the ATLAS collaboration [42]. The integrated luminosities to which the Monte Carlo samples correspond vary between $100\,\text{pb}^{-1}$ and $10\,\text{fb}^{-1}$. For the most important background of $t\bar{t}$ events about $1\,\text{fb}^{-1}$ was available.

- **Signal Production**
  For the generation of the signal events the generator PYTHIA has been used. They are inclusive $t\bar{t}$ events where one top quark decays into a charged Higgs boson and an accompanying b quark while the other top quark decays into a W boson and a b quark. The W boson is required to decay leptonically, $W \to e\nu, \mu\nu$, to provide a clean trigger signal. Since this analysis concentrates on the MSSM, the charged Higgs boson is forced to decay into a τ lepton and its neutrino. The leading order Feynman graph of this process is depicted

Table 7.1: Datasets used for the charged Higgs analysis. Only the generator for the hard process is shown. Other subsequently used QCD generators are discussed in Section 6.1. The cross sections are all calculated at next-to-leading order perturbation theory and are multiplied by the branching ratios of the top quarks to the final states indicated taken from [16] and, if applicable, by the pre-selection filter efficiency. The cross sections of the signal events are given for the MSSM m_h-max scenario with $\tan\beta = 20$.

Dataset Id	Generator	Channel	N_{Events}	$\sigma \times \mathcal{B}$/pb
6399 (90 GeV)	PYTHIA	$t\bar{t} \to (H^+b)\left(W\bar{b}\right) \to (\tau_{\text{had}}\nu b)\left(\ell\bar{\nu}\bar{b}\right)$	9950	12.1
6800 (110 GeV)	PYTHIA	$t\bar{t} \to (H^+b)\left(W\bar{b}\right) \to (\tau_{\text{had}}\nu b)\left(\ell\bar{\nu}\bar{b}\right)$	7500	8.6
6562 (120 GeV)	PYTHIA	$t\bar{t} \to (H^+b)\left(W\bar{b}\right) \to (\tau_{\text{had}}\nu b)\left(\ell\bar{\nu}\bar{b}\right)$	9500	6.7
6398 (130 GeV)	PYTHIA	$t\bar{t} \to (H^+b)\left(W\bar{b}\right) \to (\tau_{\text{had}}\nu b)\left(\ell\bar{\nu}\bar{b}\right)$	9500	5.0
6566 (150 GeV)	PYTHIA	$t\bar{t} \to (H^+b)\left(W\bar{b}\right) \to (\tau_{\text{had}}\nu b)\left(\ell\bar{\nu}\bar{b}\right)$	8000	1.9
5200	MC@NLO	$t\bar{t} \to (Wb)\left(W\bar{b}\right) \to (Xb)\left(\ell\bar{\nu}\bar{b}\right)$	436k	452
5500	ACERMC	Single Top (Wt channel, $W_1 \to (e,\mu,\tau)\,\nu, W_2 \to q\bar{q}'$)	15200	29
5501	ACERMC	Single Top (s channel, $W \to (e,\mu,\tau)\,\nu$)	9750	3.5
5502	ACERMC	Single Top (t channel, $W \to (e,\mu,\tau)\,\nu$)	18500	80
8240	ALPGEN	$W \to e\nu$+2p, $\text{N}_{\text{Jets}} \geq 3$	130661	246.1
8241	ALPGEN	$W \to e\nu$+3p, $\text{N}_{\text{Jets}} \geq 3$	69006	142.5
8242	ALPGEN	$W \to e\nu$+4p, $\text{N}_{\text{Jets}} \geq 3$	28633	61.7
8243	ALPGEN	$W \to e\nu$+5p, $\text{N}_{\text{Jets}} \geq 3$	3700	25.7
8244	ALPGEN	$W \to \mu\nu$+2p, $\text{N}_{\text{Jets}} \geq 3$	4750	18.8
8245	ALPGEN	$W \to \mu\nu$+3p, $\text{N}_{\text{Jets}} \geq 3$	12500	74.4
8246	ALPGEN	$W \to \mu\nu$+4p, $\text{N}_{\text{Jets}} \geq 3$	19323	41.4
8247	ALPGEN	$W \to \mu\nu$+5p, $\text{N}_{\text{Jets}} \geq 3$	3500	23.2
8248	ALPGEN	$W \to \tau\nu$+2p, $\text{N}_{\text{Jets}} \geq 3$	19950	100.9
8249	ALPGEN	$W \to \tau\nu$+3p, $\text{N}_{\text{Jets}} \geq 3$	13000	100.2
8250	ALPGEN	$W \to \tau\nu$+4p, $\text{N}_{\text{Jets}} \geq 3$	5750	52.8
8251	ALPGEN	$W \to \tau\nu$+5p, $\text{N}_{\text{Jets}} \geq 3$	9000	23.9

Table 7.2: Standard Model parameters used in the charged Higgs search. The branching ratios are taken from [16].

Parameter	Value
top quark mass	175 GeV
W boson mass	80.42 GeV
$\mathcal{B}(t \to bW)$ (SM)	1
$\mathcal{B}(W \to qq)$	0.6760
$\mathcal{B}(W \to e\nu)$	0.1075
$\mathcal{B}(W \to \mu\nu)$	0.1057
$\mathcal{B}(W \to \tau\nu)$	0.1125
$\mathcal{B}(\tau \to \text{hadrons}\,\nu)$	0.6480
$\mathcal{B}(\tau \to e\nu)$	0.1784
$\mathcal{B}(\tau \to \mu\nu)$	0.1736

in Figure 4.4(a). Subsequently, inclusive hadronic τ decays formig τ-jets are considered because they have a high branching ratio of 64.8% (see Table 4.2). τ-jets can be identified by the ATLAS detector (see previous chapter). In addition, as pointed out in [82], angular momentum conservation leads to significant energy enhancement of τ-jets in $H^+ \to \tau\nu$ with respect to $W \to \tau\nu$ decays which is implemented in the TAUOLA generator used for the generation of the hadronic τ decays.
The kinematic properties of τ-jets also depend on the mass of the charged Higgs boson. Higher masses lead to stronger boosts which affect the shower shape and energy. Therefore five datasets with $H^\pm$ masses of 90, 110, 120, 130 and 150 GeV are investigated covering the mass range between the LEP limit and the threshold for $H^\pm$ production in top decays. At and above the threshold mass $m_{H^\pm} \approx m_t - m_b$ other charged Higgs production processes, $gg \to \bar{t}bH^+$, $g\bar{b} \to \bar{t}H^+$, have to be considered which are not included in this study.

- **Standard Model $t\bar{t}$ Background**
  The most important background for light charged Higgs boson searches, namely $t\bar{t}$ events with two Standard Model decays to Wb bosons is generated with MC@NLO (see Table 7.1). Since these events contain only Standard Model particles it is referred to as Standard Model $t\bar{t}$ background. Only events with at least one leptonical decaying W boson are considered (see Figure 4.4(b)). The events with an additional τ-jet originating from the second W boson decay are referred to as the irreducible $t\bar{t}$ background because the final state is the same as for the signal. In addition, because neutrinos appear in both top quark decay chains, it is impossible to reconstruct a top quark or a W boson. An enrichment of signal events is only possible by exploiting the fact that $m_W < m_{H^\pm}$ and the spin correlation effects mentioned above. No signal peak can be observed over the background. Therefore a signal is only observed as an excess of τ-jet events over the Standard Model expectation.
  Another important, but reducible background is the Standard Model $t\bar{t}$ production with the

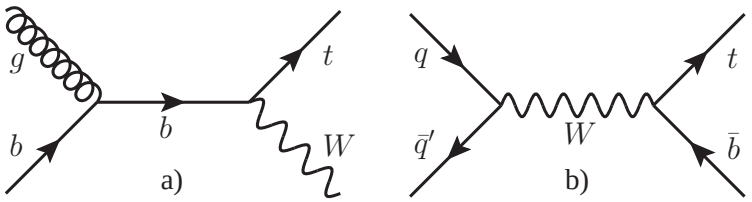

Figure 7.1: Main single top backgrounds: (a) Wt-channel, (b) s-channel.

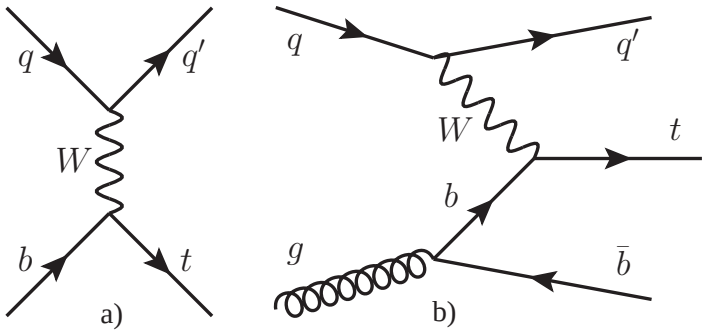

Figure 7.2: Main single top backgrounds: t-channel (a) $2 \to 2$, (b) $2 \to 3$ process.

first W boson decaying into a lepton and the second one into quarks. Using the τ-jet identification, these events are significantly suppressed. However, due to the high branching ratio $\mathcal{B}$ ($t\bar{t}$ events with $W \to q\bar{q}'$) this mode has to be taken into account. Similarly, also $t\bar{t}$ events with $W \to e\nu$ decays contribute to the background if electrons are misidentified as τ-jets.

- **Weak Single top Production**
  At tree level the weak production of single top quarks takes place via three different production modes, namely the Wt-channel, the s-channel and the t-channel (see Figure 7.1 and 7.2). As can be seen in Table 7.1, the total cross section of all single top quark production channels with one W boson decaying leptonically is expected to be roughly one quarter of the $t\bar{t}$ production cross section with one leptonic W decay. All three modes have been generated with ACERMC.
  In the Wt-channel two W bosons are present which can lead to events containing an isolated lepton and a τ-jet. However, since less b-jets are present than in the signal, such events can be rejected using a requirement on the number of tagged b-jets. Single top events produced via the s-channel or the t-channel contain only one W boson and can be suppressed by the lepton and τ-jet identification.

- ***W*+Jets Production**
  The W+jets background with at least three jets (see an example in Figure 7.3) has been generated with ALPGEN. The production cross section of W bosons with at least three accompanying jets is expected to be much higher than the $t\bar{t}$ cross section (see Table 7.1). In

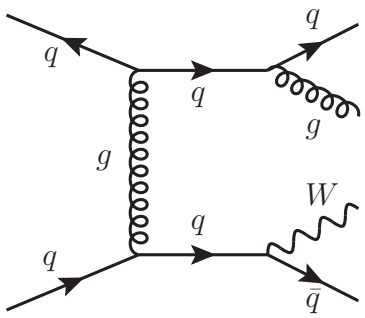

Figure 7.3: W+3 jets production.

addition, the calculated W+jets cross section has large uncertainties and may be underestimated. Hence, even if the amount of these events is strongly suppressed by b-jet, τ-jet and lepton identification, it may still contribute to the background.

- **QCD Jet Production**
  Another possible background is QCD jet production with two or more jets in the final state. It is expected to be negligible compared to the background contributions mentioned above. Due to the very high cross section at the LHC, not enough Monte Carlo events could be produced in order to give a definite answer. The background can be suppressed by τ-jet, b-jet, electron and muon identification together with a requirement of high $E_{\mathrm{T}}^{\mathrm{miss}}$.
  A dangerous contribution are multi-jet events with heavy quark jets. With semi-leptonic decays of B or D mesons they give rise to lepton+jets final states which can fake the signal. Since these leptons are close to the jets such events are rejected by employing isolation requirements for the leptons.

7.2 Event Selection

The signal is selected by several trigger signatures and cuts on discriminating variables. In this section the trigger signatures are described and the distributions of the discriminating variables are discussed. A cut optimization is performed which takes into account systematic uncertainties.

7.2.1 Selection Criteria

Trigger Conditions

Due to its clean signature in the detector, the isolated lepton originating from the leptonic W decay allows for the efficient triggering of $t\bar{t}$ events. In order to keep the trigger rate within the ATLAS event filter bandwidth of 200 Hz, trigger thresholds of $p_{\mathrm{T}} > 25\,\mathrm{GeV}$ for electrons and $p_{\mathrm{T}} > 20\,\mathrm{GeV}$ for muons are employed. Even so, already for a luminosity of $10^{33}\,\mathrm{cm}^{-2}\mathrm{s}^{-1}$ the single lepton triggers consume a rather large fraction of the bandwidth. Although such estimations are currently subject to large uncertainties and have to be determined from the data, it is for this

Table 7.3: Plateau efficiencies of electron, muon and both τ-jet trigger criteria (see text) before and after applying the selection cuts. The right two coloumns indicate the combined electron and muon trigger efficiency as well as the overall trigger The upper part of the table shows the efficiencies of the combined trigger with $E_{\mathrm{T}}^{\mathrm{miss}}$ requirements while in the bottom part the corresponding single lepton and single τ-jet trigger efficiencies alone are given for comparison. All values are evaluated for signal events with the charged Higgs boson mass of $m_{H^{\pm}} = 130\,\mathrm{GeV}$.

		Electron	Muon	τ-jet	Lepton	Overall
Comb.	Before cuts	0.22	0.24	0.27	0.46	0.54
	After cuts	0.48	0.41	0.85	0.87	1.00
Single	Before cuts	0.28	0.32	0.51	0.58	0.76
	After cuts	0.48	0.41	0.91	0.87	1.00

analysis possible to choose a more conservative trigger menu by combining the single lepton trigger signatures with an additional $E_{\mathrm{T}}^{\mathrm{miss}}$ requirement:

- Electron + $E_{\mathrm{T}}^{\mathrm{miss}}$: $p_{\mathrm{T}}^{e} > 25\,\mathrm{GeV}$ ($|\eta| < 2.5$), $E_{\mathrm{T}}^{\mathrm{miss}} > 30\,\mathrm{GeV}$,
- Muon + $E_{\mathrm{T}}^{\mathrm{miss}}$: $p_{\mathrm{T}}^{\mu} > 20\,\mathrm{GeV}$ ($|\eta| < 2.5$), $E_{\mathrm{T}}^{\mathrm{miss}} > 30\,\mathrm{GeV}$.

For the above luminosity, these trigger rates are expected to be on the order of 10 Hz, well within of the bandwidth of the ATLAS event filter [42].
For searches of light charged Higgs bosons in fully hadronic $t\bar{t}$ decays a τ-jet trigger is available. This trigger, even with the relatively high p_{T} threshold of 35 GeV, would exhaust the bandwidth of the event filter due to the large jet backgrounds at the LHC. Therefore it has to be combined with rather tight $E_{\mathrm{T}}^{\mathrm{miss}}$ and multi-jet requirements:

- τ-jet + $E_{\mathrm{T}}^{\mathrm{miss}}$: $p_{\mathrm{T}}^{\tau} > 35\,\mathrm{GeV}$ ($|\eta| < 2.5$), $E_{\mathrm{T}}^{\mathrm{miss}} > 50\,\mathrm{GeV}$,
- τ-jet + $E_{\mathrm{T}}^{\mathrm{miss}}$ + jets: $p_{\mathrm{T}}^{\tau} > 35\,\mathrm{GeV}$, ($|\eta| < 2.5$), $E_{\mathrm{T}}^{\mathrm{miss}} > 40\,\mathrm{GeV}$ + 3 jets (with: $p_{\mathrm{T}}^{\mathrm{jet}} > 20\,\mathrm{GeV}$ ($|\eta| < 5$)).

In Table 7.3 the plateau trigger efficiencies are given with respect to all simulated events which contain a high-p_{T} electron or muon before and after the remaining selection cuts (see below). The τ-jet trigger efficiencies are given for both combined τ-jet trigger criteria above simultaneously. Finally, the lepton trigger (overall) efficiency is evaluated by applying the electron and muon (and τ-jet) trigger conditions together.
As can be seen, about 87% of all offline selected signal events are triggered by the electron or muon trigger. By adding the τ-jet trigger, the remaining events are triggered as well. When dropping the $E_{\mathrm{T}}^{\mathrm{miss}}$ and multi-jet requirements, the trigger efficiency does not improve significantly because the corresponding cuts are also applied in the offline event selection described in the next section.

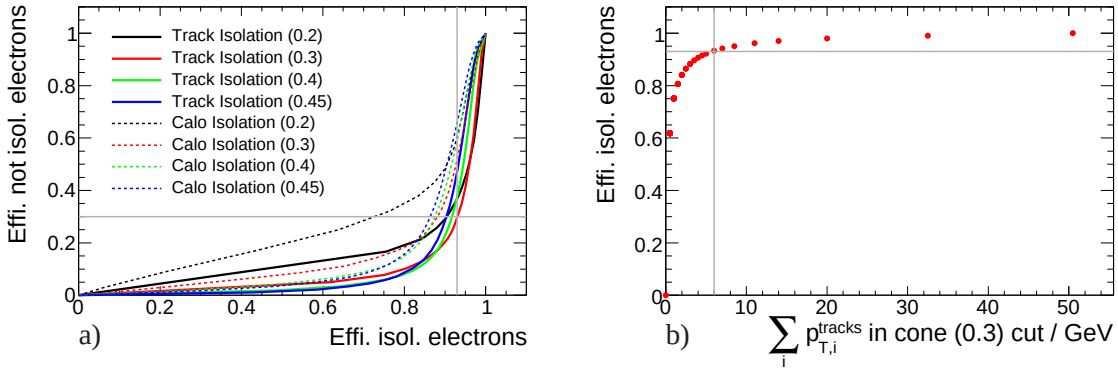

Figure 7.4: (a) Efficiencies for isolated vs. non-isolated electrons depending on the cone energy cut in $t\bar{t}$ events using track- and calorimeter based isolation criteria and various cone sizes (in parenthesis). (b) Efficiency for track based isolated electrons using a cone of the size $\Delta R < 0.3$ as a function of the cut on $\sum_i p_{T,i}^{track}$ in the cone. The efficiencies for the chosen cut $\sum_i p_{T,i}^{track} < 6\,\text{GeV}$ are indicated.

Lepton Selection

The events selected by the electron or the muon triggers are required to contain an offline reconstructed lepton with transverse momentum $p_T > 10\,\text{GeV}$ within the inner detector acceptance range $|\eta| < 2.5$. If the event is triggered only because of the τ-jet signature these requirements are tightened to $p_T > 25\,\text{GeV}$ for electrons and $p_T > 20\,\text{GeV}$ for muons.
To reject events with leptonic decays of heavy quarks, the leptons are required to be isolated. In Figure 7.4(a) the selection efficiencies for isolated and non-isolated electrons are shown as a function of the cut on the energy in the cone around the electron where the energy of the electron itself was subtracted. Several cone sizes as well as track and calorimeter based isolation are compared. The highest efficiency is obtained with the track based isolation requirement and a cone size $\Delta R < 0.3$. In order to stay well within the plateau region of the efficiency for this requirement (see Figure 7.4(b)), a cut value on the sum of all transverse track momnenta in the isolation cone of $\sum_i p_{T,i}^{track} < 6\,\text{GeV}$ has been chosen as indicated in Figure 7.4(a) and 7.4(b).
For muon isolation the calorimeter based method is used. A cone size of $\Delta R < 0.4$ and a cone energy of less than 9 GeV is required.

Jet Selection

To reduce the W+jets and QCD dijet backgrounds, the cut $N_{\text{Jets}} \geq 3$ is applied in view of the two b-jets and the τ-jet in the signal events. In Figure 7.5(a) the multiplicity of reconstructed jets with transverse momentum $p_T > 20\,\text{GeV}$ within $|\eta| < 5$ is shown for signal samples with $m_{H^\pm} = 90\,\text{GeV}$ and 150 GeV and for the Standard Model $t\bar{t}$ background. In the $t\bar{t}$ background on average a higher number of jets is observed due to the additional $W \to q\bar{q}'$ decay.
Further suppression of the backgrounds is achieved by employing the identification algorithms for τ-jets and b-jets:

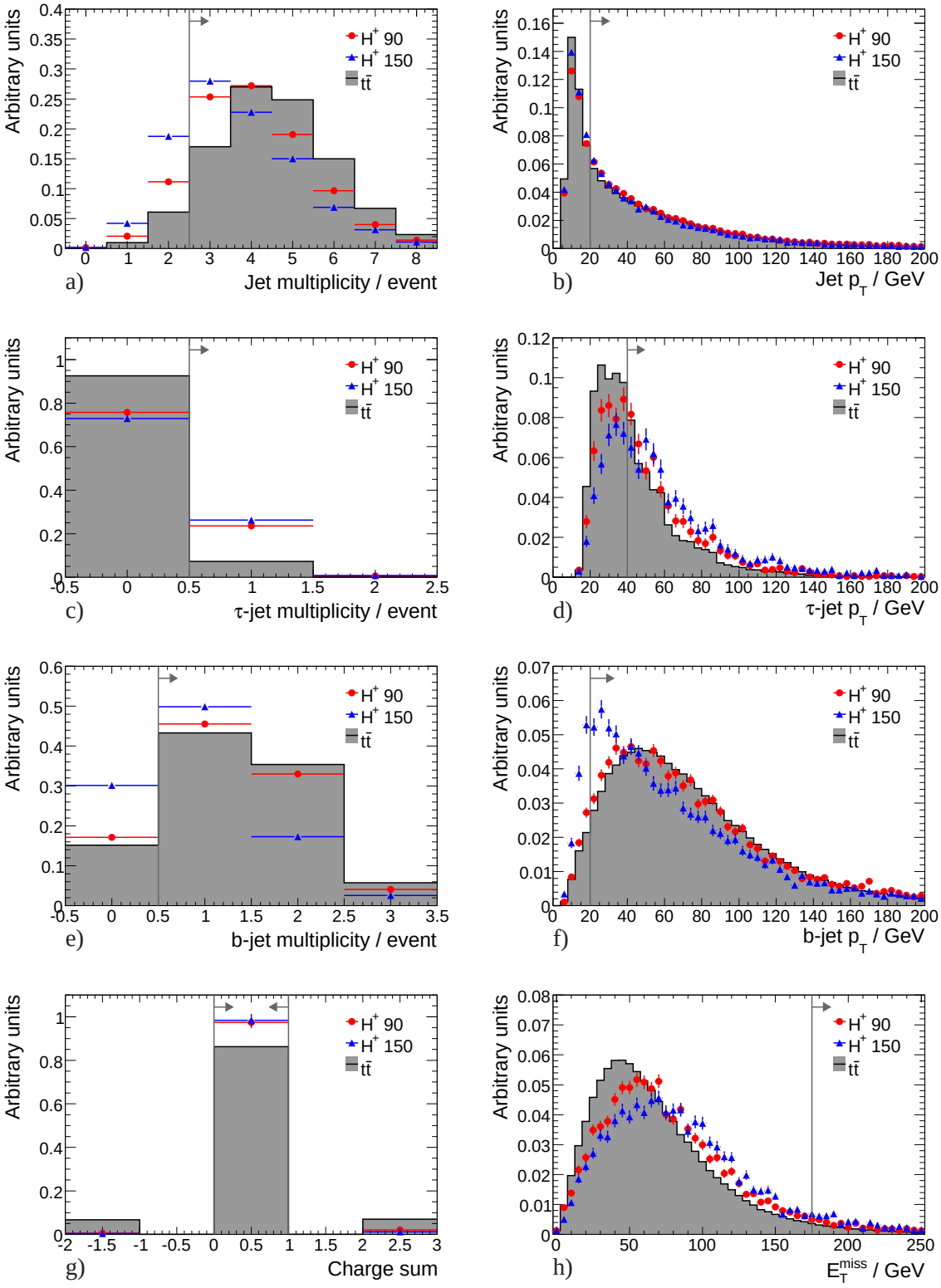

Figure 7.5: (a) Jet multiplicity, (b) jet p_{T}, (c) τ-jet candidate multiplicity, (d) τ-jet candidate p_{T}, (e) b-jet multiplicity, (f) τ-jet p_{T}, (g) lepton-τ-jet charge sum and (h) missing transverse energy $E_{\mathrm{T}}^{\mathrm{miss}}$ for jets with $p_{\mathrm{T}} > 20\,\mathrm{GeV}$. All distributions are shown for signal samples with the lowest (red circles) and highest (blue triangles) charged Higgs boson mass and for the $t\bar{t}$ background (shaded histogram) and are normalized to one. The cuts on the discriminating variables are indicated.

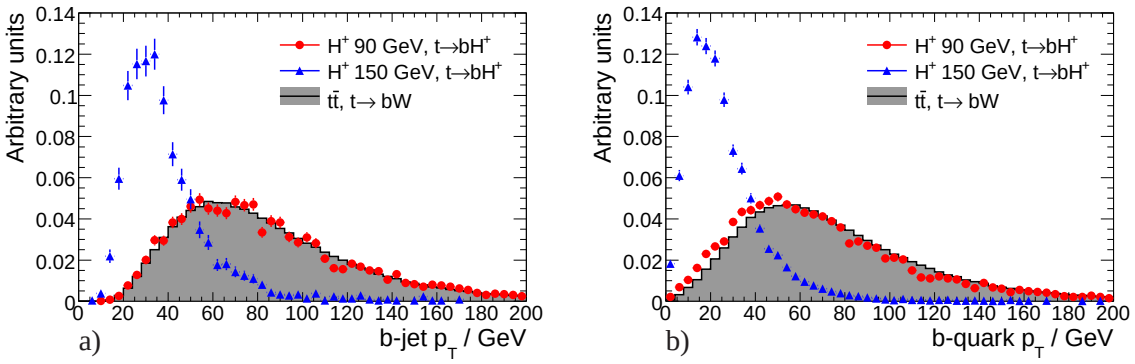

Figure 7.6: Normalized transverse momentum distributions of the (a) b-jets and (b) b quarks at the generator level for signal events with the lowest (red circles) and highest (blue triangles) charged Higgs boson mass and for the $t\bar{t}$ background (shaded histogram).

- **τ-Jet Identification**
  The τ-jet identification is performed using the likelihood discriminant method as described in Section 6.2.5. After removing overlapping electron and muon candidates, the likelihood discriminant (see Figure 7.9) of the τ-jet candidates is required to be greater than six. A further rejection of unidentified electrons is obtained by the cut on the ratio of transverse energy in the hadron calorimeter and of the p_{T} of the leading track of the τ-jet candidate of $E_{\mathrm{T}}^{\mathrm{had}}/p_{\mathrm{T}}^{\text{lead. track}} > 0.1$. This requirement makes use of the fact that the energy deposit of electrons in the hadron calorimeter is much smaller than the one of τ-jets.
  The multiplicity of identified τ-jet candidates with a $p_{\mathrm{T}}^{\tau\text{-jet}} > 20\,\mathrm{GeV}$ and $|\eta| < 2.5$ is shown in Figure 7.5(c). By demanding at least one identified τ-jet candidate in the event, the reducible part of the $t\bar{t}$ background is significantly reduced. The small deviation between the two signal samples is caused by differences in the p_{T} distributions of the τ-jet candidates. With increasing mass of the parent particle of the τ, the p_{T} spectra are shifted towards higher values (see Figure 7.5(d)). For $H^{\pm}$ bosons the τ-jet transverse momentum is increased due to spin correlation compared to the Standard Model $t\bar{t}$ events. Therefore a suppression of the irreducible $t\bar{t}$ mode is obtained by requiring a p_{T} of the identified τ-jet candidate greater than 40 GeV.
  The exact cut values on $p_{\mathrm{T}}^{\tau\text{-jet}}$ and the likelihood discriminant are determined by the cut optimization procedure described in Section 7.2.2.

- ***b*-Jet Identification**
  To reduce the W+jets, QCD and single top backgrounds, the b-tagging technique is used as described in Section 6.2.6. Two b-jets are present both in the signal and the $t\bar{t}$ background. But since the charged Higgs boson is heavier than the W boson, the b-jets in signal events tend to be softer than the b-jets in Standard Model $t\bar{t}$ events. In Figure 7.6 the p_{T} spectra of reconstructed b-jets and generated b quarks originating from the processes $t \to H^{+}b$ and $t \to Wb$ are compared. The relative shift is marginal for $m_{H^{\pm}} = 90\,\mathrm{GeV}$, but becomes increasingly pronounced when $m_{H^{\pm}}$ approaches the top mass. Since the b-tagging efficiency

Table 7.4: Summary of the cut-based selection requirements used in the analysis

Cut	Requirements
Trigger	lepton+$E_{\mathrm{T}}^{\mathrm{miss}}$ or τ-jet +$E_{\mathrm{T}}^{\mathrm{miss}}$
1 Lepton	$p_{\mathrm{T}} > 10\,\mathrm{GeV}$, $\eta < 2.5$
3 Jets	$p_{\mathrm{T}} > 20\,\mathrm{GeV}$, $\eta < 5.0$
1 τ-jet	$p_{\mathrm{T}} > 40\,\mathrm{GeV}$, $\eta < 2.5$, discr.> 6
1 b-jet	$p_{\mathrm{T}} > 20\,\mathrm{GeV}$, $\eta < 2.5$, discr.> 3
Charge balance	$q_\tau + q_{\mathrm{lep}} = 0$
$E_{\mathrm{T}}^{\mathrm{miss}}$	$E_{\mathrm{T}}^{\mathrm{miss}} > 175\,\mathrm{GeV}$

in the range $p_{\mathrm{T}}^{b\text{-jet}} \approx 20\,\mathrm{GeV}$ is poor, the multiplicity of reconstructed b-jets decreases with increasing mass of the τ parent as shown in Figure 7.5(e). Therefore, only one tagged b-jet is required and no further cut on $p_{\mathrm{T}}^{b\text{-jet}}$ is applied.

Additional Cuts

Additional rejection of the backgrounds is achieved by applying the following two cuts:

- **Charge Balance**
  Since $t\bar{t}$ quark pairs are electrically neutral, the charges of the reconstructed lepton and τ-jet candidates are required to be opposite. In Figure 7.5(g) the distributions of the sum of the charges $\sum q$ of the two charges are shown. As can be seen, a small reduction of the $t\bar{t}$ background is achieved by this cut.

- **$E_{\mathrm{T}}^{\mathrm{miss}}$ Requirement**
  The neutrinos from charged Higgs boson and subsequent τ decay are expected to be of higher energy than those from leptonic W boson decay, like the τ lepton itself. Therefore the distribution of the missing transverse energy in signal events is slightly shifted compared to Standard Model $t\bar{t}$ events (see Figure 7.5(h)). Of course also other backgrounds, especially QCD dijet production, are rejected. To optimize the signal significance, the cut value $E_{\mathrm{T}}^{\mathrm{miss}} > 175\,\mathrm{GeV}$ is chosen. For this cut optimization the systematic uncertainties have to be taken into account.

The selection requirements are summarized in Table 7.4.

7.2.2 Cut Optimization

The cuts on the likelihood discriminant, the transverse momentum of the τ-jet and the missing transverse energy are optimized such that

$$S = \frac{N_{H^\pm} - (N_{\mathrm{Back}}^{\mathrm{SM}} - N_{\mathrm{Back}}^{\mathrm{MSSM}})}{\sqrt{N_{\mathrm{Back}}^{\mathrm{SM}} + (\sigma_{\mathrm{sys}}\, N_{\mathrm{Back}}^{\mathrm{SM}})^2}} \tag{7.1}$$

Table 7.5: Cut evolution for the signal and background processes. The numbers are normalized to the production cross sections. For the MSSM signal, $\tan\beta$ is set to 20 and the remaining parameters according to the m_h-max benchmark scenario. Below the cross sections, the relative cut efficiencies are given.

Process		$N_{\text{generated}}$	Trigger	$\geq$1 e,μ	$\geq$3 jets	$\geq 1\tau$-jet	$\geq$1 b	$p_{\text{T}}^{\tau\text{-jet}}$	$\sum$ q	$E_{\text{T}}^{\text{miss}}$
H^+ (90 GeV)	[fb]	12098	6219	4972	4248	1092	929	586	582	44
			0.51	*0.80*	*0.85*	*0.26*	*0.85*	*0.63*	*0.99*	*0.08*
H^+ (110 GeV)	[fb]	8570	4510	3534	2986	772	650	439	431	30
			0.53	*0.78*	*0.84*	*0.26*	*0.84*	*0.67*	*0.98*	*0.07*
H^+ (120 GeV)	[fb]	6737	3611	2868	2440	654	535	360	354	23
			0.54	*0.79*	*0.85*	*0.27*	*0.82*	*0.67*	*0.98*	*0.06*
H^+ (130 GeV)	[fb]	4954	2670	2112	1730	512	399	270	265	20
			0.54	*0.79*	*0.82*	*0.30*	*0.78*	*0.67*	*0.98*	*0.07*
H^+ (150 GeV)	[fb]	1853	1048	836	626	177	130	94	94	7
			0.57	*0.80*	*0.75*	*0.28*	*0.74*	*0.72*	*1.00*	*0.07*
$t\bar{t}$ ($\geq 1\ell$)	[fb]	452000	169612	137928	122547	4760	4006	1915	1730	78
			0.37	*0.81*	*0.89*	*0.04*	*0.84*	*0.48*	*0.90*	*0.04*
single top	[fb]	112500	30180	25065	18081	271	168	47	38	–
			0.27	*0.83*	*0.72*	*0.02*	*0.61*	*0.28*	*0.81*	–
$W \to \ell\nu$+jets	[fb]	769547	216556	166598	101473	1549	180	92	58	–
			0.28	*0.77*	*0.61*	*0.02*	*0.12*	*0.51*	*0.63*	–

is maximized. The signal $N_{H^\pm}$ is the excess of events above the expected Standard Model background. Since in the MSSM the branching ratio $\mathcal{B}(t \to Wb)$ is reduced by $\mathcal{B}\,(t \to H^+b)$ the $t\bar{t}$ background rate is lower than in the Standard Model and part of the signal is lost in this case. Therefore, the number of signal events is corrected by the difference $N_{\text{Back}}^{\text{SM}} - N_{\text{Back}}^{\text{MSSM}}$. A relative systematic error σ_{sys} on the background of 10% is taken into account, assuming rather well understood detector performance corresponding to an integrated luminosity of about $\mathcal{L} = 10\,\text{fb}^{-1}$. The estimation of the systematic uncertainty from data is the subject of the following two chapters 8 and 9.
To avoid mass dependent cut values, only one signal sample $(m_{H^\pm} = 130\,\text{GeV})$ is used for the cut optimization. As start values $p_{\text{T}}^{\tau\text{-jet}} > 40\,\text{GeV}$ and $E_{\text{T}}^{\text{miss}} > 70\,\text{GeV}$ are chosen. As shown in Figure 7.5(d) and 7.5(h), these values correspond roughly to the crossing points of the signal and $t\bar{t}$ background distributions. In Figure 7.7(a) the signal significance is shown as a function of the likelihood discriminant cut. In addition, the signal-to-background ratio (multiplied by ten) is shown. The values of the signal significance and the fraction of signal-to-background ratio times ten are similar, indicating the dominant systematic error on the background (see Equation (7.1)). The significance rises with the cut value until a plateau is reached at about a cut value of six which is used in the analysis and the remaining cut optimization. Figure 7.7(b) shows the signal significance as a function of the $E_{\text{T}}^{\text{miss}}$ cut after the above likelihood cut. The maximum is reached for a cut value of $E_{\text{T}}^{\text{miss}} > 175\,\text{GeV}$. For values above 200 GeV the significance rises again but is subject to large statistical uncertainty.
Applying the optimized likelihood discriminant and $E_{\text{T}}^{\text{miss}}$ requirements, the cut on the τ-jet p_{T} is varied. As shown in Figure 7.7(c) two maxima at 40 GeV and 65 GeV are observed. For lower statistical error the first value is chosen.

7.2.3 Cut Evolution

In Table 7.5 the cut evolution is given for all investigated signal samples and backgrounds. The signal is normalized to the MSSM m_h-max cross sections for $\tan\beta = 20$, the background expectations are normalized to the Standard Model cross sections. Clearly, only $t\bar{t}$ events contribute to the background after the cuts. The remaining backgrounds are eliminated mainly by the τ-jet identification.
Figure 7.8 shows the $E_{\text{T}}^{\text{miss}}$ distribution after all cuts for the signal samples with the lowest and highest charged Higgs boson mass ($m_{H^\pm} = 90\,\text{GeV}$ and $150\,\text{GeV}$), the Standard Model $t\bar{t}$ background and the corresponding MSSM $t\bar{t}$ backgrounds, respectively. The excess of signal events above the Standard Model $t\bar{t}$ background is smaller for high than for low $m_{H^\pm}$, because the signal cross section decreases for higher $m_{H^\pm}$ (see Figure 4.5(a)). For an integrated luminosity of $10\,\text{fb}^{-1}$, 780 Standard Model $t\bar{t}$ events are expected while in the MSSM m_h-max model 440 (70) signal events on top of 691.4 (766.9) $t\bar{t}$ events are expected for a charged Higgs boson mass of 90 GeV (150 GeV) and $\tan\beta = 20$.

7.2.4 Composition of the $t\bar{t}$ Background

In Figure 7.9 the likelihood discriminant of all τ-jet candidates in signal and $t\bar{t}$ background events is shown. The contributions of genuine τ-jets, other jets and electrons are also indicated. While a

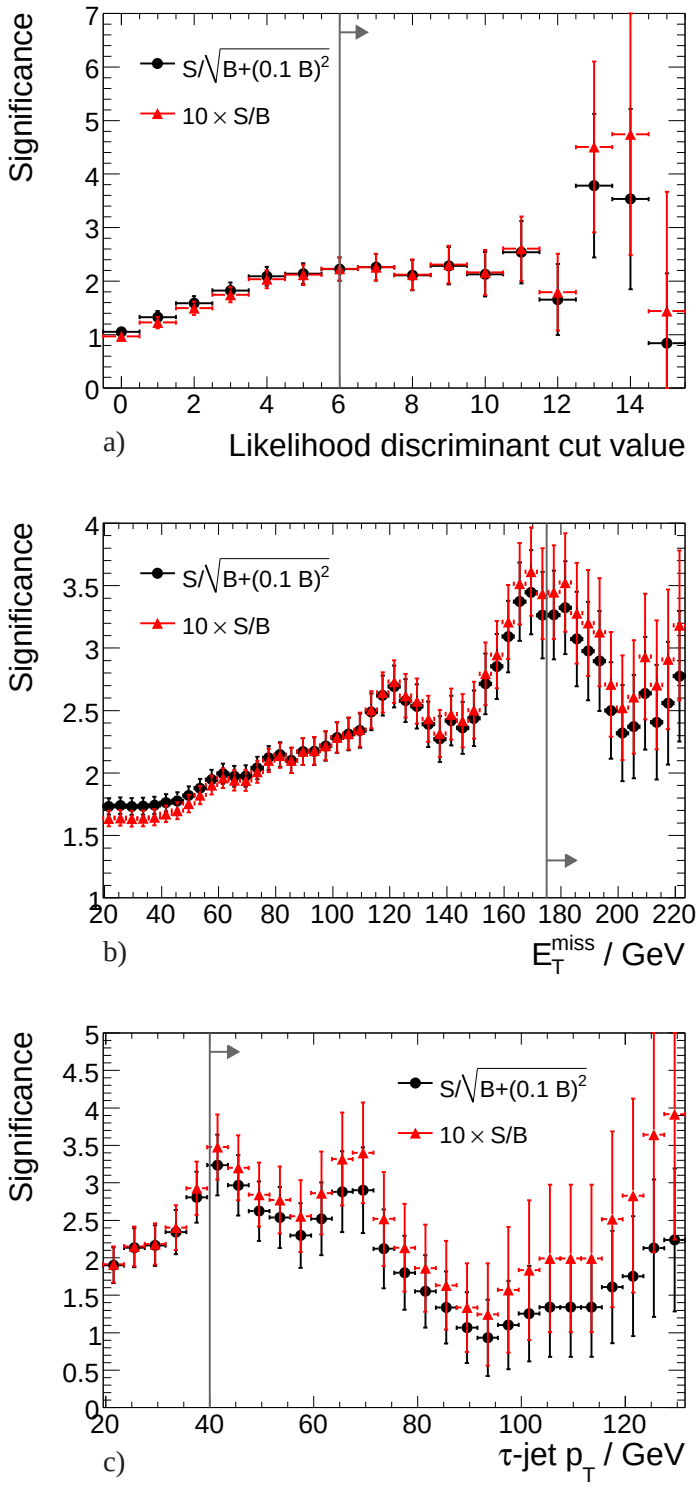

Figure 7.7: Signal significance (black circles) calculated according to Equation (7.1) as a function of (a) likelihood discriminant for τ-jet identification, (b) $E_{\mathrm{T}}^{\mathrm{miss}}$ and (c) the p_{T} of the τ-jets and signal-to-background ratio times ten (red triangles).

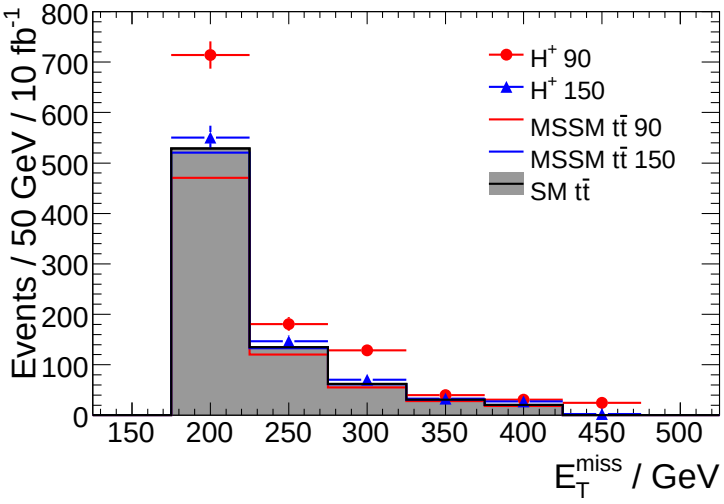

Figure 7.8: $E_{\mathrm{T}}^{\mathrm{miss}}$ distribution after all cuts for the two signal samples with the lowest (red circles) and highest (blue triangles) charged Higgs boson mass and the $t\bar{t}$ background (shaded histogram). The signal is shown above the corresponding MSSM $t\bar{t}$ background (blue and red histogram). The numbers of events are normalized to an integrated luminosity of $10\,\mathrm{fb}^{-1}$. The MSSM m_h-max cross sections are evaluated for $\tan\beta = 20$.

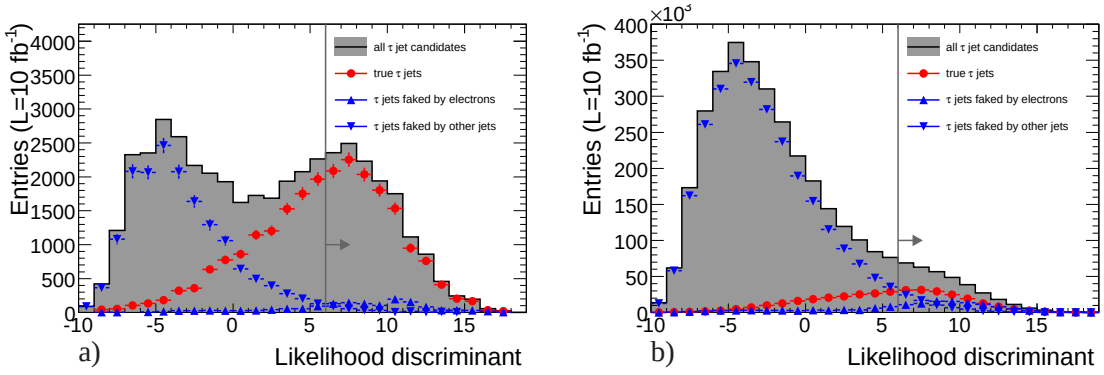

Figure 7.9: Likelihood discriminant for τ-jet identification for (a) signal and (b) Standard Model $t\bar{t}$ background. The shaded histogram shows τ-jet candidates constituted by genuine τ-jets (red squares), jets (blue up-triangles) and electrons (blue down-triangles).

Table 7.6: Contributions to the selected τ-jet candidates before and after the signal event selection.

Contribution	τ-jets	$W \to e\nu$	$W \to q\bar{q}'$	Other jets
Before cuts	0.48	0.32	0.14	0.06
After cuts	0.44	0.28	0.23	0.05

clean separation of τ-jets and other objects is possible for the signal events, the situation is difficult for the $t\bar{t}$ background. Using the cut value of six, half of the identified τ-jet candidates are genuine τ-jets. The other half consists in equal fractions of electrons as well as jets, mainly initiated by quarks from the decay $W \to q\bar{q}'$. The τ-jet candidate contributions before and after signal event selection are listed in Table 7.6. Because the τ-jet identification does not provide rejection power against electrons (see Section 6.2.5), a large part of the misidentified τ-jets originate from the process $W \to e\nu$. However, since release 14 an explicit veto against electrons is implemented such that the fraction of misidentified electrons can be considerably reduced. Considerable background of misidentified light quark and gluon jets remains because of the large branching ratio $\mathcal{B}\,(t \to Wb, W \to q\bar{q}')$ and the high jet multiplicity in $t\bar{t}$ events. Data based estimation of this background is discussed in Chapter 9.

7.3 Systematic Uncertainties

The discovery potential and exclusion limits for charged Higgs bosons are affected by the systematic uncertainties related to the detector as well as to the theoretical predictions mainly caused by missing higher order corrections in the calculation of production cross sections.

7.3.1 Experimental Uncertainties

Experimental systematic uncertainties on the following quantities have been considered:

- Energy scales of electrons, photons, muons, jets and τ-jets.
- Energy resolutions of electrons, photons, muons, jets and τ-jets.
- Electron, muon, b-jet, τ-jet identification efficiencies and misidentification rates.
- $E_{\mathrm{T}}^{\mathrm{miss}}$ scale and resolution.
- Luminosity measurement.

The systematic uncertainties listed in Table 7.7 correspond to an integrated luminosity of $10\,\mathrm{fb}^{-1}$ for which the above quantities are determined using the real data. The impact of the uncertainties on the analysis is evaluated by smearing the 4-momenta of the reconstructed objects. The energy scale uncertainties lead to shifts of the E_{T} of electrons and photons, p_{T} of muons and the energies

Table 7.7: Detector-related systematic uncertainties expected for an integrated luminosity of about $10\,\text{fb}^{-1}$. For the determination of the muon energy resolution a constant is added in quadrature.

Source	Value [GeV]
τ energy resolution	$\sigma = 0.45 \times \sqrt{E}$
τ energy scale	-5% $+5\%$
τ-tagging efficiency	$\pm 5\%$
Jet energy resolution	$\sigma = 0.45 \times \sqrt{E}$ for $\lvert\eta\rvert < 3.2$ $\sigma = 0.63 \times \sqrt{E}$ for $\lvert\eta\rvert > 3.2$
Jet energy scale	$+7\%$ for $\lvert\eta\rvert < 3.2$ $+15\%$ for $\lvert\eta\rvert > 3.2$ -7% for $\lvert\eta\rvert < 3.2$ -15% for $\lvert\eta\rvert > 3.2$
b-tagging efficiency	$\pm 5\%$
b-tagging light jet rejection	-10% $+10\%$
μ energy resolution	$\sigma = 0.011/p_{\text{T}} \oplus 0.00017$
μ energy scale	-1% $+1\%$
μ efficiency	$\pm 1\%$
e energy resolution	$\sigma = 0.0073 \times E_{\text{T}}$
e energy scale	-0.5% $+0.5\%$
e efficiency	$\pm 0.2\%$
Correction to missing energy	Indirect via the other uncertainties
Luminosity	$\pm 3\%$

of jets. The uncertainties of the resolutions are taken into account by smearing of E_{T} of electrons and photons, of the jet energies and of $1/p_{\mathrm{T}}$ of muons according to Gaussian distributions. The uncertainties on the identification efficiencies is accounted for by randomly removing a fraction of the identified objects. Finally, the rejection rate of light quark and gluon jets by the b-tagging algorithm is varied by changing the cut on the b-tagging discriminant. For each systematic variation the resulting shift in $E_{\mathrm{T}}^{\mathrm{miss}}$ is also calculated.

7.3.2 Theoretical Uncertainties

For the $t\bar{t}$ production cross section the prediction $\sigma_{t\bar{t}} = 833 \pm 100\,\mathrm{pb}^{-1}$ is used [39]. This cross section has been calculated at next-to-leading order perturbation theory and includes also further radiative corrections related to the emission of soft-gluons.
The uncertainties on the expected signal cross section are due to higher order loop corrections to the tbH^+ vertex and the running of c and s quark masses. The uncertainties of the branching ratios of the decays $t \to H^+b$ and $H^+ \to \tau\nu$ are smaller than 10% and 5%, respectively [83].

7.3.3 Effect of Systematic Uncertainties

The effect for the experimental uncertainties on signal and background expectations are given in Table 7.8. The dominant experimental error of 35% is due to the uncertainty on the jet energy scale in combination with the effect on the missing transverse energy $E_{\mathrm{T}}^{\mathrm{miss}}$ measurement. Other systematic uncertainties like the ones in the energy scale and resolution of τ-jets are smaller than 10%. Systematic effects related to the reconstruction of muons and electrons are negligible. For the signal a total systematic uncertainty of 40% is obtained and used later for the calculation of the search limits.
In principle a similar value is expected for the systematic uncertainty of the Standard Model $t\bar{t}$ background. However, such a high value makes a discovery of charged Higgs bosons with ATLAS nearly impossible. Therefore, in order to gain better knowledge of the level of the $t\bar{t}$ background, methods are developed to measure it directly from the data itself. In a first study [42] an accuracy in the determination of the $t\bar{t}$ background from data of 10% has been estimated which is used as systematic background uncertainty when calculating the discovery and exclusion limits in Chapter 10. It is confirmed by a more thorough study of the $t\bar{t}$ background estimation from data presented in Chapters 8 and 9.

Table 7.8: Effect of systematic uncertainties in Table 7.7 on the expected signal S and combined background B cross sections including the effects on $E_{\mathrm{T}}^{\mathrm{miss}}$. The total uncertainty is calculated by adding up the single uncertainties in quadrature.

Systematic uncertainty	$\Delta S[\%]$	$\Delta B[\%]$
τ energy resolution	$+8$	-3
τ energy scale	0	-9
	$+8$	$+1$
τ-tagging efficiency	-8	-1
Jet energy resolution	$+8$	$+3$
Jet energy scale	$+35$	$+19$
	-19	-17
b-tagging efficiency	0	-3
b-tagging rejection	0	0
	0	-1
μ energy resolution	0	$+1$
μ energy scale	$+4$	-1
	0	0
μ efficiency	0	0
e energy resolution	0	-1
e energy scale	0	-1
	$+4$	-1
e efficiency	0	0
Luminosity	-3	-3
	$+3$	$+3$
Total	$\sim$40	$\sim$40

Chapter 8

Estimation of the Irreducible $t\bar{t}$ Background from Data

In the Standard Model nearly 100% of the top quarks decay via $t \rightarrow bW$ [16]. Therefore, $t\bar{t}$ events with both top quarks decaying into bW constitute the main background for light charged Higgs boson searches in the channel $t\bar{t} \rightarrow (H^+b)\left(W\bar{b}\right) \rightarrow (\tau_{\text{had}}\nu b)\left(\ell\bar{\nu}\bar{b}\right)$. However, as shown in Chapter 7, the determination of this background is subject to high systematic uncertainties if one only relies on the available Monte Carlo simulations. In this case the experimental sensitivity suffers considerably.
In this chapter a data-driven method for the estimation of the irreducible background $t\bar{t} \rightarrow (Wb)$ $(W\bar{b}) \rightarrow (\tau_{\text{had}}\nu b)(\ell\bar{\nu}\bar{b})$ is presented. Generally such a background estimation is performed by selecting a *control event sample* from the collision data with similar event topology as the genuine background and low contamination with signal events. In this way many systematic uncertainties discussed in Chapter 7 are greatly reduced.
For the estimation of the irreducible $t\bar{t}$ background the "embedding technique" is used. This method was originally developed for top quark searches at the Tevatron [84] and has been implemented in ATHENA release 14 as well [85]. In Section 8.1 the method is described while in Section 8.2 the control sample distributions are compared to the direct Monte Carlo simulation of the background and the systematic uncertainty of the background estimation is determined. The results are summarized in Section 8.3.

8.1 Description of the Method

In the following, the embedding method, shown schematically in Figure 8.1, is described in detail:

- Events with a similar topology as the genuine $t\bar{t}$ background are dileptonic $t\bar{t} \rightarrow \mu\mu$+X events with both W bosons decaying into a muon and the corresponding neutrino. This particular final state has the advantage of high selection efficiency and purity. In principle final states with electrons can be used as well if the background contimination is small.
  The events are selected by requiring two combined muons, reconstructed with the STACO package as described in Section 6.2.1. To reject muons originating from meson decays, the

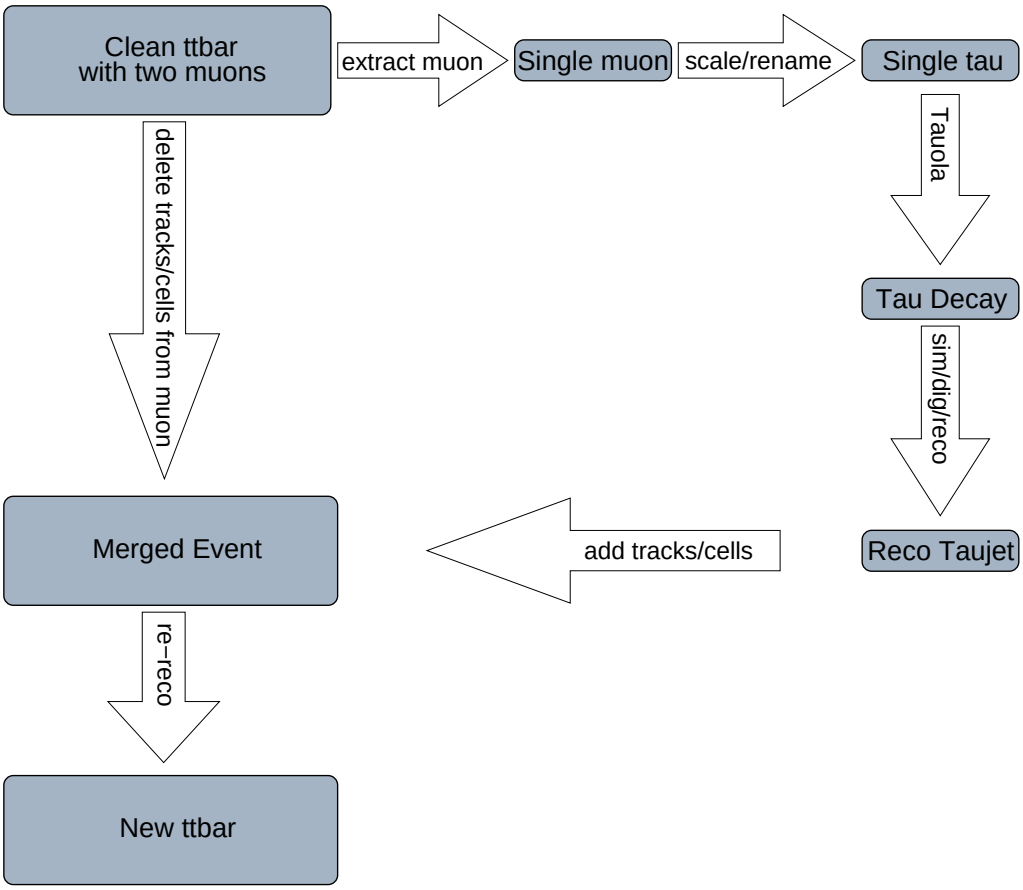

Figure 8.1: The embedding scheme used to estimate the irreducible $t\bar{t}$ background mode with $t\bar{t} \rightarrow (Wb)\left(W\bar{b}\right) \rightarrow (\tau_{\text{had}}\nu b)\left(\ell\bar{\nu}\bar{b}\right)$. In the first step (top left) $t\bar{t} \rightarrow (Wb)\left(W\bar{b}\right) \rightarrow (\mu\nu b)\left(\mu\bar{\nu}\bar{b}\right)$ events are selected. One muon is randomly removed from each event and its rescaled 4-momentum is used to generate, simulate and reconstruct a τ-jet. The τ-jet is embedded in the remnant of the event and the event reconstruction is run again on the merged event.

energy $E_{\mathrm{T}}^{\mathrm{cone}}$ in a cone of the radius $\Delta R = 0.4$ around the muon momentum vector divided by its p_{T} is required to be smaller than 0.2. A further rejection of such muons is achieved by requiring a high transverse momentum, $p_{\mathrm{T}} > 10\,\mathrm{GeV}$, and opposite charges of the two muon tracks.

- In the second step, one of the two muons is chosen randomly. Afterwards the 4-momentum p_μ of this muon is scaled to be consistent with a τ lepton of mass m_τ and energy E_μ:

$$p_\tau = p_\mu \sqrt{\frac{E_\mu^2 - m_\tau^2}{\boldsymbol{p}_\mu^2}}. \tag{8.1}$$

- The new 4-momentum p_τ is then together with the reconstructed vertex of the corresponding muon track used in TAUOLA (see Chapter 6) to generate the hadronic decay of the τ lepton. The decay products are used as an input for the ATLAS detector simulation and the event reconstruction. In this way τ-jets are obtained which have very similar p_{T} and η distributions as the genuine τ-jets in $t\bar{t} \to (Wb)\left(W\bar{b}\right) \to (\tau_{\mathrm{had}}\nu b)\left(\ell\bar{\nu}\bar{b}\right)$ events.

- In the following embedding step the muon is replaced by the generated τ-jet. For the implementation of the embedding several possibilities exists. The most simple choice is to replace the reconstructed higher-level physics object and correct the missing transverse energy $E_{\mathrm{T}}^{\mathrm{miss}}$ accordingly. This strategy has been followed for charged Higgs searches published in [42] and has been shown to reproduce the relevant p_{T} and $E_{\mathrm{T}}^{\mathrm{miss}}$ distributions of the irreducible $t\bar{t}$ background with an uncertainty of only 10%.
  However, for a realistic determination of the τ-jet identification efficiency the replacement of the muon has to be performed at the level of the constituents of the physics objects. In this study calorimeter cells and inner detector tracks assigned to the τ-jets are investigated:
  - First, one of the reconstructed muons in a $t\bar{t} \to \mu\mu$+X event is selected by searching for a simulated single τ-jet within a cone of radius $\Delta R = 0.1$. If no matching τ-jet is not found, the event is discarded.
  - The energy deposition and timing information of the calorimeter cells in a cone with radius $\Delta R = 0.5$ around the combined muon track are replaced by the information of the corresponding cells of the single τ-jet event.
  - Afterwards all track segments in a cone with radius $\Delta R = 0.1$ around the muon track in the muon spectrometer are deleted from the $t\bar{t}$ event.
  - Similarly the inner detector and muon spectrometer tracking information associated with the selected muon is removed and the tracks belonging to the single τ-jet are added to the $t\bar{t}$ event.

- Finally, all reconstruction algorithms except the track reconstruction are run on the merged $t\bar{t}$ events and the reconstruction of higher-level physics objects is repeated. The track reconstruction could not be re-run since this requires the embedding of inner detector hits which is technically challenging and not yet implemented [86].

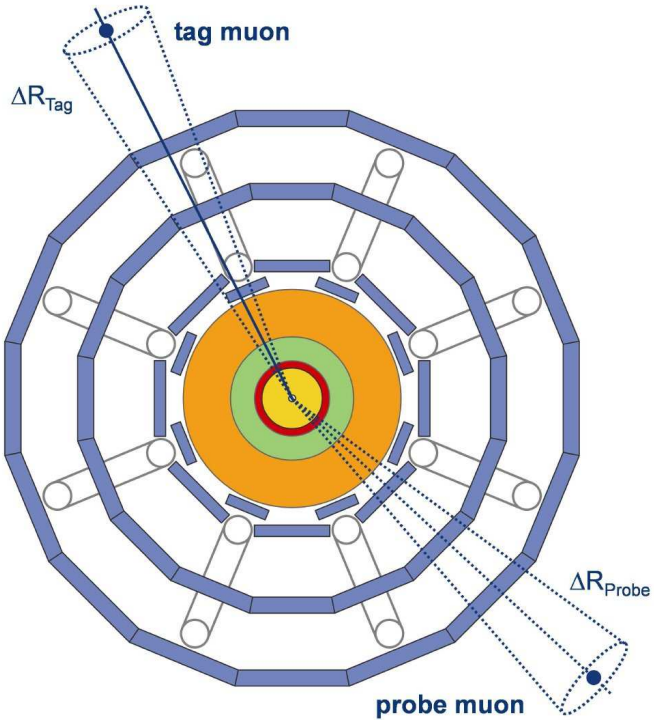

Figure 8.2: The tag-and-probe method: one muon (the tag-muon from a $Z \to \mu\mu$ decay) is used to select the event while the muon reconstruction efficiency is obtained independently from the second muon (probe-muon) [87].

8.2 Validation of the Embedding Method

8.2.1 Distributions of Variables for $H^{\pm}$ Searches

In order to provide an accurate description of the irreducible $t\bar{t}$ background for light charged Higgs boson searches, the distributions of relevant variables for the irreducible $t\bar{t}$ background $t\bar{t} \to (Wb)\left(W\bar{b}\right) \to (\tau_{\text{had}}\nu b)\left(\ell\bar{\nu}\bar{b}\right)$ have to be well reproduced by the control sample. In the following these distributions are compared between the direct background sample and the control sample by calculating their ratio. The events of both samples are required to contain one reconstructed isolated muon with transverse momentum $p_{\text{T}} > 10\,\text{GeV}$.
The measurement of the efficiency of the muon trigger and offline muon reconstruction is possible from data by employing the *tag-and-probe* method, illustrated in Figure 8.2. This method uses events with $Z \to \mu\mu$ decays with a well reconstructed muon track of high quality which tags the event. A second track, reconstructed in the inner detector, is selected if the invariant mass of the two tracks is compatible with the Z boson mass. The corresponding track in the muon spectrometer, called probe-muon, is known to correspond to a genuine muon and can be used to measure the trigger and offline reconstruction efficiencies in $Z \to \mu\mu$ events. It has been shown that the efficiencies obtained can be applied to $t\bar{t} \to \mu\mu$+X events with high jet multiplicity by re-weighting

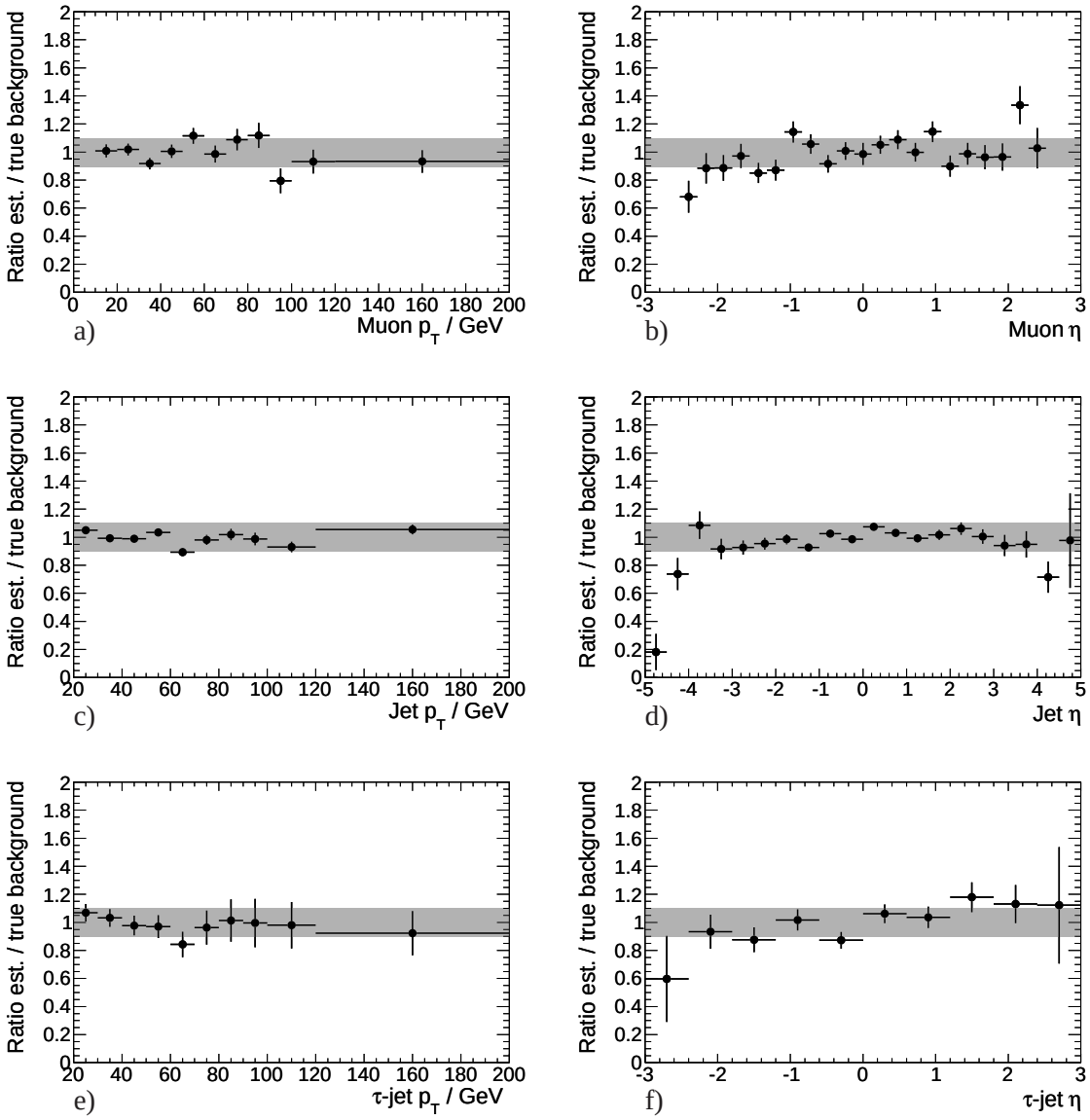

Figure 8.3: Ratios of the normalized p_{T} and η distributions of reconstructed muons, jets and τ-jets in the control sample and the direct $t\bar{t}$ background simulation.

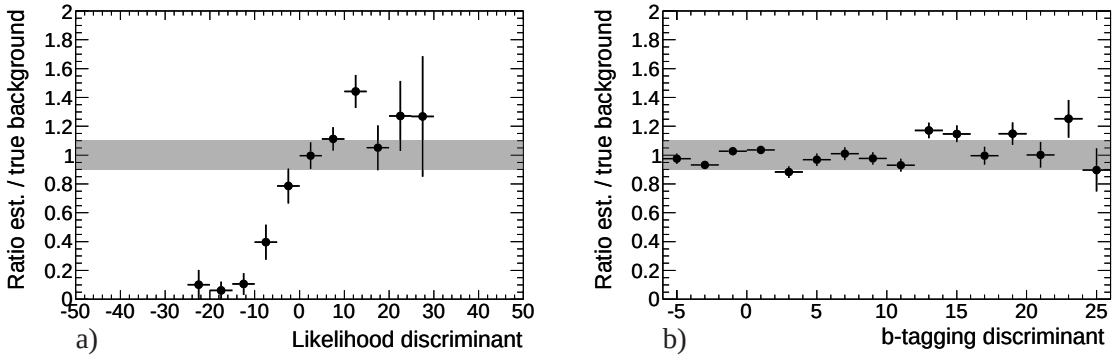

Figure 8.4: Ratios of the likelihood discriminants for (a) τ-jet and (b) b-jet identification for the control sample with respect to the direct $t\bar{t}$ background simulation

the p_{T} and η distributions of the probe-muon [87].
To compare the shapes of the relevant distributions from the direct $t\bar{t}$ background simulation (reference) and the control sample generated with the embedding method, all distributions are normalized to one. Except for the p_{T} cut for the muon no cuts are applied.
The p_{T} and η distributions of muons and jets are in good agreement (see Figures 8.3(a), 8.3(b) and 8.3(c), 8.3(d)). A higher number of τ-jets is observed in the control sample at low transverse momenta compared to the reference sample (see Figures 8.3(e) and 8.3(f)) which is due to τ-jets originating from from replaced secondary muons from the process $W \rightarrow \tau\nu \rightarrow \mu\nu\bar{\nu}$. When selecting the control sample, only direct muons from the process $W \rightarrow \mu\nu$ correctly emulate $W \rightarrow \tau\nu$. However, an unambiguous identification of leptonic τ decays is impossible and such secondary muons cannot be rejected.
In Figure 8.4(a) the distributions of the likelihood discriminants of the embedded τ-jets and the reference τ-jets from the genuine $t\bar{t}$ background events are compared (see Figures 8.4(a)). A shift towards higher values is observed in the control sample such that the efficiency is systematically overestimated (see Figure 8.6(a)). A similar effect is seen when the "safe cuts" method is applied for τ-jet identification (see Figure 8.6(c)).
One reason for this deviation is the missing re-reconstruction of the tracks after the embedding of the τ-jets in the $t\bar{t}$ events. Especially in $t\bar{t}$ events with high jet multiplicity a deterioration of the tracking performance is expected. In addition, since the energy deposits in the calorimeter cells around the original muon are replaced by the corresponding values from the single τ-jet events, contributions from the underlying event and other hadronic activity are not taken into account. Therefore the efficiency of τ-jet identification is biased to higher values in the control sample. The misidentification rates are in good agreement for both identification methods (see Figures 8.6(b) and 8.6(d)).
No deviations between control and reference sample are observed for the b-tagging discriminant (Figure 8.4(b)), and also the distributions of the sum of the charges of the muon and of the τ-jet (Figure 8.5(a)) and of the missing transverse energy $E_{\mathrm{T}}^{\mathrm{miss}}$ (Figure 8.5(b)) are well reproduced by the control sample within the statistical uncertainty.

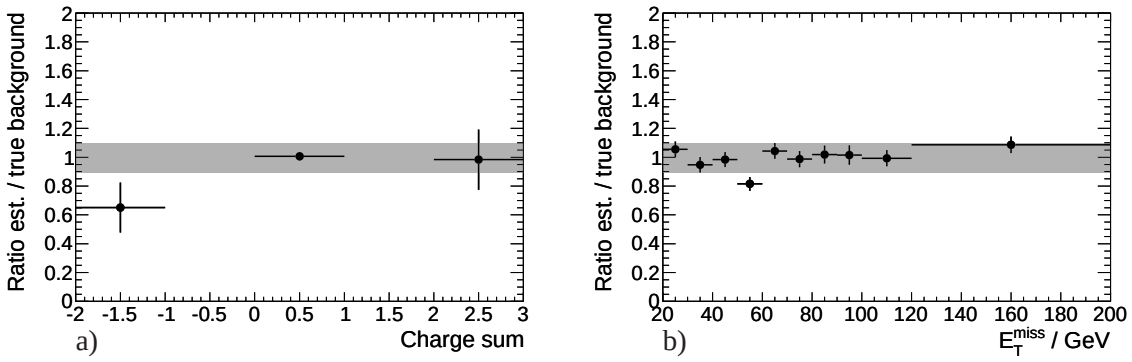

Figure 8.5: Ratios of the sum of the charges of (a) τ-jet and muon and of (b) the missing transverse energy for the control sample and the direct $t\bar{t}$ background simulation

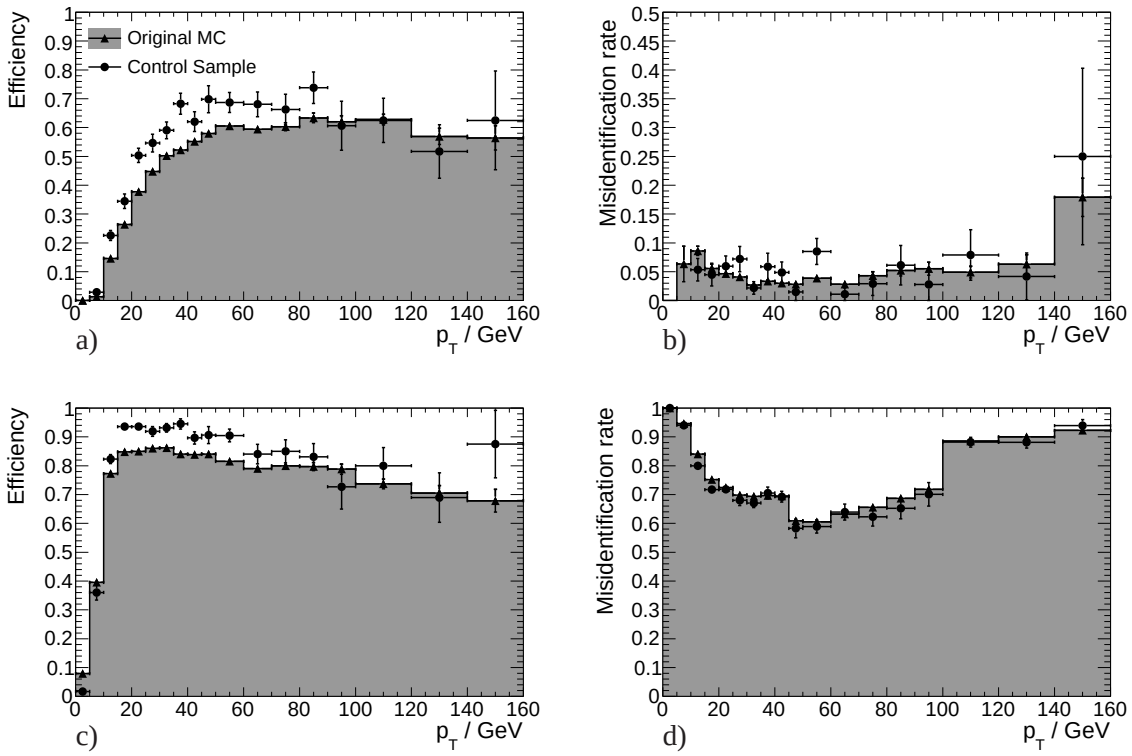

Figure 8.6: (a) τ-jet identification efficiency and (b) misidentification rate obtained with the likelihood based identification and (c,d) the "safe-cuts" method in the control sample (black circles) and the direct $t\bar{t}$ background simulation (shaded histogram and triangles). For both τ-jet identification the loose flag has been used.

Table 8.1: Fractions of events in the control and the reference sample after applying the signal selection cuts given in the text. In the last column the ratio of both fractions is given for each cut.

Cut	Control sample	Reference sample	Control / Reference
1 Muon	0.980 ± 0.023	1.000 ± 0.006	0.980 ± 0.023
3 Jets	0.783 ± 0.020	0.809 ± 0.005	0.968 ± 0.025
1 τ-jet	0.316 ± 0.011	0.276 ± 0.003	1.146 ± 0.040
1 b-jet	0.258 ± 0.009	0.223 ± 0.002	1.154 ± 0.044
τ-jet p_{T}	0.195 ± 0.008	0.171 ± 0.002	1.145 ± 0.049
Charge sum	0.191 ± 0.008	0.166 ± 0.002	1.150 ± 0.049
$E_{\mathrm{T}}^{\mathrm{miss}}$	0.146 ± 0.007	0.126 ± 0.002	1.154 ± 0.056

8.2.2 Cut Evolution

To determine the accuracy of the background estimation, the charged Higgs signal selection cuts are applied to the control and to the reference sample. Because of the limited Monte Carlo statistics, the requirements on the transverse momentum of the τ-jets and on the missing transverse energy are reduced to $p_{\mathrm{T}} > 30\,\mathrm{GeV}$ and $E_{\mathrm{T}}^{\mathrm{miss}} > 40\,\mathrm{GeV}$, respectively. Furthermore the τ-jet candidates are identified using the loose likelihood discriminant criterium. The remaining cuts are the same as the ones in Chapter 7.
In Table 8.1 the fractions of events in the control and in the reference sample left after applying each cut are given. In the last column, the ratios of the fractions for both samples are given.
After applying all cuts the background is systematically overestimated by about 15% with the control sample, mainly due to the biased efficiency of the τ-jet identification.

8.3 Conclusions

In this chapter it has been shown that the embedding method is a powerful tool to estimate the contribution of the irreducible background $t\bar{t} \rightarrow (Wb)\left(W\bar{b}\right) \rightarrow (\tau_{\mathrm{had}}\nu b)\left(\ell\bar{\nu}\bar{b}\right)$. The distributions of all discriminating variables except for the τ-jet identification likelihood discriminant are described with high precision. The efficiencies of the event selection reproduced by the control sample are within the statistical uncertainties. Room for improvement is in the modeling of the τ-jets in the control sample. Since the embedded single τ-jets are lacking the hadronic environment of $t\bar{t}$ events and their tracks are not again re-reconstructed after the embedding, the current procedure overestimates the background by about 15%.
The accuracy of the embedding method can be increased by performing the embedding already at the level of the inner detector hits. Then the track reconstruction can be performed again after the embedding and a more realistic description of the tracking performance in $t\bar{t}$ events is obtained. For the calorimeter information a more sophisticated procedure is to consider those calorimeter cells belonging to the topological cluster of the τ-jet, instead of using a cone. In this way the tails of the calorimeter shower are taken into account and the number of manipulated cells is kept as low as possible. A third possible improvement is to add the energy in the calorimeter cells associ-

ated to the embedded τ-jet to the energies of the corresponding cells in the original event instead of replacing them. For this approach the noise has to be switched off in the simulation of the single τ-jets and the energy deposit of the muon has to be subtracted. In this way the energy from the underlying event and other activity in the vicinity of the τ-jet is taken into account as well. With these improvements a systematic uncertainty of 10% can be realized which has been assumed for the cut optimization in Chapter 7 as well as for the calculation of the charged Higgs search limits in Section 10.

Chapter 9

Estimation of the $t\bar{t}$ Background Containing Misidentified τ-Jets

Due to the high jet multiplicity in $t\bar{t}$ events a considerable part of the Standard Model $t\bar{t}$ background is expected to be caused by light parton (u, d, s quark and gluon) jets misidentified as τ-jets. To estimate this background from the data, the following method is used: First the efficiency and light parton jet rejection of the τ-jet identification algorithm are measured for $t\bar{t}$ events which are then used to weight all reconstructed jets (τ-jet candidates) according to the probability that they would be correctly or falsely identified. For the measurement of the light parton jet rejection Z+jets events with Z decays to $\mu\mu$ or ee and QCD dijet events are used as unambiguous sources of jets.
In Section 9.1 the Monte Carlo samples used in this study are described. The measurement of the rejection of light parton jets is discussed in Section 9.2. Finally, the results for the background estimation from data are given in Section 9.3.

9.1 Monte Carlo Samples

In Table 9.1 the Monte Carlo data samples used in this study are summarized. They have been generated with a center of mass energy of 10 TeV. The Z+jets W+jets events have been generated with ALPGEN [63], corresponding to an integrated luminosity of about $250\,\text{pb}^{-1}$. To estimate the purity of the Z+jets selection the following backgrounds have been taken into account. W+jets and $Z \to \tau\tau$ events have been generated using ALPGEN as well with comparable statistics as the signal. The HERWIG generator [64] was used for diboson ZZ and WZ production while the $t\bar{t}$ background has been generated with MC@NLO [67]. For the generation of QCD dijet and $b\bar{b}$ events PYTHIA was used [62].
The tree-level Feynman diagrams for the Z+jets, W+jets and diboson production processes are shown in Figures 9.1 and 9.2.

Table 9.1: Monte Carlo samples of Z+jets, $Z \to \ell\ell$, relevant background processes and QCD dijet events (p=partons). For the Z+jets samples a filter requires an invariant mass larger than 60 GeV, in the samples generated with ALPGEN the transverse momentum of the outgoing partons is required to be larger than 20 GeV. In the diboson sample a lepton filter has been applied requiring $p_{\mathrm{T}} > 10$ GeV within $|\eta| < 2.8$. In the $b\bar{b}$ sample the p_{T} of one b quark must be larger than 7 GeV and within $|\eta| < 4.5$, in addition the p_{T} of the two muons must be larger than 6 GeV and 4.5 GeV, respectively, and within $|\eta| < 2.5$. Finally, in the QCD dijet sample $p_{\mathrm{T}} > 17$ GeV and $|\eta| < 2.5$ was required for one of the outgoing partons.

Dataset Id	Generator	Channel	N_{Events} /1000	$\int \mathcal{L}$ /pb^{-1}
Z+jets signal				
107650	ALPGEN	$Z \to ee$+0p	269	246
107651	ALPGEN	$Z \to ee$+1p	62	245
107652	ALPGEN	$Z \to ee$+2p	214	2422
107653	ALPGEN	$Z \to ee$+3p	63	2463
107654	ALPGEN	$Z \to ee$+4p	18	2502
107655	ALPGEN	$Z \to ee$+5p	6	2651
107660	ALPGEN	$Z \to \mu\mu$+0p	270	246
107661	ALPGEN	$Z \to \mu\mu$+1p	62	246
107662	ALPGEN	$Z \to \mu\mu$+2p	198	2331
107663	ALPGEN	$Z \to \mu\mu$+3p	46	1764
107664	ALPGEN	$Z \to \mu\mu$+4p	18	2480
107665	ALPGEN	$Z \to \mu\mu$+5p	5	2637
Z+jets backgrounds				
107690	ALPGEN	$W \to e\nu$+0p	1171	94
107691	ALPGEN	$W \to e\nu$+1p	262	102
107692	ALPGEN	$W \to e\nu$+2p	776	941
107693	ALPGEN	$W \to e\nu$+3p	224	903
107694	ALPGEN	$W \to e\nu$+4p	54	787
107695	ALPGEN	$W \to e\nu$+5p	18	864
107690	ALPGEN	$W \to \mu\nu$+0p	1299	105
107691	ALPGEN	$W \to \mu\nu$+1p	262	100
107692	ALPGEN	$W \to \mu\nu$+2p	780	936
107693	ALPGEN	$W \to \mu\nu$+3p	223	905
107694	ALPGEN	$W \to \mu\nu$+4p	59	870
107695	ALPGEN	$W \to \mu\nu$+5p	17	843
107670	ALPGEN	$Z \to \tau\tau$+0p	271	246
107671	ALPGEN	$Z \to \tau\tau$+1p	63	246
107672	ALPGEN	$Z \to \tau\tau$+2p	211	2456
107673	ALPGEN	$Z \to \tau\tau$+3p	64	2467
107674	ALPGEN	$Z \to \tau\tau$+4p	19	2511
107675	ALPGEN	$Z \to \tau\tau$+5p	6	2626
105200	MC@NLO	$t\bar{t} \to \ell$+X	1468	6746
105986	HERWIG	ZZ	10	7369
105987	HERWIG	WZ	10	2680
108412	PYTHIAB	$b\bar{b} \to \mu\mu$+X	1000	15.3
QCD dijets signal (and background for $Z \to ee$, but neglected)				
105802	PYTHIA	QCD dijets	9600	0.09

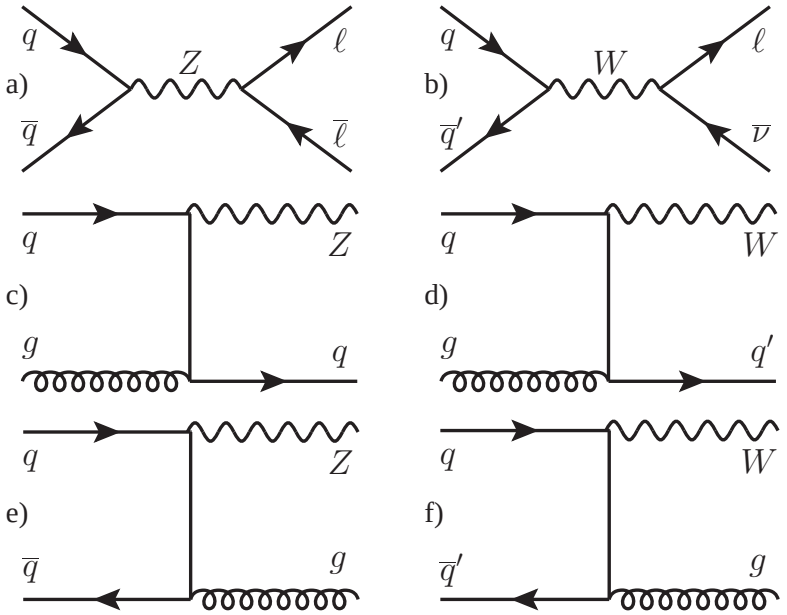

Figure 9.1: Tree-level Z and W production processes: (a) and (b) Drell-Yan production with leptonic decays, (c),(d),(e) and (f) associated production with light parton jets.

9.2 Data-Driven Estimation of the Light Parton Jet Rejection

In the following a method is introduced for measuring the light parton jet rejection using collision data. The rejection of light parton jets (originating from u, d, s quarks and gluons), especially of quark jets by the τ-jet identification is of highest interest for the $H^{\pm}$ searches since the background from quark jets faking τ-jets in Standard Model $t\bar{t}$ events is expected to dominate.
A direct measurement of the light parton jet rejection in $t\bar{t}$ events is not possible since the nature of the τ-jet candidates cannot be identified in these events. Therefore other processes are used where this is the case. The first attempt of measuring the rejection uses jets from QCD dijet production. Because of the very large cross section of this process a sizable sample will be available already in the early phase of LHC running.
While jets in QCD dijet events are mainly from gluons, additional processes are needed to measure the rejection of jets originating from quarks. Gluons carry a larger color charge than quarks and are more likely to radiate gluon bremsstrahlung. Thus the fragmentation of gluon jets starts earlier and their track multiplicity is higher than it is the case for quark jets of the same energy and their showers in the calorimeter are wider [88, 89]. Since the identification of τ-jets makes use of their narrow shower shape and low track multiplicity, a higher rejection is expected for gluon jets than for quark jets.
Once an integrated luminosity of about $100\,\mathrm{pb}^{-1}$ has been collected at a center-of-mass energy of 10 TeV, other processes with enriched light quark jet content like Z+jets or γ+jets production can be used in addition to measure the light quark jet rejection. In this study, a method using Z+jets

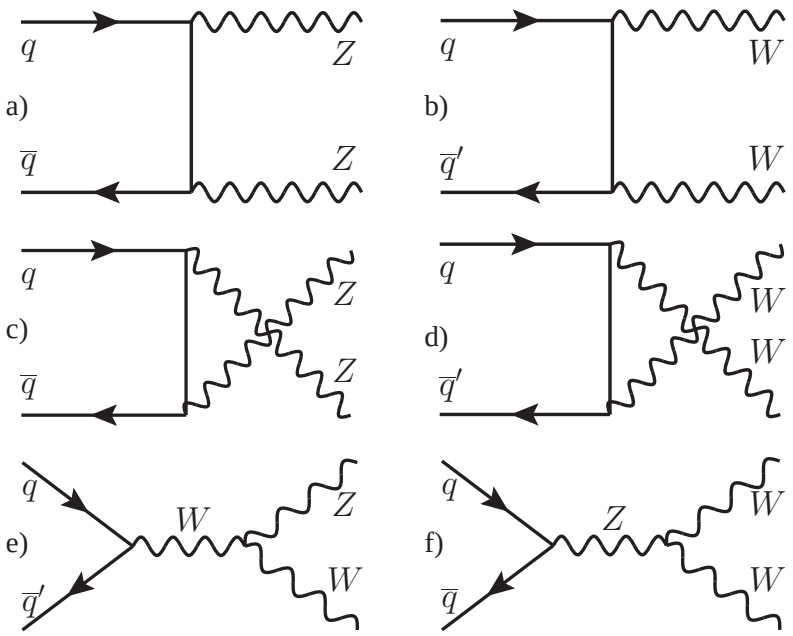

Figure 9.2: Tree-level ZZ, WW and WZ production processes: (a) and (b) t-channel, (c) and (d) u-channel, (e) and (f) s-channel production.

events is investigated and the resulting rejection is compared with the one obtained from QCD dijet events. The selection criteria for both processes are described in Section 9.2.1 and 9.2.2
Since the background is supposed to be estimated from the data, no generator information is used for measurement of the rejection rate. Knowledge about the nature of the τ-jet candidates can be obtained from the kinematical structure of the events, provided that the background is low.
The observed differences between the rejections derived from Z+jets and QCD dijet events can be traced back to the differences between the distributions of the discriminating variables used for τ-jet identification caused by the different properties of quark and gluon jets. Choosing an appropriate parameterization of the rejection, the differences of the results obtained from quark and gluon jet dominated processes are minimized leading to an almost process independent result. In order to find an optimal parameterization the rejections measured with Z+jets data are compared with those from QCD dijet events as a function of the parameters. As reference the light parton jet rejection in $t\bar{t}$ events determined from Monte Carlo truth information is used. An optimal parameterization should provide good agreement of the rejections determined for all three processes.

9.2.1 Selection of QCD Dijet Events

A detailed study of the rejection measurement with QCD dijet events can be found in [42]. QCD dijet events are selected by requiring at least two jets in the final state: One jet triggers the event while the second jet is opposite to the first one in p_{T}. Such events are produced at very high rates

exceeding all other processes involving τ-jet production by several orders of magnitude.
Although the trigger selection can potentially introduce a significant bias on the properties of the second jet, the trigger simulation has so far not been used for the comparison with Z+jets and $t\bar{t}$ events. To account for the filter requirement for the partons ($p_{\mathrm{T}} > 20\,\mathrm{GeV}$, see Table 9.1) the p_{T} cut for the jets is chosen to be 20 GeV. Furthermore, only jets within the acceptance of the inner detector $|\eta| < 2.5$ are selected and the azimuthal angle $\Delta\phi$ between the two jets is required to be larger than 2.7 rad. For the p_{T}-balance of the two jets the difference Δp_{T} of the transverse momenta of the two jets has to fulfill $\Delta p_{\mathrm{T}} < p_{\mathrm{T}}^{\mathrm{max}}/2$, where $p_{\mathrm{T}}^{\mathrm{max}}$ is the maximum transverse momentum of the two jets.

9.2.2 Selection of Z+Jets Events

A data sample enriched with light quark jets is obtained from Z+jets production with leptonic Z decays. Muonic decays of the Z bosons are triggered by a single muon trigger with threshold of 20 GeV. The offline muon reconstruction and the isolation requirement are applied as described in Section 6.2.1. The invariant mass of the two leading muons with opposite charge has to be within a mass window of $81\,\mathrm{GeV} < m_{\mu\mu} < 121\,\mathrm{GeV}$ around the Z boson mass. Events with Z boson decays into electron pairs are triggered by a single or double electron trigger with thresholds of 25 GeV and 15 GeV, respectively. The electrons are identified requiring the tight quality flag, the isolation criterium is applied as in Section 6.2.2. As will be seen in the following, the rather strict electron selection is needed for a reliable rejection measurement. As for the muon selection, the two electrons are required to be oppositely charged and consistent with the Z boson mass. Both muons and electrons have to be reconstructed within $|\eta| < 2.5$ corresponding to the acceptance of the tracking detectors. The p_{T} cuts of 20 GeV and 25 GeV for muons and electrons, respectively, correspond to the thresholds of the single lepton triggers. Finally, the accompanying jets have to be reconstructed with $p_{\mathrm{T}} > 20\,\mathrm{GeV}$ and within $|\eta| < 2.5$ by both τ-jet reconstruction algorithms.
The backgrounds to the Z+jets selection are listed in Table 9.1. In the mass window around the Z peak the background contamination is very low (see Figure 9.3(a)). From the numbers in Table 9.2 a signal-to-background ratio after the selection of $S/B = 65$ is calculated for the dimuon final state. For the dielectron final state, the ratio $S/B = 37$ is achieved neglecting the additional QCD dijet background. When requiring a τ-jet candidate to satisfy the likelihood discriminant ("safe cuts") identification criteria, the signal-to-background ratio increases to 141 (147) for muonic decays. For decays to electrons S/B of 71 (81) is obtained neglecting the QCD dijet background. Therefore, especially for the dimuon final state, the background is very low. It should be mentioned that jets in background events do not necessarily bias the rejection measurement since only a small fraction stems from τ leptons. The potentially most dangerous backgrounds are due to $WZ \to \ell\ell\tau\nu$ and $ZZ \to \ell\ell\tau\tau$ with one τ lepton decaying hadronically. However, the branching ratio of the above decays is only about 5%. Hence, the background to Z+jets events is neglected in the following for the rejection measurement of the τ-jet identification. If not mentioned otherwise, only the $\mu\mu$ final state is considered.

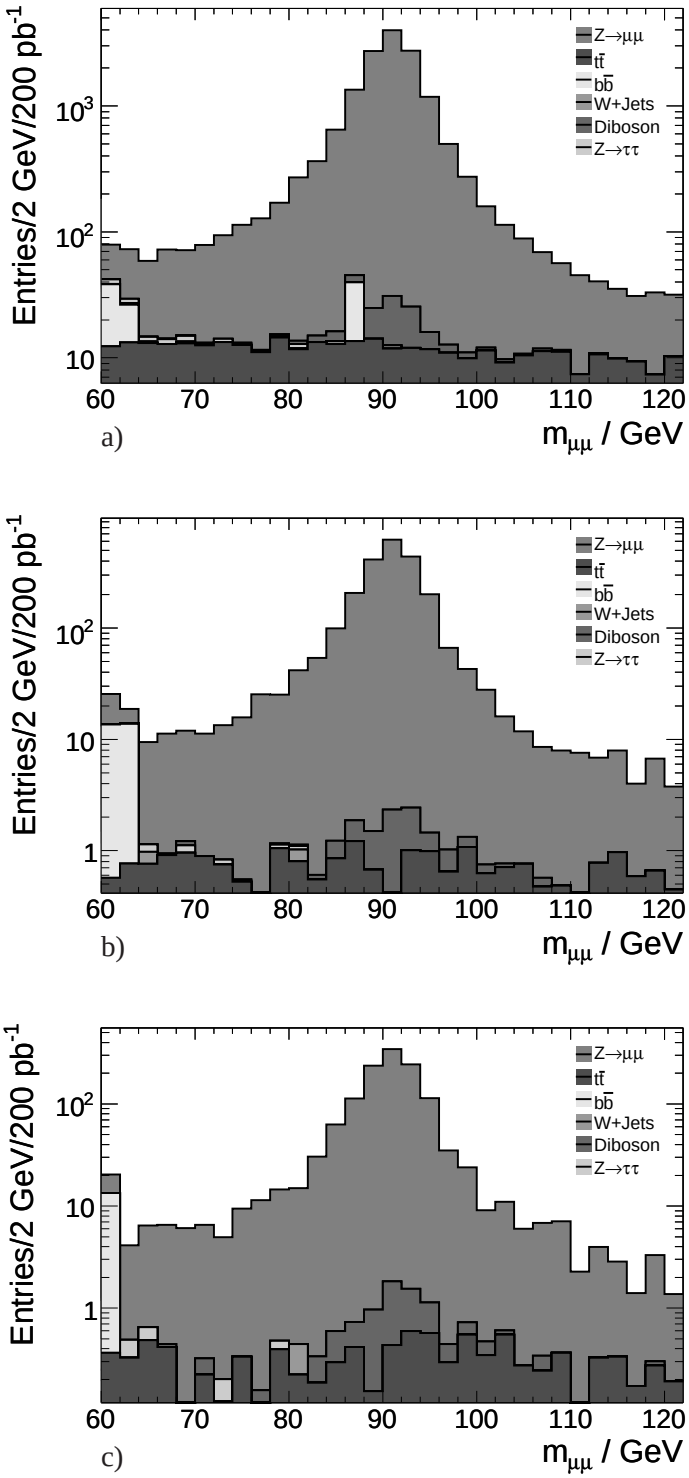

Figure 9.3: Dimuon invariant mass distribution after the Z+jets selection cuts (a) for all jets (e.g. τ-jet candidates), (b) for τ-jet candidates identified using the medium flag of the "safe cuts" identification and (c) for τ-jet candidates identified using the medium flag of the likelihood discriminant identification. There is one entry for each jet.

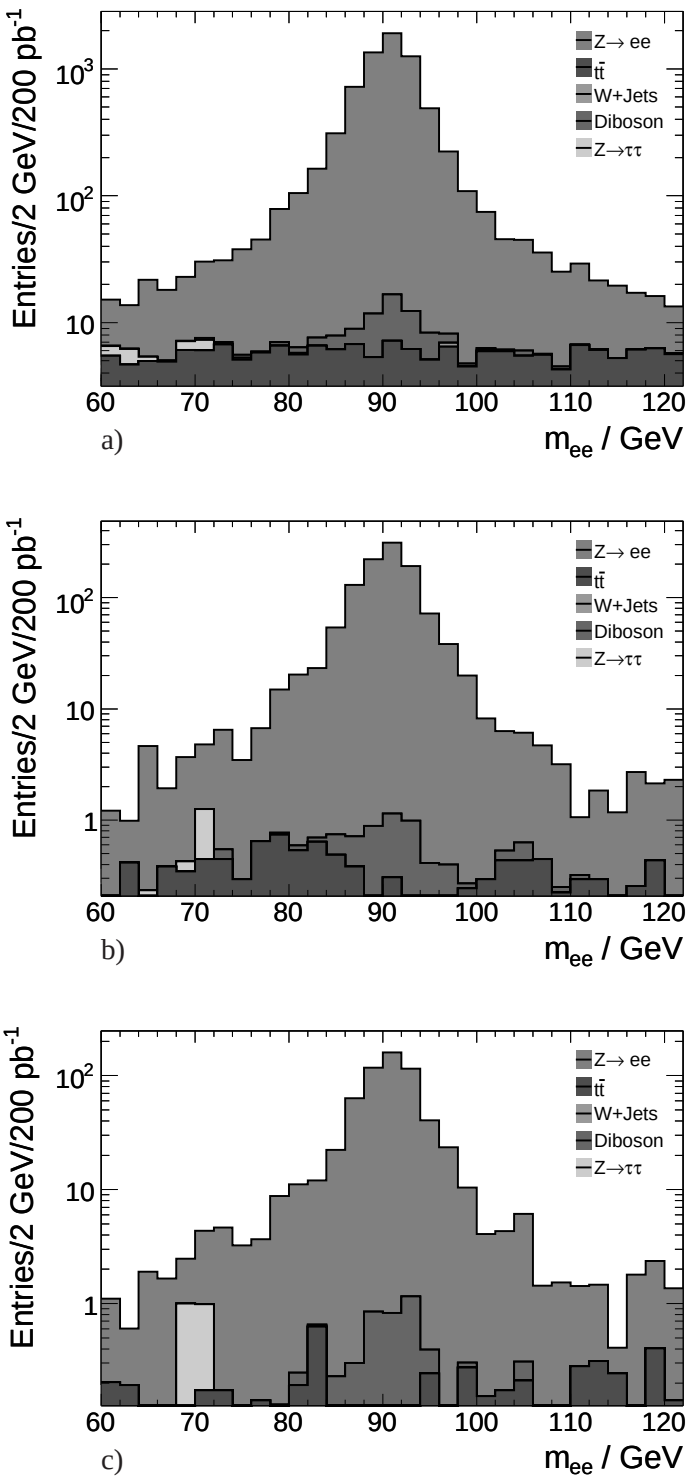

Figure 9.4: Dielectron invariant mass distribution after the Z+jets selection cuts (a) for all (e.g. τ-jet candidates), (b) for τ-jet candidates identified using the medium flag of the "safe cuts" based identification, (c) for τ-jet candidates identified using the medium flag of the likelihood discriminant identification. Each probe jet has one entry.

Table 9.2: Numbers of signal and background events after each cut for the dimuon final state corresponding to a luminosity of 200 pb^{-1} and a center-of-mass energy of 10 TeV.

Channel	All events	μ Trigger	$\mu\mu$ sel.	opp. charge	≥ 1 jet
$Z \to \mu\mu$	293825	195324	107025	107023	19814.5
$t\bar{t} \to \ell$+X	43520	11618.1	552	537.2	516.2
$b\bar{b} \to 2\mu$+X	13080000	244985	887.1	821.8	430.5
$W \to \mu\nu$	3230076	1396340	30.56	27.1	11.4
$Z \to \tau\tau$	295472	11930.4	251	251	51.9
Diboson	1245	391.5	95.8	91.5	63.2

Table 9.3: Numbers of signal and background events (two left columns) and numbers of τ-jet candidates (two right columns) in the Z mass region for the two muon final state before and after τ-jet identification corresponding to 200 pb^{-1} and 10 TeV center-of-mass energy.

Channel	Events			τ-jet candidates		
	Z Mass window	$\geq 1\tau$-jet Llh	Cuts	Z Mass window	$\geq 1\tau$-jet Llh	Cuts
$Z \to \mu\mu$	11579.7	1339.9	2400	13777.7	1350.4	2445
$t\bar{t} \to \ell$+X	70.3	3	6.9	123.3	3.1	7.2
$b\bar{b} \to 2\mu$+X	13	–	–	26.1	–	–
$W \to \mu\nu$	0.7	–	–	1.7	–	–
$Z \to \tau\tau$	0.9	–	–	0.9	–	–
Diboson	43.3	6.2	8.7	60.4	6.5	9.4

Table 9.4: Numbers of signal and background events after each cut for the dielectron final state corresponding to a luminosity of 200 pb^{-1} and a center-of-mass energy of 10 TeV.

Channel	All events	e Trigger	ee sel.	opp. charge	≥ 1 jet
$Z \to ee$	294288	186897	50074.5	49860.4	9299.1
$t\bar{t} \to \ell$+X	43520	11495.5	262.2	260.1	255.1
$W \to e\nu$	3232760	1329640	6	1.2	0.7
$Z \to \tau\tau$	295472	10517	47.6	46.8	12
Diboson	1245	386.1	50.5	48.1	35

Table 9.5: Numbers of signal and background events (two left columns) and numbers of τ-jet candidates (two right columns) in the Z mass region for the two muon final state before and after τ-jet identification corresponding to 200 pb^{-1} and 10 TeV center-of-mass energy.

Channel	Events			τ-jet candidates		
	Z Mass window	$\geq 1\tau$-jet Llh	Cuts	Z Mass window	$\geq 1\tau$-jet Llh	Cuts
$Z \to ee$	5478.4	639.1	1194.4	6530.6	644.7	1221.6
$t\bar{t} \to \ell$+X	33.7	2	11.6	59.9	2	3.1
$W \to e\nu$	0.2	–	–	0.5	–	–
$Z \to \tau\tau$	0.2	–	0.1	0.3	–	0.1
Diboson	23.6	4.4	4.8	32.2	4.5	5.1

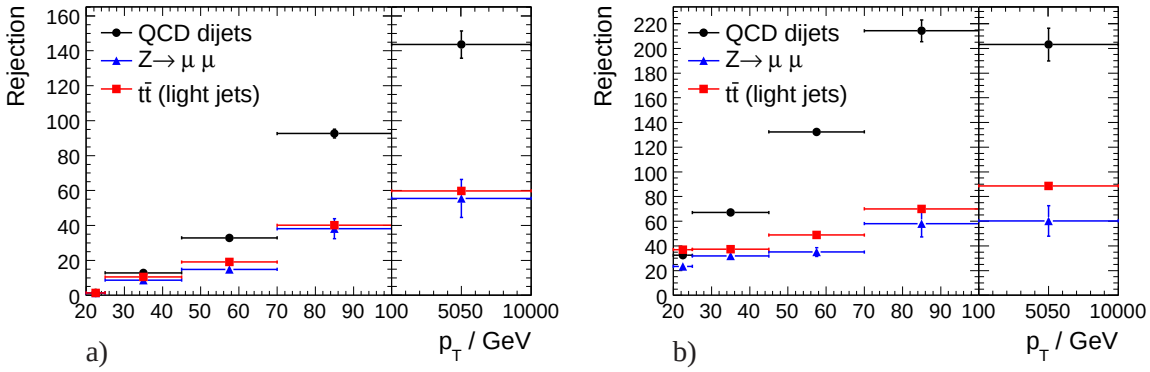

Figure 9.5: Rejection of light parton jets by the medium quality flag of the τ-jet identification with "safe cuts" and likelihood discriminant in QCD dijet (black circles), $Z \rightarrow \mu\mu$+jets (blue triangles) and $t\bar{t}$ events (red squares). The error bars of the QCD dijet and $t\bar{t}$ correspond to the available Monte Carlo statistics while they correspond to an integrated luminosity of $200\,\mathrm{pb}^{-1}$ for Z+jets events.

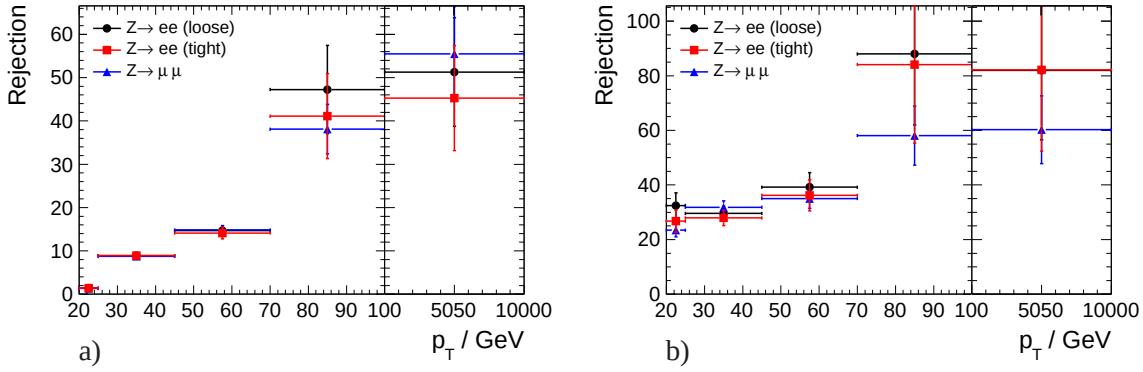

Figure 9.6: Rejection of light parton jets by the medium quality flag of the τ-jet identification with "safe cuts" and likelihood discriminant in $Z \rightarrow ee$+jets using loose and tight selected electrons (circles and squares) as well as $Z \rightarrow \mu\mu$+jets (blue triangles) events. The error bars correspond to an integrated luminosity of $200\,\mathrm{pb}^{-1}$.

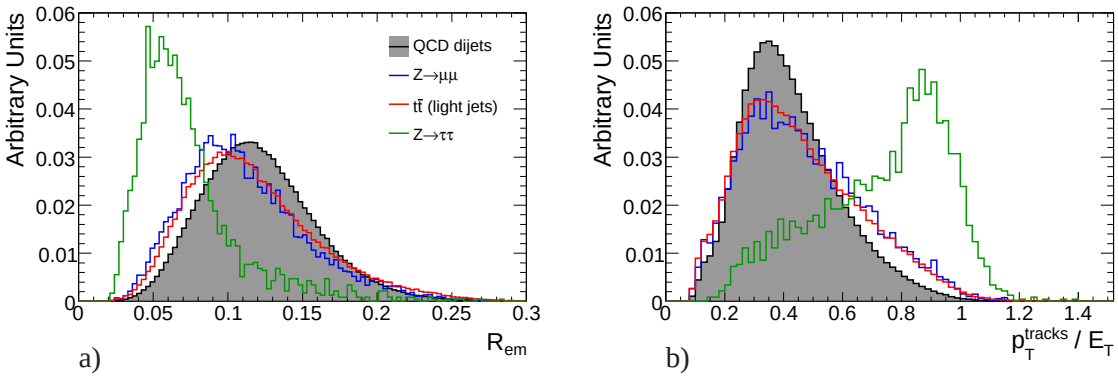

Figure 9.7: Normalized distributions of (a) EM-radius R_{em} and (b) $p_{\text{T}}^{\text{tracks}}/E_{\text{T}}$ distributions for τ-jet candidates with $45\,\text{GeV} < p_{\text{T}} < 70\,\text{GeV}$ in QCD dijet (shaded histogram), Z+jets (blue histogram) and $t\bar{t}$ (red histogram) events. For comparison, also the distributions for real τ-jets from $Z \rightarrow \tau\tau$ events (green histogram) are shown.

9.2.3 Results of the Data-Driven Rejection Measurement in p_{T} Bins

Using the above selection criteria, the rejections are calculated as a function of the p_{T} of light parton jets in QCD dijet and Z+jets events. The p_{T}-bins are chosen as for the "safe cuts" identification method (see Section 6.2.5). The medium quality flags of both identification methods are required. The results (see Figure 9.5) are compared to the reference values obtained from $t\bar{t}$ events using the Monte Carlo truth information and excluding heavy quark jets. For both τ-jet identification methods the rejection of jets from QCD dijet events is much higher than the rejection of jets from Z+jet events. As discussed in Section 9.2 this is expected because of the different jet shapes of quark and gluon jets. Also, Z+jets events show lower jet rejection compared to $t\bar{t}$ events.
The error bars of the rejection measurements for Z+jets events correspond to an integrated luminosity of $200\,\text{pb}^{-1}$. For QCD dijet and $t\bar{t}$ events they reflect the statistics of the Monte Carlo samples which correspond to $0.09\,\text{pb}^{-1}$ and $9147\,\text{pb}^{-1}$, respectively.
In Figure 9.6 the rejections measured in $Z \rightarrow ee$+jets and $Z \rightarrow \mu\mu$+jets events are compared. For the electrons results are shown for different *electron* identification criteria, e.g. the loose and tight electron identification. For the τ-jet identification with "safe cuts" agreement is found. When employing the likelihood discriminant, the sample with the loosely selected electrons shows slightly higher rejection than the sample with two muons, especially at low p_{T} (see Figure 9.6(b)). When switching to the tight electron selection a better agreement is achieved. However, since the statistics is limited, the further study is restricted to $Z \rightarrow \mu\mu$+jets events which provide a cleaner and unbiased probe sample. The corresponding results for electrons and for combinated Z+jets samples are shown in Appendix A.

9.2.4 Jet Shapes in Z+Jets and QCD Dijet Events

The differences between the rejections measured in QCD dijet and Z+jets events can be traced to the discriminating variables used for τ-jet identification. In Figure 9.7 the distributions of two

of the discriminating variables, the electromagnetic jet (EM) radius R_{em} and the ratio $p_{\text{T}}^{\text{tracks}}/E_{\text{T}}$ are shown for different processes. The EM-radius R_{em}, defined in Equation (6.3), is a measure of the shower shape while the ratio $p_{\text{T}}^{\text{tracks}}/E_{\text{T}}$ involves tracking information (see Equation (6.12)). Deviations are visible in other variables as well, but these were found to be correlated with R_{em} or $p_{\text{T}}^{\text{tracks}}/E_{\text{T}}$.
The deviations from the distributions for $t\bar{t}$ events are stronger for QCD dijet events than for Z+jets events. These observations can be explained by the differences between quark and gluon jets as discussed in Section 9.2. The shower shape variable R_{em} is different for quark and gluon jets. The variable $p_{\text{T}}^{\text{tracks}}/E_{\text{T}}$ is sensitive to the track multiplicity which is different for quark and gluon jets.

9.2.5 Jet Shape Dependence of the Rejection

The estimation of the background is only possible if the rejection of light parton jets is known for $t\bar{t}$ events. To take into account the differences discussed in Section 9.2.4, the rejection is measured as a function of the EM-radius R_{em} and $p_{\text{T}}^{\text{tracks}}/E_{\text{T}}$ in addition to the jet p_{T}. For the "safe cuts" method the R_{em} bins are chosen according to the cut values in the identification. The p_{T}, R_{em} and $p_{\text{T}}^{\text{tracks}}/E_{\text{T}}$ bins chosen are shown in Table 9.6. Two bins are employed to distinguish between single and multi-prong jets, in a third bin all jets rejected by the τ-jet identification are collected. Where enough statistics is available the bins are further divided. For the rejection measurement for the likelihood discriminant method, R_{em} and $p_{\text{T}}^{\text{tracks}}/E_{\text{T}}$ bins independent of p_{T} are chosen (see Table 9.6).
The rejection in the first R_{em} bin is shown in Figure 9.8(a) for the "safe cuts" identification. Good agreement between the different jet samples is found for all p_{T} bins. In Figure 9.8(b) the rejection of the likelihood discriminant method is shown for the middle R_{em} bin $(0.07 < R_{\text{em}} < 0.09)$. The results for Z+jets events suffer from low statistics for $p_{\text{T}} > 70\,\text{GeV}$ but agree well with the results for $t\bar{t}$ events. The rejection measured in QCD dijet events is systematically higher.
In Figure 9.9 the rejections of the likelihood method are compared with three dimensional dependence on p_{T}, $p_{\text{T}}^{\text{tracks}}/E_{\text{T}}$ and one R_{em} bin between QCD dijet and $t\bar{t}$ events. The results for both identification methods and all p_{T}, R_{em} and $p_{\text{T}}^{\text{tracks}}/E_{\text{T}}$ bins are shown in Appendix A.

9.3 Background Estimation for Light Charged Higgs Searches

9.3.1 Estimation of $t\bar{t}$ Background from Fake τ-Jets

In the following the application of the rejection measurement to the estimation of the $t\bar{t}$ background contribution for charged Higgs searches is tested. The number of reconstructed (identified) τ-jet candidates N_{reco} (N_{ID}) is the sum of the number of τ-jets N_{reco}^{τ} (N_{ID}^{τ}) and the number of quark and gluon jets $N_{\text{reco}}^{\text{jets}}$ ($N_{\text{ID}}^{\text{jets}}$):

$$N_{\text{reco}} = N_{\text{reco}}^{\tau} + N_{\text{reco}}^{\text{jets}}, \tag{9.1}$$

$$N_{\text{ID}} = N_{\text{ID}}^{\tau} + N_{\text{ID}}^{\text{jets}}. \tag{9.2}$$

Table 9.6: Binning of the rejection measurement as a function of p_{T}, R_{em}, $p_{\mathrm{T}}^{\mathrm{tracks}}/E_{\mathrm{T}}$ for (a) "safe cuts", (b) the likelihood discriminant method.

	(a)					(b)
p_{T} / GeV	$20-25$	$25-45$	$45-70$	$70-100$	$100-10000$	All
R_{em}	$-\infty < 0.095$	$-\infty < 0.063$	$-\infty < 0.049$	$-\infty < 0.044$	$-\infty < 0.033$	$-\infty < 0.05$
	$0.095-0.15$	$0.063-0.11$	$0.049-0.07$	$0.044-0.06$	$0.033-0.07$	$0.05-0.06$
	$0.15-0.3$	$0.11 > \infty$	$0.07 > \infty$	$0.06-0.075$	$0.07-0.25$	$0.06-0.07$
	$0.3 > \infty$			$0.075 > \infty$	$0.25 > \infty$	$0.07-0.09$
						$0.09-0.11$
						$0.11 > \infty$
$p_{\mathrm{T}}^{\mathrm{tracks}}/E_{\mathrm{T}}$	$-\infty < 0.15$	$-\infty < 0.12$	$-\infty < 0.088$	$-\infty < 0.071$	$-\infty < 0.061$	$-\infty < 0.8$
	$0.15-0.4$	$0.12-0.62$	$0.088-0.21$	$0.071-0.59$	$0.061-0.068$	$0.8-0.9$
	$0.4 > \infty$	$0.62 > \infty$	$0.21 > \infty$	$0.59 > \infty$	$0.068 > \infty$	$0.9-0.95$
						$0.95 > \infty$

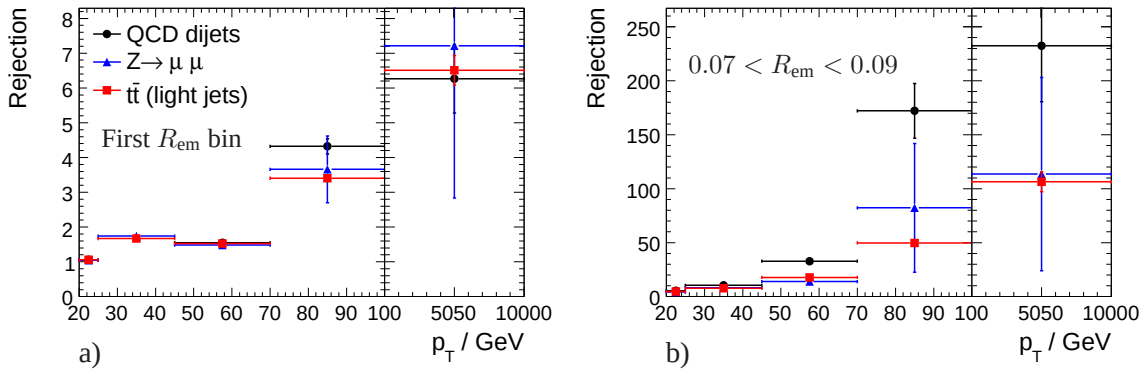

Figure 9.8: Dependence of the rejections measured in QCD dijets (black circles), Z+jets (blue triangles) and $t\bar{t}$ (red squares) events on the electromagnetic jet radius R_{em} with (a) the p_{T} dependence in the first R_{em} bin for the "safe cuts" method and (b) in the middle R_{em} bin for the likelihood discriminant method (see Table 9.6).

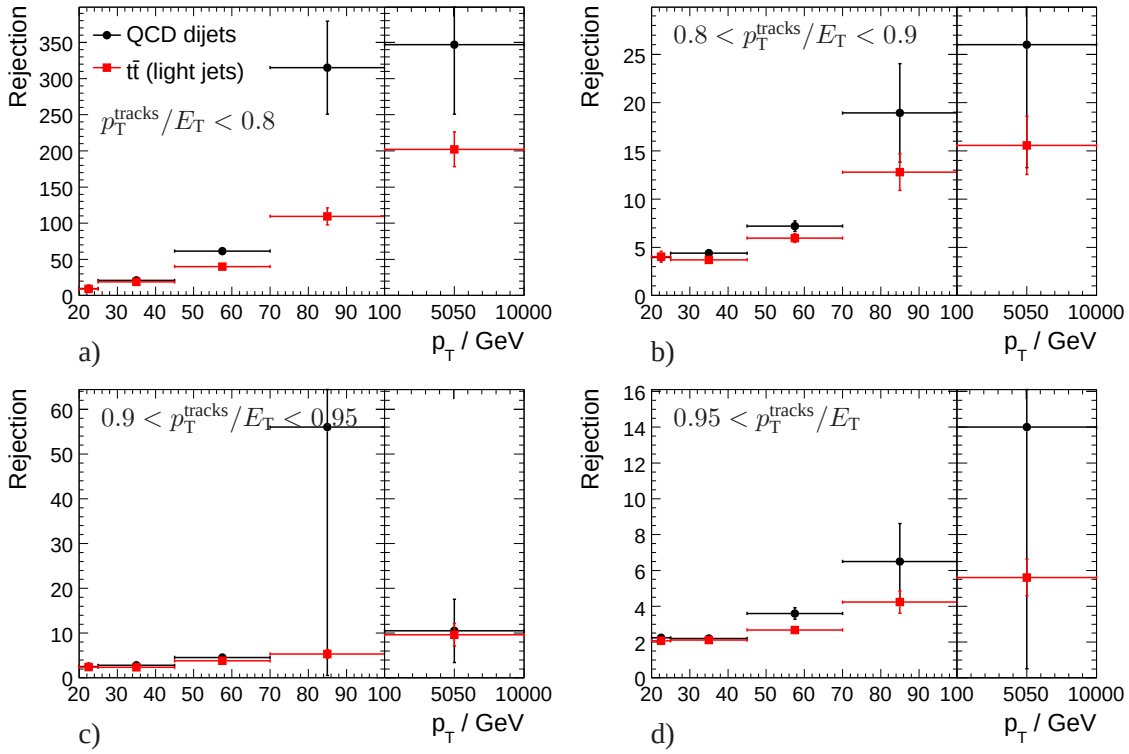

Figure 9.9: Dependence of the rejections measured in QCD dijets (black circles) and $t\bar{t}$ (red squares) events on the ratio $p_{\mathrm{T}}^{\mathrm{tracks}}/E_{\mathrm{T}}$ with the p_{T} dependence in the four $p_{\mathrm{T}}^{\mathrm{tracks}}/E_{\mathrm{T}}$ bins (a)-(d) for the likelihood discriminant method (see Table 9.6).

The numbers N_{reco} and N_{ID} can be directly obtained from the data. The identification efficiency ϵ and the rejection R of light parton jets by the τ-jet identification are given by

$$\epsilon = N^{\tau}_{\text{ID}}/N^{\tau}_{\text{reco}} \text{ and} \tag{9.3}$$

$$R = N^{\text{jets}}_{\text{reco}}/N^{\text{jets}}_{\text{ID}}. \tag{9.4}$$

The $t\bar{t}$ background with fake τ-jets is estimated using the measured rejection (see discussion above) and the efficiency [90]. The efficiency can be measured using $Z \rightarrow \tau\tau$ data [91], but is determined using Monte Carlo truth information in this study. Once these numbers are known for a given process, the number of misidentified τ-jet candidates can be calculated:

$$\begin{aligned} N^{\text{jets}}_{\text{ID}} &= N_{\text{ID}} - N^{\tau}_{\text{ID}} \\ &= N_{\text{ID}} - \epsilon N^{\tau}_{\text{reco}} \\ &= N_{\text{ID}} - \epsilon N_{\text{reco}} + \epsilon N^{\text{jets}}_{\text{reco}} \\ &= N_{\text{ID}} - \epsilon N_{\text{reco}} + \epsilon R N^{\text{jets}}_{\text{ID}}, \\ N^{\text{jets}}_{\text{ID}} &= \frac{1}{1-\epsilon R}(N_{\text{ID}} - \epsilon N_{\text{reco}}). \end{aligned} \tag{9.5}$$

The efficiency and rejection are functions of p_{T} and other parameters. Depending on the result of the identification, weights w_i and w'_i are calculated using ϵ_i and R_i in bin i of the parameter space:

$$\begin{aligned} w_i &= \frac{1}{\epsilon_i R_i - 1}(\epsilon_i - 0), \qquad \text{reconstructed } \tau\text{-jet candidate not identified,} \\ w'_i &= \frac{1}{\epsilon_i R_i - 1}(\epsilon_i - 1), \qquad \text{reconstructed } \tau\text{-jet candidate identified.} \end{aligned} \tag{9.6}$$

The total number of misidentified τ-jet candidates is the sum of the weights of all τ-jet candidates:

$$N^{\text{jets}}_{\text{ID}} = \sum_{\text{i=1}}^{N_{\text{reco}}-N_{\text{ID}}} w_i + \sum_{\text{i=1}}^{N_{\text{ID}}} w'_i. \tag{9.7}$$

In the following the contribution of misidentified τ-jets is determined for $t\bar{t}$ events using the different parameterization strategies described in the Sections 9.2.3 and 9.2.4 and compared to the true number of fake τ-jets determined using the Monte Carlo truth information.

9.3.2 Background Estimation with p_{T} Dependent Rejection

The number of misidentified τ-jet candidates is estimated using the p_{T} dependent rejection from Figure 9.5 in Equation (9.7). The identification efficiencies are directly determined from the $t\bar{t}$ events using the Monte Carlo truth information. Figure 9.10 shows the ratio of the estimated and true numbers of misidentified τ-jet candidates as a function of p_{T} for the "safe cuts" method. The estimation from QCD dijet events (see Figure 9.10(a)) clearly underestimates the background up to 55%, as can be expected from the higher rejection determined from QCD dijet events. The estimate is better for lower p_{T}, but with large uncertainty which is not due to limited statistics but

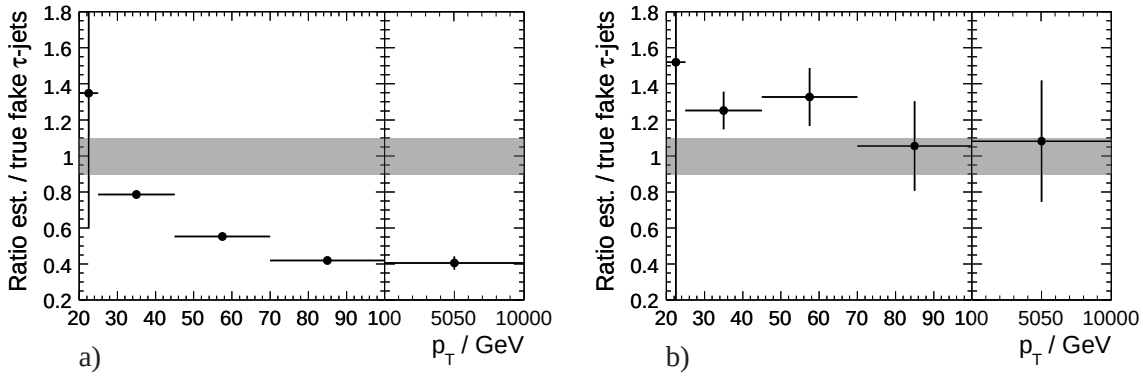

Figure 9.10: Ratio of the numbers of estimated and true misidentified τ-jet candidates as a function of p_{T} for the medium requirement of the "safe cuts" method using rejections obtained from (a) QCD dijet and (b) from Z+jets events.

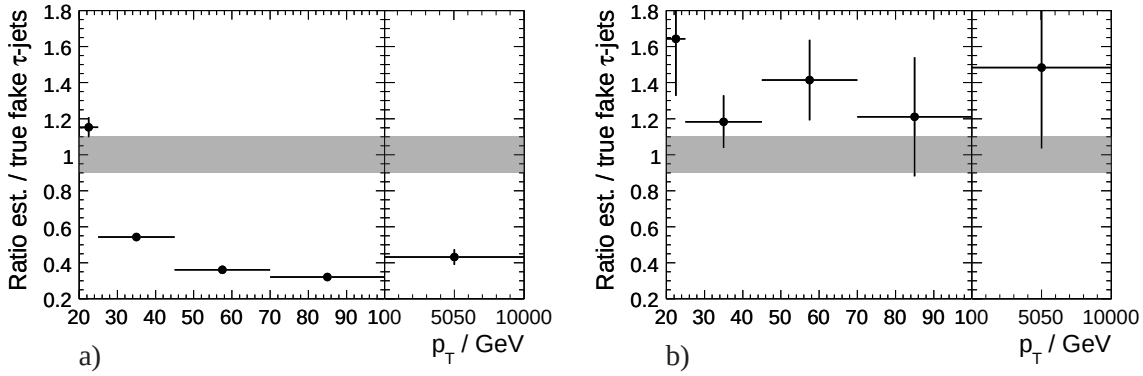

Figure 9.11: As Figure 9.10 for the medium flag of the likelihood based τ-jet identification.

because of the low discrimination power between QCD jets and hadronically decaying τ leptons at low p_{T}. In this case the values for the efficiency ϵ and the rejection R are both approximately one and the denominator in Equation (9.6) becomes small. The Monte Carlo statistics for the QCD dijet sample corresponding to an integrated luminosity much smaller than $200\,\mathrm{pb}^{-1}$ was taken into account in the error bars.
For Z+jets data (see Figure 9.10(b)), the estimated number of misidentified τ-jets disagrees by only about 30% with the true value with only small p_{T} dependence. Since the rejection is estimated slightly too low (see Figure 9.5(a)) the $t\bar{t}$ background due to fake τ-jets tends to be slightly overestimated. Again no prediction can be made for the lowest p_{T} bin.
When the likelihood based τ identification is used, the uncertainty in the first p_{T} bin becomes considerably smaller for both QCD dijet and Z+jets events as can be seen in Figure 9.11. Due to the better performance of the likelihood method in this range, the weights are estimated with smaller uncertainties as with the "safe cuts" identification. For the remaining p_{T} bins the agreement with the truth information is slightly worse compared to the "safe cuts" identification which can be explained by the complexity of the likelihood method using a large number of discriminating variables exploiting details of the jet shape to achieve higher discrimination power.

9.3.3 Background Estimation with $[p_{\mathrm{T}}, R_{\mathrm{em}}]$ Dependent Rejection

Following the reasoning in Section 9.2.3, the estimate of the number of fake τ-jets in $t\bar{t}$ events is repeated with a two dimensional parameterization of the rejection in bins of p_{T} and R_{em}. The results for the "safe cuts" τ identification are shown in Figure 9.12. Compared to the corresponding ratios in Figure 9.10 where only the p_{T} dependence is taken into account in the weights an overall improvement is achieved. In spite higher statistical uncertainties of the weights per bin, the first p_{T} bin is now more reliable. With the introduction of additional prediction in the R_{em} dependence similar efficiency and rejection values at low p_{T} are avoided. However, now the identification performance in one R_{em} bin corresponding to multi-prong τ-jet candidates in the p_{T} range 45 GeV to 70 GeV is leading to a high uncertainty.
The agreement again improves when the likelihood method is used for τ-jet identification. The results obtained with the rejection determined from QCD dijet events (see Figure 9.13(a)) show a systematic deviation of 40%. When the rejection is derived from the Z+jets data, good agreement with the true values is achieved, but the results suffer from large statistical uncertainties (see Figure 9.13(b)).

9.3.4 Background Estimation with $\left[p_{\mathrm{T}}, R_{\mathrm{em}}, p_{\mathrm{T}}^{\mathrm{tracks}}/E_{\mathrm{T}}\right]$ Dependent Rejection

Finally the variable $p_{\mathrm{T}}^{\mathrm{tracks}}/E_{\mathrm{T}}$ is added to parameterize the rejection in order to reduce the deviations between estimated and true τ-jet fake rates further. The result for the "safe cuts" identification using the rejection determination from QCD dijet events is shown in Figure 9.14(a). Several p_{T} bins acquire high uncertainties for the reason discussed in Section 9.3.2 and no improvement is gained. For the likelihood method the same R_{em} binning as in the two dimensional parameterization is applied. As can be seen in Figure 9.14, the systematic deviation of the τ-jet fake background estimation decreases further to 25%. The statistical uncertainty is still relatively low. Results for the p_{T}, R_{em} and $p_{\mathrm{T}}^{\mathrm{tracks}}/E_{\mathrm{T}}$ dependent rejection from $Z \rightarrow \mu\mu$+jets events are not

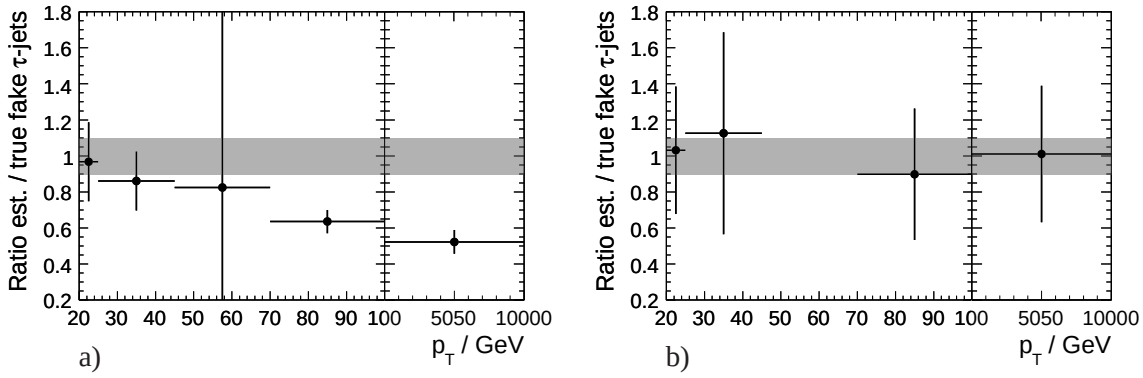

Figure 9.12: Ratio of the numbers of estimated and true misidentified τ-jet candidates as a function of p_{T} for the medium requirement of (a) the "safe cuts" and (b) the likelihood based τ-jet identification using rejection dependence on p_{T} and R_{em}. The left plot (a) represents the result using rejection factors obtained from QCD dijet events, the right plots (b) from Z+jets events.

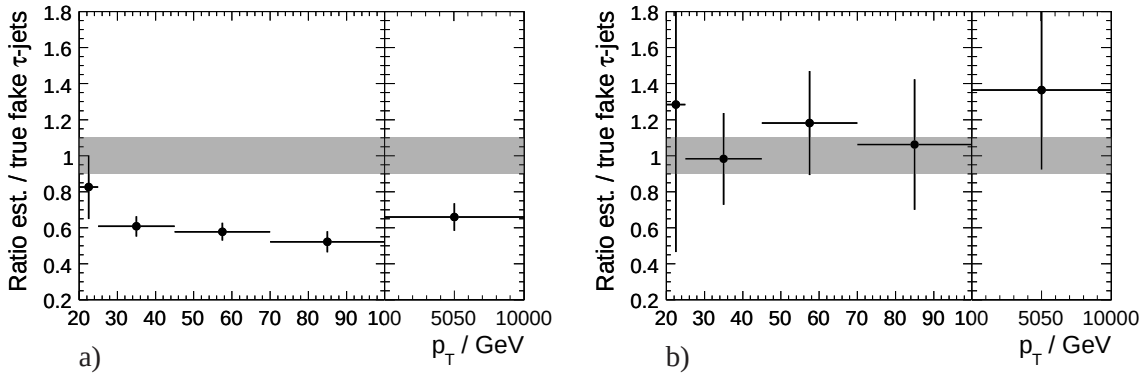

Figure 9.13: As Figure 9.12 for the medium flag of the likelihood based τ-jet identification.

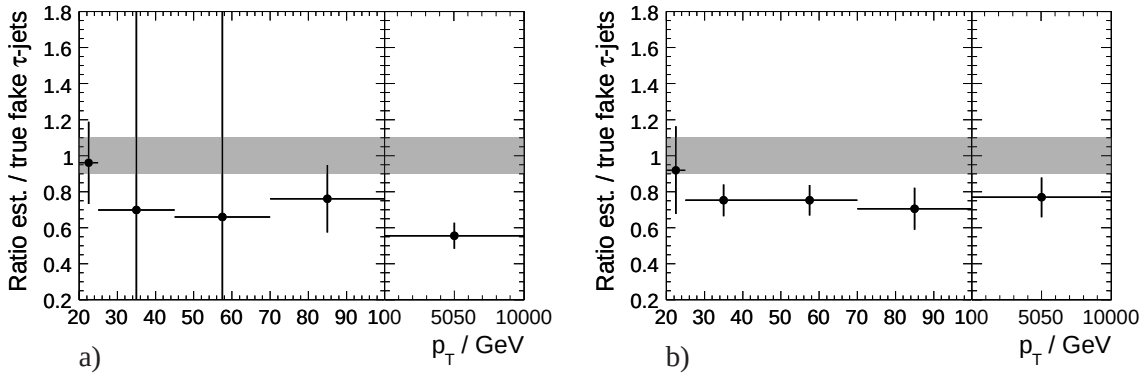

Figure 9.14: Ratio of the numbers of estimated and true misidentified τ-jet candidates as a function of p_{T} for the medium requirement of (a) the "safe cuts" and (b) the likelihood based τ-jet identification using the rejection dependence on p_{T}, R_{em} and $p_{\mathrm{T}}^{\mathrm{tracks}}/E_{\mathrm{T}}$. The rejections are obtained from QCD dijet events.

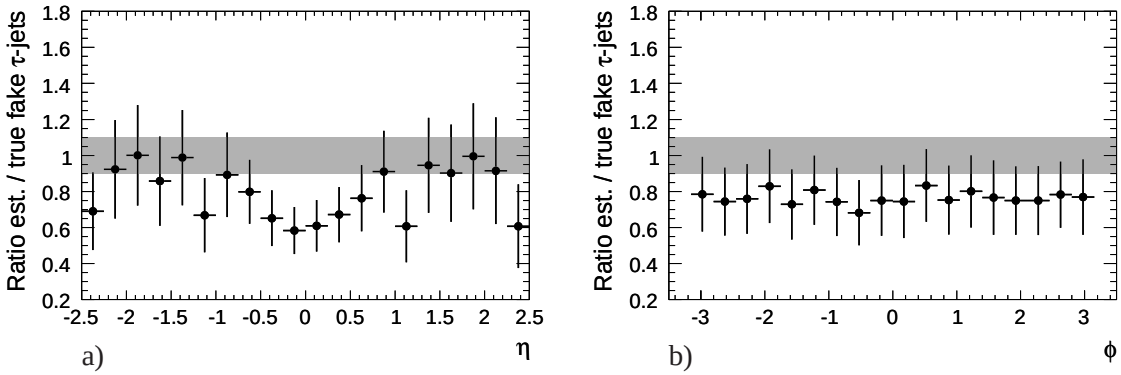

Figure 9.15: Ratio of the numbers of estimated and true misidentified τ-jet candidates as a function of (a) η and (b) ϕ for the medium requirement of the likelihood based τ-jet identification using the rejection dependence on p_{T}, R_{em} and $p_{\mathrm{T}}^{\mathrm{tracks}}/E_{\mathrm{T}}$. The rejections are obtained from QCD dijet events.

Table 9.7: Accuracy of the background estimation of the reducible $t\bar{t}$ background using the loose and medium quality criteria of the likelihood identification. All τ-jet candidates with a transverse momentum larger than 25 GeV are considered.

Sample	Parametrization	estimated / true fake τ-jets	
		loose id.	medium id.
QCD dijets	1D	0.50 ± 0.01	0.45 ± 0.01
QCD dijets	2D	0.62 ± 0.04	0.58 ± 0.03
QCD dijets	3D	0.75 ± 0.07	0.75 ± 0.06
Z+jets	1D	1.22 ± 0.04	1.27 ± 0.12
Z+jets	2D	1.04 ± 0.08	1.06 ± 0.17

available because of the too low statistics for an integrated luminosity of 200 pb^{-1}.
In Figure 9.15(a) and 9.15(b) the ratio of the estimated and true numbers of misidentified τ-jet candidates is shown as a function of η and ϕ, respectively, using QCD dijet events for the measurement of the rejection and the likelihood method for the τ-jet identification. The η dependence shows a modulation giving rise to an underestimation of up to 40% in the central region $|\eta| < 1$ while there is agreement with the true numbers in the forward and backward regions $|\eta| > 1$. Therefore taking into account η dependence is also desirable when more statistics is available. No variations in ϕ are seen with overall deviation from the true value of 25%.
Figure 9.16 shows the ratios over p_{T} for different jet multiplicities. Within the statistical uncertainties no dependence on the jet multiplicity is observed.

9.4 Background Estimation with the "loose" Identification Flag

While the rejection measurement with QCD dijet events underestimates the $t\bar{t}$ background by about 25%, a much better agreement can be achieved with Z+jets events. However, with an integrated luminosity of only $200\,\text{pb}^{-1}$ the statistics of the Z+jets sample is limited. Therefore, at least for the likelihood based method, the background estimation is performed using the loose-flag. For the cut based method this is not possible because the rejection becomes too small, typically $R < 10$, compensating the benefit of larger statistics by the intrinsic instability of the method for $eR \approx 1$ (see Equation (9.6)).
First, the QCD dijet sample is used to compare the accuracy of the background estimation for the loose and medium flags of the likelihood based τ-jet identification. As can be seen in Figure 9.17(a) and Tabel 9.7 the deviation between the results with medium flags are rather small. The numbers in Table 9.7 are the ratios of the numbers of estimated and true τ-jet candidates with transverse momentum $p_{\text{T}} > 25\,\text{GeV}$, as obtained with the loose and the medium flags of the likelihood based τ-jet identification. The low p_{T} τ-jet candidates are usually discarded in charged Higgs boson searches.
For Z+jets events the loose flag of the likelihood based τ-jet identification leads to more reliable results. Comparing Figures 9.17(c) and 9.17(d) with Figures 9.11(b) and 9.13(b), the improvement

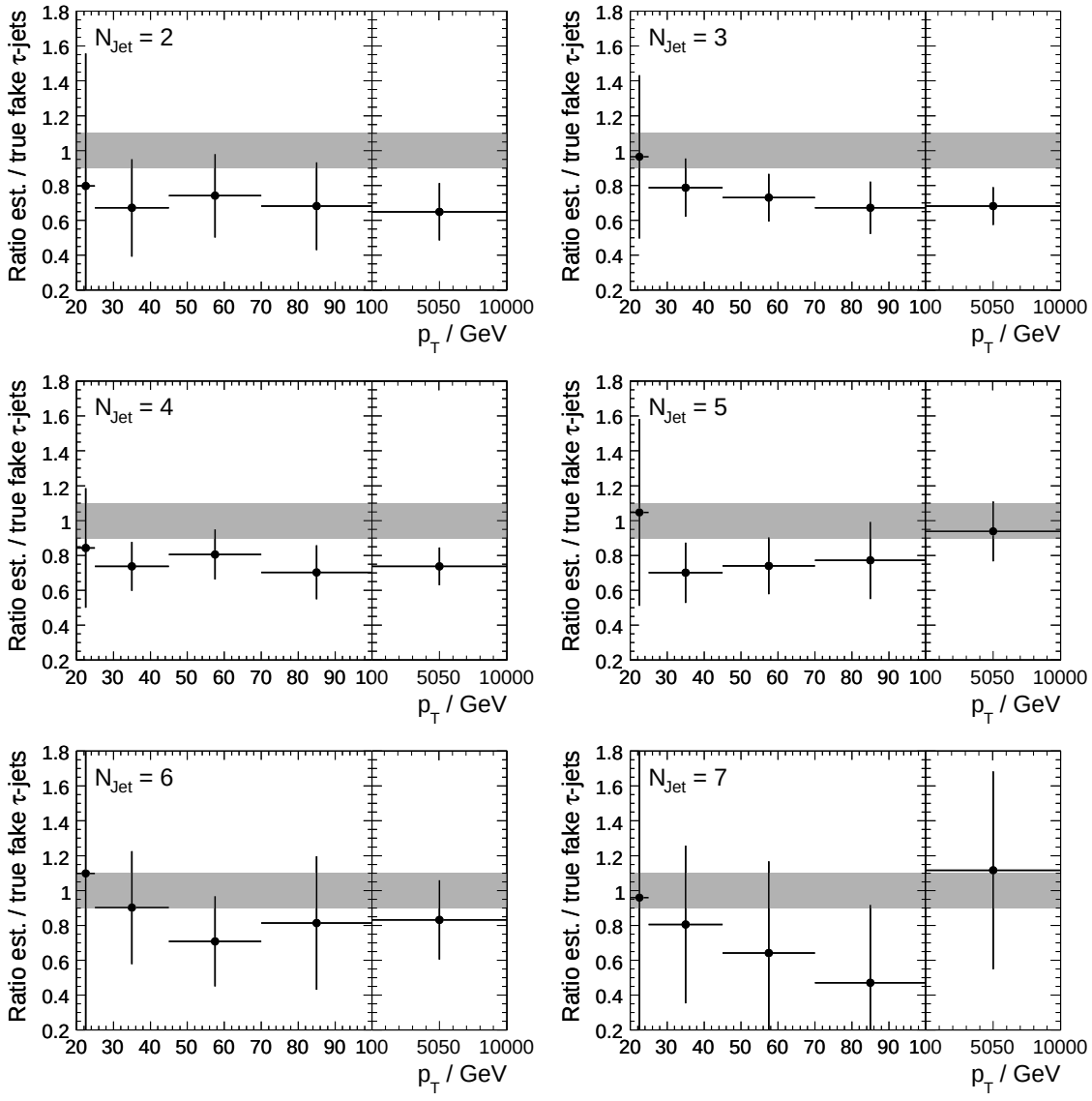

Figure 9.16: Ratio of the numbers of estimated and true misidentified τ-jet candidates as a function of p_{T} for different jet multiplicities $\mathrm{N_{jet}}$ for rejections depending on p_{T}, R_{em} and $p_{\mathrm{T}}^{\mathrm{tracks}}/E_{\mathrm{T}}$ from QCD dijet events and for the medium flag of the likelihood based τ-jet identification.

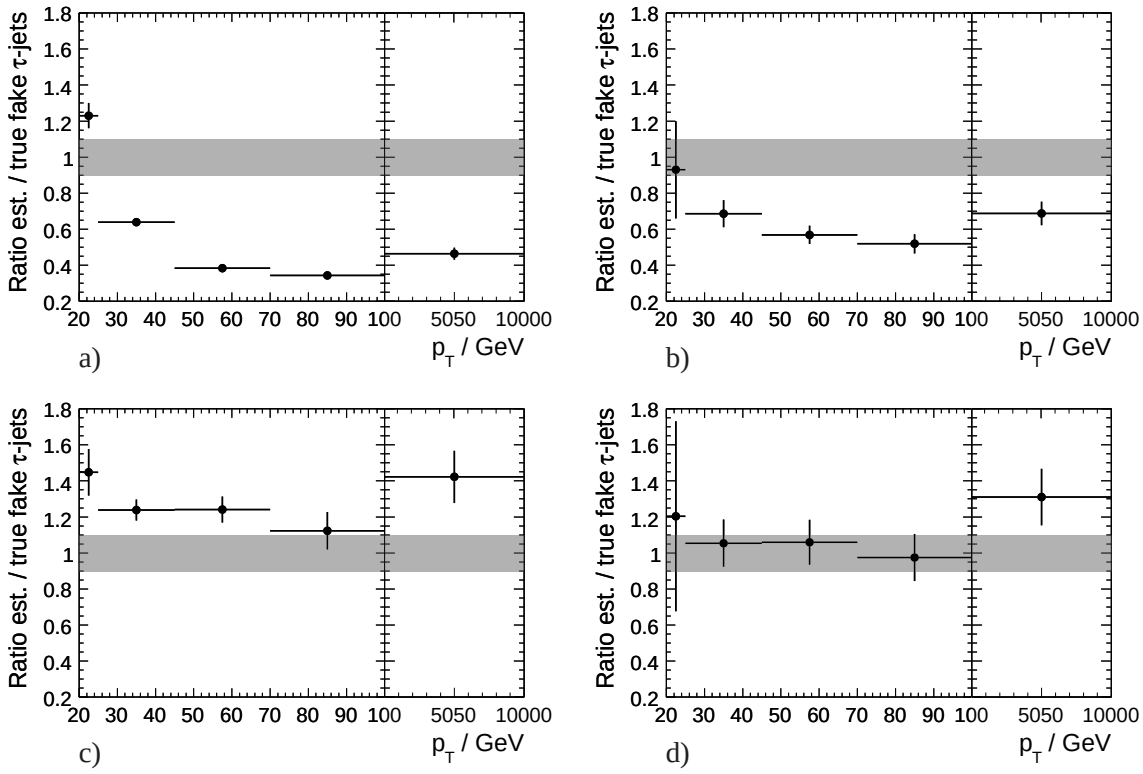

Figure 9.17: Ratio of the numbers of estimated and true misidentified τ-jet candidates as a function of p_{T} for the loose identification criterium of the likelihood based method. In (a) the results for only p_{T} dependent rejection from QCD dijet events are shown, (c) and (d) show the corresponding results for Z+jets events.

of the statistical precision is visible. While the $t\bar{t}$ background is still overestimated when only the p_{T} dependence is taken into account, the estimate of the fake τ-jet background is considerably more reliable using the p_{T} and R_{em} dependence of the rejection. With more statistics one can expect similar results with the more stringent identification criteria.

9.5 Conclusions

In order to determine the background contribution from misidentified τ-jet candidates from $t\bar{t}$ events in light charged Higgs searches, the efficiency of the τ-jet identification and the rejection of light parton jets for $t\bar{t}$ events has to be determined from data. They are used to determine weights for the τ-jet candidates from which the number of misidentified τ-jets can be calculated. In this study the rejection is evaluated with data-driven techniques, while Monte Carlo truth information is used only for the estimation of the efficiency.
Determining the rejection as a function of p_{T} from QCD dijet events the background contribution is underestimated by 32% for medium "safe cuts" τ-jet identification criteria. For the likelihood

based identification, the background is underestimated by 55%. The large deviation of the estimated from the true background contribution is mainly caused by the different jet shapes. QCD dijet events are known dominated by gluon jets while in $t\bar{t}$ events most of the jets originate from quarks. Therefore, a strategy has been proposed to measure the rejection in Z+jets events where the quark jet contribution is enhanced. In this way a more accurate estimation of the background is achieved with deviations of only about 25% for both the "safe-cuts" and the likelihood based identification method.

To correct for the effect of the different jet shapes τ-jet identification variables sensitive to the jet shape are used in addition to the p_{T} to parametrize the rejection. When using QCD dijet events for the rejection measurement with the likelihood based τ-jet identification method, the accuracy of the background estimation is improved to 42% and 25% for parametrizations with two and three variables, respectively. For the "safe cuts" method an improvement should by possible as well, but no conclusive result could be obtained due to large intrinsic errors of the method.

Using Z+jets events with a two-dimensional parametrization of the rejection improves the background estimation further. However, for an integrated luminosity of $200\,\mathrm{pb}^{-1}$ at a center-of-mass energy of 10 TeV the dominating statistical errors are too large. Therefore a relaxed identification criterium of the likelihood based method has to be used for which a ratio of estimated and true misidentified τ-jet background of 1.04 ± 0.08 is obtained. A comparision with the results obtained using QCD dijet events indicates that such an accurate result is achievable with stricter τ-jet identification criteria.

Chapter 10

Discovery Potential and Exclusion Limits

In this chapter the final results of the Monte Carlo study of the light charged Higgs boson search with ATLAS is summarized. The calculation of the discovery potential and exclusion limits, explained in Section 10.1, is performed using the profile likelihood method including statistical and systematic uncertainties. The discovery potential and the exclusion limits of charged Higgs bosons in the channel investigated are presented in Section 10.2.

10.1 The Profile Likelihood Method

The number n of events selected by the charged Higgs boson search follows a Poisson distribution with expectation value

$$E[n] \equiv \mu s + b \tag{10.1}$$

where s and b are the expected numbers of selected signal and background events and the parameter μ describes the signal strength. For $\mu = 1$, the signal agrees with the theoretical prediction, for $\mu = 0$ no signal is present. In addition, the number m of background events is measured independently from a control sample with expectation value

$$E[m] = \tau b_{\pm} \tag{10.2}$$

where τ is a scaling factor between control ans signal sample which is derived from Monte Carlo simulations and $b_{\pm}$ the expected number of background events associated with a systematic uncertainty. The likelihood function of this measurement is defined as

$$L(n|\mu, b) \tag{10.3}$$

with μ and b treated as free parameters while s is fixed to the MSSM prediction. The profile likelihood ratio $\lambda(\mu)$ [93] is then given by

$$\lambda(\mu) = \frac{L(n|\mu, \hat{\hat{b}})}{L(n|\hat{\mu}, \hat{b})} \tag{10.4}$$

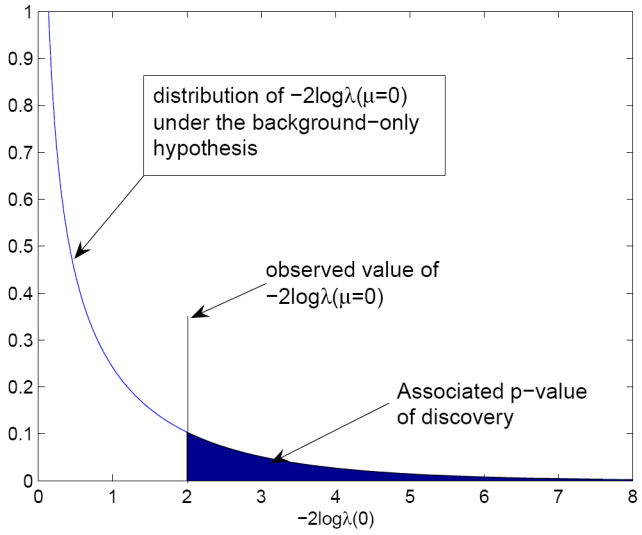

Figure 10.1: Example of a probability density function $f(q_0|0)$ for the background-only hypothesis as a function of q_0. The associated p-value for the observed value $q_{0,\mathrm{obs}}$ is shown giving the probability that the hypothesis is wrong [92].

where $\hat{\hat{b}}$ is the parameter value which maximizes the likelihood function for fixed signal strength μ, while $\hat{\mu}$ and $\hat{b}$ maximize the likelihood for simultaneously free μ and b. The values of $\lambda(\mu)$ are distributed between zero and one. $\lambda(\mu) = 1$ implies good agreement of the hypothesized value of μ with the data, while the opposite is the case for $\lambda(\mu) = 0$. Equivalently the quantity

$$q_\mu = -2 \ln \lambda(\mu) \tag{10.5}$$

is used instead of the profile likelihood ratio. Small values indicate compatibility of the hypothesis with the data, for high values the hypothesis is more unlikely to be true.
In Figure 10.1 an example of the probability density function $f(q_\mu|\mu)$ of q_μ is shown. In principle it has to be estimated by many ($\sim 10^9$) pseudo-experiments using Monte Carlo simulation. However, as stated in [93, 94], the probability density function $f(q_\mu|\mu)$ can be approximately constructed with the help of a χ^2 distribution. In case the data n is consistent with the background-only (signal+background) hypothesis, $f(q_0|0)$ ($f(q_1|1)$) approaches a χ^2 distribution with one degree of freedom.
The p-values

$$p_\mu = \int_{q_{\mu,\mathrm{obs}}}^{\infty} f(q_\mu|\mu)\, dq_\mu \tag{10.6}$$

can then be easily computed without having to simulate a very large amount of pseudo-experiments for each point in the MSSM parameter space.

10.1.1 Signal Significance and Exclusion Limits

Frequently the p-value is expressed in terms of the number of standard deviations Z of a Gaussian distribution via the relation

$$p = \int_Z^\infty \frac{1}{\sqrt{2\pi}} e^{-x^2/2} dx. \tag{10.7}$$

To calculate signal significance and exclusion limits, the "background-only" and "signal+background" hypotheses, respectively, corresponding to $\mu = 0$ and $\mu = 1$, are tested for compatibility with the data. The signal significance corresponds to the probability that a background fluctuation will fake a signal. To claim a discovery, the p-value of the "background-only" hypothesis corresponding to $\mu = 0$ has to be smaller than 2.87×10^{-7} corresponding to $Z_{\text{discovery}} = 5$. Similarly the "signal+background" hypothesis corresponding to $\mu = 1$ is rejected and a signal excluded at 95% C.L. if the p-value is smaller than 0.05 or $Z_{\text{exclusion}} = 1.64$.
Using the properties of the χ^2 distribution it has been shown [93] that the signal significance and exclusion limit are given by:

$$\begin{aligned} Z_{\text{discovery}} &= \sqrt{-2 \ln \lambda(\mu = 0)}, \\ Z_{\text{exclusion}} &= \sqrt{-2 \ln \lambda(\mu = 1)}. \end{aligned} \tag{10.8}$$

10.1.2 The Likelihood Function

To calculate the profile likelihood ratio $\lambda(\mu)$, the parameter values of the background $\hat{b}$ and $\hat{\hat{b}}$ and the signal strength parameter $\hat{\mu}$ have to be determined as described in Section 10.1. The likelihood function is given by:

$$\begin{aligned} L(n|\mu, b) = &\frac{(\mu s + \tau b)^n}{n!} e^{-(\mu s + \tau b)} \times \frac{b_+^{m_+}}{m_+!} e^{-m_+} \times \frac{b_-^{m_-}}{m_-!} e^{-m_-} \times \\ &f_\Gamma\left((b^+ - b^-)|k_b, \theta_b\right) \times f_\Gamma\left(s^0|k_s, \theta_s\right). \end{aligned} \tag{10.9}$$

The first term reflects the Poisson probability for observing n events in the signal region. The next two Poisson probabilities reflect the background measurement with the help of the control sample. Since in the $t\bar{t}$ background simulation events with positive $(+)$ and negative $(-)$ weights are generated, the background measurement has to be described by two separate terms for the Monte Carlo studies, where the number of background events estimated in the control region is m_+ and m_- with the expectation values b_+ and b_- associated with a systematic uncertainty. To incorporate a systematic uncertainty on the background, the values b^+, b^- and s^0 are treated as random variables distributed around the "correct" expectation values b and s. As probability density function gamma distributions

$$f_\Gamma(x|k, \theta) = x^{k-1} \frac{e^{-x/\theta}}{\theta^k \, \Gamma(k)} \tag{10.10}$$

with parameters

$$\begin{aligned} k_s &= s^2/\sigma_s^2, \quad \theta_s = \sigma_s^2/s, \\ k_b &= b^2/\sigma_b^2, \quad \theta_b = \sigma_b^2/b \end{aligned} \tag{10.11}$$

and systematic uncertainties $\sigma_s = 0.4\,s$, $\sigma_b = 0.1\,b$ for signal and background are used [92]. The gamma distribution has been used because the background can only be positive. For large values of k the gamma distribution converges to a Gaussian distribution with mean $k\theta$ and width $k\theta^2$.

10.2 Charged Higgs Discovery and Exclusion

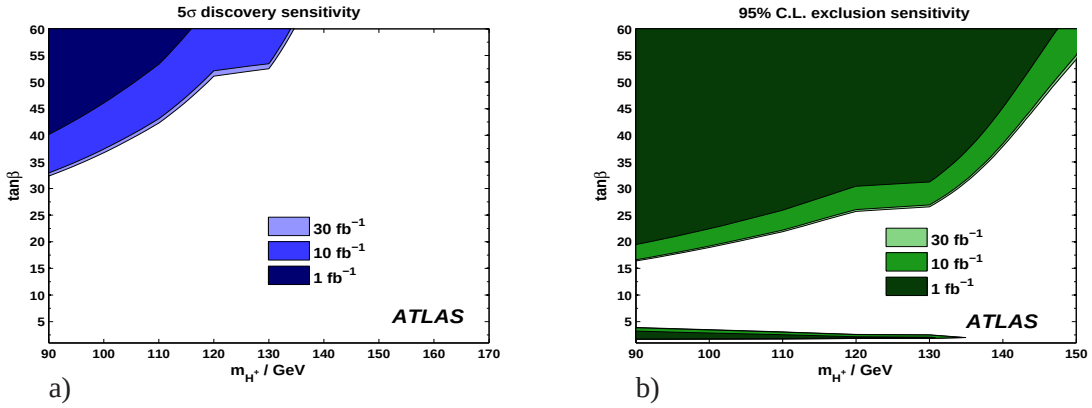

Figure 10.2: (a) 5σ discovery contours and (b) 95% C.L. exclusion regions in the $\tan\beta$,$m_{H^\pm}$ parameter plane for the MSSM m_h-max benchmark scenario for different integrated luminosities, taking into account systematic uncertainties including limited Monte Carlo statistics.

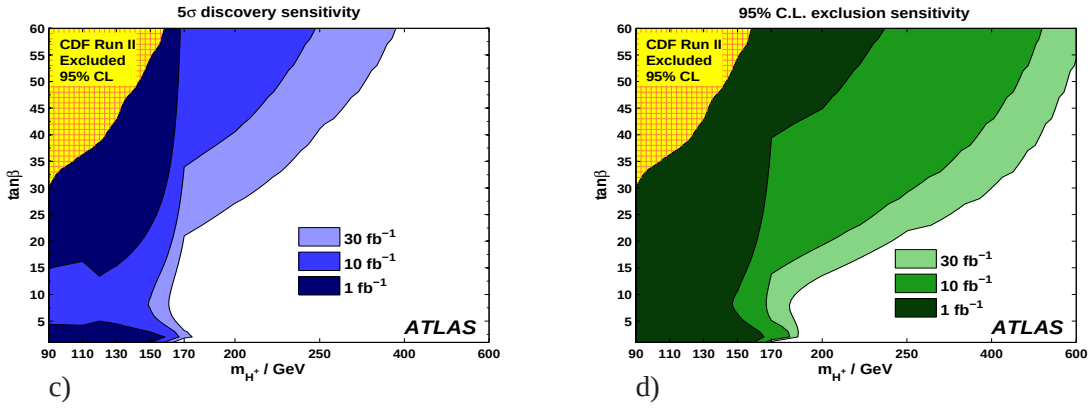

Figure 10.3: Results from the combination with all charged Higgs boson search channels at the LHC: (a) discovery contours and (b) exclusion limits for the MSSM m_h-max benchmark scenario including systematic uncertainties without Monte Carlo statistical errors [83].

The discovery potential and exclusion limits of the charged Higgs boson search in this study are shown in Figures 10.2(a) and 10.2(b) including systematic uncertainties and assuming the MSSM m_h-max scenario. In the investigated production and decay channel charged Higgs bosons with mass $m_{H^\pm} = 90\,\text{GeV}$ can be discovered for $\tan\beta > 32$ and an integrated luminosity of $10\,\text{fb}^{-1}$.

For larger masses, $m_{H^\pm} = 130\,\text{GeV}$, discovery is only possible for $\tan\beta > 57$. In the mass range up to 130 GeV exclusion is possible for $\tan\beta > 25$. For lower $\tan\beta$ the cross section for $H^\pm$ production is significantly reduced as described in Section 4.2.3.
In the Figures 10.3(a) and 10.3(b) the results from the combination of all investigated $H^\pm$ production and decay channels at the LHC are shown for the m_h-max scenario [83]. The statistical uncertainty arising from the limited number of Monte Carlo events is neglected. For an integrated luminosity of $10\,\text{fb}^{-1}$, charged Higgs bosons with masses $m_{H^\pm} < 100\,\text{GeV}$ are within the discovery reach and can be excluded for the masses below 170 GeV for all $\tan\beta$.

Chapter 11

Summary

The predictions of the Standard Model have been confirmed by accelerator experiments with very high accuracy. Only the Higgs boson has not yet been discovered. In order to be compatible with the electroweak precision measurements, it has to be rather light ($m_H < 186\,\text{GeV}$) and is therefore well within the discovery reach of the ATLAS experiment at the LHC. However, in the Standard Model the Higgs boson mass is subject to large quantum corrections driving its value towards the Planck scale. Therefore, even if the Standard Model Higgs boson is found at the LHC the question remains why its mass is that small. An elegant solution to this so called hierarchy problem is to extend the Standard Model to a supersymmetric theory which would also allow for the unification of the gauge coupling constants at high energies and provide a candidate for the observed dark matter in the universe. A feature of all supersymmetric extensions of the Standard Model is that a second Higgs isospin doublet is required, giving rise to five Higgs bosons, three of them neutral (h, H, A) and two of them charged ($H^{\pm}$). In contrast to a light neutral Higgs boson the observation of charged Higgs bosons would clearly demonstrate the existence of physics beyond the Standard Model and possibly the realization of Supersymmetry in nature. The most favored supersymmetric model to be studied at the LHC is the Minimal Extension of the Standard Model (MSSM) with minimum number of new particles. It has been also used for this study.
If the charged Higgs bosons are light, $m_{H^{\pm}} < m_t - m_b$, they will be copiously produced via on-shell top quark decays $t \rightarrow H^+ b$ reducing the Standard Model decay $t \rightarrow Wb$ accordingly. Since in most of the MSSM parameter space, for $\tan\beta > 3$, where $\tan\beta$ is the ratio of the vacuum expectation values of the two Higgs doublets, the decay $H^+ \rightarrow \tau\nu$ is the dominant decay channel with the signal being observable as an excess of τ lepton production in $t\bar{t}$ events.
In this study a search strategy for light charged Higgs bosons in the channel $t\bar{t} \rightarrow (H^+ b)\left(W\bar{b}\right) \rightarrow (\tau_{\text{had}}\nu b)\left(\ell\bar{\nu}\bar{b}\right)$ with a hadronically decaying τ lepton (τ-jet) with the ATLAS detector has been developed. The experimental signature of τ-jets, the low track multiplicity, slim shower shape and displaced secondary vertex, provides high rejection power against the large QCD backgrounds from QCD multi-jet and W+jets and single top quark production. For the search of light charged Higgs bosons the most important irreducible background, however is from $t\bar{t}$ events with Standard Model top quark decays to $t\bar{t} \rightarrow (Wb)\left(W\bar{b}\right) \rightarrow (\tau_{\text{had}}\nu b)\left(\ell\bar{\nu}\bar{b}\right)$. In this channel neutrinos are present in both top decay chains such that no signal peak above a smooth background can be reconstructed. However, a slight $t\bar{t}$ background suppression is possible due to the fact that the energy

of the τ-jets originating from charged Higgs boson decays is enhanced because of $m_W < m_{H^\pm}$ and due to the different spin of charged Higgs and W bosons. The signal selection cuts have been optimized by maximizing the signal significance taking into account systematic uncertainties.
When using Monte Carlo simulations to predict signal and background, the most important systematic errors were found to be the uncertainties in the jet energy scale and the missing transverse energy. The resulting total systematic uncertainty of 40% considerably restricts the signal sensitivity of the ATLAS experiment. The reduction of the systematic uncertainty is possible by estimating the background from $t\bar{t} \to \mu\mu$+X data events which can be selected with high purity. One of the two muons is replaced by a simulated τ-jet. In this way the irreducible $t\bar{t}$ background is emulated. This control data sample can be used to estimate the background after applying the selection cuts and the related systematic uncertainty is significantly decreased. The largest systematic bias is caused by the identification efficiency of the τ-jets which is overestimated by 15% since the embedded simulated τ-jets are lacking the jet environment of $t\bar{t}$ events. However, since the τ identification efficiency will be measured in $Z \to \tau\tau$ events eventually, a systematic uncertainty of only 10% on the irreducible $t\bar{t}$ background is feasible.
Due to misidentification of quark and gluon jets as τ-jets also $t\bar{t}$ events without top decays to τ leptons but high jet multiplicity contribute to the background. The misidentified jets mostly stem from hadronic W decays. The number of misidentified τ-jets can be obtained if the efficiency and rejection of parton jets is known in $t\bar{t}$ events. Since the rejection factor of parton jets by the τ-jet identification algorithms cannot be measured in $t\bar{t}$ data events directly, it has to be obtained from other processes where the origin of the τ-jet candidates is known. The usual approach is to select QCD dijet events which are produced at very high rates at the LHC. However, while the jets in $t\bar{t}$ events originate from quarks, the jets in QCD dijet events are mainly gluon induced resulting in an overestimation of the rejection. A method has been presented which determines the rejection from Z+jets events where the jets predominantly originate from quarks. A multi-dimensional parameterization of the measured rejection factor using τ-jet identification variables is used which leads to good agreement between the rejections in $t\bar{t}$ events and Z+jets events with only $(4 \pm 8)\%$ uncertainty and to a significant improvement of the predictions from QCD dijet events.
Finally, the achievable signal significances and exclusion limits for the search for light charged Higgs bosons in the m_h-max scenario of the Minimal Supersymmetric Extension of the Standard Model (MSSM) with the ATLAS detector have been determined taking into account systematic uncertainties and the data-driven determination of the background discussed above. With an integrated luminosity of $10\,\text{fb}^{-1}$, a discovery of a light charged Higgs boson with a mass of 90 GeV (130 GeV) is possible for $\tan\beta > 32$ (57) while it can be excluded for $\tan\beta > 17$ (25). The limits can be further improved by combining the results with other charged Higgs boson searches [42].

Appendix A

Results of Data-Driven QCD Jet Rejection Measurements

In all figures the error bars for QCD dijet and $t\bar{t}$ events correspond to the available Monte-Carlo statistics while they correspond to an integrated luminosity of 200 pb^{-1} for Z+jets events.

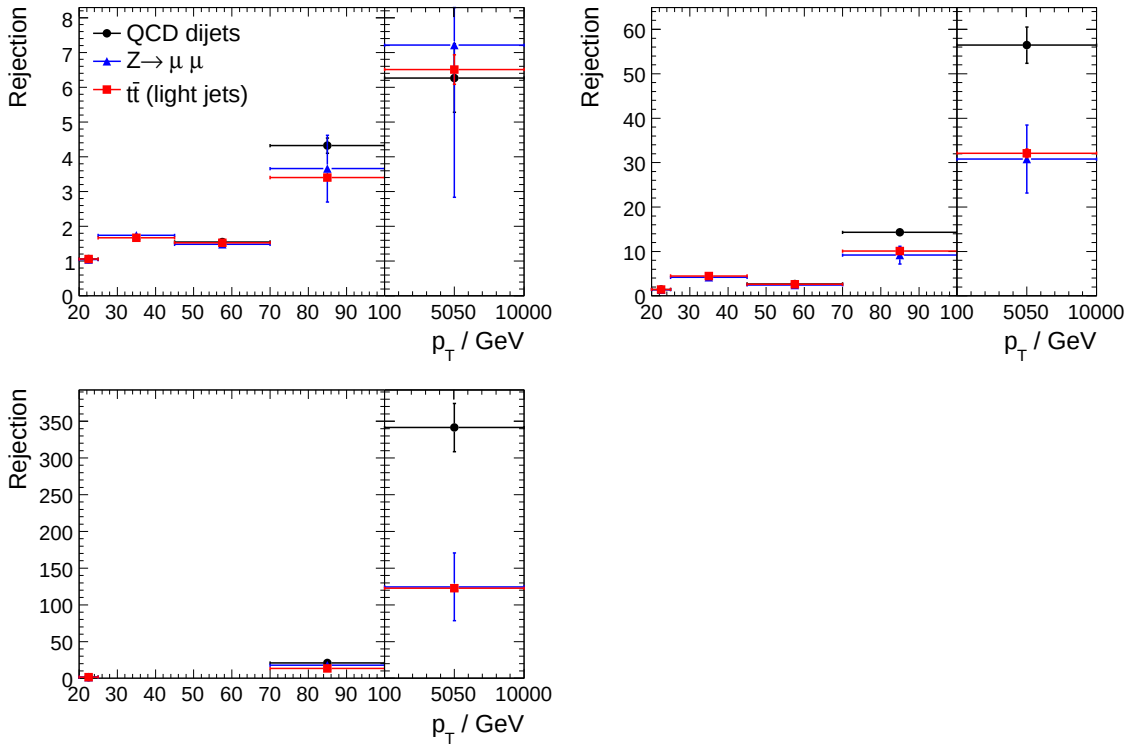

Figure A.1: Dependence of the rejections measured in QCD dijets (black circles), Z+jets (blue triangles) and $t\bar{t}$ (red squares) events on the electromagnetic jet radius R_{em} with the p_{T} dependence in the three R_{em} bins for the "safe cuts" method (see Table 9.6).

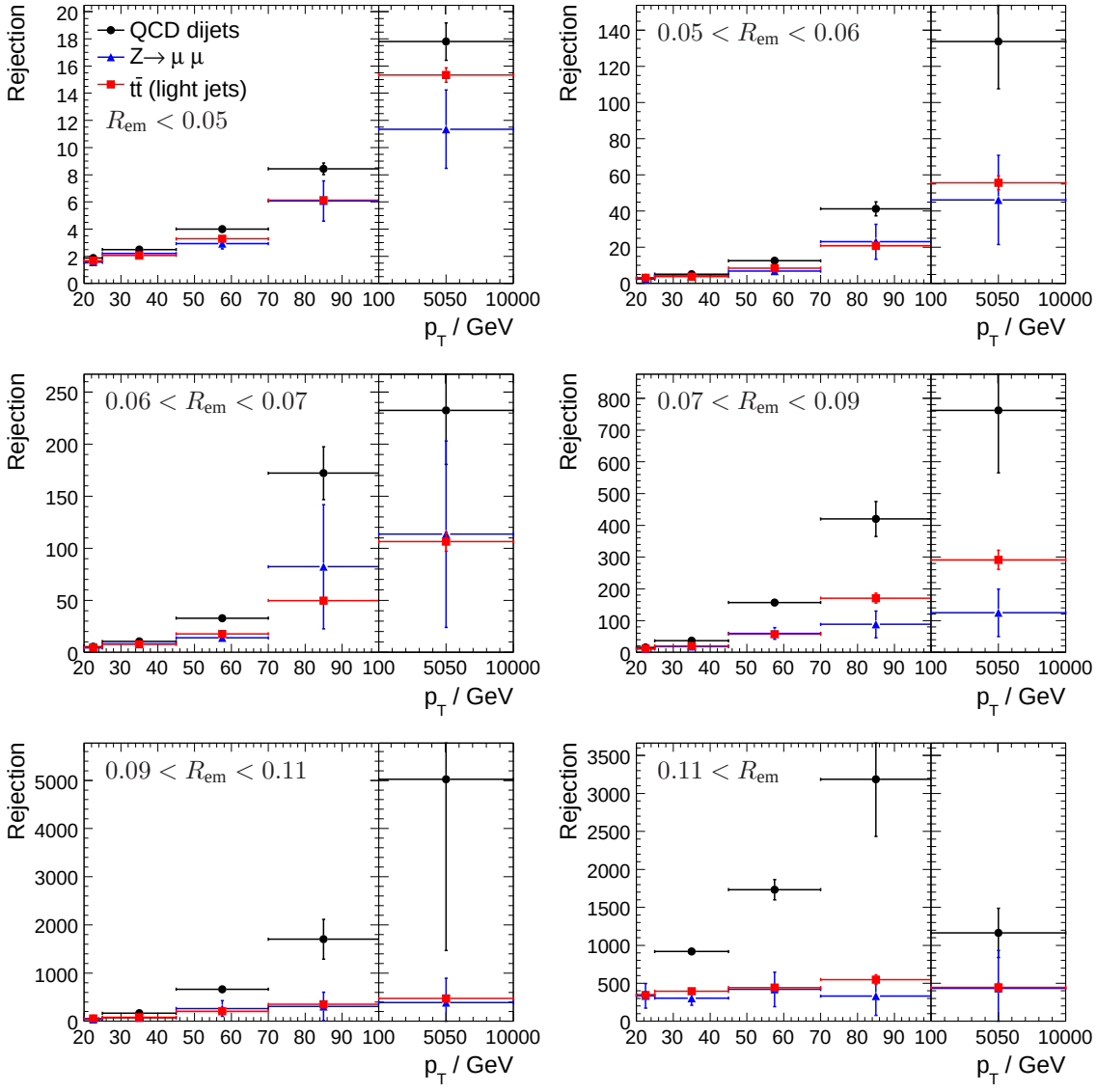

Figure A.2: Dependence of the rejections measured in QCD dijets (black circles), Z+jets (blue triangles) and $t\bar{t}$ (red squares) events on the electromagnetic jet radius R_{em} with the p_{T} dependence in the six R_{em} bins for the likelihood discriminant method (see Table 9.6).

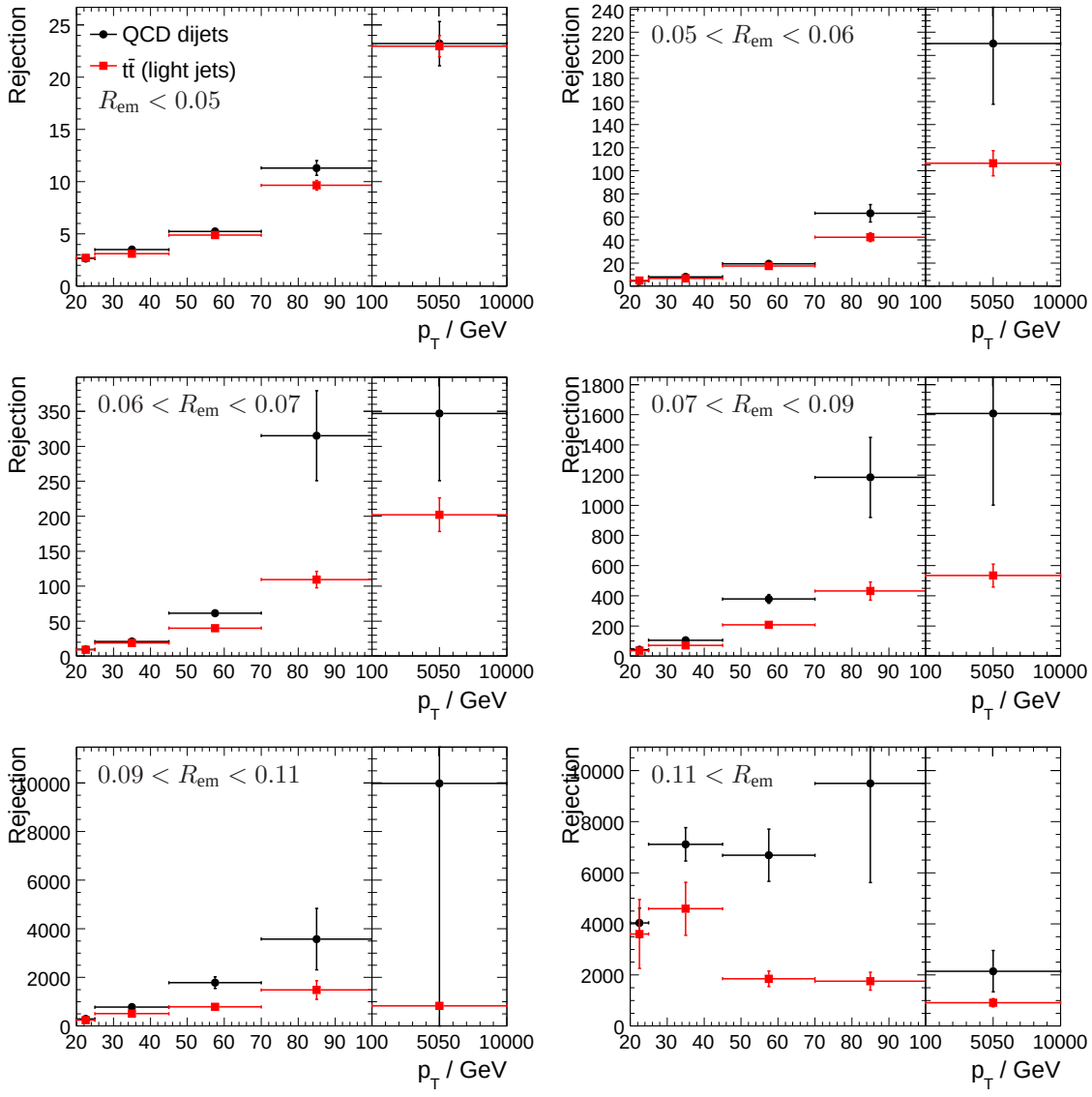

Figure A.3: Dependence of the rejections measured in QCD dijets (black circles) and $t\bar{t}$ (red squares) events on the electromagnetic jet radius R_{em} and the ratio $p_{\mathrm{T}}^{\mathrm{tracks}}/E_{\mathrm{T}}$ with the p_{T} dependence in the six R_{em} bins and the first $p_{\mathrm{T}}^{\mathrm{tracks}}/E_{\mathrm{T}}$ bin for the likelihood discriminant method (see Table 9.6).

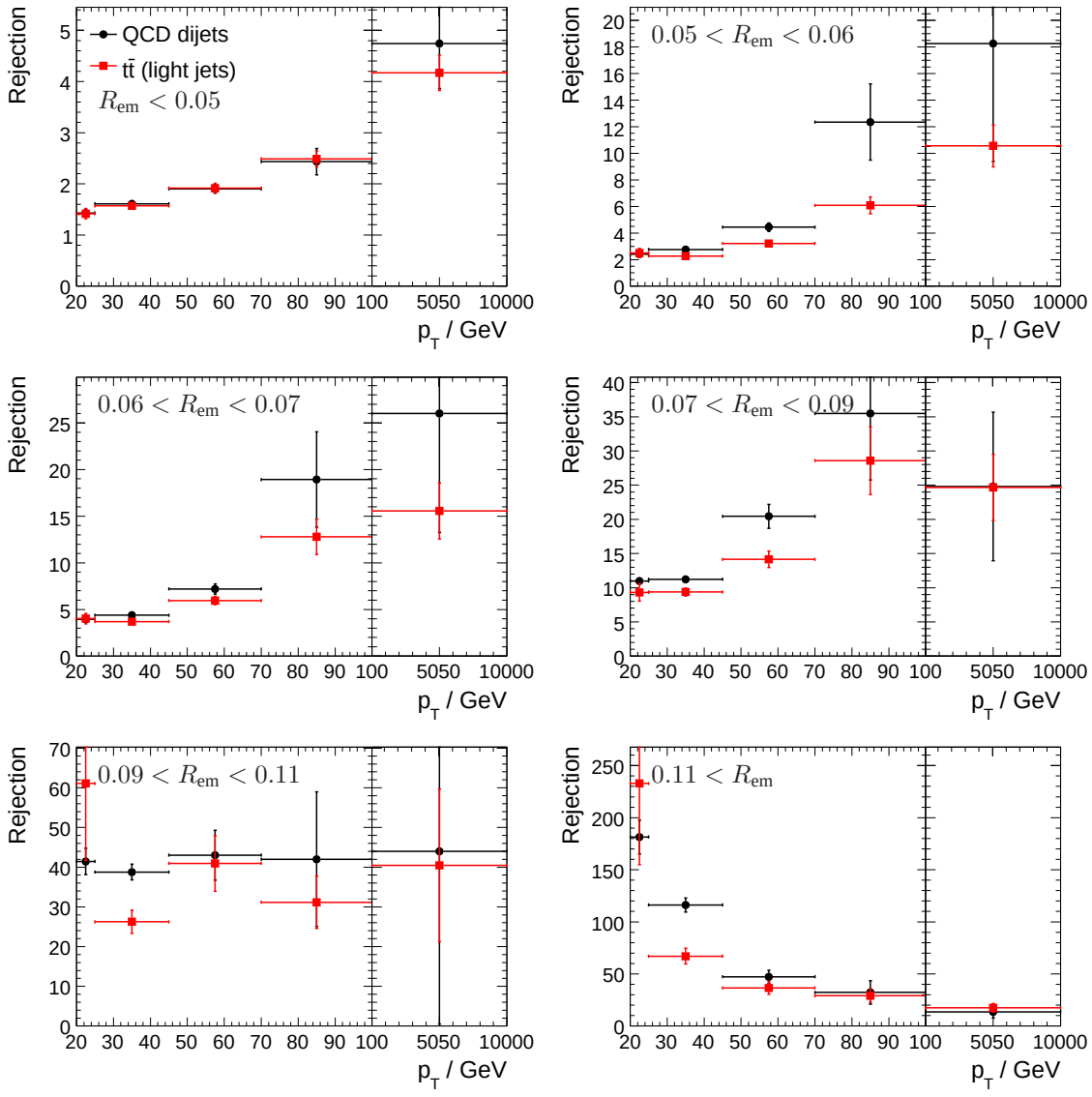

Figure A.4: Dependence of the rejections measured in QCD dijets (black circles) and $t\bar{t}$ (red squares) events on the electromagnetic jet radius R_{em} and the ratio $p_{\mathrm{T}}^{\mathrm{tracks}}/E_{\mathrm{T}}$ with the p_{T} dependence in the six R_{em} bins and the second $p_{\mathrm{T}}^{\mathrm{tracks}}/E_{\mathrm{T}}$ bin for the likelihood discriminant method (see Table 9.6).

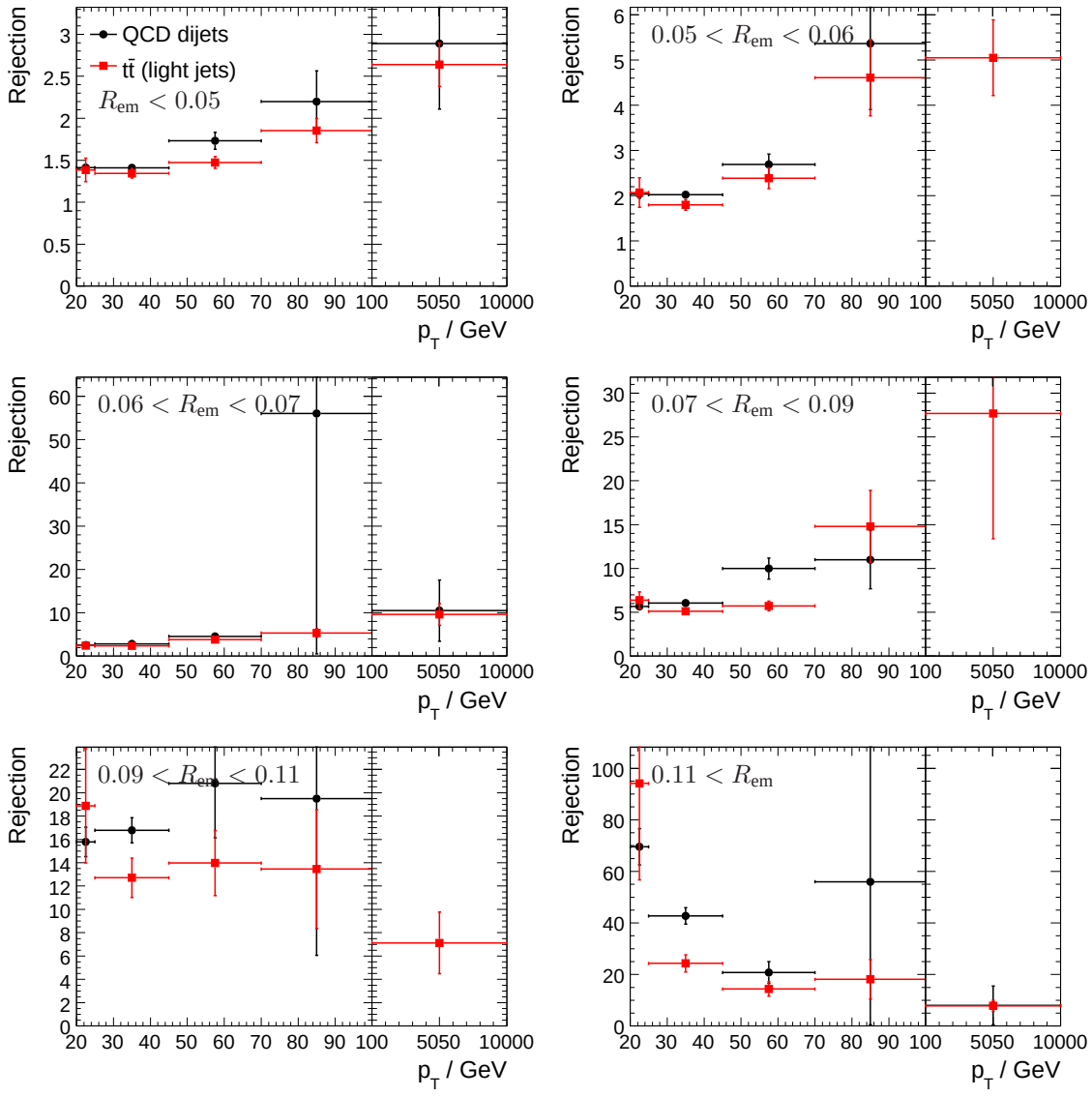

Figure A.5: Dependence of the rejections measured in QCD dijets (black circles) and $t\bar{t}$ (red squares) events on the electromagnetic jet radius R_{em} and the ratio $p_{\mathrm{T}}^{\mathrm{tracks}}/E_{\mathrm{T}}$ with the p_{T} dependence in the six R_{em} bins and the third $p_{\mathrm{T}}^{\mathrm{tracks}}/E_{\mathrm{T}}$ bin for the likelihood discriminant method (see Table 9.6).

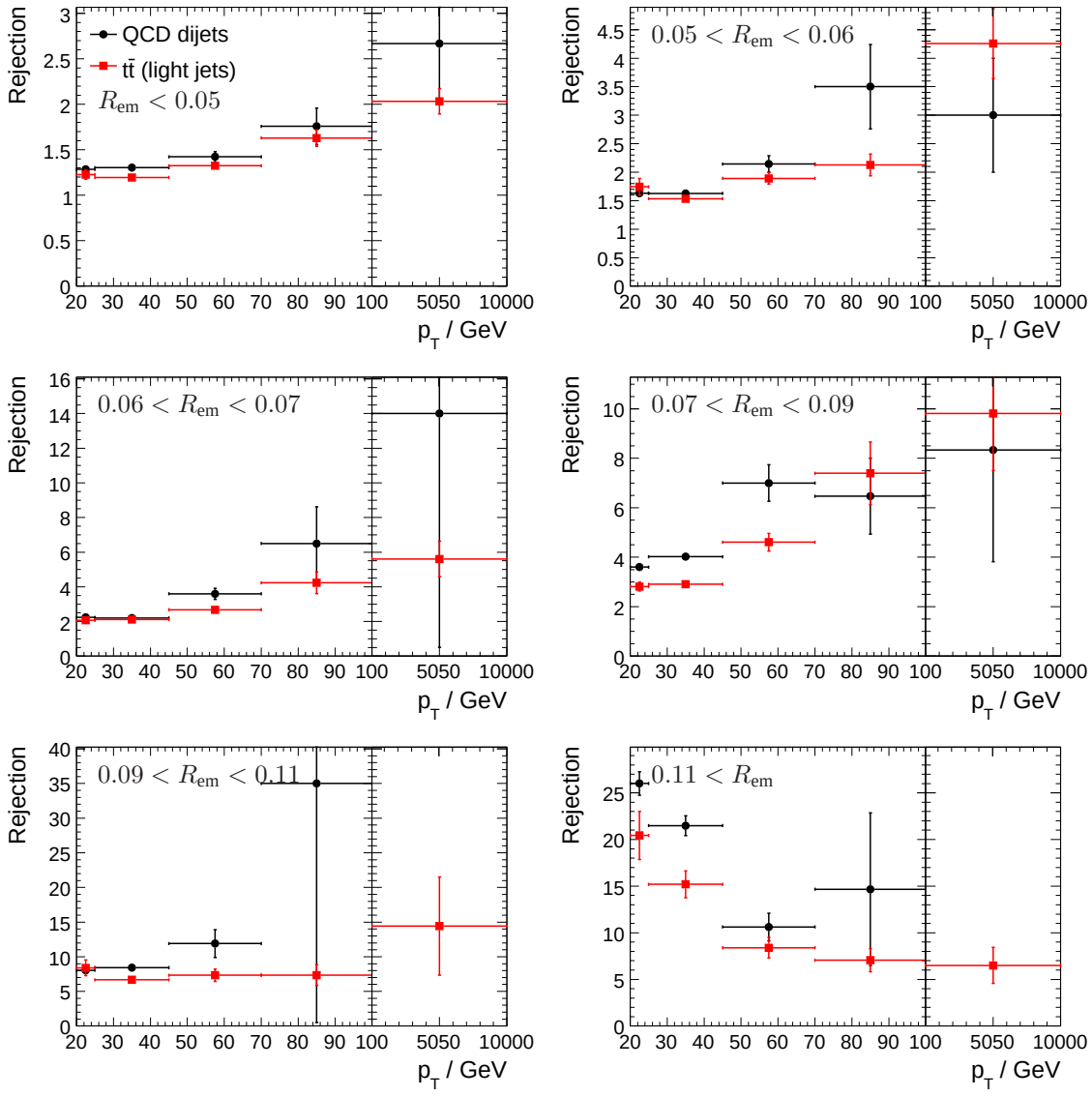

Figure A.6: Dependence of the rejections measured in QCD dijets (black circles) and $t\bar{t}$ (red squares) events on the electromagnetic jet radius R_{em} and the ratio $p_{\mathrm{T}}^{\mathrm{tracks}}/E_{\mathrm{T}}$ with the p_{T} dependence in the six R_{em} bins and the fourth $p_{\mathrm{T}}^{\mathrm{tracks}}/E_{\mathrm{T}}$ bin for the likelihood discriminant method (see Table 9.6).

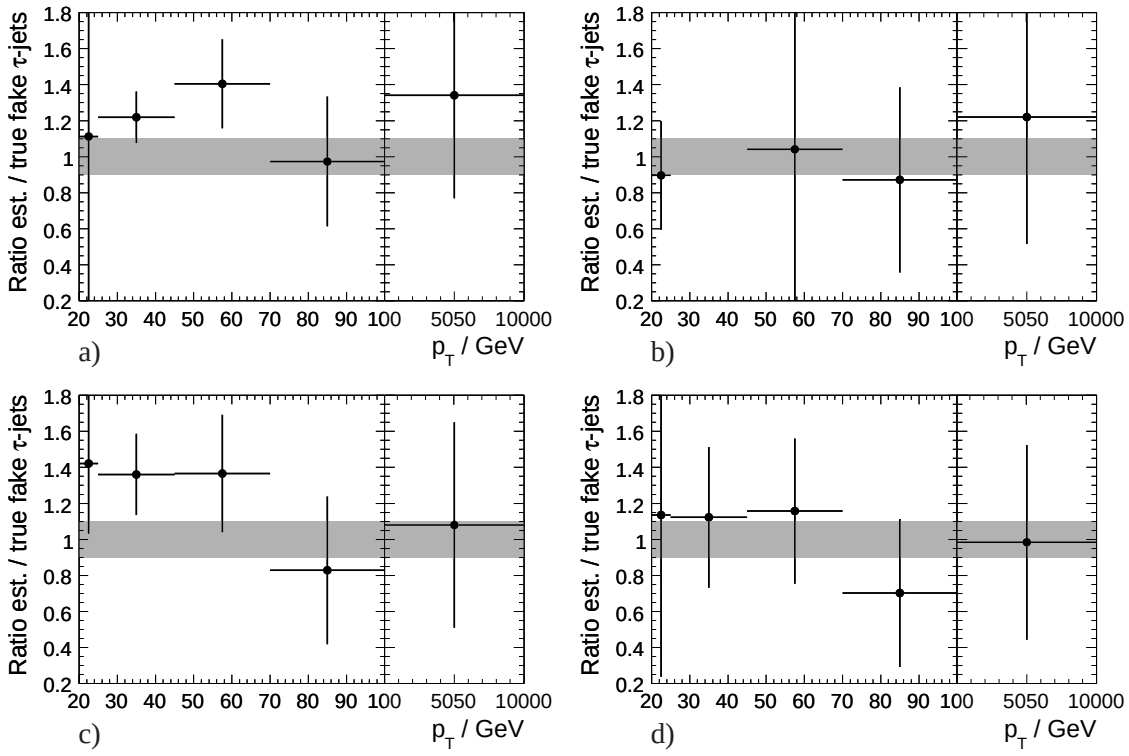

Figure A.7: Ratio of the numbers of estimated and true misidentified τ-jet candidates as a function of p_{T} for the medium requirement of the (a,b,) "safe cuts" and (c,d) likelihood discriminant method using rejections obtained from $Z \rightarrow ee$+jets events.

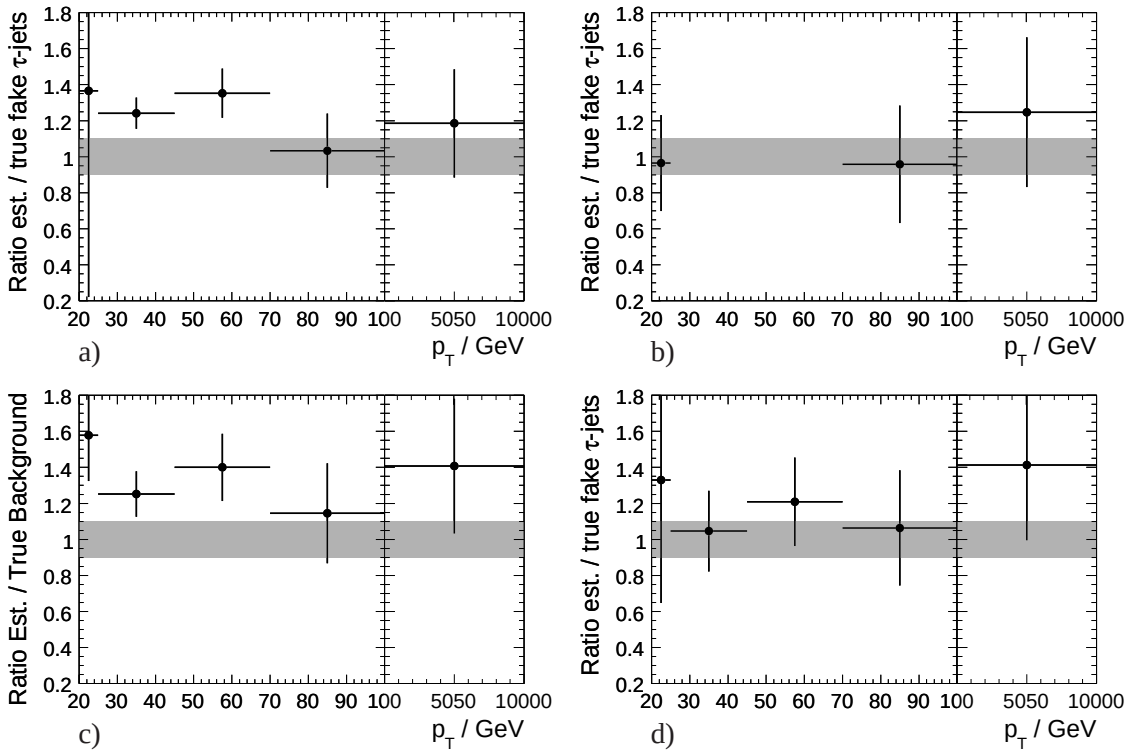

Figure A.8: Ratio of the numbers of estimated and true misidentified τ-jet candidates as a function of p_{T} for the medium requirement of the (a,b,) "safe cuts" and (c,d) likelihood discriminant method using averaged rejections obtained from $Z \rightarrow ee$+jets and $Z \rightarrow \mu\mu$+jets events.

Appendix B

Performance of the τ-Jet and b-Jet Identification

In the following the τ-jet and b-jet reconstruction and identificarion efficiency and misidentification rate as well as the rejection factors of the various background sources are shown as functions of p_{T}, η and azimuthal angle ϕ of the τ-jet and b-jet candidates for the two reconstruction software releases studied (see Chapter 6). Thw two τ-jet identification methods are also compared.

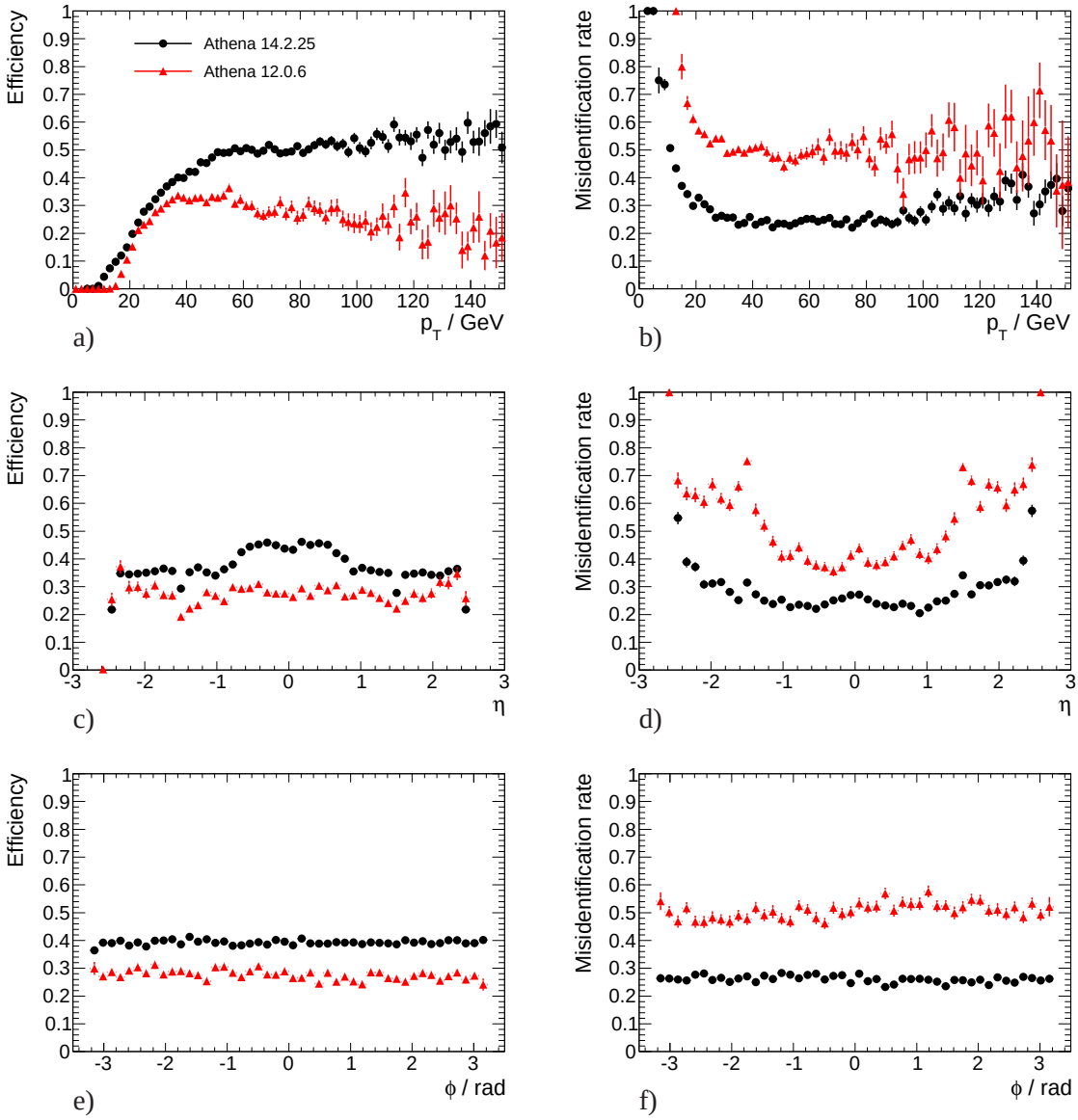

Figure B.1: Performance of the likelihood-based τ-jet identification method in release 12.0.6 and 14.2.25. The p_{T} dependence of (a) efficiency and (b) misidentification rate is shown for $|\eta| < 2.5$, (c), (d), (e) and (f) show the rejections of the τ-jet identification of light parton (u, d, s quark and gluon) jets, electrons, c-jets and b-jets as a function of p_{T}. The red triangles indicate the results for the cut-based, the black circles the ones for the likelihood-based identification method.

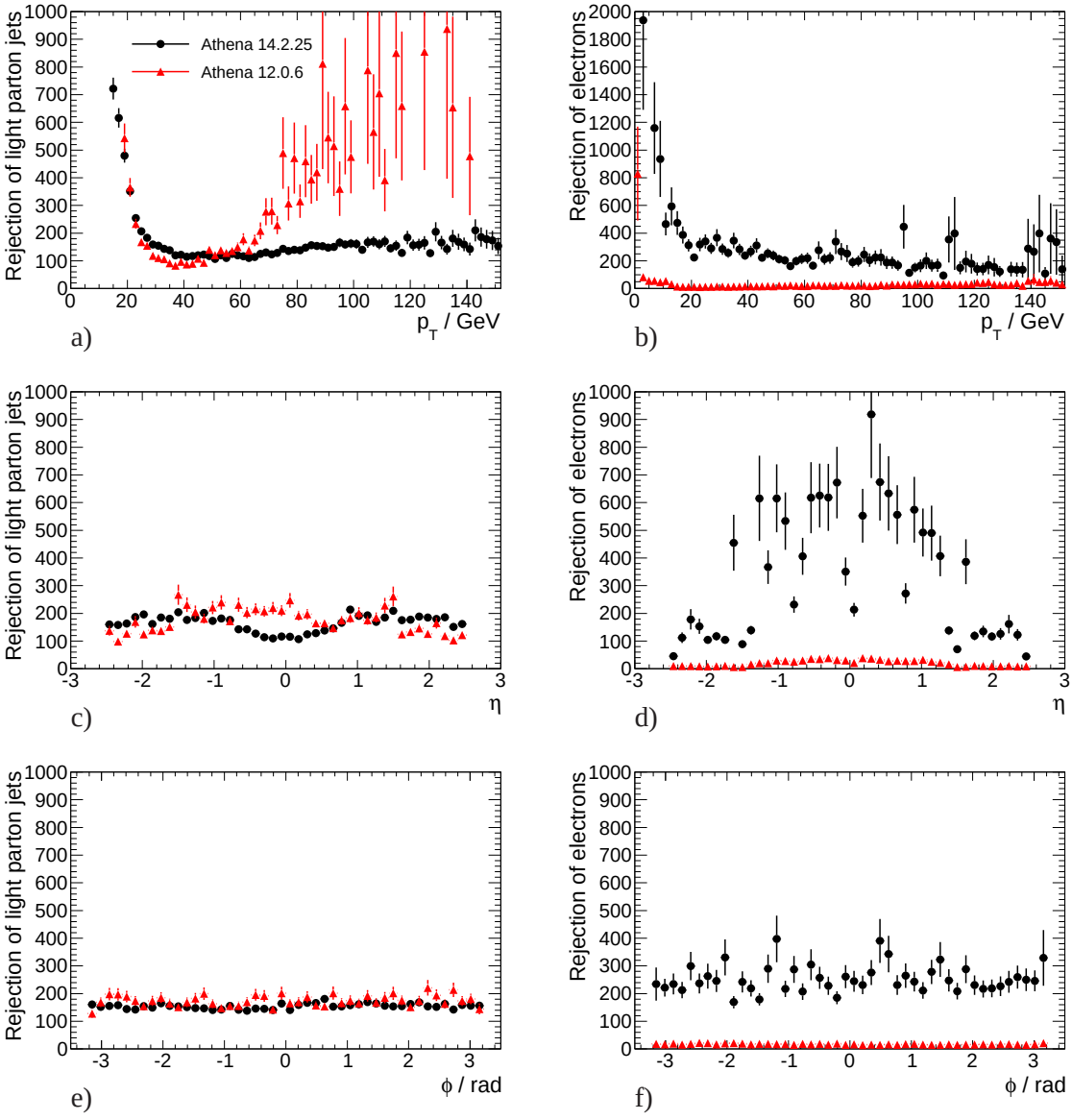

Figure B.2: Rejection of the likelihood based τ-jet identification method. The p_{T} dependence of the rejection of (a) light parton jets and (b) electrons is shown for $|\eta| < 2.5$, (c) and (d) show the η dependence for $p_{\mathrm{T}} > 20\,\mathrm{GeV}$. For the ϕ dependence (e,f) both cuts are applied. The red triangles indicate the results for ATHENA release 12.0.6, the black circles the ones for release 14.2.25.

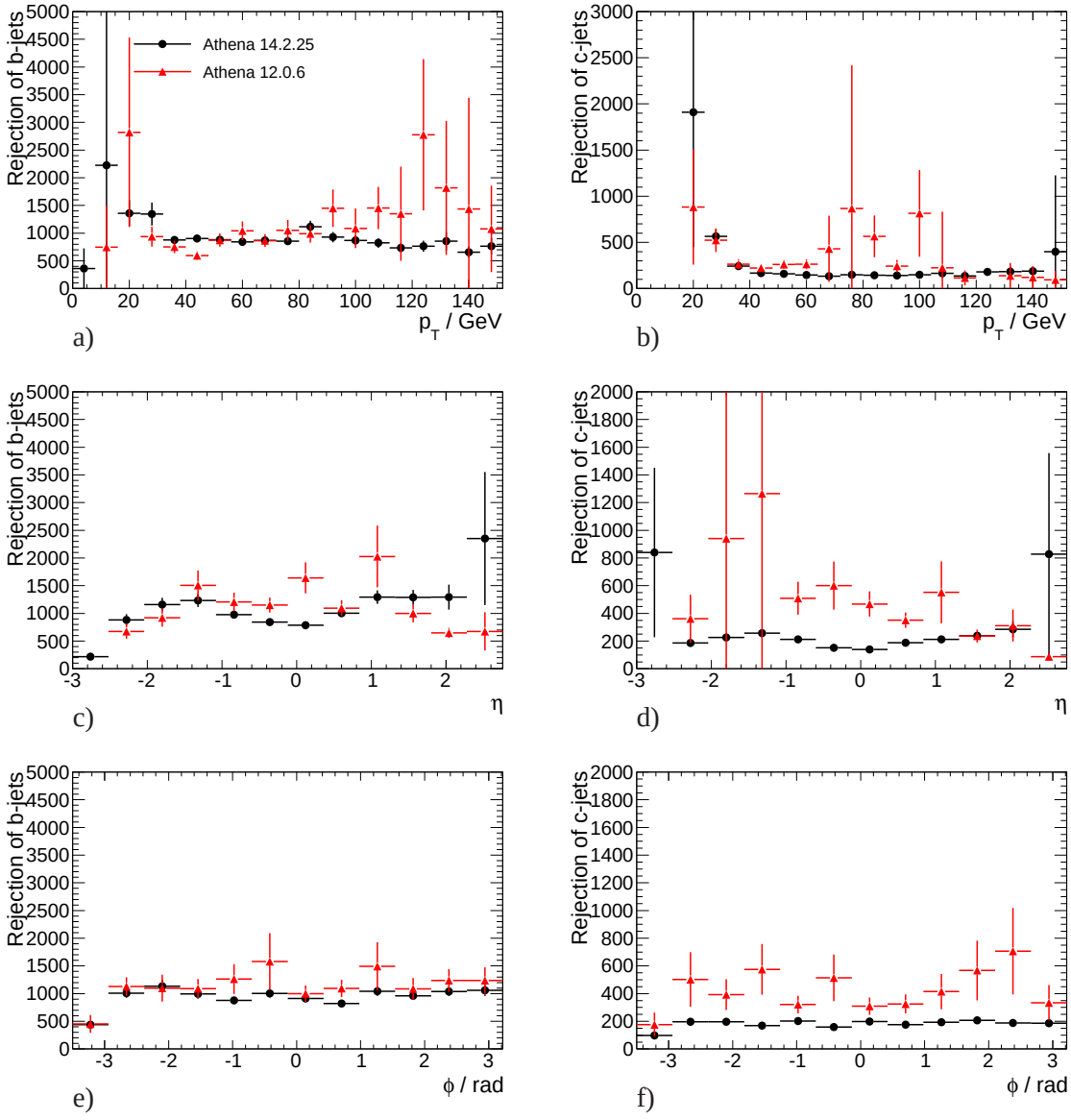

Figure B.3: Rejection of the likelihood based τ-jet identification method. The p_{T} dependence of the rejection of (a) b-jets and (b) c-jets is shown for $|\eta| < 2.5$, (c) and (d) show the η dependence for $p_{\mathrm{T}} > 20\,\mathrm{GeV}$. For the ϕ dependence (e,f) both cuts are applied. The red triangles indicate the results for ATHENA release 12.0.6, the black circles the ones for release 14.2.25.

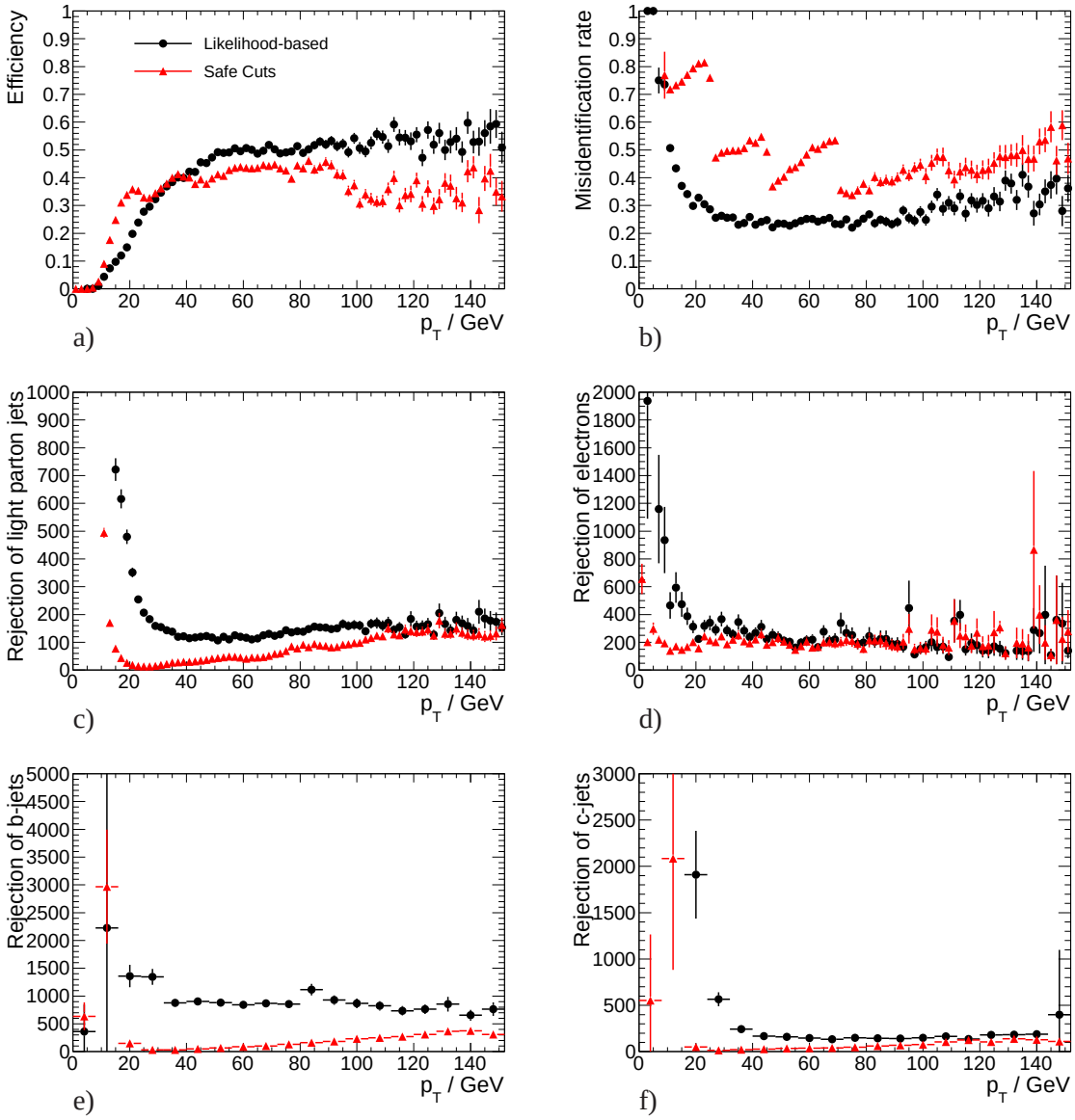

Figure B.4: Performance of the cut-based and the likelihood-based τ-jet identification methods in release 14.2.25. The p_{T} dependence of (a) efficiency and (b) misidentification rate is shown for $|\eta| < 2.5$, (c), (d), (e) and (f) show the rejections of the τ-jet identification of light parton (u, d, s quark and gluon) jets, electrons, c-jets and b-jets as a function of p_{T}. The red triangles indicate the results for the cut-based, the black circles the ones for the likelihood-based identification method.

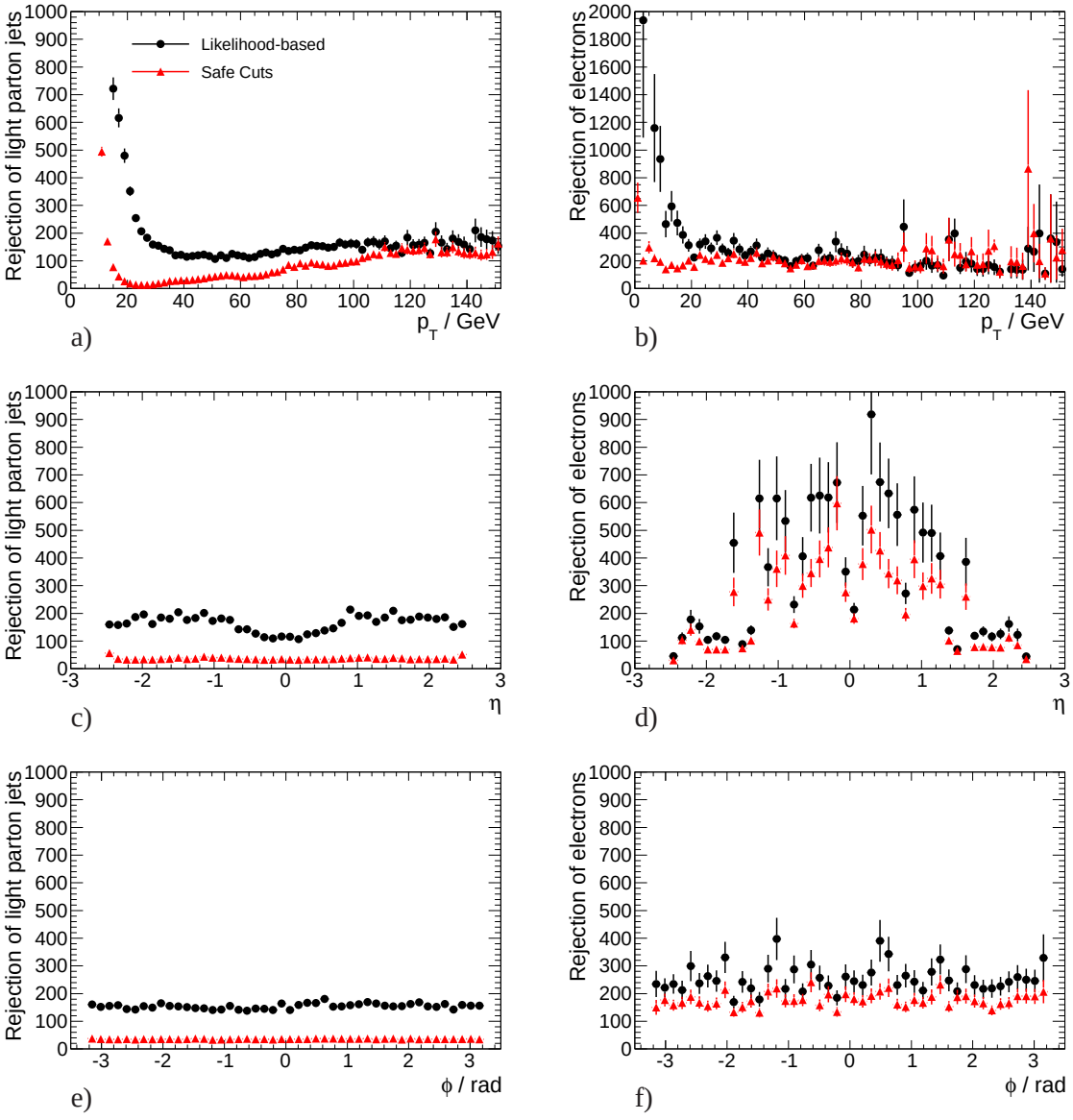

Figure B.5: Rejection of the τ-jet identification method. The p_{T} dependence of the rejection of (a) light parton jets and (b) electrons is shown for $|\eta| < 2.5$, (c) and (d) show the η dependence for $p_{\mathrm{T}} > 20\,\mathrm{GeV}$. For the ϕ dependence (e,f) both cuts are applied. The red triangles indicate the results for ATHENA release 12.0.6, the black circles the ones for release 14.2.25.

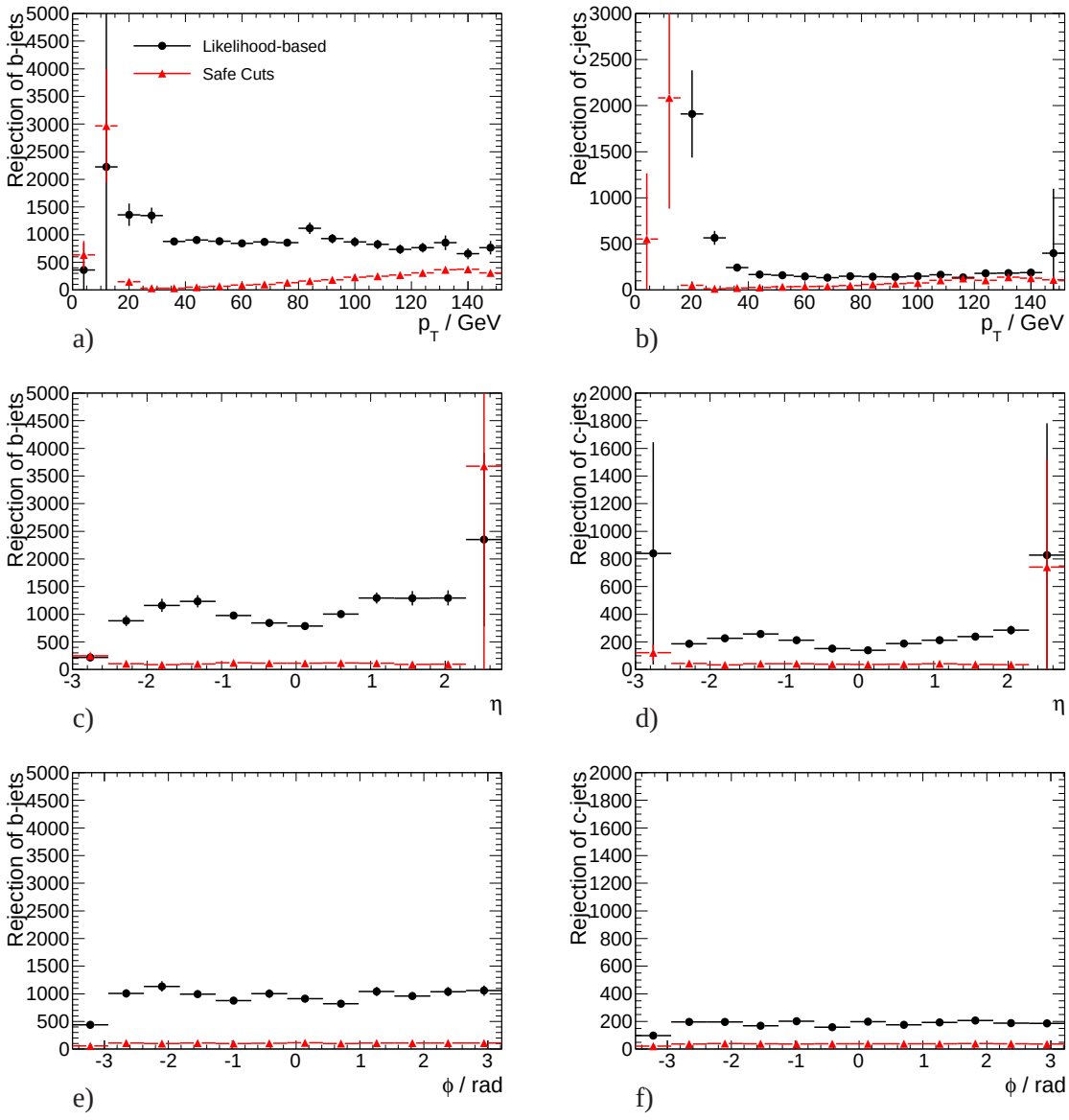

Figure B.6: Rejection of the τ-jet identification method. The p_{T} dependence of the rejection of (a) b-jets and (b) c-jets is shown for $|\eta| < 2.5$, (c) and (d) show the η dependence for $p_{\mathrm{T}} > 20\,\mathrm{GeV}$. For the ϕ dependence (e,f) both cuts are applied. The red triangles indicate the results for ATHENA release 12.0.6, the black circles the ones for release 14.2.25.

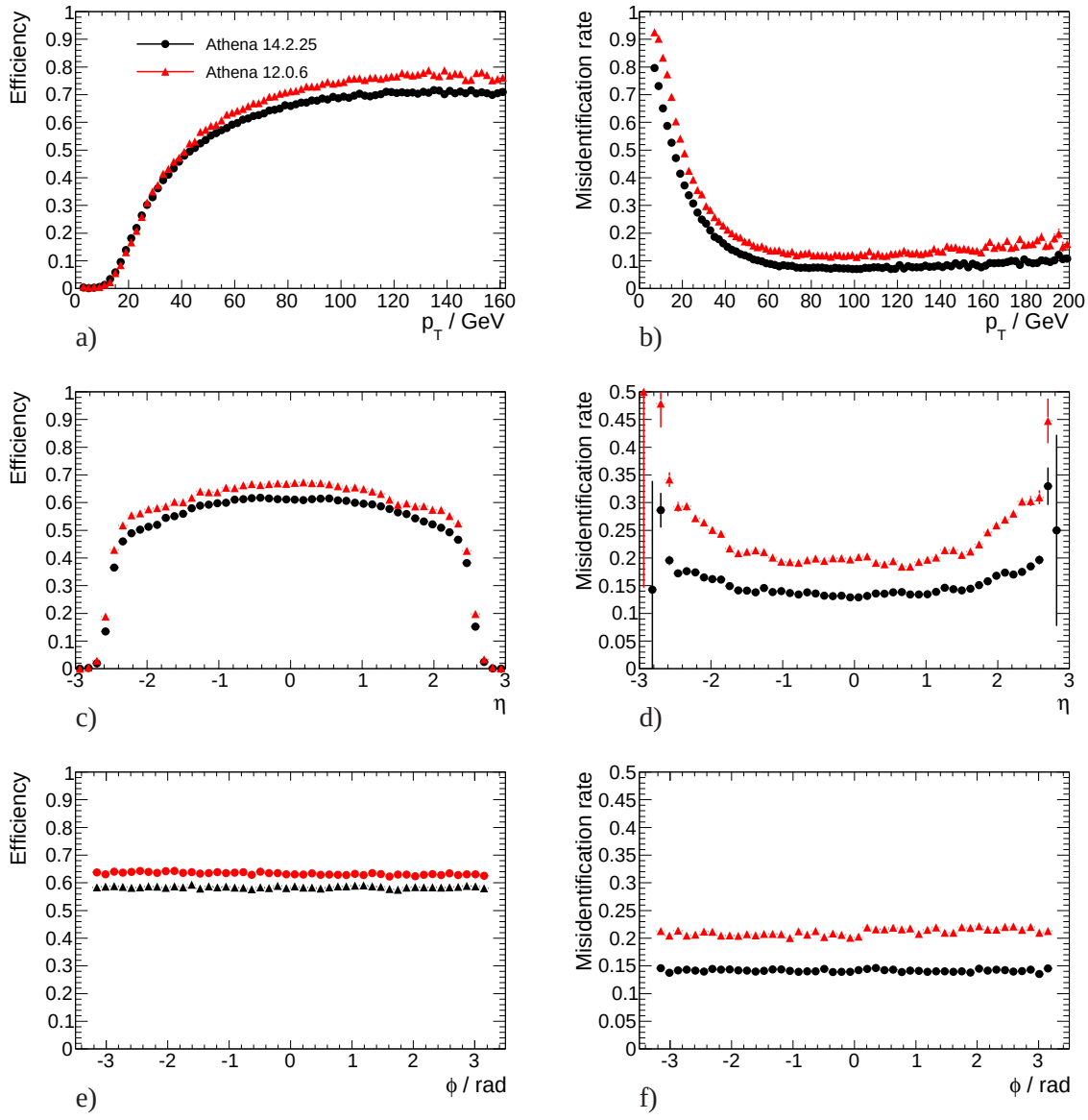

Figure B.7: Performance of the b-jet identification method in releases 12.0.6 and 14.2.25. The p_{T} dependence of (a) efficiency and (b) misidentification rate is shown for $|\eta| < 2.5$, (c) and (d) show the η dependence for $p_{\mathrm{T}} > 20\,\mathrm{GeV}$. For the ϕ dependence (e,f) both cuts are applied. The red triangles indicate the results for ATHENA release 12.0.6, the black circles the ones for release 14.2.25.

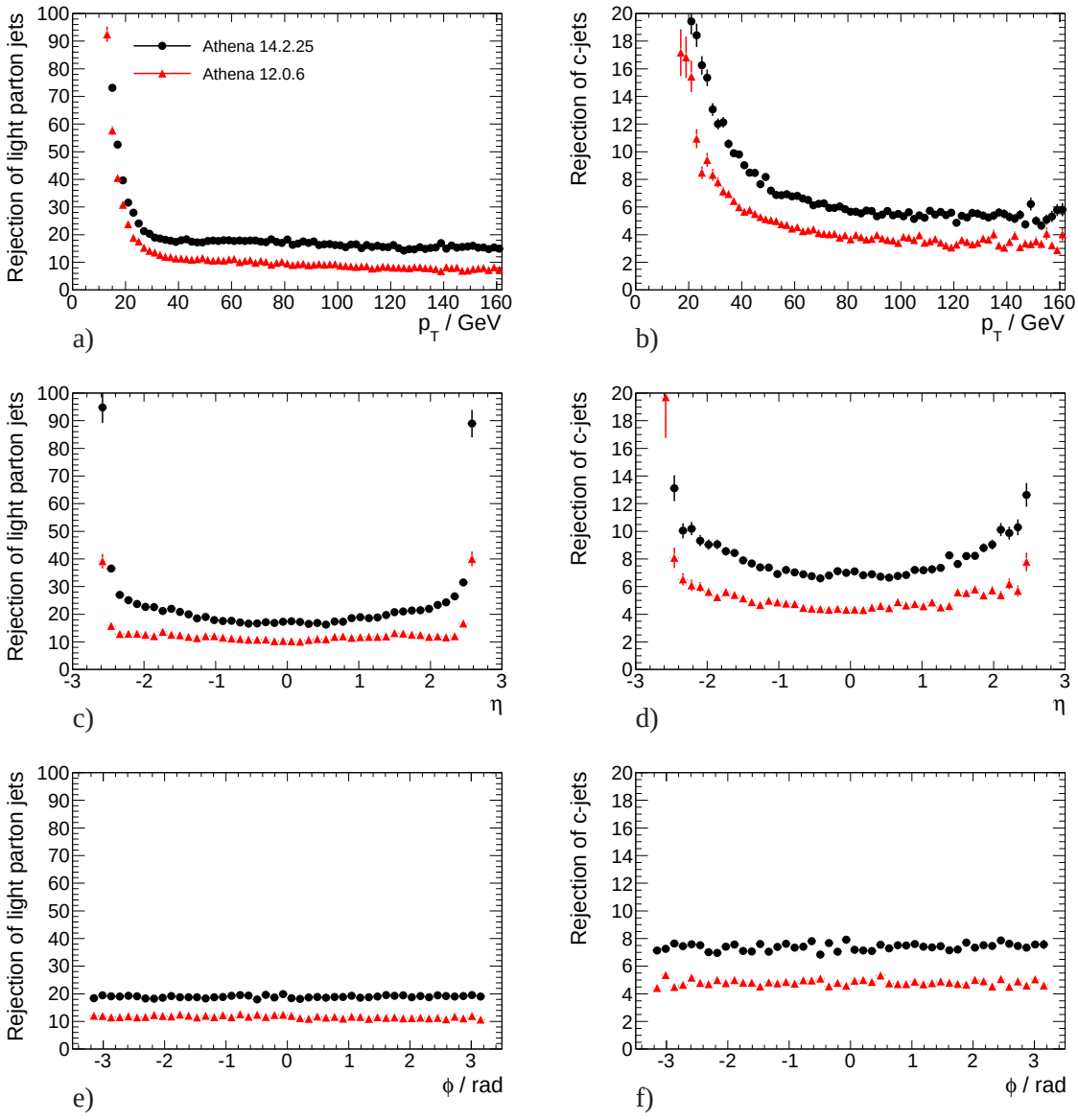

Figure B.8: Rejection of the b-jet identification method. The p_{T} dependence of the rejection of (a) light parton jets and (b) electrons is shown for $|\eta| < 2.5$, (c) and (d) show the η dependence for $p_{\mathrm{T}} > 20\,\mathrm{GeV}$. For the ϕ dependence (e,f) both cuts are applied. The red triangles indicate the results for ATHENA release 12.0.6, the black circles the ones for release 14.2.25.

List of Figures

List of Tables

Bibliography

[1] H. Römer and J. Honerkamp, *Grundlagen der klassischen theoretischen Physik*. Springer, 1986.

[2] F. Halzen and A. D. Martin, *Quarks and Leptons: An Introductory Course in Modern Particle Physics*. Wiley, 1984.

[3] D. Ebert, *Eichtheorien - Grundlagen der Elementarteilchenphysik*. VCH-Verlag, 1989.

[4] S. L. Glashow, *Partial Symmetries of Weak Interactions*, Nucl. Phys. **22** (1961) 579–588.

[5] S. Weinberg, *A Model of Leptons*, Phys. Rev. Lett. **19** (1967) 1264–1266.

[6] A. Salam, *Weak and Electromagnetic Interactions*, originally printed in "Svartholm: Elementary Particle Theory, Proceedings of the Nobel Symposium held 1968 at Lerum, Sweden", Stockholm 1968, 367-377.

[7] H. Fritzsch and M. Gell-Mann, *Current algebra: Quarks and what else?*, eConf **C720906V2** (1972) 135–165, `arXiv:hep-ph/0208010`.

[8] H. Fritzsch, M. Gell-Mann, and H. Leutwyler, *Advantages of the color octet gluon picture*, Physics Letters B **47** (1973) no. 4, 365 – 368.

[9] D. J. Gross and F. Wilczek, *Ultraviolet Behavior of Non-Abelian Gauge Theories*, Phys. Rev. Lett. **30** (1973) 1343–1346.

[10] H. D. Politzer, *Reliable Perturbative Results for Strong Interactions?*, Phys. Rev. Lett. **30** (1973) 1346–1349.

[11] S. Bethke, *Experimental tests of asymptotic freedom*, Prog. Part. Nucl. Phys. **58** (2007) 351–386, `arXiv:hep-ex/0606035`.

[12] P. W. Higgs, *Broken symmetries, massless particles and gauge fields*, Phys. Lett. **12** (1964) 132–133.

[13] P. W. Higgs, *Broken Symmetries and the Masses of Gauge Bosons*, Phys. Rev. Lett. **13** (1964) 508–509.

[14] F. Englert and R. Brout, *Broken Symmetry and the Mass of Gauge Vector Mesons*, Phys. Rev. Lett. **13** (1964) 321–322.

[15] G. S. Guralnik, C. R. Hagen, and T. W. B. Kibble, *Global Conservation Laws and Massless Particles*, Phys. Rev. Lett. **13** (1964) 585–587.

[16] Particle Data Group Collaboration, C. Amsler et al., *Review of particle physics*, Phys. Lett. **B667** (2008) 1.

[17] K. Riesselmann, *Limitations of a standard model Higgs boson*, DESY-97-222 (1997), arXiv:hep-ph/9711456.

[18] LEP Working Group for Higgs boson searches Collaboration, R. Barate et al., *Search for the standard model Higgs boson at LEP*, Phys. Lett. **B565** (2003) 61–75, arXiv:hep-ex/0306033.

[19] J. Baglio and A. Djouadi, *Predictions for Higgs production at the Tevatron and the associated uncertainties*, arXiv:1003.4266 [hep-ph].

[20] ALEPH Collaboration, CDF Collaboration, DØ Collaboration, DELPHI Collaboration, L3 Collaboration, OPAL Collaboration, SLD Collaboration, LEP Electroweak Working Group, Tevatron Electroweak Working Group, SLD electroweak heavy flavour groups, *Precision Electroweak Measurements and Constraints on the Standard Model*, arXiv:0911.2604 [hep-ex].

[21] N. Cabibbo, *Unitary Symmetry and Leptonic Decays*, Phys. Rev. Lett. **10** (1963) no. 12, 531–533.

[22] M. Kobayashi and T. Maskawa, *CP Violation in the Renormalizable Theory of Weak Interaction*, Prog. Theor. Phys. **49** (1973) 652–657.

[23] G. Bertone, D. Hooper, and J. Silk, *Particle dark matter: Evidence, candidates and constraints*, Phys. Rep. **405** (2005) 279–390, arXiv:hep-ph/0404175.

[24] S. P. Martin, *A Supersymmetry Primer*, arXiv:hep-ph/9709356.

[25] J. Wess and B. Zumino, *Supergauge transformations in four dimensions*, Nuclear Physics **B70** (1974) no. 1, 39 – 50.

[26] S. R. Coleman and J. Mandula, *All possible Symmetries of the S Matrix*, Phys. Rev. **159** (1967) 1251–1256.

[27] R. Haag, J. T. Lopuszanski, and M. Sohnius, *All Possible Generators Of Supersymmetries Of The S Matrix*, Nucl. Phys. **B88** (1975) 257.

[28] H. P. Nilles, *Supersymmetry, supergravity and particle physics*, Physics Reports **110** (1984) no. 1-2, 1 – 162.

[29] Higgs Working Group Collaboration, M. S. Carena et al., *Report of the Tevatron Higgs working group*, arXiv:hep-ph/0010338.

[30] ATLAS HLT/DAQ/DCS Group, *ATLAS high-level trigger, data-acquisition and controls: Technical Design Report*, CERN-LHCC-2003-022, CERN, Geneva, 2003. http://cdsweb.cern.ch/record/616089.

[31] H1 Collaboration, F. D. Aaron et al., *Combined Measurement and QCD Analysis of the Inclusive ep Scattering Cross Sections at HERA*, JHEP **01** (2010) 109, arXiv:0911.0884 [hep-ex].

[32] J. F. Gunion, R. Vega, and J. Wudka, *Higgs triplets in the standard model*, Phys. Rev. **D42** (1990) no. 5, 1673–1691.

[33] N. Arkani-Hamed, A. G. Cohen, and H. Georgi, *Electroweak symmetry breaking from dimensional deconstruction*, Phys. Lett. **B513** (2001) 232–240, arXiv:hep-ph/0105239.

[34] J. C. Pati and A. Salam, *Lepton number as the fourth color*, Phys. Rev. **D10** (1974) no. 1, 275–289.

[35] M. S. Carena, S. Heinemeyer, C. E. M. Wagner, and G. Weiglein, *Suggestions for improved benchmark scenarios for Higgs- boson searches at LEP2*, arXiv:hep-ph/9912223.

[36] M. Frank et al., *The Higgs boson masses and mixings of the complex MSSM in the Feynman-diagrammatic approach*, JHEP **02** (2007) 047, arXiv:hep-ph/0611326.

[37] S. Heinemeyer, W. Hollik, and G. Weiglein, *FeynHiggs: a program for the calculation of the masses of the neutral CP-even Higgs bosons in the MSSM*, Comput. Phys. Commun. **124** (2000) 76–89, arXiv:hep-ph/9812320.

[38] M. Drees, E. Ma, P. N. Pandita, D. P. Roy, and S. K. Vempati, *Light charged Higgs bosons in supersymmetric models*, Physics Letters B **433** (1998) no. 3-4, 346 – 354.

[39] R. Bonciani, S. Catani, M. L. Mangano, and P. Nason, *NLL resummation of the heavy-quark hadroproduction cross- section*, Nucl. Phys. **B529** (1998) 424–450, arXiv:hep-ph/9801375.

[40] T. Plehn, *Charged Higgs boson production in bottom gluon fusion*, Phys. Rev. **D67** (2003) 014018, arXiv:hep-ph/0206121.

[41] S. Dittmaier, M. Kramer, M. Spira, and M. Walser, *Charged-Higgs-boson production at the LHC: NLO supersymmetric QCD corrections*, arXiv:0906.2648 [hep-ph].

[42] ATLAS Collaboration, G. Aad et al., *Expected performance of the ATLAS experiment: detector, trigger and physics*, CERN-OPEN-2008-020, CERN, Geneva, September, 2008. arXiv:0901.0512.

[43] A. G. Akeroyd, A. Arhrib, and Q.-S. Yan, *Charged Higgs in the NMSSM*, arXiv:0812.4704 [hep-ph].

[44] CDF Collaboration, T. Aaltonen et al., *Search for charged Higgs bosons in decays of top quarks in $p - \bar{p}$ collisions at $\sqrt{s} = 1.96$ TeV*, Phys. Rev. Lett. **103** (2009) 101803, arXiv:0907.1269 [hep-ex].

[45] DØ Collaboration, V. M. Abazov et al., *Search for charged Higgs bosons in decays of top quarks*, Phys. Rev. **D80** (2009) 051107, arXiv:0906.5326 [hep-ex].

[46] LEP Higgs Working Group for Higgs boson searches, *Search for charged Higgs bosons: Preliminary combined results using LEP data collected at energies up to 209 GeV*, arXiv:hep-ex/0107031.

[47] ALEPH Collaboration, A. Heister et al., *Search for charged Higgs bosons in e^+e^- collisions at energies up to $\sqrt{s} = 209$ GeV*, Phys. Lett. **B543** (2002) 1–13, arXiv:hep-ex/0207054.

[48] DELPHI Collaboration, J. Abdallah et al., *Search for charged Higgs bosons at LEP in general two Higgs doublet models*, Eur. Phys. J. **C34** (2004) 399–418, arXiv:hep-ex/0404012.

[49] L3 Collaboration, P. Achard et al., *Search for charged Higgs bosons at LEP*, Phys. Lett. **B575** (2003) 208–220, arXiv:hep-ex/0309056.

[50] OPAL Collaboration, G. Abbiendi et al., *Search for Charged Higgs Bosons in e^+e^- Collisions at $\sqrt{s} = 189 - 209$ GeV*, arXiv:0812.0267 [hep-ex].

[51] UTfit Collaboration, M. Bona et al., *An Improved Standard Model Prediction Of BR(B$\to \tau\nu$) And Its Implications For New Physics*, arXiv:0908.3470 [hep-ph].

[52] U. Haisch, *$\bar{B} \to X_s\gamma$: Standard Model and Beyond*, arXiv:0805.2141 [hep-ph].

[53] W.-S. Hou, *Enhanced charged Higgs boson effects in $B^- \to \tau\overline{\nu}, \mu\overline{\nu}$ and $b \to \tau\overline{\nu} + X$*, Phys. Rev. D **48** (1993) no. 5, 2342–2344.

[54] L. Evans et al., *LHC Machine*, JINST **3** (2008) S08001.

[55] ALICE Collaboration, K. Aamodt et al., *The ALICE experiment at the CERN LHC*, JINST **3** (2008) S08002.

[56] LHCb Collaboration, A. A. Alves et al., *The LHCb Detector at the LHC*, JINST **3** (2008) S08005.

[57] ATLAS Collaboration, G. Aad et al., *The ATLAS Experiment at the CERN Large Hadron Collider*, JINST **3** (2008) S08003.

[58] CMS Collaboration, R. Adolphi et al., *The CMS experiment at the CERN LHC*, JINST **3** (2008) S08004.

[59] N. Arkani-Hamed, S. Dimopoulos, and G. R. Dvali, *The hierarchy problem and new dimensions at a millimeter*, Phys. Lett. **B429** (1998) 263–272, arXiv:hep-ph/9803315.

[60] ATLAS Computing Group, *ATLAS Computing: Technical Design Report*, CERN-LHCC-2005-022, CERN, Geneva, 2005. http://cdsweb.cern.ch/record/837738.

[61] GEANT4 Collaboration, S. Agostinelli et al., *GEANT4: A simulation toolkit*, Nucl. Instrum. Meth. **A506** (2003) 250–303.

[62] T. Sjostrand, S. Mrenna, and P. Skands, *PYTHIA 6.4 Physics and Manual*, JHEP **05** (2006) 026, arXiv:hep-ph/0603175.

[63] M. L. Mangano, M. Moretti, F. Piccinini, R. Pittau, and A. D. Polosa, *ALPGEN, a generator for hard multiparton processes in hadronic collisions*, JHEP **07** (2003) 001, arXiv:hep-ph/0206293.

[64] G. Corcella et al., *HERWIG 6.5: an event generator for Hadron Emission Reactions With Interfering Gluons (including supersymmetric processes)*, JHEP **01** (2001) 010, arXiv:hep-ph/0011363.

[65] M. L. Mangano, M. Moretti, and R. Pittau, *Multijet matrix elements and shower evolution in hadronic collisions: $Wb\bar{b}$ + n jets as a case study*, Nucl. Phys. **B632** (2002) 343–362, arXiv:hep-ph/0108069.

[66] J. M. Butterworth, J. R. Forshaw, and M. H. Seymour, *Multiparton interactions in photoproduction at HERA*, Z. Phys. **C72** (1996) 637–646, arXiv:hep-ph/9601371.

[67] S. Frixione and B. R. Webber, *Matching NLO QCD computations and parton shower simulations*, JHEP **06** (2002) 029, arXiv:hep-ph/0204244.

[68] B. P. Kersevan and I. Hinchliffe, *A consistent prescription for the production involving massive quarks in hadron collisions*, JHEP **09** (2006) 033, arXiv:hep-ph/0603068.

[69] S. Jadach, J. H. Kuhn, and Z. Was, *TAUOLA: A Library of Monte Carlo programs to simulate decays of polarized tau leptons*, Comput. Phys. Commun. **64** (1990) 275–299.

[70] E. Barberio and Z. Was, *PHOTOS: A Universal Monte Carlo for QED radiative corrections. Version 2.0*, Comput. Phys. Commun. **79** (1994) 291–308.

[71] S. Hassani et al., *A muon identification and combined reconstruction procedure for the ATLAS detector at the LHC using the (MUONBOY, STACO, MuTag) reconstruction packages*, Nucl. Instrum. Meth. **A572** (2007) 77–79.

[72] T. Lagouri et al., *A muon identification and combined reconstruction procedure for the ATLAS detector at the LHC at CERN*, IEEE Trans. Nucl. Sci. **51** (2004) 3030–3033.

[73] ATLAS Collaboration, *Reconstruction and Identification of Electrons*, ATL-PHYS-PUB-2009-004. ATL-COM-PHYS-2009-170, CERN, Geneva, April, 2009.

[74] W. Lampl, S. Laplace, D. Lelas, P. Loch, H. Ma, S. Menke, S. Rajagopalan, D. Rousseau, S. Snyder, and G. Unal, *Calorimeter Clustering Algorithms: Description and Performance*, ATL-LARG-PUB-2008-002. ATL-COM-LARG-2008-003, CERN, Geneva, April, 2008.

[75] G. C. Blazey et al., *Run II jet physics*, arXiv:hep-ex/0005012.

[76] H1 Calorimeter Group Collaboration, B. Andrieu et al., *The H1 liquid argon calorimeter system*, Nucl. Instrum. Meth. **A336** (1993) 460–498.

[77] M. Heldmann and D. Cavalli, *An improved tau-Identification for the ATLAS experiment*, ATL-PHYS-PUB-2006-008. ATL-COM-PHYS-2006-010, CERN, Geneva, December, 2005.

[78] A. Christov, Y. Coadou, Z. Czyczula, M. Janus, L. Janyst, A. Kaczmarska, A. Kalinowski, J. Komaragiri, S. Lai, W. Mader, N. Meyer, E. Richter-Was, C. Ruwiedel, and M. Wolter, *Performance of the tau reconstruction and identification algorithm with release 14.2.20 and mc08 data*, ATL-COM-PHYS-2009-229, CERN, Geneva, April, 2009.

[79] A. Kalinowski and K. Benslama, *Tau identification with the logarithmic likelihood method*, ATL-PHYS-INT-2008-037. ATL-COM-PHYS-2008-125, CERN, Geneva, September, 2008.

[80] Z. Czyczula and M. Dam, *Cut-based electron veto algorithm for the track-seeded part of tauRec*, ATL-PHYS-INT-2009-023. ATL-COM-PHYS-2009-077, CERN, Geneva, February, 2009.

[81] ATLAS Collaboration, P. Bechtle, B. Gosdzik, and S. Lai, *Cut based identification of hadronic tau decays*, ATL-PHYS-PUB-2010-001, CERN, Geneva, Jan, 2010.

[82] T. Pierzchala, E. Richter-Was, Z. Was, and M. Worek, *Spin effects in tau-lepton pair production at LHC*, Acta Phys. Polon. **B32** (2001) 1277–1296, arXiv:hep-ph/0101311.

[83] K. Assamagan, S. Behar, E. Coniavitis, M. A. Dufour, T. Ehrich, M. Flechl, E. Gross, J. Lane, B. Mohn, S. Mohrdieck-Möck, C. Potter, S. Robertson, Y. Rozen, A. Sopczak, M. Talby, B. Vachon, T. Vickey, O. Vitells, U. K. Yang, and R. Zaidan, *ATLAS Charged Higgs Boson Searches*, ATL-PHYS-INT-2008-046. ATL-COM-PHYS-2008-090, CERN, Geneva, June, 2008.

[84] F. Abe et al., *Evidence for top quark production in $p\bar{p}$ collisions at $\sqrt{s} = 1.8$ TeV*, Phys. Rev. D **50** (1994) no. 5, 2966–3026.

[85] N. Möser, M. Schmitz, J. Kroseberg, M. Schumacher, and N. Wermes, *Estimation of $Z \to \tau\tau$ Background in VBF $H \to \tau\tau$ Searches from $Z \to \mu\mu$ Data using an Embedding Technique*, ATL-PHYS-INT-2009-109. ATL-COM-PHYS-2009-446, CERN, Geneva, December, 2009.

[86] M. Elsing and C. Schmitt. Private communication, 2009.

[87] F. Kohn, C. Hensel, J. Meyer, and A. Quadt, *ATLAS High-Level Muon Trigger Studies – Development of a Method to Extract Trigger Efficiencies from Data*, ATL-DAQ-INT-2008-001. ATL-COM-DAQ-2008-005, CERN, Geneva, July, 2008.

[88] G. Alexander et al., *A direct observation of quark-gluon jet differences at LEP*, Physics Letters B **265** (1991) no. 3-4, 462 – 474.

[89] K. Shizuya and S. H. H. Tye, *Gluon Jets from Quantum Chromodynamics*, Phys. Rev. Lett. **41** (1978) no. 12, 787–791.

[90] P. Bechtle et al., *Identification of hadronic tau decays with ATLAS detector*, ATL-PHYS-INT-2008-003. ATL-COM-PHYS-2007-066, CERN, Geneva, September, 2007.

[91] A. Kalinowski and A. Nikitenko, *Measurement of the tau tag efficiency using the $Z \to \tau\tau \to \mu$ + hadrons +X events*, CMS-NOTE-2006-074. CERN-CMS-NOTE-2006-074, CERN, Geneva, May, 2006.

[92] O. Vitells and G. Eilam, *Statistical combination of charged Higgs channels in ATLAS*, Proceedings of Science **038** (2008) .

[93] ATLAS Collaboration, *Statistical Combination of Several Important Standard Model Higgs Boson Search Channels.*, ATL-PHYS-PUB-2009-063. ATL-COM-PHYS-2009-222, CERN, Geneva, April, 2009.

[94] S. S. Wilks, *The Large-Sample Distribution of the Likelihood Ratio for Testing Composite Hypotheses*, The Annals of Mathematical Statistics **9** (1938) no. 1, 60–62.

Acknowledgements

The last page is devoted to the people who made this thesis possible and my time in the ATLAS collaboration such a valuable experience. It is impressive how many nice people are working in this community.
First, I am indebted to Hubert Kroha for giving me the possibility to prepare my thesis in the ATLAS MDT group at the Max-Planck-Institute in Munich. A big "THANKS!" goes to Susanne Mohrdieck-Möck for her great supervision and help at every day during almost three years. Next I would like to thank countless people from the Institute who made my stay nice and enjoyable. These are especially my two office mates, Jörg alias Jorgino and Sebastian, who kept me company for a long time and prepared me with lots of inside knowledge of the FC Bayern. I would like to thank Steffen for countless table tennis matches and of course Manfred who prepared us with a hot plate, a coffee machine and soap to clean it. Next there are the Italians: Daniela, Alessia, Federica and Daniele – grazie per il buonissimo tempo con voi. I would also like to thank the second Jörg alias Jorgone for the nice times at CERN, I will always remember our post-lunch Armagetron battles. I should not forget the ATLAS charged Higgs community, especially Martin and Elias, for many fruitful discussions in the meetings and conferences.
Nothing would have been possible without my family who have always supported me during the last years. Above all I would like to thank Amaya for true love.